KOCAELI JOURNAL OF SCIENCE AND ENGINEERING

Kocaeli University

Kocaeli Journal of Science and Engineering

http://dergipark.org.tr/kojose

Unrestricted Pell and Pell – Lucas 2^N-ons

Öznur BAYRAKCI ÖZSOY [1] (iD) , Göksal BİLGİCİ [2, *] (iD)

[1] Department of Mathematics, Kastamonu University, Kastamonu, 37150, Turkey, **ORCID:** 0000-0003-2297-4183
[2] Department of Elementary Mathematics Education, Kastamonu University, Kastamonu, 37200, Turkey, **ORCID:** 0000-0001-9964-5578

Abstract

In this study, we define unrestricted Pell and Pell – Lucas hyper-complex numbers. We choose arbitrary Pell and Pell – Lucas numbers for the coefficients of the ordered basis $\{e_0, e_1, \cdots, e_{N-1}\}$ of hyper-complex 2^N-ons where $N \in \{0,1,2,3,4\}$ and call these hyper-complex numbers unrestricted Pell and Pell-Lucas 2^N-ons. We give generating functions and Binet formulas for these type of hyper-complex numbers. We also obtain some generalization of well – known identities such as Catalan's, Cassini's and d'Ocagne's identities.

1. Introduction

Pell numbers and Pell – Lucas numbers are defined by the following recursive relations

$P_0 = 0, \ P_1 = 1$ and $P_n = 2P_{n-1} + P_{n-2}$ for $n \geq 2$,
and

$Q_0 = 1, \ Q_1 = 1$ and $Q_n = 2Q_{n-1} + Q_{n-2}$ for $n \geq 2$
respectively. Pell numbers take their name from English mathematician John Pell after his studies on the equation $x^2 - dy^2 = (-1)^n$ where d is not a perfect square integer. Generating functions for the sequences $\{P_n\}_{n=0}^{\infty}$ and $\{Q_n\}_{n=0}^{\infty}$ are

$\sum_{n=0}^{\infty} P_n x^n = \frac{x}{1-2x-x^2}$ and $\sum_{n=0}^{\infty} Q_n x^n = \frac{2-x}{1-2x-x^2}$
respectively. Binet formulas for the Pell and Pell – Lucas numbers are

$$P_n = \frac{\gamma^n - \delta^n}{\gamma - \delta} \text{ and } Q_n = \frac{\gamma^n + \delta^n}{2}$$

respectively, where $\gamma = 1 + \sqrt{2}$ and $\delta = 1 - \sqrt{2}$ are the roots of the characteristic equation $x^2 - 2x - 1 = 0$. The positive root γ is known as "silver ratio" and plays a similar role to the golden ratio of Fibonacci and Lucas numbers.

There are some interesting applications of Fibonacci and Pell numbers. For example, all repdigits are expressed as the products of a Fibonacci or a Pell number [1]. Pell sequence is used for solving some Diophantine equations [2].

Hyper-complex numbers are usually constructed by using Cayley-Dickson Process. Complex numbers, quaternions, octonions and sedenions with Pell and Pell-Lucas numbers' coefficients are investigated in this study. There are many studies about Pell and Pell-Lucas hyper-complex numbers. We can refer to [3, 4, 5, 6, 7, 8, 9, 10, 11] for Pell and Pell-Lucas quaternions, to [5, 8, 10] for Pell and Pell-Lucas octonions and to [5] for Pell and Pell-Lucas sedenions. In all of these studies, authors choose the consecutive Pell and Pell-Lucas numbers as coefficients. The difference between this study and previous studies is that we choose random Pell and Pell-Lucas numbers as coefficients of hyper-complex numbers. A similar idea can be seen in [4]. In that study, the authors investigated the

---

* Corresponding Author: gbilgici@kastamonu.edu.tr

unrestricted Pell and Pell-Lucas quaternions, which is a special case of our study.

For $N = 0,1,2,3,4$ and $\vec{c} = (c_0 = 0, c_1, \ldots, c_{2^N-1})$ where $c_1, c_2, \ldots, c_{2^N-1}$ are integers, unrestricted Pell and Pell-Lucas 2^N-ons are defined by

$$P_{N,r}^{\vec{c}} = \sum_{i=0}^{2^N-1} P_{r+ci}\, e_i \text{ and } Q_{N,r}^{\vec{c}} = \sum_{i=0}^{2^N-1} Q_{r+ci}\, e_i \quad (1)$$

Table 1. Multiplication rules of the 2^N-ons for $N = 0,1,2,3,4$.

.	0	1	2	3	4	5	6	7	8	9	10	11	12	13	14	15
0	0	1	2	3	4	5	6	7	8	9	10	11	12	13	14	15
1	1	-0	3	-2	5	-4	-7	6	9	-8	-11	10	-13	12	15	-14
2	2	-3	-0	1	6	7	-4	-5	10	11	-8	-9	-14	-15	12	13
3	3	2	-1	-0	7	-6	5	-4	11	-10	9	-8	-15	14	-13	12
4	4	-5	-6	-7	-0	1	2	3	12	13	14	15	-8	-9	-10	-11
5	5	4	-7	6	-1	-0	-3	2	13	-12	15	-14	9	-8	11	-10
6	6	7	4	-5	-2	3	-0	-1	14	-15	-12	13	10	-11	-8	9
7	7	-6	5	4	-3	-2	1	-0	15	14	-13	-12	11	10	-9	-8
8	8	-9	-10	-11	-12	-13	-14	-15	-0	1	2	3	4	5	6	7
9	9	8	-11	10	-13	12	15	-14	-1	-0	-3	2	-5	4	7	-6
10	10	11	8	-9	-14	-15	12	13	-2	3	-0	-1	-6	-7	4	5
11	11	-10	9	8	-15	14	-13	12	-3	-2	1	-0	-7	6	-5	4
12	12	13	14	15	8	-9	-10	-11	-4	5	6	7	-0	-1	-2	-3
13	13	-12	15	-14	9	8	11	-10	-5	-4	7	-6	1	-0	3	-2
14	14	-15	-12	13	10	-11	8	9	-6	-7	-4	5	2	-3	-0	1
15	15	14	-13	-12	11	10	-9	8	-7	6	-5	-4	3	2	-1	-0

According to the context mentioned above, we regard 1-ons: real numbers, 2-ons: complex numbers, 3-ons: quaternions, 4-ons: octonions and 5-ons: sedenions. From the definition (1) and the definitions of Pell and Pell-Lucas numbers following recursive relations can be found easily:

$$P_{N,r}^{\vec{c}} = 2P_{N,r-1}^{\vec{c}} + P_{N,r-2}^{\vec{c}} \text{ and } Q_{N,r}^{\vec{c}} = 2Q_{N,r-1}^{\vec{c}} + Q_{N,r-2}^{\vec{c}}. \quad (2)$$

The special cases for unrestricted Pell and Pell-Lucas 2^N-ons are in the following table.

Table 2. Special cases

N	$\vec{c}$	Sequences
0	(0)	Classical Pell and Pell-Lucas numbers
1	(0,1)	Gaussian Pell and Pell-Lucas numbers
2	(0,1,2,3)	Pell and Pell-Lucas quaternions
3	(0,1,...,7)	Pell and Pell-Lucas octonions
4	(0,1,...,15)	Pell and Pell-Lucas sedenions

Example 1. The octonion $P_8 + P_{12}e_1 + P_{-16}e_3 + P_{21}e_7$ can be represent by $P_{3,8}^{(0,4,-8,-24,-8,-8,-8,13)}$

The well-known identities $P_{-n} = (-1)^{n+1}P_n$ and $Q_{-n} = (-1)^n Q_n$ give

$$P_{N,-r}^{\vec{c}} = (-1)^{r+1}\left[\sum_{i=0}^{2^N-1} (-1)^{c_i} P_{r-c_i}e_i\right]$$

and

$$Q_{N,-r}^{\vec{c}} = (-1)^{r}\left[\sum_{i=0}^{2^N-1} (-1)^{c_i} Q_{r-c_i}e_i\right].$$

2. Binet Formulas and Generating Functions

The next theorem gives the Binet formulas for the unrestricted Pell and Pell – Lucas 2^N-ons.

Theorem 2.1. For $N = 0,1,2,3,4$ and any integers $c_1, c_2, \ldots, c_{2^N-1}$, the r-th unrestricted Pell and Pell-Lucas 2^N-on are

$$P_{N,r}^{\vec{c}} = \frac{\breve{\gamma}\gamma^r - \breve{\delta}\delta^r}{\gamma - \delta} \text{ and } Q_{N,r}^{\vec{c}} = \frac{\breve{\gamma}\gamma^r + \breve{\delta}\delta^r}{2}$$

where

$$\breve{\gamma} = \sum_{i=0}^{2^N-1} \gamma^{c_i} e_i \text{ and } \breve{\delta} = \sum_{i=0}^{2^N-1} \delta^{c_i} e_i.$$

respectively.

Proof. From the definitions of unrestricted Pell 2^N-ons and the Binet formula for the Pell numbers, we have

$$P_{N,r}^{\vec{c}} = P_r + P_{n+c_1}e_1 + \cdots + P_{n+c_{2^N-1}}e_{2^N-1}$$

respectively. Here multiplication rules of the standard basis $\{e_0 = 1, e_1, e_2, \ldots, e_{2^N-1}\}$ of the hyper-complex numbers for $N = 0,1,2,3,4$ are in the following table [12]. We set $i \equiv e_i$ for $i = 0,1,\ldots,15$.

$$= \frac{1}{\gamma - \delta}(\gamma^r - \delta^r + (\gamma^{r+c_1} - \delta^{r+c_1})e_1$$
$$+ (\gamma^{r+c_2} - \delta^{r+c_2})e_2$$
$$+ \qquad \cdots$$
$$+ (\gamma^{r+c_{2^N-1}} - \delta^{r+c_{2^N-1}})e_{2^N-1})$$

$$= \frac{1}{\gamma - \delta}[\gamma^r(\gamma^{c_1} + \gamma^{c_2} + \cdots + \gamma^{c_{(2^N-1)}})$$
$$+ \delta^r(\delta^{c_1} + \delta^{c_2} + \cdots + \delta^{c_{(2^N-1)}})]$$

The last equation gives the Binet formula for the unrestricted Pell 2^N-ons. Binet formula for the unrestricted Pell-Lucas 2^N-ons can be obtained similarly. ∎

Generating functions for the unrestricted Pell and Pell – Lucas 2^N-ons sequences are given in the next theorem.

Theorem 2.2. The generating functions for the sequences $\{P_{N,r}^{\vec{c}}\}_{r=0}^{\infty}$ and $\{Q_{N,r}^{\vec{c}}\}_{r=0}^{\infty}$ are

$$\sum_{i=0}^{\infty} P_{N,i}^{\vec{c}} x^i = \frac{P_{N,0}^{\vec{c}} + x(P_{N,1}^{\vec{c}} - 2P_{N,0}^{\vec{c}})}{1 - 2x - x^2}$$

and

$$\sum_{i=0}^{\infty} Q_{N,i}^{\vec{c}} x^i = \frac{Q_{N,0}^{\vec{c}} + x(Q_{N,1}^{\vec{c}} - 2Q_{N,0}^{\vec{c}})}{1 - 2x - x^2}.$$

respectively.

Since the proofs are very straightforward, we don't give the proofs. Now we need to define the following set for later use. For $i \in \{1,2,\dots,2^{N-1}-1\}$, we define the set

$$S_i = \{(j,k): e_i e_j = e_k, 1 \le j, k \le 2^{N-1}-1, i \ne j, i \ne k \ ve \ j \ne k\}. \quad (3)$$

By using this set, we give the following lemma.

Lemma 2.3. For $N \in \{0,1,2,3,4\}$, we have
$$\breve{\gamma}\breve{\delta} = Y_N^{\vec{c}} + 2\sqrt{2}Z_N^{\vec{c}} \text{ and } \breve{\delta}\breve{\gamma} = Y_N^{\vec{c}} - 2\sqrt{2}Z_N^{\vec{c}} \quad (4)$$
where

$$Y_N^{\vec{c}} = 2Q_{N,0}^{\vec{c}} - \sum_{i=0}^{2^N-1}(-1)^{c_i}$$

and

$$Z_N^{\vec{c}} = \sum_{i=1}^{2^N-1} e_i \sum_{(j,k)\in S_i}(-1)^{c_k} P_{c_j-c_k}.$$

Proof. We prove the case N = 4. The others can be proved similarly. We have
$$Y_4^{\vec{c}} = Q_{4,0}^{\vec{c}} + (-1)^{c_1+1} + (-1)^{c_2+1} + \cdots$$
$$+ (-1)^{c_{15}+1} - 1. \quad (5)$$
Each versor e_i (i = 1,…,15) in $Z_4^{\vec{c}}$ contains seven terms. We have to calculate the sets S_i for each versor e_i. From Table 1, we obtain
$S_1 = \{(2,3),(4,5),(7,6),(8,9),(11,10),(13,12),(14,15)\}$,
$S_2 = \{(3,1),(4,6),(5,7),(8,10),(9,11),(14,12),(15,13)\}$,

$S_3 = \{(1,2),(6,5),(4,7),(10,9),(8,11),(15,12),(13,14)\}$,
$S_4 = \{(5,1),(6,2),(7,3),(8,12),(9,13),(10,14),(11,15)\}$,
$S_5 = \{(7,2),(1,4),(3,6),(12,9),(14,11),(8,13),(10,15)\}$,
$S_6 = \{(5,3),(2,4),(1,7),(15,9),(12,10),(11,13),(8,14)\}$
$S_7 = \{(6,1),(3,4),(2,5),(13,10),(12,11),(9,14),(8,15)\}$,
$S_8 = \{(9,1),(10,2),(11,3),(12,4),(13,5),(14,6),(15,7)\}$,
$S_9 = \{(11,2),(13,4),(14,7),(1,8),(3,10),(5,12),(6,15)\}$,
$S_{10} = \{(9,3),(14,4),(15,5),(2,8),(1,11),(6,12),(7,13)\}$,
$S_{11} = \{(10,1),(15,4),(13,6),(3,8),(2,9),(7,12),(5,14)\}$,
$S_{12} = \{(9,5),(10,6),(11,7),(4,8),(1,13),(2,14),(3,15)\}$,
$S_{13} = \{(12,1),(14,3),(10,7),(5,8),(4,9),(6,11),(2,15)\}$,
$S_{14} = \{(15,1),(12,2),(11,5),(6,8),(7,9),(4,10),(3,13)\}$,
and
$S_{15} = \{(13,2),(12,3),(9,6),(7,8),(5,10),(4,11),(1,14)\}$.
So we have

$$Z_4^{\vec{c}} = [(-1)^{c_3}P_{c_2-c_3} + (-1)^{c_5}P_{c_4-c_5} + (-1)^{c_6}P_{c_7-c_6}$$
$$+ (-1)^{c_9}P_{c_8-c_9} + (-1)^{c_{10}}P_{c_{11}-c_{10}}$$
$$+ (-1)^{c_{12}}P_{c_{13}-c_{12}} + (-1)^{c_{15}}P_{c_{14}-c_{15}}]e_1$$
$$+ [(-1)^{c_1}P_{c_3-c_1} + (-1)^{c_6}P_{c_4-c_6} + (-1)^{c_7}P_{c_5-c_7}$$
$$+ (-1)^{c_{10}}P_{c_8-c_{10}} + (-1)^{c_{11}}P_{c_9-c_{11}}$$
$$+ (-1)^{c_{12}}P_{c_{14}-c_{12}} + (-1)^{c_{13}}P_{c_{15}-c_{13}}]e_2$$
$$+ [(-1)^{c_2}P_{c_1-c_2} + (-1)^{c_5}P_{c_6-c_5} + (-1)^{c_7}P_{c_4-c_7}$$
$$+ (-1)^{c_9}P_{c_{10}-c_9} + (-1)^{c_{11}}P_{c_8-c_{11}}$$
$$+ (-1)^{c_{12}}P_{c_{15}-c_{12}} + (-1)^{c_{14}}P_{c_{13}-c_{14}}]e_3$$
$$+ [(-1)^{c_1}P_{c_5-c_1} + (-1)^{c_2}P_{c_6-c_2} + (-1)^{c_3}P_{c_7-c_3}$$
$$+ (-1)^{c_{12}}P_{c_8-c_{12}} + (-1)^{c_{13}}P_{c_9-c_{13}}$$
$$+ (-1)^{c_{14}}P_{c_{10}-c_{14}} + (-1)^{c_{15}}P_{c_{11}-c_{15}}]e_4$$

$$+ [(-1)^{c_2}P_{c_7-c_2} + (-1)^{c_4}P_{c_1-c_4} + (-1)^{c_6}P_{c_3-c_6}$$
$$+ (-1)^{c_9}P_{c_{12}-c_9} + (-1)^{c_{13}}P_{c_{14}-c_{11}}$$
$$+ (-1)^{c_{13}}P_{c_8-c_{13}} + (-1)^{c_{15}}P_{c_{10}-c_{15}}]e_5$$
$$+ [(-1)^{c_3}P_{c_5-c_3} + (-1)^{c_4}P_{c_2-c_4} + (-1)^{c_7}P_{c_1-c_7}$$
$$+ (-1)^{c_9}P_{c_{15}-c_9} + (-1)^{c_{10}}P_{c_{12}-c_{10}}$$
$$+ (-1)^{c_{13}}P_{c_{11}-c_{13}} + (-1)^{c_{14}}P_{c_8-c_{14}}]e_6$$
$$+ [(-1)^{c_1}P_{c_6-c_1} + (-1)^{c_4}P_{c_3-c_4} + (-1)^{c_5}P_{c_2-c_5}$$
$$+ (-1)^{c_{10}}P_{c_{13}-c_{10}} + (-1)^{c_{11}}P_{c_{12}-c_{11}}$$
$$+ (-1)^{c_{14}}P_{c_9-c_{14}} + (-1)^{c_{15}}P_{c_8-c_{15}}]e_7.$$

The last equation and Eq.(5) give the first equation in Eq.(4) for N = 4. ∎

3. Some Identities

In this section, we give generalizations for some well-known identities about Pell and Pell-Lucas hyper-complex numbers. We use $P_r^{\vec{c}}$ and $Q_r^{\vec{c}}$ instead of $P_{N,r}^{\vec{c}}$ and $Q_{N,r}^{\vec{c}}$ respectively for abbreviation.

Theorem 3.1. (Vajda's identity). For any integers $n, r, s, c_0, c_1, c_2, \ldots, c_{2^N-1}$, we have

$$P_{n+r}^{\vec{c}} P_{n+s}^{\vec{c}} - P_n^{\vec{c}} P_{n+r+s}^{\vec{c}} = (-1)^n P_r (P_s Y_N^{\vec{c}} - 2Q_s Z_N^{\vec{c}}) \quad (6)$$

and

$$Q_{n+r}^{\vec{c}} Q_{n+s}^{\vec{c}} - Q_n^{\vec{c}} Q_{n+r+s}^{\vec{c}} = 2(-1)^{n+1} P_r (P_s Y_N^{\vec{c}} - 2Q_s Z_N^{\vec{c}}). \quad (7)$$

Proof. From the Binet formula for the unrestricted Pell 2^N-ons, we get

$$P_{n+r}^{\vec{c}} P_{n+s}^{\vec{c}} - P_n^{\vec{c}} P_{n+r+s}^{\vec{c}}$$
$$= \frac{1}{(\gamma - \delta)^2} [(\breve{\gamma}\gamma^{n+r} - \breve{\delta}\delta^{n+r})(\breve{\gamma}\gamma^{n+s} - \breve{\delta}\delta^{n+s})$$
$$- (\breve{\gamma}\gamma^n - \breve{\delta}\delta^n)(\breve{\gamma}\gamma^{n+r+s} - \breve{\delta}\delta^{n+r+s})]$$
$$= \frac{1}{(\gamma - \delta)^2} [(\breve{\gamma})^2\gamma^{2n+r+s} + (\breve{\delta})^2\delta^{2n+r+s}$$
$$- \overline{(\gamma\delta)}\gamma^{n+r}\delta^{n+s} - \overline{(\delta\gamma)}\gamma^{n+s}\delta^{n+r}$$
$$- (\breve{\gamma})^2\gamma^{2n+r+s} - \overline{(\gamma)}^2\delta^{2n+r+s}$$
$$+ \overline{(\gamma\delta)}\gamma^n\delta^{n+r+s} + \overline{(\delta\gamma)}\gamma^{n+r+s}\delta^n]$$
$$= \frac{(\gamma\delta)^n}{(\gamma - \delta)^2} [-\overline{(\gamma\delta)}\gamma^r\delta^s - \overline{(\delta\gamma)}\gamma^s\delta^r + \overline{(\gamma\delta)}\delta^{r+s}$$
$$+ \overline{(\delta\gamma)}\gamma^{r+s}]$$
$$= \frac{(-1)^n}{(\gamma - \delta)^2} [(\gamma^r - \delta^r)(-\overline{(\gamma\delta)}\delta^s + \overline{(\delta\gamma)}\gamma^s)]$$
$$= \frac{(-1)^n P_r}{(\gamma - \delta)} [\overline{(\delta\gamma)}\gamma^s - \overline{(\gamma\delta)}\delta^s]$$
$$= \frac{(-1)^n P_r}{2\sqrt{2}} [(Y_N^{\vec{c}} - 2\sqrt{2}Z_N^{\vec{c}})\gamma^s - (Y_N^{\vec{c}} - 2\sqrt{2}Z_N^{\vec{c}})\delta^s].$$

The last equation gives Eq.(6). Eq.(7) can proved similarly. ∎

If we take $s = -r$ and use the identities $P_r P_{-r} = -(-1)^r P_r^2$ and $2P_r Q_{-r} = (-1)^r P_{2r}$, we obtain Catalan's identities for the unrestricted Pell and Pell – Lucas 2^N-ons given in the next theorem.

Theorem 3.2. (Catalan's identities) For $N \in \{0,1,2,3,4\}$ and any integers $n, r, c_1, c_2, \cdots, c_{2^N-1}$, we have

$$P_{n+r}^{\vec{c}} P_{n-r}^{\vec{c}} - [P_n^{\vec{c}}]^2 = (-1)^{n+r+1} (Y_N^{\vec{c}} P_r^2 + Z_N^{\vec{c}} P_{2r}) \quad (8)$$

and

$$Q_{n+r}^{\vec{c}} Q_{n-r}^{\vec{c}} - [Q_n^{\vec{c}}]^2 = 2(-1)^{n+r} (Y_N^{\vec{c}} P_r^2 + Z_N^{\vec{c}} P_{2r}). \quad (9)$$

If we take $r = 1$ in Theorem 3.2, we obtain Cassini's identities the unrestricted Pell and Pell – Lucas 2^N-ons.

Theorem 3.3. (Cassini's identities) For $N \in \{0,1,2,3,4\}$ and any integers $r, c_1, c_2, \cdots, c_{2^N-1}$, we have

$$P_{n+1}^{c} P_{n-1}^{c} - [P_n^{c}]^2 = (-1)^n (Y_N^{\vec{c}} + 2Z_N^{\vec{c}}) \quad (10)$$

and

$$Q_{n+1}^{c} Q_{n-1}^{c} - [Q_n^{c}]^2 = -2(-1)^n (Y_N^{\vec{c}} + 2Z_N^{\vec{c}}) \quad (11)$$

The following theorem gives the d'Ocagne's identities for the unrestricted Pell and Pell – Lucas 2^N-ons.

Theorem 3.4. (d'Ocagne's identities) For $N \in \{0,1,2,3,4\}$ and any integers $m, n, c_1, c_2, \cdots, c_{2^N-1}$, we have

$$P_m^{c} P_{n+1}^{c} - P_{m+1}^{c} P_n^{c} = (-1)^n (Y_N^{\vec{c}} p_{m-n} + 2Z_N^{\vec{c}} q_{m-n}) \quad (12)$$

and

$$Q_m^{c} Q_{n+1}^{c} - Q_{m+1}^{c} Q_n^{c} = -2(-1)^n (Y_N^{\vec{c}} p_{m-n} + 2Z_N^{\vec{c}} q_{m-n}). \quad (13)$$

Proof. By using the Binet formula for the unrestricted Pell 2^N-ons, we obtain

$$P_m^{c} P_{n+1}^{c} - P_{m+1}^{c} P_n^{c}$$
$$= \frac{1}{8} [(\breve{\gamma}\gamma^m - \breve{\delta}\delta^m)(\breve{\gamma}\gamma^{n+1}$$
$$- \breve{\delta}\delta^{n+1})$$
$$- (\breve{\gamma}\gamma^{m+1} - \breve{\delta}\delta^{m+1})(\breve{\gamma}\gamma^n - \breve{\delta}\delta^n)]$$
$$= \frac{1}{8} (-\breve{\gamma}\breve{\delta}\gamma^m\delta^{n+1} - \breve{\delta}\breve{\gamma}\gamma^{n+1}\delta^m + \breve{\gamma}\breve{\delta}\gamma^{m+1}\delta^n$$
$$+ \breve{\delta}\breve{\gamma}\gamma^n\delta^{m+1})$$
$$= \frac{(-1)^n}{8} [\breve{\gamma}\breve{\delta}(\gamma - \delta)\gamma^{m-n} - \breve{\delta}\breve{\gamma}(\gamma - \delta)\delta^{m-n}]$$
$$= \frac{(-1)^n}{2\sqrt{2}} [\breve{\gamma}\breve{\delta}\gamma^{m-n} - \breve{\delta}\breve{\gamma}\delta^{m-n}]$$
$$= \frac{(-1)^n}{2\sqrt{2}} [(Y_N^{\vec{c}} + 2\sqrt{2}Z_N^{\vec{c}})\gamma^{m-n} - (Y_N^{\vec{c}} - 2\sqrt{2}Z_N^{\vec{c}})\delta^{m-n}]$$

The last identity gives Eq.(12). Eq.(13) can be obtained similarly. ∎

We give many identities in the next theorem, which can be proved by using the Binet formulas or definitions of the unrestricted Pell and Pell – Lucas 2^N-ons and well-known identities for the classical Pell and Pell-Lucas numbers.

Theorem 3.5. For $N \in \{0,1,2,3,4\}$ and any integers $m, n, c_1, c_2, \cdots, c_{2^N-1}$, we have

$$P_m^{\vec{c}} + P_{m-1}^{\vec{c}} = Q_m^{\vec{c}},$$
$$Q_m^{\vec{c}} + Q_{m-1}^{\vec{c}} = 2P_m^{\vec{c}},$$
$$P_m^{\vec{c}} + Q_m^{\vec{c}} = P_{m+1}^{\vec{c}},$$
$$P_{m+1}^{\vec{c}} + P_{m-1}^{\vec{c}} = 2Q_m^{\vec{c}}$$
$$Q_{m+1}^{\vec{c}} + Q_{m-1}^{\vec{c}} = 4P_m^{\vec{c}},$$
$$Q_{m+n}^{\vec{c}} + (-1)^n Q_{m-n} = 2q_n Q_m^{\vec{c}},$$
$$P_{m+n}^{\vec{c}} + (-1)^n P_{m-n}^{\vec{c}} = 2q_n P_m^{\vec{c}},$$
$$P_{m-n}^{\vec{c}} = (-1)^n (P_{n-1} P_m^{\vec{c}} - P_n P_{m-1}^{\vec{c}}),$$
$$[Q_m^{\vec{c}}]^2 - 2[P_m^{\vec{c}}]^2 = (-1)^m Y_N^{\vec{c}}$$

$$P_n^{\vec{c}} + P_{n-1}^{\vec{c}} = Q_n^{\vec{c}},$$
$$Q_n^{\vec{c}} + Q_{n-1}^{\vec{c}} = 2P_n^{\vec{c}},$$
$$P_n^{\vec{c}} + Q_n^{\vec{c}} = P_{n+1}^{\vec{c}},$$
$$2P_n^{\vec{c}} + Q_n^{\vec{c}} = Q_{n+1}^{\vec{c}},$$
$$2Q_n^{\vec{c}} + 3P_n^{\vec{c}} = P_{n+2}^{\vec{c}}$$
$$3Q_n^{\vec{c}} + 4P_n^{\vec{c}} = Q_{n+2}^{\vec{c}}$$
$$Q_{n+1}^{\vec{c}} - Q_n^{\vec{c}} = 2P_n^{\vec{c}},$$
$$P_{n+1}^{\vec{c}} + P_{n-1}^{\vec{c}} = 2Q_n^{\vec{c}},$$
$$Q_{n+1}^{\vec{c}} + Q_{n-1}^{\vec{c}} = 4P_n^{\vec{c}}$$
$$P_n^{\vec{c}} + P_{n+1}^{\vec{c}} + P_{n+3}^{\vec{c}} = 2P_{n+2}^{\vec{c}}$$
$$Q_n^{\vec{c}} + Q_{n+1}^{\vec{c}} + Q_{n+3}^{\vec{c}} = 3Q_{n+2}^{\vec{c}},$$
$$P_{n+1}^{\vec{c}} - P_{n-1}^{\vec{c}} = 2P_n^{\vec{c}}$$
$$Q_{n+1}^{\vec{c}} - Q_{n-1}^{\vec{c}} = 2Q_n^{\vec{c}},$$
$$P_{n+2}^{\vec{c}} + P_{n-2}^{\vec{c}} = 6P_n^{\vec{c}},$$
$$Q_{n+2}^{\vec{c}} + Q_{n-2}^{\vec{c}} = 6Q_n^{\vec{c}}$$
$$P_{n+2}^{\vec{c}} - P_{n-2}^{\vec{c}} = 4Q_n^{\vec{c}},$$
$$Q_{n+2}^{\vec{c}} - Q_{n-2}^{\vec{c}} = 8P_n^{\vec{c}},$$
$$2P_n^{\vec{c}} + Q_n^{\vec{c}} = Q_{n+1}^{\vec{c}},$$
$$2P_n^{\vec{c}} + Q_{n+2}^{\vec{c}} = 3Q_{n+1}^{\vec{c}},$$
$$P_{n+1}^{\vec{c}} + Q_{n-1}^{\vec{c}} = 3P_n^{\vec{c}}$$
$$Q_n^{\vec{c}} Q_{n+1}^{\vec{c}} - 2P_n^{\vec{c}} P_{n+1}^{\vec{c}} = (-1)^n \left[Y_N^{\vec{c}} - 4Z_N^{\vec{c}} \right],$$
$$P_n^{\vec{c}} P_{n+3}^{\vec{c}} - P_{n+1}^{\vec{c}} P_{n+2}^{\vec{c}} = (-1)^{n+1} \left[2Y_N^{\vec{c}} - 6Z_N^{\vec{c}} \right],$$
$$Q_n^{\vec{c}} Q_{n+3}^{\vec{c}} - Q_{n+1}^{\vec{c}} Q_{n+2}^{\vec{c}} = (-1)^n \left[4Y_N^{\vec{c}} - 12Z_N^{\vec{c}} \right],$$
$$P_n^{\vec{c}} Q_{n-1}^{\vec{c}} - Q_n^{\vec{c}} P_{n-1}^{\vec{c}} = (-1)^{n-1} \left[Y_N^{\vec{c}} + 2Z_N^{\vec{c}} \right].$$

4. Conclusions

There are many studies on hyper-complex numbers, such as quaternions, octonions and sedenions, whose coefficients are Pell and Pell-Lucas numbers. Current study differs from all of them by the choice of coefficients. Placing successive Pell and Pell-Lucas numbers in order for the coefficients of versors is common. Our definition provides to select arbitrary Pell or Pell-Lucas numbers for the coefficients of versors. We call this kind of hyper-complex numbers unrestricted Pell and unrestricted Pell-Lucas hyper-complex numbers. After introducing these numbers, we present Binet-like formulas for them and using Binet formulas, we obtain a numbers of identities for Pell and Pell-Lucas quaternions, octonions and sedenion. Although we limit N to 1 to 4, one can easily realize that there is no need such a restriction actually.

Declaration of Ethical Standards

The author(s) of this article declare that the materials and methods used in this study do not require ethical committee permission and/or legal-special permission

Conflict of Interest

The authors declare that they have no known competing financial interests or personal relationships that could have appeared to influence the work reported in this paper.

References

[1] Çağman, A., 2021. Repdigits as product of Fibonacci and Pell numbers. Turkish Journal of Science, **6**(1), pp. 31-35.

[2] Çağman, A., 2021. An approach to Pillai's problem with the Pell sequence and the powers of 3. Miskolc Mathematical Notes, **22**(2), pp. 599-610.

[3] Aydın F. T., Köklü K., Yüce S., 2017. Generalized dual Pell quaternions. Notes on Number Theory and Discrete Mathematics, **23**(4), pp. 66-84.

[4] Bilgici G., Catarino P., 2018. Unrestricted Pell and Pell-Lucas quaternions. International Journal of Mathematics and Systems Science, **1**(3), pp. 1-10.

[5] Catarino P., 2016. The modified Pell and the modified k-Pell quaternions and octonions. Advances in Applied Clifford Algebras, **26**(2), pp. 577-590.

[6] Catarino P., 2018. Bicomplex k-Pell quaternions. Computational Methods and Function Theory, pp. 1-12.

[7] Catarino P., 2018. k-Pell, k-Pell–Lucas and modified k-Pell sedenions. Asian-European Journal of Mathematics, **12**(2), 1950018, pp. 1-10.

[8] Catarino P., Vasco P., 2017. On dual - Pell quaternions and octonions. Mediterranean Journal of Mathematics, **14**(2), 75.

[9] Çimen C.B., İpek A., 2016. On Pell quaternions and Pell-Lucas quaternions. Advances in Applied Clifford Algebras, **26**(1), pp. 39-51.

[10] Szynal-Liana A., Włoch I., 2016. The Pell quaternions and the Pell octonions. Advances in Applied Clifford Algebras, **26**(1), pp. 435-440.

[11] Tokeşer Ü., Ünal Z., Bilgici G., 2017. Split Pell and Pell–Lucas quaternions. Advances in Applied Clifford Algebras, **27**(2), pp. 1881-1893.

[12] Cawagas R.E., 2004. On the structure and zero divisors of the Cayley-Dickson sedenion algebra. Discussiones Mathematicae-General Algebra and Applications, **24**(2), pp. 251-265.

Kocaeli University

Kocaeli Journal of Science and Engineering
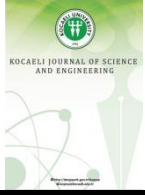
Energy Consideration of a Capacitor Modelled Using Conformal Fractional-Order Derivative

Utku PALAZ [1] (iD), Reşat MUTLU [2, *] (iD)

[1] University of Birmingham, Birmingham, United Kingdom, **ORCID:** *0000-0003-4579-0424*
[2] Department of Electronics and Telecommunication Engineering, Namık Kemal University, Çorlu, Tekirdağ, Turkey, **ORCID:** *0000-0003-0030-7136*

Abstract

Fractional order circuit elements have become important parts of electronic circuits to model systems including supercapacitors, filters, and many more. The conformal fractional derivative (CFD), which is a new basic fractional derivative, has been recently used to model supercapacitors successfully. It is essential to know how electronic components behave under excitation with different types of voltage and current sources. A CFD capacitor is not a well-known element and its usage in circuits is barely examined in the literature. In this research, it is examined how to calculate the stored energy of a CFD capacitor with a series resistor supplied from a DC voltage source. The solutions given in this study may be used in circuits where supercapacitors are used.

1. Introduction

Fractional derivative (FD) first appeared in a note which was written to L'Hospital in 1695 [1]. In the last decades, the application of fractional calculus has attracted the attention of many fields of science thanks to its applicability in many subjects [2-3]. The electrical transmission line analysis circa 1890 was described by using fractional derivate operators by Oliver Heaviside [4]. The fractional-order circuits are suitable elements to model different types of elements including capacitors, inductors and memristors [5-10]. Moreover, the fractional-order circuits elements can be used to model or design all sorts of filters, controllers and oscillators [7-8, 11-15]. The new simple fractional derivative is called "the conformable fractional derivative (CFD)" depending on the familiar limit definition of the derivative of a function and that breaks with other definitions in 2014 [16]. This theory is analysed and improved with some approaches in [17-18]. Nonetheless, a

CFD is simply not a fractional derivative; it is clearly a first-order derivative which is multiplied by an additional factor depending on the independent variable. This new description has the benefits of being dissimilar from other types of fractional differentials and can be thought of as a natural extension of the classical one. It is usable and suitable for many enlargements to classical use of calculus, such as Taylor power series extension, the mean value problem, the product of two functions, and many other fields in Math. There is an obvious difference between the Riemann-Liouville fractional derivative of which a constant is not zero and the conformal fractional derivative of which a constant equal zero. Because of this property, the conformal fractional derivative has become an interesting topic and a hot study area for researchers. The conformal derivative has also outweighed the other types of fractional derivatives when compared with them due to its simpleness and showing similar performance [18]. Fractional RC and LC electrical circuits have been examined in [19]. Along

---

with other electrical circuit elements, supercapacitors have also been modelled with fractional circuit elements in [20-22]. Caputo and CFD fractional-order derivatives are applied in the analysis of the fractional electrical circuits fed with a sinusoidal signal [23-24]. Analytical solutions of electrical circuits modelled with CFD are given in [25]. Electrical circuits described by fractional conformable derivatives have been examined in [25]. An electric circuit containing a supercapacitor modelled with the CFD has been inspected in [26].

The stored energy in an LTI capacitor is formulated in the essential course books. Furthermore, energy efficiency is an important area in many fields of electronics. Studies of the circuits with LTI capacitors and their efficiency are examined in the literature [27-28]. A capacitor is designed for storing energy; therefore, energy consideration is one of the most important topics for all kinds of capacitors such as LTIs, supercapacitors, CFD capacitors, etc. [29]. The energy of the CFD capacitor is considered an interesting research area [26]. The energy of the capacitors modeled with FD is inspected in [29-30] to find usable results. To the best of our knowledge, a method to calculate the energy of the CFD capacitors is not given in the literature yet. In this study, first, it is shown that just a voltage-dependent energy formula for the CFD capacitors is not possible due to the time dependence, and then, it is shown that using the CFD voltage and current as a function of time obtained from the circuit analysis, the energy stored in a CFD capacitor can be found. As an example, the energy stored in a CFD capacitor connected to a series resistor supplied from a constant source has been calculated and its charging energy efficiency is examined. The required waveforms are plotted with Matlab™. Energy and the energy efficiency of the circuit are examined for different α values to provide insight into how a CFD capacitor gives different responses with respect to time. Its charging energy efficiency has been compared to that of an LTI capacitor.

The remainder of the paper is organized as follows. In the second section, the CFD and the CFD capacitor model are presented. In the third section, an LTI capacitor circuit with a series resistor by a DC supply and its stored energy is reviewed. In the fourth section, it is shown that it is not possible to find a generic stored energy formula for a CFD capacitor. In the fifth section, the charging of a CFD capacitor with a series resistor supplied from a constant voltage source is examined and its stored energy is found using the incomplete gamma function. In the sixth section, the circuit is simulated, and the energy of all circuit elements and their charging efficiency are calculated. The paper is finished with the conclusion section.

2. The Conformal Fractional Derivative and the CFD Capacitor Constitutional Law

The Conformal Fractional Derivative (CFD), which is introduced in [16], for $0 < \alpha \leq 1$ and $t \geq 0$, it is described as :

$$D_\alpha f(t) = \frac{d^\alpha f(t)}{dt^\alpha} = f'(t)t^{1-\alpha} = \frac{df(t)}{dt}t^{1-\alpha} \tag{1}$$

More information about the CFD can be found in [16-18]. In literature, it has been shown that the fractional derivate can be used to model supercapacitors [26, 31-33]. The CFD capacitor constitutive law given in [29] can be expressed as follows:

$$i_{c_\alpha}(t) = C_\alpha \frac{d^\alpha v_C(t)}{dt^\alpha} \tag{2}$$

where $i_C(t), v_C(t)$ and C_α are current, voltage and capacitor coefficient of the CFD capacitor respectively.

Eq. (2) is used to model the CFD capacitor throughout the rest of the paper.

3. The Stored Energy in an LTI Capacitor and the Energy Efficiency of such Circuit when Charged Throughout a Series Resistor by a DC Voltage Source

The circuit of an LTI capacitor is shown in Figure 1 when the LTI capacitor is connected in series with an LTI resistor supplied by a DC input signal. The fundamental solution of circuit is well-known and can be found in most of the fundamentals of the circuit theory books [34-36]. Also, the current, voltage and energy of the LTI capacitor are given as:

$$i_C(t) = \frac{V_{DC}e^{-t/\tau}}{R_s} \tag{3}$$

$$V_C(t) = V_{DC}\left(1 - e^{-t/\tau}\right) \tag{4}$$

$$E_C = \frac{C_s V_c^2}{2} \tag{5}$$

If the LTI capacitor is not initially charged, its voltage rises from zero to V_{DC}. Total energy loss in the resistor and the energy radiated into the medium is simply equal to the energy stored in the LTI capacitor. In [37], it is shown that the total energy needed to charge the LTI capacitor does not depend on the resistance of the circuit shown in Figure 1. The energy value would not change even though the resistance of the series resistor was time-dependent [37]. The energy efficiency of the circuit is equal to fifty percent.

When the capacitor is charged by a constant voltage source, the same amount of energy is dissipated.
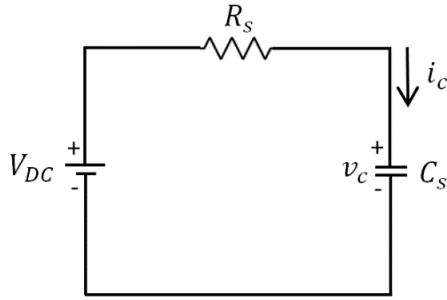
Figure 1. An LTI Capacitor supplied a constant voltage source

4. The Energy Formula of a CFD Capacitor

In this part of the study, the stored energy of a CFD capacitor is shown to be time dependent. Using Eq. (2), the CFD capacitor power is written as

$$P_{c_\alpha} = V_{c_\alpha}(t) i_{c_\alpha}(t) = V_{c_\alpha}(t) C_\alpha \frac{d^\alpha v_C(t)}{dt^\alpha} = C_\alpha V_{c_\alpha}(t) \frac{dv_{c_\alpha}(t)}{dt} t^{1-\alpha} \quad (6)$$

Then, the energy of the CFD capacitor could be described as

$$E_{c_\alpha}(t) = \int_{t=0}^{t} P_{c_\alpha}(t) dt = \int_{t=0}^{t} V_{c_\alpha}(t) C_\alpha \frac{d^\alpha v_C(t)}{dt^\alpha} dt$$

$$E_{c_\alpha} = C_\alpha \int_{t=0}^{t} V_{c_\alpha}(t) \frac{dv_{c_\alpha}(t)}{dt} t^{1-\alpha} dt \quad (7)$$

The Eq. (7) is time dependent. That's why a general energy formula just depending on the capacitor voltage like Eq. (5) cannot be obtained except for $\alpha = 1$. However, if the CFD voltage as a function of time is known, it might be possible to obtain an energy formula for the circuit where it is placed. The integral may still be not solvable for some input waveforms. In this case, numerical integration methods such as the trapezoidal rule can be employed to calculate the stored energy in the CFD capacitor.

5. The Energy Calculation of a CFD Capacitor

When the LTI capacitor in Figure 1 is replaced with a CFD capacitor, the circuit shown in Figure 2 is obtained. For $t \geq 0$, the circuit is described with the following differential equation:

$$V_{DC} = i_{c_\alpha}(t) R_s + v_{c_\alpha}(t) \quad (8)$$

Using Eq. (2), the differential equation is arranged as

$$V_{DC} = R_s C_\alpha \frac{dv_{c_\alpha}(t)}{dt} t^{1-\alpha} + v_{c_\alpha}(t) \quad (9)$$

By arranging both sides of equation, it is turned into a first order differential equation;

$$\frac{dv_{c_\alpha}(t)}{dt} + \frac{t^{\alpha-1}}{R_s C_\alpha} v_{c_\alpha}(t) = \frac{V_{DC}}{R_s C_\alpha} t^{\alpha-1} \quad (10)$$
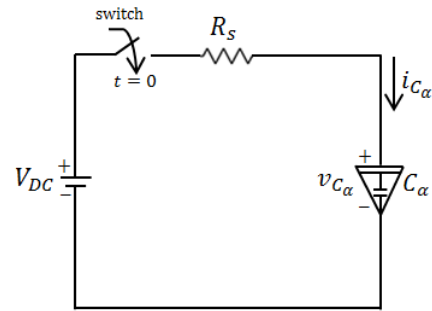
Figure 2. The CFD capacitor connected to a series resistor is fed by a constant voltage source

For a first order differential equation, whose form is of $v_{c_\alpha}(t)' + p(t) v_{c_\alpha}(t) = q(t)$, an integral factor can be used to solve the equation [38]. The both side of equation is multiplied with the integrating factor μ to find the function $v_{c_\alpha}(t)$:

$$\mu = e^{\int p(t) dt} \rightarrow \mu(v_{c_\alpha}(t)' + p(t) v_{c_\alpha}(t)) = \mu q(t) \quad (11)$$

$$(\mu v_{c_\alpha}(t))' = \mu q(t)$$

$$\int (\mu v_{c_\alpha}(t))' dt = \int \mu q(t) dt \rightarrow \mu v_{c_\alpha}(t) = \int \mu q(t) dt \quad (12)$$

The integration factor is found as

$$\mu = e^{\int \frac{t^{\alpha-1}}{R_s C_\alpha} dt} = e^{\frac{t^\alpha}{R_s C_\alpha \alpha}} \quad (13)$$

The CFD capacitor voltage now can be written as

$$v_{c_\alpha}(t) = \frac{1}{\mu} \int \mu q(t) dt = e^{-\frac{t^\alpha}{R_s C_\alpha \alpha}} \int e^{\frac{t^\alpha}{R_s C_\alpha \alpha}} \frac{V_{DC}}{R_s C_\alpha} t^{\alpha-1} dt$$

$$v_{c_\alpha}(t) = V_{DC} e^{-\frac{t^\alpha}{R_s C_\alpha \alpha}} \int \frac{1}{R_s C_\alpha} e^{\frac{t^\alpha}{R_s C_\alpha \alpha}} t^{\alpha-1} dt \quad (14)$$

Making the following substitution:

$$u = e^{\frac{t^\alpha}{R_s C_\alpha \alpha}} \rightarrow du = \frac{1}{R_s C_\alpha} e^{\frac{t^\alpha}{R_s C_\alpha \alpha}} t^{\alpha-1} dt,$$ the Eq. (14) is converted into;

$$v_{c_a}(t) = V_{DC} e^{-\frac{t^\alpha}{R_s C_\alpha \alpha}} \int du$$

$$v_{c_a}(t) = V_{DC} e^{-\frac{t^\alpha}{R_s C_\alpha \alpha}} (u + K) \tag{15}$$

When reverse substitution is performed, the CFD capacitor voltage is found as

$$v_{c_a}(t) = V_{DC} e^{-\frac{t^\alpha}{R_s C_\alpha \alpha}} (e^{\frac{t^\alpha}{R_s C_\alpha \alpha}} + K)$$

$$v_{c_a}(t) = V_{DC} + V_{DC} e^{-\frac{t^\alpha}{R_s C_\alpha \alpha}} K \tag{16}$$

If the initial condition at t=0 is applied, the integration constant K is found;

$$v_{c_a}(0) = V_{DC} + V_{DC} K \rightarrow K = \frac{v_{c_a}(0)}{V_{DC}} - 1 \tag{17}$$

The equation is rearranged after finding K, the $v_{c_a}(t)$ is written as

$$v_{c_a}(t) = V_{DC} + v_{c_a}(0) e^{-\frac{t^\alpha}{R_s C_\alpha \alpha}} - V_{DC} e^{-\frac{t^\alpha}{R_s C_\alpha \alpha}}$$

$$v_{c_a}(t) = V_{DC}(1 - e^{-\frac{t^\alpha}{R_s C_\alpha \alpha}}) + v_{c_a}(0) e^{-\frac{t^\alpha}{R_s C_\alpha \alpha}} \tag{18}$$

After $v_{c_a}(t)$ is found, the CFD capacitor current is written with using the terminal equation. Then, it is described as

$$i_{c_a} = C_\alpha t^{1-\alpha} \frac{d}{dt} \left(V_{DC} + e^{-\frac{t^\alpha}{R_s C_\alpha \alpha}} (v_{c_a}(0) - V_{DC}) \right)$$

$$= \frac{1}{R_s} e^{-\frac{t^\alpha}{R_s C_\alpha \alpha}} (V_{DC} - v_{c_a}(0)) \tag{19}$$

For the circuit given in Figure 2, both the CFD voltage and current are obtained. Then, the power of CFD the capacitor is obtained as

$$p(t) = i_{c_a}(t) v_{c_\alpha}(t) \tag{20}$$

$$p(t) = \frac{1}{R_s} e^{-\frac{t^\alpha}{R_s C_\alpha \alpha}} (V_{DC} - v_{c_a}(0))$$

$$\left(V_{DC} + e^{-\frac{t^\alpha}{R_s C_\alpha \alpha}} (v_{c_a}(0) - V_{DC}) \right) \tag{21}$$

$$p(t) = e^{-\frac{t^\alpha}{R_s C_\alpha \alpha}} \left(-\frac{V_{DC}}{R_s} v_{c_a}(0) + \frac{V_{DC}^2}{R_s} \right)$$

$$+ e^{-\frac{2t^\alpha}{R_s C_\alpha \alpha}} \left(-\frac{1}{R_s} v_{c_a}^2(0) + \frac{2V_{DC}}{R_s} v_{c_a}(0) - \frac{V_{DC}^2}{R_s} \right) \tag{22}$$

The power can be used to come up with a solution for the energy stored within the CFD capacitor which is designated as *E(t)*. If the integral is divided into two parts, the equation of energy is written as

$$E(t) = \int_0^t p(t) dt = \int_0^t E_1(t) dt + \int_0^t E_2(t) dt \tag{23}$$

$$E_1(t) = \int_0^t e^{-\frac{t^\alpha}{R_s C_\alpha \alpha}} \left(-\frac{V_{DC}}{R_s} v_{c_a}(0) + \frac{V_{DC}^2}{R_s} \right) dt \tag{24}$$

$$E_2(t) = \int_0^t e^{-\frac{2t^\alpha}{R_s C_\alpha \alpha}} \left(-\frac{1}{R_s} v_{c_a}^2(0) + \frac{2V_{DC}}{R_s} v_{c_a}(0) - \frac{V_{DC}^2}{R_s} \right) dt \tag{25}$$

Eq. (25) can be simplified using a special integral function called the incomplete gamma function [39]. The gamma function $\Gamma(s)$ can be described to the incomplete gamma function $\Gamma(s,x)$ such that $\Gamma(a) = \Gamma(s,0)$. As a result of this, the upper incomplete gamma function is given by

$$\Gamma(s,x) = \int_x^\infty t^{s-1} e^{-t} dt \tag{26}$$

When the substitution $u_1 = \frac{t}{(R_s C_\alpha \alpha)^{1/\alpha}}$ is applied in $E_1(t)$ integral, $\frac{du_1}{dt} = \frac{1}{(R_s C_\alpha \alpha)^{1/\alpha}} \rightarrow dt = (R_s C_\alpha \alpha)^{1/\alpha} du_1$ is found and the equation is converted into the incomplete gamma function.

$$E_1(t) = \left(-\frac{V_{DC}}{R_s} v_{c_a}(0) + \frac{V_{DC}^2}{R_s} \right) (R_s C_\alpha \alpha)^{1/\alpha} \int e^{-u_1^\alpha} du_1$$

$$= \left(-\frac{V_{DC}}{R_s} v_{c_a}(0) + \frac{V_{DC}^2}{R_s} \right) (R_s C_\alpha \alpha)^{1/\alpha} \left(-\frac{\Gamma(\frac{1}{\alpha}, u_1^\alpha)}{a} \right) \tag{27}$$

If the substitution is reversed, $E_1(t)$ is found as

$$E_1(t) = -\frac{\Gamma\left(\frac{1}{\alpha}, \frac{t^\alpha}{R_s C_\alpha \alpha}\right)t}{a\left(\frac{t^\alpha}{R_s C_\alpha \alpha}\right)^{1/\alpha}}\left(-\frac{V_{DC}}{R_s}v_{c_a}(0) + \frac{V_{DC}^2}{R_s}\right) \tag{28}$$

Similarly, $E_2(t)$ can be simplified solved with using same method. When the substitution $u_2 = \frac{2^{1/\alpha}t}{(R_s C_\alpha \alpha)^{1/\alpha}}$ is used, $\frac{du_2}{dt} = \frac{2^{1/\alpha}}{(R_s C_\alpha \alpha)^{1/\alpha}} \rightarrow dt = \frac{(R_s C_\alpha \alpha)^{1/\alpha}}{2^{1/\alpha}}du_2$ is written and, using the incomplete gamma function, the integral is found as

$$\begin{aligned} E_2(t) &= \left(-\frac{1}{R_s}v_{c_a}^2(0) + \frac{2V_{DC}}{R_s}v_{c_a}(0) - \frac{V_{DC}^2}{R_s}\right)\frac{(R_s C_\alpha \alpha)^{1/\alpha}}{2^{1/\alpha}}\int e^{-u_2^\alpha}du_2 \\ &= \left(-\frac{1}{R_s}v_{c_a}^2(0) + \frac{2V_{DC}}{R_s}v_{c_a}(0) - \frac{V_{DC}^2}{R_s}\right)\frac{(R_s C_\alpha \alpha)^{1/\alpha}}{2^{1/\alpha}}\left(-\frac{\Gamma\left(\frac{1}{\alpha}, u_2^\alpha\right)}{a}\right) \end{aligned} \tag{29}$$

When reverse substitution is performed, $E_2(t)$ is found as

$$E_2(t) = -\frac{\Gamma\left(\frac{1}{\alpha}, \frac{2t^\alpha}{R_s C_\alpha \alpha}\right)t}{a2^{1/\alpha}\left(\frac{t^\alpha}{R_s C_\alpha \alpha}\right)^{1/\alpha}}\left(-\frac{1}{R_s}v_{c_a}^2(0) + \frac{2V_{DC}}{R_s}v_{c_a}(0) - \frac{V_{DC}^2}{R_s}\right) \tag{30}$$

Then $E(t) = \int_0^t E_1(t)dt + \int_0^t E_2(t)dt$ is applied, the energy equation of the CFD capacitor is written as

$$\begin{aligned} E(t) &= -\frac{\Gamma\left(\frac{1}{\alpha}, \frac{t^\alpha}{R_s C_\alpha \alpha}\right)t}{\alpha\left(\frac{t^\alpha}{R_s C_\alpha \alpha}\right)^{1/\alpha}}\left(-\frac{V_{DC}}{R_s}v_{c_a}(0) + \frac{V_{DC}^2}{R_s}\right) \\ &\quad -\frac{\Gamma\left(\frac{1}{\alpha}, \frac{2t^\alpha}{R_s C_\alpha \alpha}\right)t}{\alpha 2^{\frac{1}{\alpha}}\left(\frac{t^\alpha}{R_s C_\alpha \alpha}\right)^{1/\alpha}}\left(-\frac{1}{R_s}v_{c_a}^2(0) + \frac{2V_{DC}}{R_s}v_{c_a}(0) - \frac{V_{DC}^2}{R_s}\right) \end{aligned} \tag{31}$$

The energy loss within the equivalent series resistor is written as

$$E_{LOSS} = \int_{t=0}^{t=T_{last}} i_{c_a}^2 R_s dt = \int_{t=0}^{t=T_{last}}\left(\frac{1}{R_s}e^{-\frac{t^\alpha}{R_s C_\alpha \alpha}}(V_{DC} - v_{c_a}(0))\right)^2 R_s dt \tag{32}$$

$$E_{LOSS} = \int_{t=0}^{t=T_{last}}\frac{1}{R_s}e^{\frac{-2t^\alpha}{R_s C_\alpha \alpha}}(V_{DC} - v_{c_a}(0))^2 dt$$

When the circuit is supplied by DC signal, the power supplied by the source is calculated as

$$p_s(t) = V_{DC}i_{c_a} \tag{33}$$

The energy supplied by the source is given as

$$E_s(t) = \int_0^t V_{DC}i_{c_a} = \int_0^t V_{DC}\frac{1}{R_s}e^{-\frac{t^\alpha}{R_s C_\alpha \alpha}}(V_{DC} - v_{c_a}(0))dt \tag{34}$$

$$E_s(t) = \frac{V_{DC}}{R_s}(V_{DC} - v_{c_a}(0))\int_0^t e^{-\frac{t^\alpha}{R_s C_\alpha \alpha}}dt \tag{35}$$

Using the incomplete gamma funcion, Eq. 35 can be simplied and written as

$$E_s(t) = -\frac{\Gamma\left(\frac{1}{\alpha}, \frac{t^\alpha}{R_s C_\alpha \alpha}\right)t}{a\left(\frac{t^\alpha}{R_s C_\alpha \alpha}\right)^{1/\alpha}}\left(\frac{V_{DC}}{R_s}(V_{DC} - v_{c_a}(0))\right) \tag{36}$$

Also, it can be written using charge equation and it is described as

$$E_S = \int_{t=0}^{t=T_{last}} V_{DC}dq_C = V_{DC}\int_{t=0}^{t=T_{last}} dq_C = V_{DC}\left(q(T_{last}) - q(0)\right) \tag{37}$$

The energy efficiency of the charging process is calculated as

$$\eta = \frac{E_{STORED}}{E_S} = \frac{E_C}{E_S} \tag{38}$$

6. Simulations and Results

In this section, the voltage and current of the CFD capacitor for three different α values calculated when the circuit is fed by the constant voltage source are shown in Figures 3 and 4, respectively. Moreover, $V_{DC} = 5\ V$, $v_{c_a}(0) = 0\ V/s^{1-\alpha}$, $R_s = 2.5\ \Omega$ and $C_\alpha = 1\ F/s^{1-\alpha}$ are applied in the CFD capacitor equations.
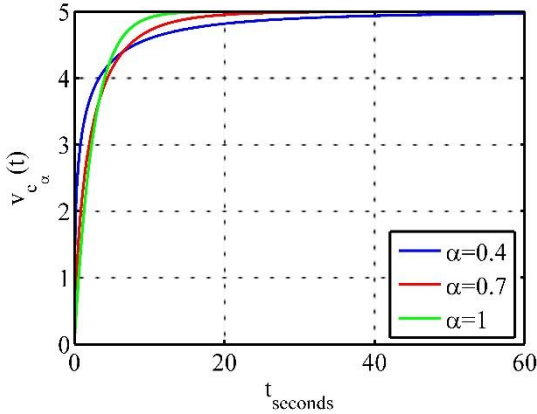
Figure 3. The voltage of the CFD capacitor for three different α values
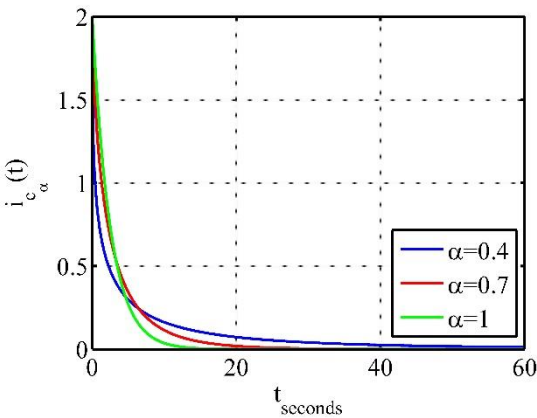
Figure 4. The current of the CFD capacitor for three different α values

The stored energy of the CFD capacitor, the supplied energy by the source, and the CFD capacitor charging energy efficiency are simulated for three different α values as shown in Figures 5-7. A Matlab code has been written to calculate the energy of the CFD capacitor. Furthermore, $V_{DC} = 5\ V$, $v_{c_\alpha}(0) = 0\ V/s^{1-\alpha}$, $R_s = 2.5\ \Omega$ and $C_\alpha = 1\ F/s^{1-\alpha}$ are used in the equations.

Figure 5. The energy of the CFD capacitor for three different α values
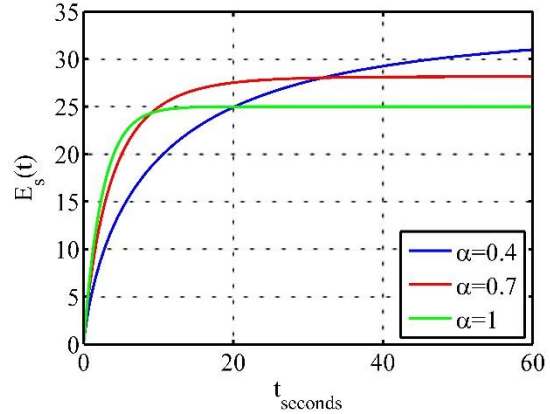
Figure 6. The supplied energy for three different α values.
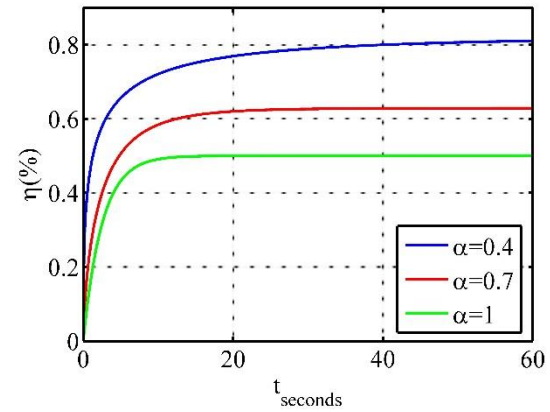
Figure 7. The energy efficiency for three different α values.

The graphs of energy loss within the series resistor for three different resistor values are sketched in Figures 8-10 when $\alpha = 0.4$, $\alpha = 0.7$, and $\alpha = 1$ are applied, respectively. Moreover, $V_{DC} = 5\ V$, $v_{c_\alpha}(0) = 0\ V/s^{1-\alpha}$, and $C_\alpha = 1\ F/s^{1-\alpha}$ are used in the equations. According to Figures 8-10, the energy loss within the resistor does depend on its resistance except for the case $\alpha = 1$.
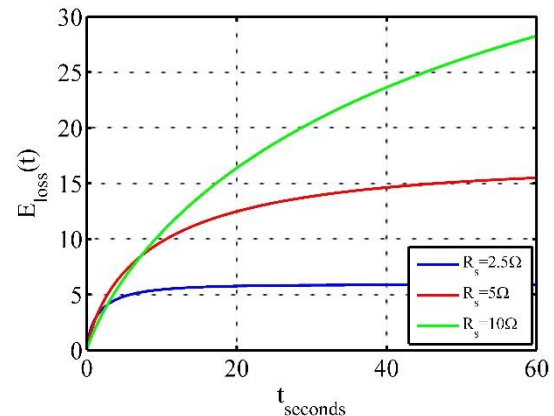
Figure 8. The energy loss within the series resistor for three different resistor values for $\alpha = 0.4$
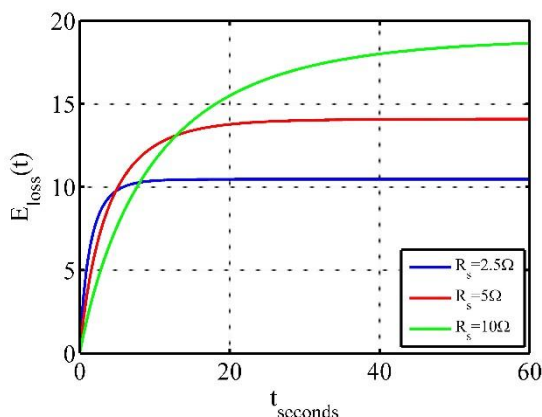
Figure 9. The energy loss within the series resistor for three different resistor values for $\alpha = 0.7$.
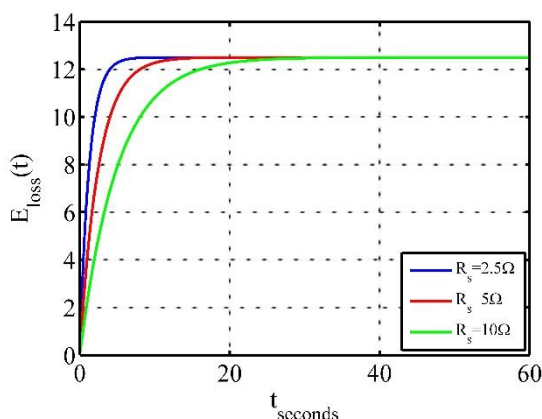
Figure 10. The energy loss within the series resistor for three different resistor values for $\alpha = 1$.

7. Conclusion

Supercapacitors or ultra-capacitors can be modelled with fractional-order derivatives. If a supercapacitor is modelled with the CFD, its energy cannot be calculated as easily as it can be done for an LTI capacitor. Therefore, it should be examined how to calculate the energy stored in a CFD capacitor. In this study, a method is given to calculate the energy of a CFD capacitor if it is charged through a resistor from a DC supply. The solution of its energy has been found as a special function called the incomplete gamma function. The energy equations in the circuit are simulated using Matlab. The charging efficiency of the CFD capacitor is shown to be dependent on the parameter and the series resistor resistance. It is shown that it can be higher than 50%, which the value is obtained for the LTI capacitor case. It is imperative to comprehend that the energy formula given here could not be used for different sources and different circuits. The CFD capacitor is a new circuit element and its analysis with the other circuit elements combined with different waveforms should be made. After the analysis of each new circuit topology, the energy of the

CFD capacitor can be found using the method given here. For each case, a different energy formula would be obtained. Such analysis detailed in the paper may pave the way to understanding the CFD capacitor better, make its usage easier, and find new usage areas.

Declaration of Ethical Standards

The author(s) of this article declare that the materials and methods used in this study do not require ethical committee permission and/or legal-special permission.

Conflict of Interest

The authors declare that they have no known competing financial interests or personal relationships that could have appeared to influence the work reported in this paper.
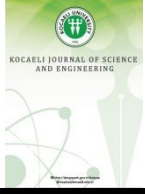
References

[1] Diethelm K., 2010. The Analysis of Fractional Differential Equations: An Application-oriented Exposition Using Differential Operators of Caputo Type, 1st ed., Springer Science & Business Media, Berlin, Germany.

[2] Hilfer R., 2000. Applications of Fractional Calculus in Physics, 1st ed., World scientific, Singapore.

[3] Babiarz A., Czornik A., Klamka J., and Niezabitowski M., 2017. Theory and applications of non-integer order systems. Lecture Notes Electrical Engineering, vol. 407.

[4] Ross B., 1977. The development of fractional calculus 1695–1900. Historia Mathematica, 4(1), pp. 75-89.

[5] Azar A. T., Radwan A. G., and Vaidyanathan S., 2018. Fractional Order Systems: Optimization, Control, Circuit Realizations and Applications, 1st ed., Elsevier Science & Technology, New York, USA.

[6] T. J. Freeborn, 2013. A survey of fractional-order circuit models for biology and biomedicine. IEEE Journal on Emerging and Selected Topics in Circuits and Systems, 3(3), pp. 416-424.

[7] Kartci A., Agambayev A., Herencsar N., and Salama K. N., 2018. Series-, parallel-, and inter-connection of solid-state arbitrary fractional-order capacitors: theoretical study and experimental verification. IEEE Access, 6, pp. 10933-10943.

[8] Tsirimokou G., Psychalinos C., and Elwakil A., 2017. Design of CMOS Analog Integrated Fractional-Order Circuits: Applications in Medicine and Biology, 1st

ed., Springer, Cham, Switzerland: Springer.

[9] Oldham K. B., Spanier J., 1974. Fractional Calculus: Theory and Applications, Differentiation and Integration to Arbitrary Order, 1st ed., Academic Press, New York, USA.

[10] Bošković M. Č., Šekara T. B., Lutovac B., Daković M., Mandić P. D., and Lazarević M. P., 2017. Analysis of electrical circuits including fractional order elements. Paper presented at Proceedings of the 6th Mediterranean Conference on Embedded Computing (MECO), Bar, Montenegro, 11-15 June, pp. 1-6.

[11] Kilbas A. A., Srivastava H. M., and Trujillo J. J., 2006. Theory and Applications of Fractional Differential Equations, 1st ed., Elsevier, Amsterdam, Holland: Elsevier.

[12] Sotner R., Jerabek J., Kartci A., Domansky O., Herencsar N., Kledrowetz V., and Yeroglu C., 2019. Electronically reconfigurable two-path fractional-order PI/D controller employing constant phase blocks based on bilinear segments using CMOS modified current differencing unit. Microelectronics Journal, 86, pp. 114-129.

[13] Podlubny I., 1994. Fractional-order systems and fractional-order controllers. Institute of Experimental Physics, Slovak Academy of Sciences, Kosice, vol. 12(3), pp. 1-18.

[14] Mainardi F., 1996. Fractional relaxation-oscillation and fractional diffusion-wave phenomena. Chaos, Solitons & Fractals, 7(9), pp. 1461-1477.

[15] Alagöz B. B., Alisoy H., 2018. "Estimation of reduced order equivalent circuit model parameters of batteries from noisy current and voltage measurements. Balkan Journal of Electrical and Computer Engineering, 6(4), pp. 224-231.

[16] Khalil R., al Horani M., Yousef A., and Sababheh M., 2014. A new definition of fractional derivative. Journal of Computational and Applied Mathematics, 264, pp. 65–70.

[17] Abdeljawad T., 2015. On conformable fractional calculus. Journal of computational and Applied Mathematics, 279, pp. 57-66.

[18] Zhao D., and Luo M., 2017. General conformable fractional derivative and its physical interpretation. Calcolo, 54(3), pp. 903-917.

[19] Francisco G. A. J, Juan R. G., Manuel G. C., and Roberto R. H. J., 2014. Fractional RC and LC electrical circuits. Ingeniería Investigación y Tecnología, 15(2), pp. 311-319.

[20] Freeborn T. J., Maundy B., and Elwakil A. S., 2013. Measurement of supercapacitor fractional-order model parameters from voltage-excited step response. IEEE Journal on Emerging and Selected Topics in Circuits and Systems, 3(3), pp. 367-376.

[21] Freeborn T. J., Maundy B., and Elwakil A. S., 2015. Fractional-order models of supercapacitors, batteries and fuel cells: a survey. Materials for Renewable and Sustainable Energy, 4(3), pp. 1-7.

[22] Kopka R., 2017. Estimation of supercapacitor energy storage based on fractional differential equations. Nanoscale research letters, 12(1), pp. 636.

[23] Piotrowska E., Rogowski K., 2017. Analysis of fractional electrical circuit using Caputo and conformable derivative definitions. Paper presented at Conference on Non-integer Order Calculus and Its Applications, Łódź, Poland, 2017, 11-13 October, pp. 183-194.

[24] Piotrowska E., 2019. Analysis of fractional electrical circuit with sinusoidal input signal using Caputo and conformable derivative definitions. Poznan University of Technology Academic Journals. Electrical Engineering, 97, pp. 155-167.

[25] Martínez L., Rosales J. J., Carreño C. A., and Lozano J. M., 2018. Electrical circuits described by fractional conformable derivative. International Journal of Circuit Theory and Applications, 46(5), pp. 1091-1100.

[26] Piotrowska E., 2018. Analysis the conformable fractional derivative and Caputo definitions in the action of an electric circuit containing a supercapacitor. Paper presented at Proc. of SPIE, Wilga, Poland, 3-10 June, pp. 108081T.

[27] Sumper A., Baggini A., 2012. Electrical energy efficiency: technologies and applications, 1st ed., John Wiley & Sons, West Sussex, United Kingdom.

[28] Cheung C. K., Tan S. C., Chi K. T., and Ioinovici A., 2012. On energy efficiency of switched-capacitor converters. IEEE Transactions on Power Electronics, 28(2), pp. 862-876.

[29] Fouda M. E., Elwakil A. S., Radwan A. G., and Allagui A., 2016. Power and energy analysis of fractional-order electrical energy storage devices. Energy, 111, pp. 785-792.

[30] Hartley T. T., Veillette R. J., Adams J. L., and Lorenzo C. F., 2015. Energy storage and loss in fractional-order circuit elements. IET Circuits, Devices & Systems, 9(3), pp. 227-235.

[31] Martynyuk V., Ortigueira M., 2015. Fractional model of an electrochemical capacitor. Signal Processing, 107, pp. 355-360.

[32] Quintana J. J., Ramos A., and Nuez I., 2006. Identification of the fractional impedance of ultracapacitors. IFAC Proceedings, 39(11), pp. 432-436.

[33] Bertrand N., Sabatier J., Briat O., and Vinassa J. M., 2010. Embedded fractional nonlinear supercapacitor model and its parametric estimation method. IEEE Transactions on Industrial Electronics, 57(12), pp. 3991-4000.

[34] Halliday D., Resnick R., and Walker J., 2014. Fundamentals of Physics, 10th ed., John Wiley & Sons, New York, USA.

[35] Voldman S. H., 2015. ESD: Circuits and Devices, 2nd ed., John Wiley & Sons, New York, USA.

[36] Irwin J. D., Nelms R. M., 2015. Basic Engineering Circuit Analysis, 11th ed., John Wiley & Sons, New York, USA.

[37] Abu-Labdeh A. M., and Al-Jaber S. M., 2008. Energy consideration from non-equilibrium to equilibrium state in the process of charging a capacitor. Journal of Electrostatics, 66(3-4), pp. 190-192.

[38] Morse P. M., Feshbach H., 1954. Methods of theoretical physics. American Journal of Physics, 22(6), pp. 410-413.

[39] Thompson I., 2011. NIST Handbook of Mathematical Functions, 1st ed., Cambridge University Press, New York, USA.

Kocaeli University

Kocaeli Journal of Science and Engineering

Characterization of Cr-Mo Alloyed Steel Foams Produced by Evaporative and Leachable Space Holder Techniques

Nuray BEKÖZ ÜLLEN [1], * iD

[1] Department of Metalurgical and Materials Engineering, İstanbul University-Cerrahpaşa, İstanbul, 34320, Turkey, **ORCID: 0000-0003-2705-2559**

Article Info

Abstract

Steel foams have attracted a lot of attention in both academia and industry with unique properties such as low density, high strength-to-weight ratio, operating temperature, good energy absorption, electrical conductivity, and large specific surface. The development of production methods will increase the use of steel foam. In this paper, Cr-Mo alloyed steel foams having porosities in the range of 46.8-71.3% were produced by evaporative and leachable space holder techniques in powder metallurgy. The effect on the properties of removing the carbamide used as a space holder material from the porous structure by different methods was compared. Microstructural evaluations of the pore wall, pore size, pore wall thickness, and the compressive deformation behavior of steel foam were evaluated. Steel foams produced by both routes have a rather similar macropore structure but differences in pore wall structure such as micropore ratio and pore wall thickness. The differences increase with increasing porosity content. The mechanical properties are higher in foams produced by the evaporative route as compared to the leachable route at similar porosity due to its stronger cell wall. The compressive stress and energy absorption of the leachable and evaporative process are in the range of 15-84 and 102 MPa and 1.91-6.03 and 2.98-7.83 J/mm^2, respectively.

1. Introduction

Metallic foam is a good candidate for structural and functional applications due to new process developments for obtaining materials with a good correlation between properties and costs [1,2]. Many metals and alloys can be produced in foam form. Among them, steel foams offer a unique combination of properties derived from their cellular structure and metallic behavior such as low density, high strength, high energy absorption, sound absorption capability, low thermal conductivity, high-temperature heat resistance, and recyclability [3]. The exclusive properties of metallic foams depend on the properties of the main alloy, porosity, the type (open, closed, and a combination of open and close), size, shape, and distribution of cells, cell wall defects, and the operational factors of the manufacturing process [4,5].

Many techniques have been developed for the production of metallic foams (direct foaming of metals,

casting, deposition, powder metallurgy routes, etc.) [6]. Among these techniques, the space holder technique in powder metallurgy is very simple and cost-effective, which can produce complex parts with easy control of pore characteristics of the foam such as porosity, pore morphology, and pore size distribution [6–9]. In this technique, the starting materials are metal powders, space holders, and binders [10]. Then, these materials go through processes such as mixing and pressing, etc. Process control is critical to achieve uniform pore structures and consistent properties, which is currently a challenge for producing metallic foams [6,11]. In this technique, the final foam structure is affected by the spacer. For this reason, it is extremely important to choose the proper space holder for the metal foam and to apply the appropriate separation process. Due to the importance of this situation, it has been included in many studies in recent years [3-21]. The space holder materials have two types, such as evaporative and leachable in a suitable solvent [6,12]. Many researchers have produced and characterized steel foams and other metallic foams through the evaporative and leachable process using space holder techniques [3,6,13]. Many

* Corresponding Author: nbekoz@iuc.edu.tr

materials are used as low-temperature evaporative space holders in the manufacturing of metal foams, such as polymer, magnesium, ammonium hydrogen carbonate, saccharose, tropical starch, and carbamide [14-18]. Furthermore, water-leachable materials such as carbamide, salt, sodium and potassium chloride and potassium bromide are generally used to produce metal foams [6,7,11,19-21]. Among the space holder materials, carbamide is very attractive for fabricating foam structures due to its low melting point, high solubility in water, and very low cost. As an additional advantage, it does not corrode the foam structure [6,11,20]. Many steel foams having different porosities and chemical compositions have been manufactured by evaporative [6,11,22] and water-leaching [6,9,19,20] techniques in powder metallurgy using irregular and spherical carbamide particles as space holders. It is observed from research in the literature that there are many advantages and disadvantages to these techniques. The water-leachable process is attractive and environmentally friendly, given that it does not lead to any dangerous by-products or emissions and does not employ any toxicity. As an additional benefit, the equipment necessary for water-leaching is very simple [6,20,22]. However, this process shows distortion in the shape and size of cells because of micro-porosities in the cell wall regions. Mechanical properties of metal foam strongly depend on cell size, aspect ratio, cell wall thickness, and micro-porosity in the cell wall surface [21,23]. Some researchers have reported that the mechanical properties of the specimens produced by the evaporative route are significantly higher than those produced by the leachable route [6,20]. However, the main problem with this evaporative process of carbamide takes a long time since a slow heating rate is required to obtain crack-free specimens, and its decomposition releases environmentally harmful gases, especially with low relative densities [23].

Many studies have emphasized that the performance of metal foams depends on the relative density, the macropore structure of the foam, and the micropores formed in the pore wall, and the pore morphology notably depends on the manufacturing process [3,4,22,24]. The aforementioned removal routes in the production process also have an intense effect on these properties of the foam structure. The use of steel foams on a large scale and successful applications of them depend on a detailed understanding of the impacts of the removal process on the properties of metal foams. The aim of this study is in this direction.

As a result of the production and characterization studies of many steel foam materials with different chemical compositions, the properties of metallic foams will be improved, and the rate of metallic foam usage will

increase. The powder grade Astaloy CrM is a water-atomized iron powder pre-alloyed with Cr and Mo exhibiting excellent hardenability. The low oxygen content gives good compressibility. Very high strength and hardness can be achieved after the sintering process. The fully pre-alloyed composition results in a homogenous microstructure. The dimensional and mechanical properties are very satisfactory. Warm compaction combined with high-temperature sintering has been outstandingly successful [25]. CrM steel foams can be used at many points as crash energy absorption, exhaust mufflers, vibration and noise control for the automotive industry, filters, heat exchangers, and high-strength wall panels for sound insulation [22]. In past years, many researchers manufactured high-density Astaloy CrM steel specimens by powder metallurgy technique and investigated the mechanical and microstructural properties [26-28]. However, no study has been found in the literature on Astaloy CrM steel foams. This paper provides the opportunity to compare the properties of Cr-Mo alloy steels based on Astaloy CrM foam and conventional materials such as Fe-Cu and Ni-Mo-Cu alloyed steel foams produced from Distaloy and Astaloy powder groups.

All these studies in the literature have shown that the "metallic foams" research area is still quite up to date and still has aspects to be researched. The adoption of steel foam relies on the manufacturing method, particularly its cost, and the resulting properties of the steel foam. In particular; the manufacturing process determines the pore morphology, properties, and performance of the metal foams. Therefore, it is important to complete the gaps in the manufacturing process. Although metal foams can be fabricated by the evaporative and leachable space holder method, it is necessary to compare the results of both routes to obtain a good foam structure. In this study, Cr and Mo based Astaloy CrM steel foams having different porosity were produced by evaporative and water-leachable space holder techniques in powder metallurgy. The structural and mechanical property variations resulting from removal from the structure of space holder particles were investigated and correlated.

2. Experimental Procedure

2.1. Materials

Cr-Mo pre-alloyed water atomized Astaloy CrM steel powder was used as parent materials, which is a registered trademark of Höganäs Company, Sweden. The chemical composition of the steel powder was 3.0 wt.% Cr, 0.5 wt.% Mo, and balance- Fe. Carbon in fine graphite form and zinc stearate were obtained from Merck Company,

Germany. 0.2 wt.% of carbon was added as fine graphite (UF4) to provide raw strength in the compression process, and it was mixed by adding 0.8 wt.% of zinc stearate as a lubricant to facilitate compression in the mold and removal after pressing. Apparent, tap and theoretical densities of the Astaloy CrM steel powders were determined to be 2.85 g/cm^3, 4.55 g/cm^3 and 7.78 g/cm^3, respectively. The steel powders were irregularly shaped and ranged in size from 45 µm to 150 µm. The mean size distribution of the powders was 107 µm. Polyvinyl alcohol (PVA) that purchased from Merck Company (Germany) and it was used as a binder for green strength. Spherical carbamide particles were purchased from Merck Company (Germany) and were used as space holders for the ease of water-leaching or thermally. The particles had a density of 1.34 g/cm^3, melting temperature of 133 ºC, and solubility in water at 20 ºC of more than 1000 g/L. Spherical carbamide particles were sieved to obtain a fraction of +710 -1000 µm. Figure 1 shows the typical morphologies of the irregular-shaped Astaloy CrM steel powder and the spherical-shaped carbamide particles.

evaporative and leachable space holder techniques in powder metallurgy. PVA solution (1 wt.% PVA and 99 wt.% distilled water) was used as a binder for the green strength of the foam specimens. Initially, the steel powders were mixed by adding a 2% by weight PVA solution. Next, the PVA added steel powders mixture and carbamide particles were mixed in different volume percentages of 50, 60, 70, and 80 wt% in order to obtain specimens with different porosities. The mixture was performed in a Turbula type mixer for 60 min. The photograph of carbamide particles after coating with the steel powders is shown in Figure 2(a). A homogeneous coating of carbamide particles with the steel powders was obtained. The coated carbamide particles were then compressed with a hydraulic press machine at 200 MPa to a diameter of 10 mm and a height of about 15 mm in a cylindrical stainless steel mold. The applied compaction pressure was chosen to be 200 MPa because the green samples had lower strength at lower applied stress and the carbamide particles were fractured at higher applied pressure. The green specimens after compacting are shown in Figure 2 (b).

Figure 1. (a) SEM image of Astaloy CrM steel powder and (b) Photograph of carbamide particles.

2.2. Manufacturing of Cr-Mo Steel Foams

Cr-Mo alloyed steel foams were produced by
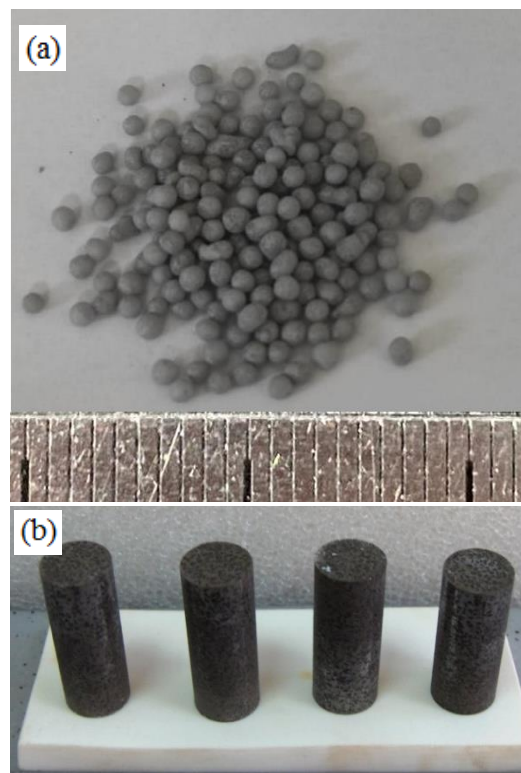
Figure 2. (a) Photograph of coated carbamide particles and (b) green specimens

After compaction to obtain a porous structure; the removal of carbamide particles was performed in two different techniques as leachable and evaporative routes. The main stages for manufacturing the Cr-Mo alloyed steel foams are schematically shown in Figure 3.
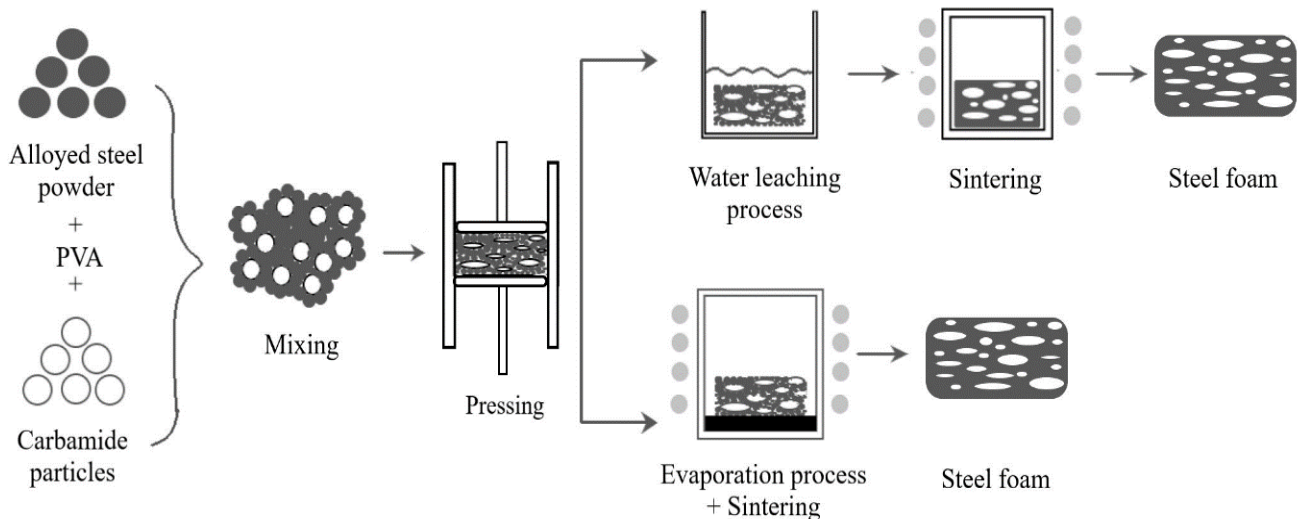
Figure 3. Schematic representation of the steel foam production process produced by leachable and evaporation techniques.

In the leachable route, the green specimens were immersed in distilled water at room temperature and held for times ranging from 30 to 120 min to leach the carbamide. The leached specimens were then rinsed with ethanol and dried in the oven at 50 °C for 2 h. More than 90% of the carbamide could be removed for theoretical porosities of 70% and 80%. About 15% to 20% of carbamide remained in the green specimens for theoretical porosities of 50% and 60%.

In the evaporative route, the green specimens were heat-treated from room temperature at 200 °C for 10 h and kept at this temperature for about 10 hours for thermal debinding of the vast majority of carbamide particles. The green porous structure was achieved by performing water-leaching and thermal decomposition of carbamide.

Both routes of techniques of removing the space holder were then heated at 450 ºC for 60 min at a heating rate of 5 °C/min for further removal of PVA and remaining carbamide. Finally; all the green specimens were sintered in a laboratory tube furnace at 1150 ºC for 60 min at a heating rate of 10 °C/min in an atmosphere of 50% nitrogen/50% hydrogen, with methane addition.

2.3. Characterization of Sintered Cr-Mo Foams

The density and porosity content of steel foam specimens were determined employing Archimedes' principle, using Sartorius precision balance equipped with a density-determination kit. The ratios of open and closed porosity were determined by weight measurements before and after the samples were dipped in boiling paraffin at 150 ºC. The pore morphology of the foam specimens was examined using Scanning Electron Microscopy (SEM). The size, shape, and size distribution of the pores were determined using commercial image analysis software (Clemex Vision PE). The micro porosities of the cell wall region in the steel foam samples were calculated by the Image-J software. To study the mechanical properties of the fabricated steel foams, compressive tests were performed at 0.5 mm/min cross speed at room temperature using the Zwick-Roell Z050 material testing machine.

3. Results and Discussion

3.1. The removal process of carbamide particles

The removal of carbamide can be considered as the most important part of the production step because if any carbamide remains at this stage, these carbamide residues can react with steel powder or alloying elements at sintering temperatures. As a result, the mechanical properties of the final product may deteriorate. There are many studies supporting this in the literature [6,7,20,21,29].

The increase in the temperature of the water in the leaching process caused an increase in the carbamide removal rate and caused cracking and fragmentation of the sample. Therefore, the leaching process was carried out at room temperature. Also, the leaching was done in a stagnant environment when the turbulence of the water caused the outer surfaces of the specimens to be destroyed. In the leachable route, the green specimens were immersed in distilled water at 25 °C to leach the carbamide. More than 90% of the carbamide was removed in specimens with

70% and 80% porosity by volume. About 10% to 20% carbamide remained in the green specimens with %50 and 60% porosity by volume.

In the evaporative route, various experiments were carried out considering the holding temperature, heating rate, and holding time in order to remove the carbamide from the porous structure. Previous studies in the literature have been taken into account in the removal of carbamide [6,7,20, 21,29,30]. Firstly, the samples that were heated for 2 hours and kept in a furnace previously heated up to 200°C for 2 hours were observed. However, it was observed that the gas pressure created by the sudden decomposition of the carbamide caused the sample to rupture. It was observed that the carbamide melted rapidly due to the rapid heating of the sample. The removal of powder with the resulting carbamide melt caused the specimens to deform as seen in Figure 4.
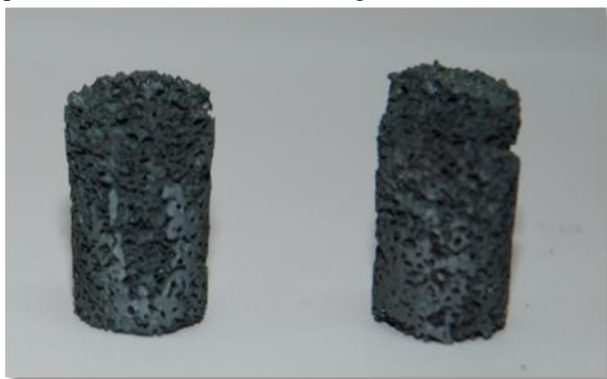
Figure 4. The deformed specimens by melting of carbamide

The melting temperature of carbamide is ~135°C but higher temperatures can be reached without melting because it needs time for the completion of melting and during that time some decomposition reactions start. Around 140°C both urea decomposition and biuret formation start, so at 150°C the carbamide removal could be possible without melting it [31]. It was observed that at 150°C after a certain period removal proceeds very slowly. Experiments showed that when the sample was heated up to 150°C and kept at this temperature observable removal started not earlier than 2 hours, and after a time period of 20 hours, only 50% of the area in the sample could be removed. Also, biuret formation cannot be prevented at this temperature, and as little dots and white particles form on the samples as shown in Figure 5. These were considered as a reformation of solid carbamide or formation of biuret from carbamide vapor. As a result, since only 50% of the carbamide could be removed after 20 hours of keeping at 150 ºC this process was eliminated. In the case of 150 ºC the process was slow, took 20 hours for optimum removal so 150°C was left out of consideration.

As a result; according to the experiments, the optimum pre-removal was determined as heating the sample from room temperature to ~200 °C for 10 hours and keeping it at this temperature for about 10 hours. Removal of the very small amount of remaining carbamide was removed by thermal pyrolysis during the sintering process. The selection of an appropriate thermal debinding of carbamide ensures that the carbamide particles can be removed from the green compacted specimens without breaking them [29,32].

Figure 5. Image of the sample as a result of biuret formation from carbamide vapor

3.2. The Pore Morphology and Porosity

Cr-Mo steel foams with porosities ranging between 46.3% and 71.3% were produced with both techniques. The SEM images at a different magnification of the surfaces of the foams containing about 70% porosity produced by the leachable and evaporative routes are shown in Figures 6 (a) and (b), respectively. As can be seen from the figures; two types of pores are observed in the steel foam. One type (macropore) is related to the resolved carbamide particles; the other type (micropore) is formed between the agglomerated iron particles during the sintering process. Thus, the total porosity consists of the amounts of macro and micro porosity in the pore wall. The formation of porosity at the micro and macro scales was investigated by many researchers for metallic foams [6,13,22,23,30,32]. It is observed that the specimens have a relatively uniform pore distribution. Mostly, pores are open and interconnected to each other with the pore wall. Pore walls separating each pore from its neighbors can be clearly visible. The morphology of the pores in the final products was similar to that of the carbamide particles for all the specimens. Steel foams produced by the evaporative route clearly show that the pore is interconnected and dense without any distortions in the pore wall regions.
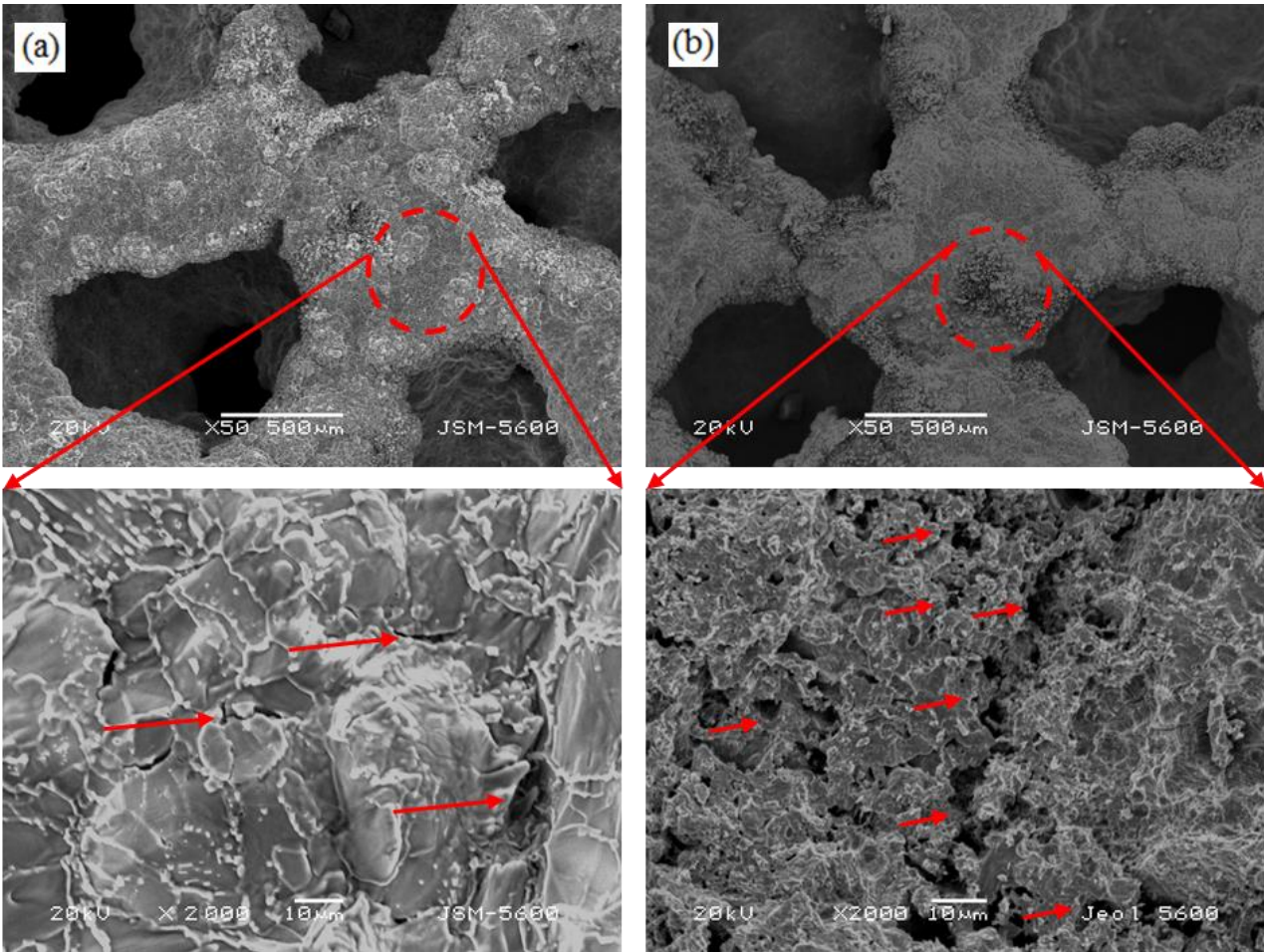
Figure 6. SEM images of 70% porosity steel foams: (a) leachable process, (b) evaporative process.

The lesser microporosity content in the pore wall regions are due to excellent localized fusion during sintering. But in the case of steel foams made by the leachable route, the highly porous specimens are distorted, and the pore wall is broken because carbamide particles are highly soluble in water. Also, numerous micropores have formed in the cell walls. These defects included cracks, holes, local porosity, and inhomogeneous composition. It has been theorized that the major occurrence of micron-level defects results from the sintering fabrication process. The interconnectivity of the foams also increases with porosity. This situation is also supported by studies dealing with similar issues in the literature [6,7,21,29,32].

Table 1 presents the density, the total porosity, the amount of open and closed porosity, the average value of microporosities, pore size, and pore wall thickness of the steel foams produced by different carbamide removal processes. In the specimens produced by both processes; it was observed that when the amount of carbamide particles used increased, the total porosity increased, and the sintered density decreased. It was determined that when the total porosity level increased in the sintered samples, the open porosity of the samples increased. The probability

of connection of the pores in sintered samples is expected to increase at high porosity levels. The pore wall thickness decreases with increasing carbamide content simultaneously due to increased pore size. The probability that the pores in the steel foam samples produced by the leachable process are connected will increase at high porosity levels. It was also found that the cell size and micro porosities in the pore wall surface are higher in steel foams produced by the leachable process compared to the evaporative process. It may be due to the higher percentage of shrinkage and a lesser micro porosity content in the pore wall surface in the case of the evaporative process. Also, this may be possible due to the less densification that occurred during the sintering process in the case of the leaching. In some studies, on the metallic foams, the macropore obtained as a result of spacer and micropore in the pore wall produced by leachable route formation has been explained similarly [6,12,21,30,32]. Jain et al. [6] reported the strong cell walls and lesser microporosities in the cell wall regions for the evaporative as compared to the leachable route. The increase in the ratio between values with the increase of the pore ratio; is very likely due to the difference in the cleanliness of the

specimens between the two methods.

Table 2 shows the mechanical properties such as compressive stress, plateau stress, and energy absorption of the steel foams produced by different carbamide removal processes. Compression test results showed that the compressive strength decreased with increasing porosity of the foam samples having different porosities. As a result of the increasing porosity, the interconnections of macropores in foams also increase, so the structure tends to be weaker under compressive load. Also, the wall thickness of the pores decreases as a result of the increased amount of total porosity, which weakens the mechanical behavior of the steel foam samples. The mechanical properties are higher in foams produced by the evaporative route as compared to the leachable route in all porosity conditions. This may be due to the larger amount of microporosity in the pore wall region caused by the dissolution of carbamide in water, and lesser particles to particle bonding in the case of leaching. The removal of the carbamide process significantly affected the plateau stress value in all porosity content. The plateau stress of steel foams produced by the evaporative route is higher. This is probably a consequence of the less microporosity of the pore walls. The high content of micro porosities in the pore wall region makes the structure fragile and mostly distorted. When the porosity is increased, there are significant differences between the two removal methods. Some research results show that the porous steel specimens produced by the decomposition route were generally much stronger and stiffer than those produced by the dissolution route. They explained the main reason for this as the decomposition route uses a higher sintering temperature, resulting in better bonding between the steel particles [6,18,22,31,33]. Lu and Zhao [19] reported that the decomposition removal process is the best option in the terms of maximizing the stiffness and strength of the porous steel. The energy absorption depends on the porosity of the foam and increases with decreasing the porosity of the steel foam [3,6,34]. It was found that the energy absorption values are higher in the evaporative route as compared to the leachable route, and also the value of energy absorption is decreasing with an increase in porosity.

Table 1. The density, total, open and closed porosities, micro porosities in pore wall region, pore size, pore wall thickness of the steel foams.

Carbamide removal process	Carbamide fraction (vol.%)	Density (g cm^{-3})	Total porosity (%)	Open porosity (%)	Closed porosity (%)	Micropore ratio in pore wall (%)	Pore size (μm)	Pore wall thickness (μm)
Leachable	50	4.12 ±0.12	47.2 ±1.5	32.7	14.5	5.46±0.41	975.5±158	651±45
	60	3.57 ±0.06	54.2 ±1.4	42.2	12.0	6,87±0.32	992.4±147	558±34
	70	2.97 ±0.07	62,0 ±1.6	50.2	11.8	9.48±0.38	1026.7±169	451±25
	80	2.33 ±0.05	70.2 ±1.2	62.9	7.3	11.75±0.32	1158.4±187	325±19
Evaporative	50	4.19 ±0.09	46.3 ±1.3	32.9	13.4	2.16±0.32	898.3±102	611±38
	60	3.61 ±0.08	53.7 ±1.4	43.7	10.0	2.38±0.39	976.2±124	422±35
	70	2.84 ±0.06	63.6 ±1.5	52.9	10.7	3.46±0.31	988.4±132	358±28
	80	2.24 ±0.08	71.3 ±1.7	65.7	5.6	4.16±0.30	1052.2±144	328±21

Table 2. The compressive stress, plateau stress and energy absorption of the steel foams.

Carbamide removal process	Total porosity (%)	Compressive stress (MPa)	Average plateau stress (MPa)	Energy absorption Joule/mm^2
Leachable	47.2	84±1.75	68±0.98	6.03±0.08
	54.2	68±1.82	45±2.82	4.88±0.06
	62,0	36±1.68	24±3.17	3.29±0.07
	70.2	15±2.71	9±1.84	1.91±0.05
Evaporative	46.3	102±2.71	86±1.12	7.83±0.07
	53.7	82±1.83	61±2.58	6.16±0.04
	63.6	47±1.68	38±3.81	4.28±0.06
	71.3	24±2.38	19±2.11	2.98±0.03

4. Conclusions

Cr-Mo-based steel foams having different porosity were produced by evaporative and water-leachable space holder techniques in powder metallurgy. The effects of the removal process of carbamide on macro and micro porosity structure, microstructure, and mechanical properties were investigated and evaluated. The following

conclusions have been reached:

- In the space holder-sintering technique, the crucial step is the removal of the carbamide from the green compacts such as leachable and evaporative processes.
- Steel foams produced by both routes have a rather similar macropore structure but differences in pore wall structure such as micropore ratio and pore wall thickness.
- The presence of microporosity in the pore wall regions as a result of the carbamide removal process has a significant impact on the mechanical characteristics of the steel foams.
- The strong cell walls and lesser microporosities in the cell wall regions for the evaporative process as compared to the leachable process. Therefore; steel foam produced by the evaporative route was generally stronger and stiffer than those produced by the leachable route. The differences increased with increasing porosity content.
- As a result, if both methods are compared; the leachable process is more economical, takes a shorter time, and is an environmentally friendly method. However, the mechanical properties of the product are worse. In the evaporation process, the removal of carbamide occurs at the sintering stage of production, so it is not economical because it requires long-term work at high temperatures. In addition, the gases formed during the removal of carbamide are also harmful to the environment. But in terms of the final product, the mechanical properties result in better.

Declaration of Ethical Standards

The author of this article declare that the materials and methods used in this study do not require ethical committee permission and/or legal-special permission.

Conflict of Interest

The author declare that they have no known competing financial interests or personal relationships that could have appeared to influence the work reported in this paper.

References

[1] Mapelli C., Mombelli D., Gruttadauria A., Barella S., Castrodeza E.M., 2013. Performance of stainless steel foams produced by infiltration casting techniques, J. Mater. Process. Technol. **213**, pp. 1846–1854

[2] Hu L., Ngai T., Peng H., Li L., Zhou F., Peng Z., 2018. Microstructure and properties of porous high-N Ni-free austenitic stainless steel fabricated by powder metallurgical route, Materials, **11** (7), 1058.

[3] Smith B. H., Szyniszewski S., Hajjar, J.F., Schafer B. W., Arwade, S. R., 2012. Steel foam for structures: A review of applications, manufacturing and material properties. Journal of Constructional Steel Research, **71**, 1-10.

[4] Banhart J., 2001 "Manufacture, characterization and application of cellular metals and metal foams", Progress in Materials science **46**, p. 561.

[5] Fathy A., Kamal M., Klingner A., Abd El Aziz A., Saif E., 2012. Steel foam: Heat treatment, mechanical and corrosion behavior. In 2012 International Conference on Engineering and Technology (ICET) (pp. 1-5).

[6] Jain H., Mondal D.P., Gupta G., Kumar R., Singh S., 2020. Synthesis and characterization of 316L stainless steel foam made through two different removal process of space holder method. Manufacturing Letters, **26**, 33-36.

[7] Jain H., Mondal D.P., Gupta G., Kumar, R., 2021. Effect of compressive strain rate on the deformation behaviour of austenitic stainless steel foam produced by space holder technique. Materials Chemistry and Physics, **259**, 124010.

[8] Gülsoy H. Ö., German R. M., 2013. Sintered foams from precipitation hardened stainless steel powder. Powder Metall, **51**, 350–353.

[9] Kato K., Yamamoto A., Ochiai S., Wada M., Daigo Y., Kita K., 2013. Cytocompatibility and mechanical properties of novel porous 316L stainless steel. Mater Sci Eng, C, **33**, 2736–2743.

[10] Babcsán N., Banhart J., Leitlmeier D., 2003. Metal Foams-Manufacture and Physics of Foaming, 5-14.

[11] Wang H, Zhou X.Y, Long B., 2014. Fabrication of stainless steel foams using polymeric sponge impregnation technology. Adv Mater Res. **1035**. 219–224.

[12] Jain H, Gupta G, Kumar R, Mondal D.P., 2019. Microstructure and compressive deformation behavior of SS foam made through evaporation of urea as space holder. Mater Chem Phys. **223**. 737–744.

[13] Sazegaran H., Feizi A., Hojati M. 2019. Effect of Cr contents on the porosity percentage, microstructure, and mechanical properties of steel foams manufactured by powder metallurgy. Transactions of the Indian Institute of Metals, **72** (10), 2819-2826.

[14] Lefebvre L.P., Banhart J., Dunand D.C., 2008. Porous Metals and Metallic Foams: Current Status and Recent Developments, Advanced Engineering Materials, **10**, 775-787.

[15] Aşık E.E., Bor Ş., 2015. Fatigue behavior of Ti–6Al–4V foams processed by magnesium space holder technique, Mater. Sci. Eng., A, **621**, 157–165.

[16] Mansourighasri A., Muhamad N., Sulong A.B., 2012. Processing titanium foams using tapioca starch as a space holder, J. Mater. Process. Technol. **212,** 83–89.

[17] Jakubowicz J., Adamek G., Pałka K., Andrzejewski D., 2015. Micro-CT analysis and mechanical properties of Ti spherical and polyhedral void composites made with saccharose as a space holder material, Mater. Char. **100**. 13–20.

[18] Salvo C., Aguilar C., Lascano S., P´erez L., L´opez M., Mangalaraja R.V., 2018. The effect of alumina particles on the microstructural and mechanical properties of copper foams fabricated by space-holder method, Mater. Res. Express 5, 056514.

[19] Lu M., Zhao Y. 2010. Mechanical properties of LCS porous steel: comparison between the dissolution and decomposition routes. Minerals, Metals and Materials Society/AIME, 420 Commonwealth Dr., P. O. Box 430 Warrendale PA 15086 USA. [np].

[20] Bafti H., Habibolahzadeh A., 2013. Compressive properties of aluminum foam produced by powder-Carbamide spacer route, Mater. Des. **52** 404–411.

[21] Bekoz N., Oktay E. 2012. Effects of carbamide shape and content on processing and properties of steel foams. Journal of Materials Processing Technology, **212**(10), 2109-2116.

[22] Bekoz N., Oktay E., 2013. Mechanical properties of low alloy steel foams: Dependency on porosity and pore size. Materials Science and Engineering: A, **576**, 82-90.

[23] Mirzaei M., Paydar M.H., 2019. Fabrication and characterization of core–shell density-graded 316L stainless steel porous structure. Journal of Materials Engineering and Performance, **28**(1), 221-230.

[24] Huang B.S., Fu S., Zhang S.S., Ju C.Y., Wu S.S., Peng H. 2019. Preparation and property test of porous Cu–Sn alloy by powder filling and sintering method. Materials Research Express, **6**(10), 1065g6.

[25] Höganäs Handbook for Sintered Components, 2004. Höganäs Iron and Steel Powder for Sintered Components. Höganäs AB, Sweden.

[26] Danninger H., Kremel S., Molinari A., Puscas T. M, Torralba J., Campos M., Yu Y. 2001. Heat treatment of Cr-Mo sintered steels based on Astaloy CrM. In EURO PM 2001, European Congress and Exhibition on Powder Metallurgy (pp. 28-33).

[27] Andersson O., Berg S. 2005. Machining of Chromium-Alloyed PM Steels. Advances in Powder Metallurgy and Particulate Materials, 2, 6.

[28] Hu B., Klekovkin A., Milligan D., Engstrom U., Berg S., Maroli B. 2004. Properties of High Density Cr-Mo Pre-Alloyed Materials High-Temperature Sintered. Advances in Powder Metallurgy & Particulate Materials, **2**, 7-28.

[29] Kotan G., Bor A.Ş. 2007. Production and characterization of high porosity Ti-6Al-4V foam by space holder technique in powder metallurgy. Turkish Journal of Engineering and Environmental Sciences, **31**(3), 149-156.

[30] Bafti H, Habibolahzadeh A., 2010. Production of aluminum foam by spherical carbamide space holder technique-processing parameters. Mater Des, **31**, 4122–4129.

[31] Schaber P.M., Colson J., Higgins S., Thielen D., Anspach B., Brauer J. 2004. Thermal decomposition (pyrolysis) of urea in an open reaction vessel. Thermochimica acta, **424**(1-2), 131-142

[32] Kotan G., 2006. Production and Characterization of Porous Titanium and Ti-6Al-4V, A Thesis Submitted to the Graduate School of Natural and Applied Sciences of Middle East Technical University. The Degree of Master of Science In Metallurgical and Materials Engineering

[33] Gülsoy H.O., Timac G. 2020. Ni-90 superalloy foam processed by space-holder technique: microstructural and mechanical characterization. Nanomaterials Science & Engineering, **2**(3), 113-123.

[34] Park C., Nutt S.R. 2001. Effects of process parameters on steel foam synthesis. Materials Science and Engineering: A, **297**(1-2), 62-68.

[35] Park C., Nutt S.R. 2002. Strain rate sensitivity and defects in steel foam. Materials Science and Engineering: A, **323**(1-2), 358-366.

Kocaeli University

Kocaeli Journal of Science and Engineering

http://dergipark.org.tr/kojose

Stabilization of Dredged Materials Using Cement and a Pozzolanic Binder Mineral Additive

Aydın KAVAK [1] iD , Kaan KURTOĞLU [2, *] iD

[1] *Department of Civil Engineering, Kocaeli University, Kocaeli, 41001, Turkey,* **ORCID:** *0000-0003-3445-5946*
[2] *Department of Civil Engineering, Kocaeli University, Kocaeli, 41001, Turkey,* **ORCID:** *0000-0001-8575-6955*

Abstract

In this study, it was aimed to stabilize the dredged materials with low bearing capacity, brought from Edirne, by using cement and pozzolanic binder mineral additives. In the first stage of the study, the geotechnical properties of the dredging materials were determined. Then, the optimum water contents and maximum dry unit weight values of the soil samples without additives and with different additive ratios were found by compaction tests. Pure and additive unconfined compressive samples were prepared with the optimum water contents obtained in the compaction tests. Samples were prepared by adding 8%, 10% and 12% cement and 2% pozzolanic binder additive by weight to the dredged materials. Unconfined compressive tests were performed on the samples at the end of instant, 1-day, 7-day and 28-day curing periods. In addition, soaked CBR, permeability and flexural tests were performed on 12% cement+pozzolanic added samples. As a result of the experiments, with the addition of cement and pozzolanic binder additives in different ratio to the dredged materials, permeability decreased, unconfined compressive strength, soaked CBR values and flexural strength increased significantly.

1. Introduction

Dredging is generally the job of taking the material from the water environment and moving it to another location. Dredging operations are carried out to increase the depth of the open seas, inland waters, canals, shallow, polluted areas, to protect the existing water depth, to create a safe waterway, coastal protection, land reclamation, flood and erosion control. The depth of the channel or stream bed is increased by dredging works. These are excavations performed for many different purposes such as increasing the bearing capacity. A considerable amount of material is obtained as a result of dredging processes carried out on the sea floor, channels and stream beds. These materials become waste materials and their storage may cause environmental problems. Today, with the increase of environmental awareness, dredging materials are used in construction instead of being stored as waste [1-3].

Dredging materials with low bearing capacity have the opportunity to be reused by improving engineering properties with various chemical additives such as lime, cement, fly ash and bitumen. With this process, which is defined as soil stabilization, the negative properties of the weak soil are corrected, the soil becomes more stable, and the bearing capacity increases. Soil stabilization with cement is one of the most preferred methods in soil stabilization. In traditional soil stabilization methods using cement, cement alone is insufficient to react with the existing soil and can not meet the desired project criteria [4]. The use of pozzolanic, pure, binder, mineral additives together with cement in soil stabilization is one of the new methods. In this method, the powdered pozzolanic binder mineral additive allows the soil to react rapidly with the cement. In this way, a waterproof, high-strength, homogeneous and flexible ground layer with the engineering properties required by the specifications and standards is produced [5].

The pozzolanic binder material is made from 100% mineral contended alkaline and soil alkaline constituents. It

---

* Corresponding Author: kaan01kurtoglu@gmail.com

contains natural oxides, chlorides, sulfates and carbonate minerals. Pozzolanic mineral is a white colored powder, that is non-toxic, non-detrimental for the health and environmentally friendly. It is used by adding 2% to cement and mixing with soil. Pozzolanic binder mineral combined with cement and optimal water content increases the crystallized formations during the hydration process, resulting in higher strengths, neutralizes ph levels, and provides water impermeability. The pozzolanic binder mineral neutralizes the existing acids and supports the hydration process by allowing the formation of longer crystals. Soil stabilization with pozzolanic additive can be applied on clayey, sandy, organic matter-containing soils on almost all kinds of soils. It can transform almost all kinds of soils or bases into a very strong typical 150 MN/m^2 foundation layer without replacing the existing soil in the field. The stabilized surface does not allow the penetration of the water or ice. Stabilized surface is resistant against oil, salt, acids and chemicals. Therefore, it significantly increases the physical life of the stabilized layer and does not need maintenance costs for a long time. Stabilization with cement and pozzolanic additive is applied in any type of roads, railways, storage and industrial surfaces, mines, rural roads, garbage dumping areas and airports. Cement and pozzolanic binder additive can be used as sub-base and foundation layer in road superstructures by improving the weak soils brought from off-side, in road, railway and highway constructions, and in the stabilization of infrastructure filling layers. For this purpose, it is widely used in many projects in our country [6].

Soil stabilization with cement and pozzolanic binder additive has been applied in many highway and railway projects in our country. Soil stabilization studies using cement and pozzolanic binder mineral additives were carried out in 2013 for the first time in railway projects in our country. Pozzolanic additive was used in the rehabilitation and signalization project of the Irmak-Karabük-Zonguldak railway line of the State Railways of the Republic of Turkey. Within the scope of the project, improvement was made in Çaycuma station in 2 days using the existing material on the ground, cement and pozzolanic additives, without excavating, without bringing any material from off-side. The application was applied to a clay layer with high plasticity (CH) and low strength. A homogeneous layer was obtained by using 42 kg to 62.5 kg cement and pozzolanic additive at the rate of 2% of the cement in 1 m^2 area. The soaked CBR value of the soil before the improvement was 4%. The 7-day soaked CBR value of the soil after improvement was found to be 122%. After the application, the soil layer reached a high bearing capacity in a short time. Within the scope of the State Railways of the Republic of Turkey Denizli-

Afyonkarahisar Railway Line Renovation Project, weak soil layer has been stabilized by using cement and pozzolanic additive. The project was carried out on a very low strength clay layer. The soaked CBR value of this layer is about 3%. For stabilization 50 kg to 56 kg cement and a pozzolanic additive at the rate of 2% of the cement in 1 m^2 area were used. The field and laboratory tests performed in the base soil layer, which was stabilized after the production. Results were found to be quite above the values defined in the specification. Accordingly, the plate loading value, which was required to be 60 MPa in the project, was found to be 160 MPa after stabilization. Unconfined compressive tests were carried out on cement and pozzolanic added samples. The unconfined compressive strength, which is required to be at least 500 kPa in the project specification, has been determined as 1140 kPa. Cement and pozzolanic additives were used in the improvement of the filling layers in the State Railways of the Republic of Turkey Samsun-Kalın railway modernization project. Within the scope of this project, it was decided to stabilize the project with cement and pozzolanic additives, instead of rock fill, in order to complete the project more quickly. In the project, 60 kg cement per m^2 and 2%-of-the-cement pozzolanic additive were added to the low strength clay layer. It was observed that the soaked CBR values of the mixtures prepared by adding cement and pozzolanic additives were increased significantly compared to the natural material [6,7]. Kavak has determined that this stabilization method has many advantages, that this method will reduce typical road sections and provide both economic and environmental benefits. With this stabilization method, transportation costs will decrease significantly with the use of on-site material in the fillings [8].

In this study, an innovative pozzolanic binder mineral additive was used together with cement to improve the engineering properties of dredging materials with low bearing capacity, and the effects of additives on soil samples were investigated with experimental studies.

2. Materials and Methods

2.1. Cement

The cement used in the experimental studies is 32.5R pozzolanic cement, which is sold in 50 kg bags in the market. Cement complies with the conditions specified in TS EN 197-1 [9]. Standard properties are given in Table 1.

Table 1. Standard properties of cement

Strength Class	Compressive Strength (Mpa)			Setting Start Time (minute)	Expansion (mm)
	Early Strength		Standard Strength		
	2 Days	7 Days	28 Days		
32.5R	≥10.0	-	≥32.5	≤52.5	≥75	≤10.0
	TS EN 196-1			TS EN 196-3	

2.2. Pozzolanic Binder Mineral Additive

The pozzolanic powder binder mineral additive material used by mixing with cement in the study has 100% mineral content and consists of alkaline and earth alkaline structures. It contains natural oxides, chlorides, sulphates, and carbonate minerals. It is a white, non-toxic, environmentally friendly, natural mineral powder. The material added to the cement at the ratio of 2% is mixed with the soil [6].

2.3. Materials of Dredging

The dredging materials with low bearing capacity used in the stabilization processes were brought from a river bed from the district of Edirne. In the first stage, some experiments were carried out in order to determine the geotechnical properties of the materials brought to the Kocaeli University geotechnical laboratory and to make soil classifications. The experiments were carried out in accordance with ASTM, TS1500, TS1900-1 and TS 1900-2 standards [10-20]. Natural water content determination, organic matter determination, Atterberg consistency limits tests, wet sieve analysis, specific gravity and standard compaction tests were performed on the dredging materials, respectively. Stabilization process is applied to soil samples containing less than 4% organic matter as specified in the specification [21,22]. As a result of the organic matter determination experiments, it was determined that the organic matter content of the dredging materials was less than 4% and it was found to be 2.95%. The soil classification result and geotechnical properties are given in Table 2. It was determined that the soil class of the dredging materials is silty clayey sand (SM-SC) according to Unified Soil Classification System. As a result of the Atterberg consistency limit tests, the liquid limit value of the dredging material is 22%, the plastic limit value is 17%, and the plasticity index value is 5%. The liquid limit value was determined with the Casagrande test instrument. The specific gravity value was found by pycnometer test. The specific gravity of the dredging material was determined as 2.67. The clay + silt ratio was found to be 36.5% and the sand ratio to be 63.5% by wet sieve analysis.

Optimum water contents and maximum dry densities of the dredging materials were found by standard proctor compaction tests. The optimum water content of the dredging material was found to be 10.94%, and the maximum dry unit weight was found to be 1.74g/cm^3.The results are given in Table 2. Mixtures were formed by adding cement and pozzolanic binder mineral additives to the dredging materials whose geotechnical properties were determined.

Table 2. Properties of dredging materials

Sample	Dredging Material
Classification (USCS)	SM-SC
Liquid Limit (%)	22
Plastic Limit (%)	17
Plasticity Index (%)	5
Clay+Silt (%)	36,5
Sand (%)	63,5
Gravel (%)	0
Specific Gravity	2,67
Organic Matter (Content %)	2,95
Optimum Water Content (%w$_{opt}$)	10,94
Maximum Dry Density (g/cm^3)	1,74

The amount of additive to be used in soil stabilization with cement and pozzolanic additives is determined by taking into account the soil class, soil CBR value, the strength required from the project, traffic load, traffic volume, field and laboratory test results. The amount of cement to be used in the study was determined according to the technical specifications of the manufacturer of pozzolanic binder material. Soil class and CBR value have great importance in the determination of the amount of cement to be used. According to this specification, the amount of cement to be used for sandy soils varies between 140-200 kg/m^3. The amount of cement to be used for laboratory tests varies between 8% and 12% of the dry unit weight of the soil. This ratio was selected to be between 8% and 12% for laboratory experiments. According to the material manufacturer, the ratio of pozzolanic additive to be used is 2% by weight of the cement amount.

Atterberg consistency limits, Harvard miniature compaction and unconfined compressive tests were carried out by adding 8%, 10% and 12% cement and pozzolanic binder mineral additive at the rate of 2% of cement to the dredging material. Permeability, soaked CBR (California Bearing Ratio) and beam flexural tests were carried out by adding 12% cement and pozzolanic binder mineral additive at the rate of 2% of cement to the dredging material. In order to obtain the highest strength ratio, experiments were carried out by choosing a single additive ratio in permeability, soaked CBR and flexural tests. Since the highest strengths were obtained at 12% additive rate as a result of unconfined compressive tests, this ratio was preferred in the tests. Atterberg consistency limit tests were

applied by adding 8%, 10% and 12% cement and 2% pozzolanic binder additive to the dredging materials. The prepared mixtures were cured for 1 hour. Due to pozzolanic reactions, mixtures were cured for one hour. After curing for 1 hour, changes in the Atterberg consistency limits were observed. Harvard miniature compaction experiments were carried out by adding 8%, 10% and 12% cement and 2% pozzolanic binder additives to the dredging materials. Due to less time and materials are used, Harvard miniature compaction experiments were applied on the with additive samples. As a result of the Harvard miniature compaction tests, optimum water content and maximum dry unit weight of the mixtures were found. Unconfined compressive strength test samples were prepared with optimum moisture contents obtained by compaction tests. Cylindrical specimens were prepared using Harvard miniature compaction mold. Unconfined compressive test samples were prepared by adding cement (8%, 10%, 12%) and pozzolanic binder additive (2% of cement) to the dredging materials. Samples were prepared for instant, 1-day, 7-day and 28-day curing periods for unconfined compressive test. Three samples were prepared for each additive ratio and curing time. A total of thirty-six cement and pozzolanic added samples were prepared. Six natural samples were prepared for unconfined compressive strength tests. Three of these samples were cured for 1 day. For the others, instant tests were carried out. For comparison with cement and pozzolanic added samples, six samples with 12% cement were prepared. Three of the 12% cement samples were cured for 7 days. The others cured for 28 days. A total of forty-eight unconfined compressive samples were prepared. The samples were firstly wrapped with aluminum foil and then kept in a desiccator during the curing period. The graphs were created by taking the average of the strength values of the prepared samples. As a result of unconfined compressive tests, soaked CBR test was carried out by using 12% additive ratio, which gives the highest strength. Due to the amount of material being low, only 7- day- cured soaked CBR test was performed. The sample with 12% cement and pozzolanic added was kept in the curing room for 3 days and in water for 4 days. Falling head permeability tests were carried out to determine the permeability of the samples with and without additives. Due to the amount of material being low, only 12% cement and pozzolanic added test were carried out. The samples were prepared in the standard proctor mold at optimum water content and cured for a certain period of time. Measurements were made by saturating the samples for two weeks. Then the permeability coefficients were calculated. Finally, 40x40x160 mm prismatic samples were prepared to determine the flexural strength of the samples with additive. Due to the amount of material being low, samples

with 12% cement and 12% cement + pozzolanic additives were prepared. Mixtures were prepared using optimum water contents. The mold was lubricated before the mixtures were placed in the mold. The mixtures were placed in the mold as at least 3 layers. Each layer was rammed with a plastic mallet to ensure that the mixtures were well compacted. Samples were cured for 7 and 28 days. After the samples with additive were placed in the mold, samples were kept in the curing room for 1 day. At the end of 1 day, samples were taken out of the mold and put into bags. At the end of the curing period, 3-point beam flexural tests were carried out by placing the beam in the flexural apparatus.

3. Results and Discussion

3.1. Atterberg Consistency Limits

Atterberg consistency limits tests were conducted by adding 8%, 10% and 12% cement and pozzolanic binder additive at the rate of 2% to the dredging materials. Changes in the Atterberg consistency limits were observed after curing for a certain period of time. As a result of the experiments, it was determined that the plastic limits of the samples increased, and the plasticity indices decreased as the additive ratios increased. With the addition of 8% cement and pozzolanic binder mineral additives to the dredging materials, the liquid limit value of the dredging materials was 24.55%. Plastic limit values increased to 21.22%. The plasticity index of the dredging materials decreased to 3.33%. With the addition of cement (C) and pozzolanic additives (PA), the workability of the dredging materials increased. The changes in the Atterberg consistency limits with the addition of additives in different ratios to the dredging materials are shown on the graphic in Figure 1.
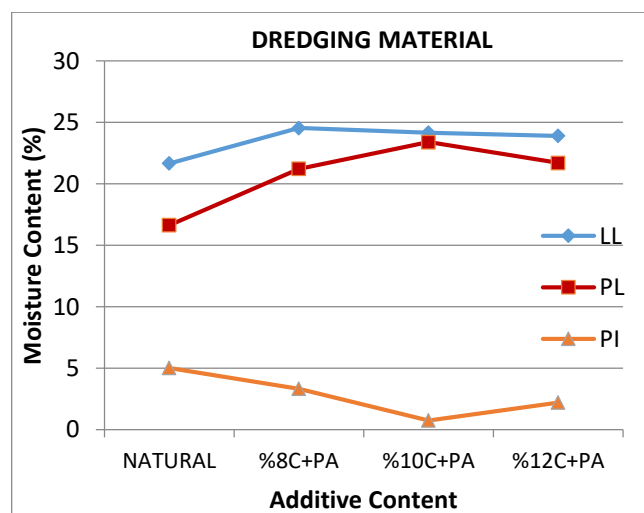
Figure 1. The Atterberg consistency limits of the dredging material with different additive ratios.

3.2. Harvard Miniature Compaction

Harvard miniature compaction experiments were carried out by adding 8%, 10% and 12% cement and 2% pozzolanic binder additives to the dredging materials by weight. As a result of the compaction tests, optimum water content and maximum dry unit volume weight of the mixtures were determined. In all the with additive samples, the optimum water content increased compared to the natural state. The maximum dry densities of the with-additive dredging materials increased compared to the natural state. The Harvard miniature compaction test results of the samples with additives are given in Table 3.

Table 3. Harvard Miniature compaction test results

Mixtures	Optimum Moisture Content (% w_{opt})	Maximum Dry Density (g/cm^3)
(SM-SC)+%8C+PA	14,48	1,79
(SM-SC)+%10C+PA	14,76	1,78
(SM-SC)+%12C+PA	13,93	1,80

3.3. Permeability

In this study, the permeability of dredging materials and with additive samples was found by decreasing level permeability tests. The permeability coefficients were found by adding 12% cement and with pozzolanic binder mineral additive at the ratio of 2% to the dredging materials. The impermeability degrees of the samples were determined by comparing the permeability coefficients of the samples with and without additives. For this purpose, additive and non-additive mixtures have been formed by using the optimum water contents obtained in compaction experiments. The resulting mixtures were compressed with standard proctor energy in a standard compaction mold at optimum water contents. The prepared samples with additives were cured for a certain period of time. Then, the compressed and cured samples with and without additives were placed in the falling head permeability mechanism and the samples were waited until they became saturated. The samples were allowed to become saturated for about a two week. Later, falling-head permeability experiments were carried out, and readings of the falling water level were made periodically. Permeability coefficients were calculated with the data obtained. At the end of the study, it was calculated that the permeability coefficients of the non-additive samples were greater than the permeability coefficients of the samples with 12% cement + pozzolanic additive.

It was observed that the permeability of the with additive samples decreased as the permeability coefficients decreased. According to Terzaghi and Peck's (1967) soil permeability coefficient classification, it was concluded that samples with additives can be considered practically impermeable. Table 4 gives Terzaghi and Peck's (1967) classification of soils according to their permeability coefficients [23]. In Table 5, the permeability coefficients of the without- additive and with- additive samples are shared. The permeability of the dredging material decreased with the addition of cement (C) and pozzolanic additives. Dredging materials have become impermeable. As a result of impermeability, water does not enter the soil, so the soil does not freeze. As a result, the soil is resistant to salt, acids and chemicals.

Table 4. Coefficient of permeability (Terzaghi and Peck)

Degree of Permeability	Coefficient of Permeability, k (cm/s)
High	Over 10^{-1}
Medium	10^{-1}-10^{-3}
Low	10^{-3}-10^{-5}
Very Low	10^{-5}-10^{-7}
Practically Impermeable	Less Than 10^{-7}

Table 5. Permeability coefficients of the specimens

Specimens	Coefficient of Permeability, k (cm/s)
Natural Soil (SM-SC)	$5,13x10^{-7}$
Natural Soil+%12C+PA	$9,84x10^{-9}$

3.4. Soaked CBR (California Bearing Ratio)

The soaked CBR (California Bearing Ratio) test is used to determine the bearing strength of soils. In the scope of the study, soaked California Bearing Ratio (CBR) tests were carried out in accordance with TS EN 1900-2 specification by using the optimum water contents obtained by compaction tests. Firstly, the soaked CBR values of natural samples were found. Then, 12% cement and 2% pozzolanic binder mineral additives were added to the dredging material and the mixtures were prepared. All samples prepared were kept in water for four days. The samples with additives were placed in the curing room before being kept in water and cured for a certain period of time, and soaked CBR tests were applied at the end of seven days. The soaked CBR values of the natural samples were determined as 2.5%. The soaked CBR values of the 12% cement and pozzolanic added dredging materials were found to be 120%. The soaked CBR value of the dredging materials with cement + pozzolanic additives at the end of the seven-day curing period has increased forty-seven times compared to the natural state. The seven-day soaked CBR values of the stabilized dredging materials increased

significantly compared to the natural state, and the dredging materials with low bearing capacity became usable in construction. In Figure 2, the soaked CBR (California Bearing Ratio) values of the additive and non-additive samples are graphically given.
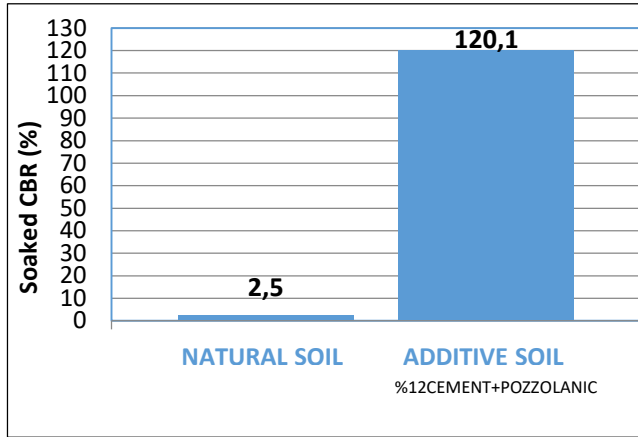
Figure 2. Soaked CBR values

3.5. Unconfined Compressive Strength

Unconfined compressive strength test samples were prepared with optimum moisture contents obtained by compaction tests. Firstly, samples with instant and 1 day curing time were prepared using optimum water contents without additive to the dredging material. The average unconfined compressive strength value of the dredging material was found to be 23 kPa for instant. The average of unconfined compressive strength value of the 1 day cured samples was determined as 40 kPa. Then, instant, 1-day, 7-day and 28-day unconfined compressive samples were prepared by adding 8%, 10% and 12% cement and 2% pozzolanic binder additives to the dredging materials by weight. At the end of the curing period, the unconfined compressive strengths were determined. The average of unconfined compressive strength of dredging materials with 8% cement and pozzolanic binder mineral additive were found as 313 kPa, 870 kPa, 1517 kPa, 2130 kPa for instant, 1 day, 7 days and 28 days curing times, respectively. The average unconfined compressive strength values of samples with 10% cement and pozzolanic additives were found as 330 kPa, 985 kPa, 1700 kPa, 2460 kPa for instant, 1 day, 7 days and 28 days curing times, respectively. In the samples with 12% cement + pozzolanic additives, the average unconfined compressive strengths were found as 390 kPa, 1090 kPa, 1720 kPa and 2600 kPa for instant tests, after 1 day, after 7 days and after 28 days respectively. In addition, 12% by weight of cement was added to the dredging materials and strength test samples were prepared for 7-day and 28-day curing times and their compressive strength was compared with the cement +

pozzolanic binder added samples. According to the compressive test results, the 7-day unconfined compressive strength of the dredging material with 12% cement additive was found to be 1500 kPa, and the 28-day strength was found as 1660 kPa. The unconfined compressive strength values of the dredging materials without additives and with cement + pozzolanic additives in different ratios are given in Figure3
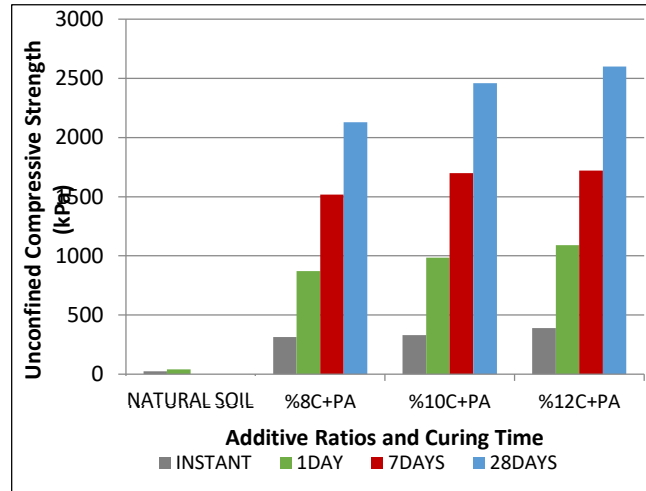
Figure 3. Unconfined compressive strengths

Figure 3 shows the without-additive and with-additive unconfined compressive strength values of the dredging materials. The highest strength in the samples with additives was obtained with 12% cement + pozzolanic binder mineral additive added to the dredging material. 12% cement and pozzolanic additive were added to the dredging material, and the unconfined compressive strength of over 2.5Mpa was obtained at the end of the 28-day curing period. It was also observed that their strength is considerably lower than pozzolanic additive ones. Figure 4 shows the unconfined compressive strength graphs formed by adding 12% cement to the dredging materials.
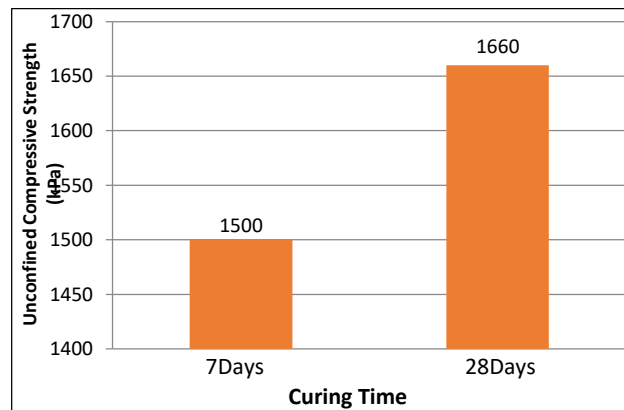
Figure 4. Unconfined compressive strength with 12% cement added

Figure 5 shows the stress unit deformation graph that occurs at the end of the twenty-eight day curing period when cement and pozzolanic additives are added to the dredging materials in different ratios. In Figure 6, the natural and different ratios of cement + pozzolanic additive instant samples stress-strain graphs for the dredging materials are given. The unit deformation of samples decreased as the amount of additive materials increased. The unit deformation of samples decreased as the curing period of samples increased.
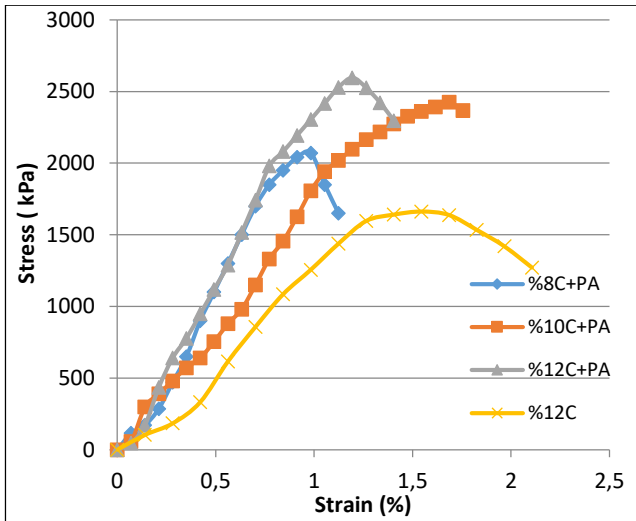
Figure 5. Stress-strain curves of 28 day cured samples
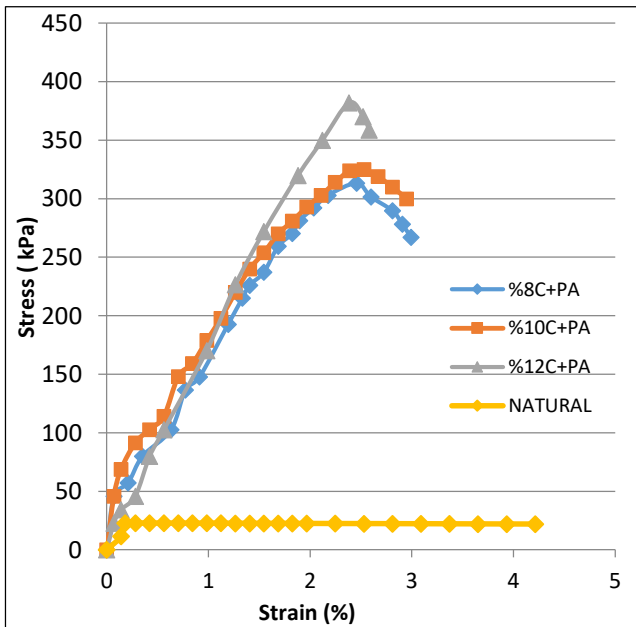
Figure 6. Stress-strain curves of instant samples

3.6. Flexural Strength

In the study, 40x40x160 mm prismatic samples were prepared in order to determine the flexural strength of the with- additive dredging materials. The samples were

prepared by adding 12% cement and 12% cement + pozzolanic additives to the dredging materials. The prepared samples with additives were kept in the curing room for 7 days and 28 days, then 3-point flexural tests were conducted using the beam flexural apparatus. According to the test results, it was seen that the cement + pozzolanic added samples have higher flexural strength than the cement-added samples. The flexural strength results are given in Figure 7 and Figure 8. According to the flexural strength test results, it was determined that the cement + pozzolanic binder mineral added samples were more flexible than the cement-added samples.
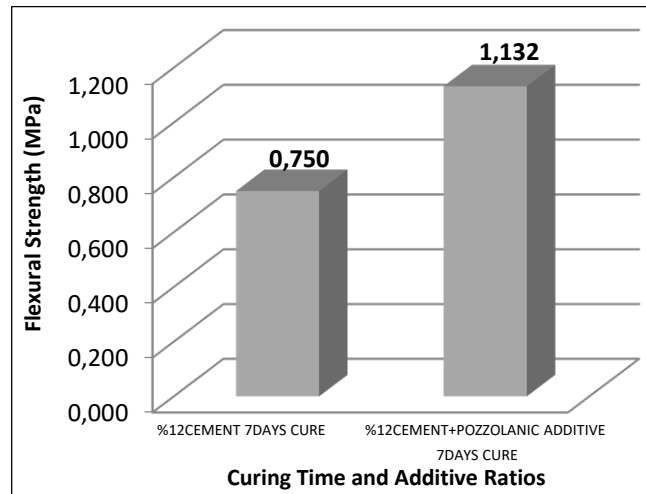
Figure 7. Flexural strengths for 7 days curing time
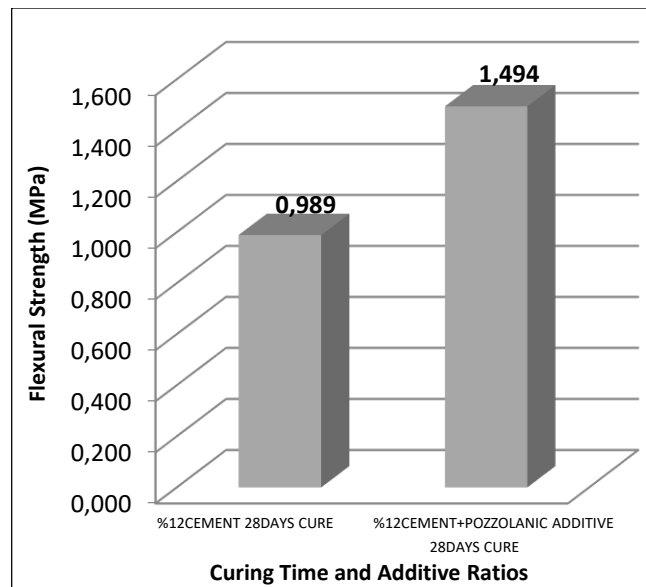
Figure 8. Flexural strengths for 28 days curing time

4. Conclusions

In this study, an innovative pozzolanic binder mineral additive was used together with cement to improve the engineering properties of dredging materials with low

bearing capacity, and the effects of additives on soil samples were investigated with experimental studies. Unconfined pressure tests were carried out by adding cement (8%, 10%, 12%) and pozzolanic binder additive (2% cement) to the dredging materials. The unconfined compressive strength of dredging materials significantly increased with the amount of cement and pozzolanic additive.The unconfined compressive strengths of dredging materials increased with curing time increase. In the study, it was determined that the strength of the cement + pozzolanic-added dredging materials was higher than the cement-added materials.

With the addition of cement and pozzolanic binder additives to the dredging materials, the plastic limits increased, and the plasticity indices decreased. This shows that the dredging materials turn rigid with the addition of cement + pozzolanic additive and their workability increases.

With the increase in the rate of additives and curing time added to the dredging materials, there has been a serious increase in their strength. Increases were observed in the unconfined compressive strengths of the dredging materials with 12% cement + pozzolanic binder additive, with a curing time of 28 days compared to the dredging materials in natural state.

The soaked CBR values of the dredging material with 12% cement + pozzolanic binder with 7 days curing time has increased approximately 48 times compared to the natural state. The soaked CBR values for stabilized materials increased from 2.5% to 120.1%. The high CBR values obtained, by reducing the thickness of the road layer in road constructions, enable more economical and low-cost roads.

Mixtures formed by adding 12% cement + pozzolanic binder additive to the dredging materials were subjected to permeability tests and their permeability coefficients were calculated and permeability degrees were determined. Dredging materials have become impermeable. In this way, dredging materials is more resistant to acids, salts and chemicals.

As a result of the flexural strength tests, it was determined that the flexural strength of the cement + pozzolanic additive dredging materials was higher than the only cement-added samples. The stabilized material becomes more flexible through the addition of pozzolanic additives compared to the traditional stabilization made with cement. This has enabled the disadvantages of the extremely rigid structure seen in the stabilization with cement to be eliminated. The high flexural strengths show that the cement + pozzolanic binder-added soil has become more flexible and more resistant to fractures.

Through the stabilization process with cement + pozzolanic binder additive, the dredging materials with low bearing capacity, taken from the field, can be used as filling, sub-base and base material in construction sites. In this way, instead of being stored as waste, it is used in constructions and the damage to the environment can be prevented.

As a result, in this study, considering high strength, high elasticity and impermeability, it was revealed that stabilization with cement and pozzolanic additives is much more effective than traditional soil stabilization with cement in the stabilization of low bearing capacity dredging materials.

Declaration of Ethical Standards

The authors of this article declare that the materials and methods used in this study do not require ethical committee permission and legal-special permission.

Conflict of Interest

The authors declare that they have no known competing financial interests or personal relationships that could have appeared to influence the work reported in this paper.

References

[1] Hoff J., Kolff A.N., 2012. Hydraulic Fill Manual: For Dredging and Reclamation Works, CRC Press, Boca Raton.

[2] T.R. Official Gazette, Sea and Inland Waters Dredging Regulation, 09.08.2016, Number:29796, Prime Ministry Printing House, Ankara.

[3] URL-1: http:// www.european-dredging.eu, (Visit date: 20 March 2021).

[4] Yemenici B., Coruk Ö., 2018. Novocrete® Technology And Applications In Soil Stabilization With Cement, 71st Geological Congress of Turkey, 23-27 April, pp.287-288.

[5] Coruk Ö., Kavak A., Aydıner A., 2018. NovoCrete® Applications in Soil Improvement in Railways, Railway Engineering Journal, **6**, 73-78.

[6] URL-2: http://www.jags.com.tr, (Visit date: 10 March 2021)

[7] Yemenici B., Coruk Ö., 2017. Novocrete® Technology And Applications in Stabilization of In-Situ Soils, International Engineering Geological and Geotechnical Symposium, Adana, 12-14 October 2017, pp.239-244.

[8]   Kavak A., Coruk Ö., Aydıner A., A New Binder Mineral for Cement Stabilized Road Pavement Soils, Sixth International Conference On Advances in Civil, Structural and Mechanical Engineering, Bangkok, Tayland, 25-26 Şubat 2017, pp.68-71.

[9]   TS EN 197-1 Cement Part 1: Compositions and Conformity Criteria for Common Cements, Turkish Standards Institution, (2002).

[10]   TS 1500 Classification of Soil for Civil Engineering Purposes, Turkish Standards Institution, (2000).

[11]   TS 1900-1 Methods of Testing Soils for Civil Engineering Purposes in the Laboratory Part 1: Determination of Physical Properties, Turkish Standards Institution, (2006).

[12]   TS 1900-2 Methods of Testing Soils for Civil Engineering Purposes in the Laboratory Part 2: Determination of Mechanical Properties, Turkish Standards Institution, (2006).

[13]   ASTM D422-63 (2007) e2, Standard Test Method for Particle Size Analysis of Soils, ASTM International, West Conshohocken, PA, 2007, www.astm.org.

[14]   ASTM D698-12e1, Standard Test Methods for Laboratory Compaction Characteristics of Soil Using Standard Effort, ASTM International, West Conshohocken, PA, 2012, www.astm.org.

[15]   ASTM D1635/D1635M-19, Standard Test Method for Flexural Strength of Soil-Cement Using Simple Beam with Third-Point Loading, ASTM International, West Conshohocken, PA, 2019, www.astm.org.

[16]   ASTM D1883-14, Standard Test Method for California Bearing Ratio (CBR) of Laboratory Compacted Soils, ASTM International, West Conshohocken, PA, 2014, www.astm.org.

[17]   ASTM D2166/ D2166M-16, Standard Test Method for Unconfined Compressive Strength of Cohesive Soil, ASTM International, West Conshohocken, PA, 2016, www.astm.org.

[18]   ASTM D2487-11, Standard Practice for Classification of Soils for Engineering Purposes (Unified Soil Classification System), ASTM International, West Conshohocken, PA, 2011, www.astm.org.

[19]   ASTM D2974-20e1, Standard Test Methods for Determining the Water (Moisture) Content, Ash Content, and Organic Material of Peat and Other Organic Soils, ASTM International, West Conshohocken, PA, 2020, www.astm.org.

[20]   ASTM D4318-17e1, Standard Test Methods for Liquid Limit, Plastic Limit, and Plasticity Index of Soils, ASTM International, West Conshohocken, PA, 2017, www.astm.org.

[21]   TS EN 1744-1+A1 Tests for Chemical Properties of Aggregates Part 1: Chemical Analysis, Turkish Standards Institution, (2013).

[22]   Highways Technical Specification, General Directorate of Highways, (2013).

[23]   Terzaghi K., and Peck R.B., (1967). Soil Mechanics in Engineering Practice, Second Edition, John Wiley, New York.
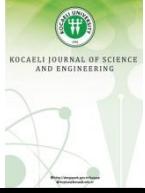
Photovoltaic Mobile Charging System Design (Solar Pole) - in Gümüşhanevi Campus of Gümüşhane University

Mustafa Engin BAŞOĞLU [1, *] (iD) , Muzaffer ÇAYIR [2] (iD) , Nurgül ŞEN [3] (iD) , Murat Han ERTUĞRUL [4] (iD)

[1] Department of Electrical - Electronics Engineering, Gümüşhane University, Gümüşhane, 29100, Turkey, **ORCID:** 0000-0002-6228-4112
[2] Department of Electrical - Electronics Engineering, Gümüşhane University, Gümüşhane, 29100, Turkey, **ORCID:** 0000-0002-1706-8576
[3] Department of Electrical - Electronics Engineering, Gümüşhane University, Gümüşhane, 29100, Turkey, **ORCID:** 0000-0002-7836-2971
[4] Department of Electrical - Electronics Engineering, Gümüşhane University, Gümüşhane, 29100, Turkey, **ORCID:** 0000-0002-2401-1260

Abstract

The decrease in fossil-based resources, the pollution of the environment and the threat of sustainability constantly increase the interest in renewable energy sources. Solar energy is one of the leading renewable energy sources due to its large capacity. Today, solar energy appears in many applications. In this study, a photovoltaic-based solar pole design has been realized and a prototype that can be applied almost anywhere in open-air conditions has been produced. The prototype produced was tested and installed at Gümüşhane University's Gümüşhanevi Campus. The prototype mobile phones produced have a fast charging feature with 5V-2A. In future studies, it is planned to provide the solar tracking feature to the photovoltaic (PV) panel in the system, and it is aimed to bring such systems to the campus in general.

1. Introduction

Today, the use of solar energy has become possible in almost every area where energy is needed. Electricity generation from solar energy ranges from power levels of a few kW to hundreds of MW [1]. Apart from this, solar-powered bus stops, solar powered tents, solar-powered backpacks, solar-powered led lighting equipment, electric or hybrid vehicles equipped with solar panels and many similar small powerful applications are commercially applied today. Among these applications, solar-powered charging stations are very popular, solar charging stations, which usually only charge mobile phones, are very popular in the streets, city centers or bus stops, in non-closed environments where people wait and spend time.

There are many studies for solar energy applications. In [2], LED lighting and irrigation pumps, where electronic devices can be charged via USB, were supplied with a PV

system isolated from the electricity grid. Different DC voltage levels were obtained from step-down and step-up converters in the system. Solar energy can be used for charging mobile phones in wearable applications such as arm bags. In such an application in [3], the efficiency problem arises because the solar cells on the bag are exposed to different radiations. In this study, five different converter configurations were tested according to the differential power processing strategy and the parallel DPP converters were determined as the most suitable converter. In another study, single-axis and double-axis solar tracking systems were proposed to make maximum use of the sun [4]. The solar panel can be used as an energy source in mobile robot applications. PV system design and implementation have been done for Mars rovers. The tracking of a 20W solar panel was provided with a single axis azimuth and elevation angle setting, and around 44% more power was obtained with this tracking [5]. For wireless sensor networks, PV systems can be a viable energy source solution. In [6], a system in which the current and voltage measurement of the battery and the load of the microcontroller-based PV system was

---

proposed. PV energy can be used at charging stations for fast charging of electric vehicles. In [7], a model was developed in MATLAB Simulink for the design and sizing of solar charging stations. It is predicted that the proposed system acts as a mobile power system and electric vehicles can be charged at 80% capacity in 10.25 seconds. Three-wheeler vehicles are one of the most cost-effective options for short-distance transportation. In [8], an intelligent energy management system for PV-based charging station was proposed for such three-wheeled vehicles. Intelligent energy management performs energy management by using data such as PV data, user requirement and battery charge. A solution offering parking reservation via mobile application was proposed for these three wheeled taxi vehicles. In another study [9], a PV charging system that charges mobile phones with USB 3.0 technology with 5V - 2A values has been proposed. In a study [10], solar tree application was proposed for charging mobile phones in open urban areas. The solar tree consists of four leaves and a total solar panel power of 200W. Solar tree has six USB ports and two 110V-200W electrical outputs in total. In a different study [11], one-year data was examined to examine the performances of different types of solar panels. According to the results, it has been seen that Cd-Te type solar panels were less affected by temperature and perform better. The work on the prototype of the solar powered backpack was given in [12]. A study in which the performance analysis of solar power plants was examined and the performance data were analyzed over a sample power plant was presented in [13], and the performance ratio of the small power PV plant within Kocaeli University was 87.5% - 98.1%.

In this study, a single solar panel solar pole application for charging mobile phones was carried out at the Faculty of Engineering and Natural Sciences in Gümüşhane University Gümüşhanevi Campus. With the 42W solar panel and the energy stored in the 12V 9Ah lead acid battery, 5V-2A fast charging is provided thanks to two USB outputs. The number of USB outputs can be increased thanks to the modular structure. The study was carried out within the scope of the undergraduate thesis, and in the next section, the basis and general characteristics of solar energy are mentioned. Then, the solar energy potential for Gümüşhane province is given within the framework of basic information. In the fourth chapter, the mechanical and electrical details of the design are given and the results of the study are given in the last section.

2. Materials and Methods

Solar energy is one of the cleanest renewable energy sources on earth, without any gas emissions. Radiation energy is formed because of some chemical events that occur in the sun. Solar radiation can be converted into electrical energy with PV modules. Systems that use the energy from the sun to generate electricity are called PV systems. PV systems have many uses. Some of these are; roof-integrated systems, solar energy systems for lighting purposes, large-powered solar fields, auxiliary energy source in electric vehicles, mobile robots, mobile devices, calculators, backpacks and many wearable applications.

Among the listed PV applications, there are solar panels as a power source, a charge controller USB module for battery charging, a battery for storage, in the structure of systems where mobile devices can be charged. Examples of PV systems that allow charging mobile devices are given in Figure 1 and Figure 2. As can be seen in the examples, the solar panels are positioned at different angles in order to make the best use of the solar irradiation.

Figure 1. PV system example-1 [14].

Figure 2. PV system example-2 [14].

Solar energy systems are generally divided into two groups as grid-connected and off-grid systems. In grid-

connected systems, the electricity produced is directly consumed or some of it is transferred to the grid. In systems that are not connected to the grid, the energy produced can be used instantly, or it can be stored in batteries and used for use when solar electricity is low.

2.1. Solar Energy Potential in Gümüşhane

Solar energy is one of the most common renewable energy sources on earth. Electrical energy and heat energy can be obtained from this type of energy. On the other hand, since the costs of PV panels are higher than fossil fuel-based production, only 0.04% of the solar energy coming to the earth is used by people.

Turkey is lucky compared to many countries in terms of its solar energy potential due to its geographical location and structure. According to the study made by using the data of sunshine duration and solar irradiation measured in 1966-1982 at the General Directorate of Meteorology Affairs, the average annual total sunshine duration of Turkey. It was determined that the duration of the study was 2.640 hours (7.2 hours in total per day), and the average total intensity of heating was 1.311 kWh/m² per year (total 3.6 kWh/m² per day). In Turkey, which has a high solar energy potential of 110 days, there is potential to produce an average of 1.100 kWh of solar energy per square meter per year if the necessary investments are made (Energy Sector Report, GEKA).

The sunshine duration (hour-year) of Gümüşhane province is 2.349. The radiation value (kWh/m²-year) is between 1.400-1.600. The map in Figure 3 shows the solar energy potential of the Gümüşhane province as kWh/m²-year. As can be seen on the map in Gümüşhane province, the highest solar energy potential is seen in Kelkit and the least in Kürtün region.
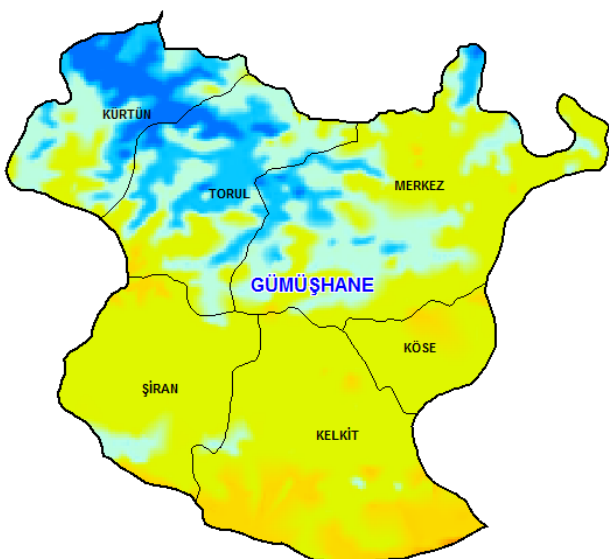
Figure 3. Solar energy potential map of Gümüşhane.

2.2. Photovoltaic Pole System

The electrical materials required for solar pole design can be listed as solar panel, battery, charge controller and USB module. The solar pole has been planned to have four USB modules, and since the charging voltage and current for mobile phones are determined as 5V-2A, 10W power will be needed for a mobile phone during charging. If 4 USB modules are used in the system, the total power requirement will be 40W. At the same time, 8A current should be obtained from the battery instantly for four USB outputs. The solar panel will need to produce 40Wh energy per hour. Although the determination of the battery capacity is relative, the excess capacity offers technical advantages when a cost is not taken into account. For example, when solar radiation is low, batteries cannot benefit from solar energy sufficiently. In this case, the battery capacity is high, allowing the user to charge their mobile phones without power interruption [15].

As seen in Figure 4, the system includes a solar panel, charge controller, battery and USB module. In this type of system, the rays coming from the sun are produced on the panel and electrical energy in DC form. This energy is stored in batteries. However, the voltage obtained at this stage should be converted to the voltage level at which the battery can be charged, and at the same time, full charge and full discharge of the battery should be prevented. For this purpose, a converter circuit or charge controller is needed. The connection of the charge controller is made between the panel group and the battery group. Voltage converter circuits are used between the battery connection and the USB modules.
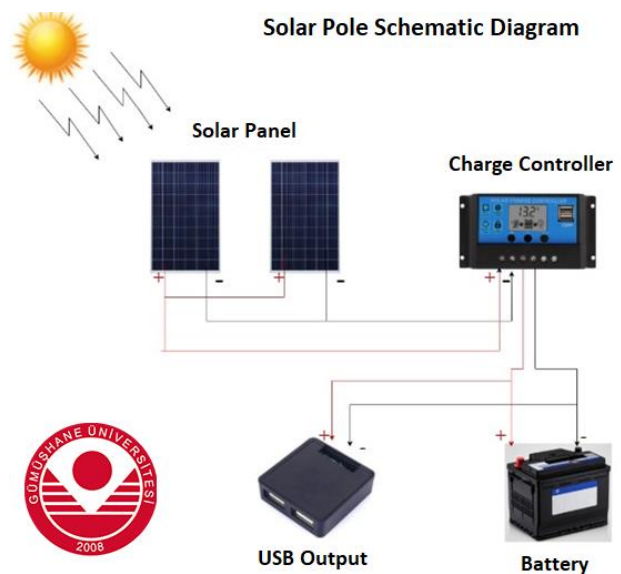
Figure 4. Schematic diagram of solar pole.

3. Results and Discussion

Within the scope of this study, the drawing of the targeted system was created with the help of SketchUp program. According to this drawing, the front, back and side views of the system are given in Figure 5.

As seen in Figure 5, since there will be a charge controller and battery in the section behind the solar panel, this section has been closed. The purpose of this process is to prevent damage to the battery and charge controller located under the solar panel in bad weather conditions. In addition, the sheet on the back of the solar panel is produced in a structure that can be opened easily so that it can be easily intervened in case of any malfunction or material change. Then, the system carrying the solar panel was fixed on the top of the iron pole to be used. At this stage, the anchorage system was finally made to the base of the pole. The purpose of the anchor system is to fix the substrate on the concrete and to mount the lower base of the pole to this structure. Specifications of the solar pole are listed in Table 1.

Table 1. Specifications of the solar pole.

Maximum power	42W
Open circuit voltage	22.1V
Short circuit current	2.58A
Maximum power voltage	18V
Maximum power current	2.58A
Dimensions	670x430x25mm
Weight	3.8kg
Battery capacity	12V-9Ah
Recommended charge current	900mAhx10 hours
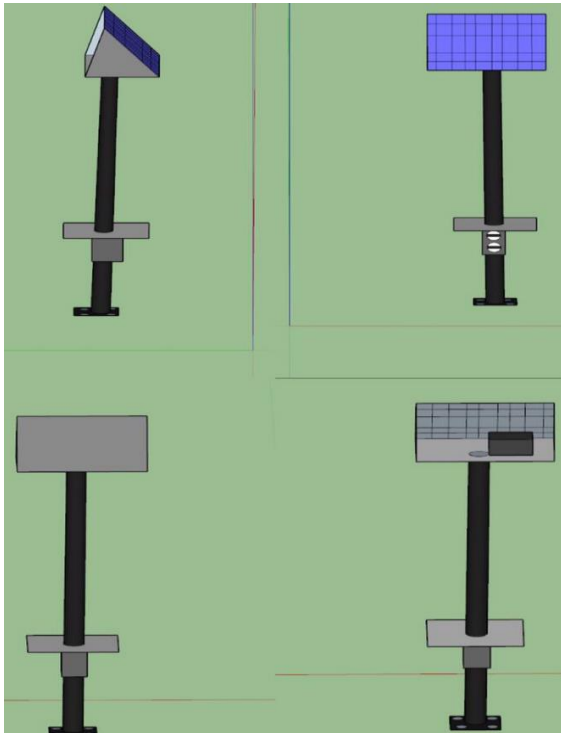
Figure 5. Technical drawing of the solar pole.
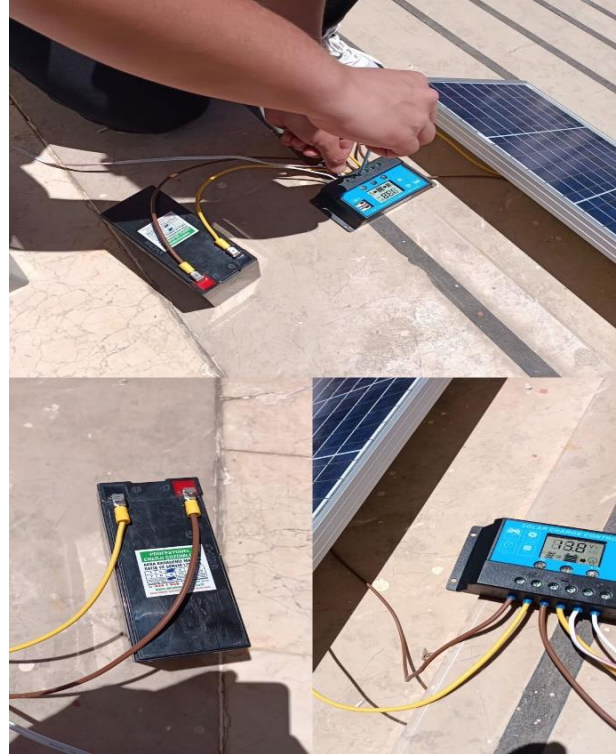
Figure 6. Electrical connection and testing of the system.

In the next step, the necessary electrical connections were made. In this part, the battery and charge controller are connected first. This is because the charge controller must recognize the battery type. Afterwards, the solar panel and the charge controller were connected. Then, a connection was applied from the device and the USB modules were connected to the system. Connection procedures are given in Figure 6.

Finally, some improvements were made to the system. First, the output slot was designed with the help of a 3D printer in order to protect the connection parts of the USB modules. This design is shown in Figure 7. This design was placed on the body of the iron pole, which gets ready, by opening a suitable area. Thus, the system was completed and fixed on the concrete surface.

Different mobile devices were charged on the system for test purposes, and no technical problems were detected. In addition, it has been determined that there is a need for security protection against weather events such as rain and snow in the section where the USB modules are located. For this purpose, a design was made and a protection equipment was produced with the help of a 3D printer. Figure 8 shows the design of this part created in the SOLIDWORKS program.

Figure 7. USB outputs and their structure.
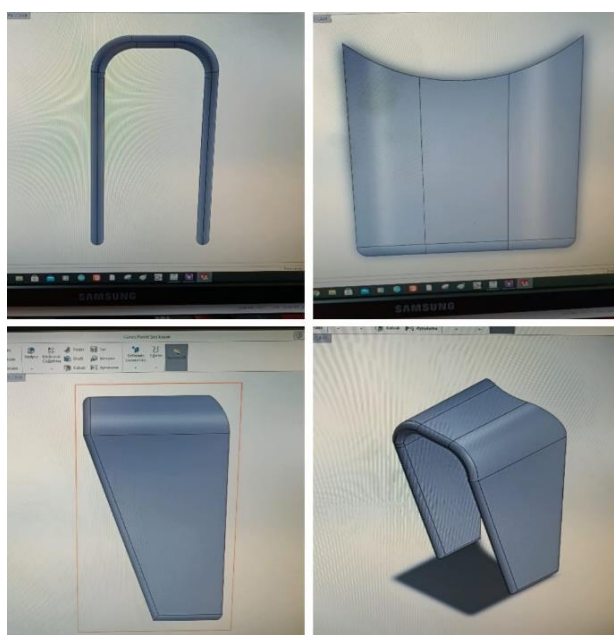
Figure 8. Image of the 3D design of the USB holder.

In Figure 9, the 3D printer output of this designed part is shown. Finally, this part is fixed on the part where the USB modules are located with the help of silicon, ensuring the safety of the system against weather conditions. Because of all these processes, the system has become completely ready. The image of the system in the planned area is given in Figure 10.

Figure 9. Image of the USB holder

Figure 10. Image of the solar pole.

4. Conclusions

Solar energy systems have become highly preferred systems with the widespread use of renewable energy sources. Harnessing these systems efficiently provides advantages in terms of energy production. Therefore, attention should be paid to factors that will increase efficiency. In this study, the solar pole was designed and constructed in such a way that it faces south with an inclination angle of 25°, considering the geographical conditions of Gümüşhane province. In the solar pole, a 42W solar panel, a 12V-9Ah lead-acid battery, a 10A charge controller and two dual-output USB modules were used in the system. The purpose of establishing this system is to perform the charging process of mobile devices that can be charged with 5V, and this aim has been achieved. In the continuation of the study, a solar tracking system will be implemented in order to benefit more from solar energy. Thus, more energy will be obtained from a single PV module.

Declaration of Ethical Standards

The authors of this article declare that the materials and methods used in this study do not require ethical committee permission and/or legal-special permission.

Conflict of Interest

The authors declare that they have no known competing financial interests or personal relationships that could have appeared to influence the work reported in this paper.

References

[1] Başoğlu M. E., Kazdaloğlu A., Erfidan T., Bilgin M. Z., Çakır B., 2015. Performance analyzes of different photovoltaic module technologies under İzmit,

Kocaeli climatic conditions. Renewable and Sustainable Energy Reviews, **12**, pp. 357-365.

[2] Brar A., Sanborn R., Radwan A., Jiang X., 2020. A mobile photovoltaic-battery system for off-grid applications. Paper presented at the 2nd International Conference on Electrical, Communication and Computer Engineering, İstanbul, Turkey, 12-13 June, pp. 1-6.

[3] Lee H., Kim K.A., 2015. Comparison of photovoltaic converter configurations for wearable applications. Paper presented at the IEEE 16th Workshop on Control and Modeling for Power Electronics, Vancouver, Canada, 12-15 July, pp. 1-6.

[4] Ray S., Tripathi A.K., 2016. Design and development of tilted single axis and azimuth-altitude dual axis solar tracking systems. Paper presented at the 1st IEEE International Conference on Power Electronics, Intelligent Control and Energy Systems, Delhi, India, 4-6 July, pp. 1-6.

[5] Geng C., Schmidt K., 2021. Design and implementation of a photovoltaic system for self-sufficient energy supply of mobile robots. Paper presented at the 3rd International Congress on Human-Computer Interaction, Optimization and Robotic Applications, Ankara, Turkey, 11-13 June, pp. 1-5.

[6] Murugesh R., Hanumanthaiah, Ramanadhan U., Vasudevan N., 2018. Designing a wireless solar power monitor for wireless sensor network applications. Paper presented at the IEEE 8th International Advance Computing Conference, Greater Noida, India, 14-15 Dec., pp. 79-84.

[7] Oruganti K. S. P., Vaithilingam C.A., Rajendran, Ramasamy A, 2019. Design and sizing of mobile solar photovoltaic power plant to support rapid charging for electric vehicles. Energies, **12**, Article No. 3579.

[8] Illangarathna S., Binduhewa P., 2020. Energy management system for neighbourhood EV based taxi-parking station. Paper presented at the 15th IEEE International Conference on Industrial and Information Systems, Rupnagar, India, 26-28 November, pp. 69-74.

[9] Encinas S. H., Castanon N. J. B., Mamani V. S., Mamani L. E. H., Paredes R. I. T., Mamani R. J. C., Molero M. R. R., Apaza A. P., 2020. Photovoltaic charger system for mobile devices using quick charge 3.0 technology. Paper presented at the 18th LACCEI International Multi-Conference for Engineering, Education, and Technology, Buenos Aires, Argentina, 29-31 July pp. 1-4.

[10] Duque E., Isaza A., Ortiz P., Chica S., Lujan A., Molina J., 2017. Urban sets innovation: design of a solar tree PV system for charging mobile devices in Medellin-Colombia. Paper presented at the 6th International Conference on Renewable Energy Research and Applications, Sandiego, USA, 5-8 November, pp. 495-498.

[11] Başoğlu M. E., Kazdaloğlu A., Erfidan T., Bilgin M. Z., Çakır B., 2015. Seasonal based energy performance analyzes of Cd-Te and c-Si photovoltaic modules. Paper presented at the IEEE 15th International Conference on Environment and Electrical Engineering (EEEIC) Rome, Italy, 10-13 June, pp. 208-212.

[12] Başoğlu M. E., Üstek S. M., 2021. Prototype development of a solar-powered backpack for camping applciations. Journal of Science Part C: Design and Technology, **9(4)**, pp. 589-596.

[13] Al-Shagea E., Sezen S., Özdemir E., 2021. Lisanssız elektrik üretiminde şebeke bağlantılı fotovoltaik sistemlerin performans analizi. Paper presented at the International Marmara Sciences Congress, Kocaeli, Turkey, May, pp. 209-217.

[14] https://solarchargingstation.com/gallery/ (Access Date: 27 December 2021).

[15] Lin Y., Jiang B., Dai H., 2021. Battery capacity estimation based on incremental capacity analysis considering charging current rate. World Electric Vehicle Journal, **12**, 224, pp. 1-12.

Kocaeli University

Kocaeli Journal of Science and Engineering

Linear Delta Robot Controlled with PLC Based On Image Processing

Sıtkı ÖZTÜRK [1] (iD) , Fatma KUNCAN [2], * (iD)

[1] Department of Electronics and Communication Engineering, Kocaeli University, Kocaeli, 41001, Turkey, **ORCID: 0000-0003-3804-5581**
[2] Department of Computer Engineering, Siirt University, Siirt, 56100, Turkey, **ORCID: 0000-0003-0712-6426**

Abstract

Delta Robot is taking an important place in industry 4.0. Its ability to work fast and with precision is the reason why this robot now is used worldwide in the industrial field. Delta robots are mostly used for packaging, 3D printing, pick and place, etc. This robot can be controlled using programmable logic controller (PLC) devices. In recent years, image processing methods have been widely used in many robot applications. In this study, it is aimed to ensure that the robot successfully moves to the determined points by using image processing methods. Images for this study were obtained by attaching a camera to the robot system. In this study, the aim is to set the robot to move based on the visual data that is taken by the camera. The coordinates of each object are defined after several steps in image processing. To be able to move the robot to the desired coordinates, inverse and forward kinematic analysis is proposed. The obtained values are transferred to PLC using OPC. The necessary coding in TIA Portal is done to control the motor drivers so that the three stepper motors can ensure the delta robot moves to the desired coordinate position.

1. Introduction

The Delta Robot was invented by Reymond Clavel in 1985. He came up with the brilliant idea of using parallelograms to build a parallel robot with three translational and one rotational degree of freedom. Robots are now actively working in many areas such as military security, health and transportation. These robots are evaluated in 2 classes according to their area of utilization, which are serial and parallel robots [1]. While these robots are being classified, criterias such as speed, quality control, durability and load carrying capacity are taken into consideration [2]. There are many studies on serial and parallel robots in industrial applications and academic studies. With the help of these studies, the most efficient robot type can be easily selected according to the desired application area [3]. In this study is done based on image processing linear delta robot. It is chosen in this work since its design exceeds this part because of its three translational degrees of freedom, and its acceleration. Linear delta robot is a type of parallel robot.

Parallel robots have many benefits and drawbacks. Their most significant drawback is requiring a small and complicated workspace. Because of this, they can only be practiced when the task can be accomplished in a limited area [4]. Nevertheless, the benefits points that parallel robots are the optimal decision in many circumstances. Because their motors are attached to the robot's frame, the weight and inertia of the moving parts are weak. This results in higher top speeds and accelerations.

In this work, the aim is to get the exact position coordinates of each object on the workspace of the delta robot and set the robot to move to that position. After the linear delta robot is built, there are two big steps to make this study successful. The first step is to determine the coordinate position of the objects correctly and the second step is to get a correct trajectory result for three legs of the delta robot from the kinematic analysis.

In section 3 of this study, the image processing step is explained. Logitech C310 HD webcam is used. A camera calibration needs to be done before doing image processing. This step is very crucial to get an accurate coordinate position of the object on the workspace of the delta robot.

Coordinates of objects can be obtained by a process consisting of several steps. The image taken from the

---

* Corresponding Author: fatmakuncan@siirt.edu.tr

camera needs to be segmented so the only desired object will be processed further. From there this image that has been segmented using HSV color space will be analyzed using BLOB analysis to get the centroid and the bounding box feature of the object in interest.

The acquired coordinates can't be directly transferred to PLC. Each leg of the delta robot needs to be converted to trajectory. This is done by doing inverse kinematic analysis. In this work, to prove that the calculation of legs trajectory from inverse kinematic is correct, forward kinematic is done [5-8].

After the trajectory of each leg is calculated in MATLAB with the help of OPC, these data are transferred to the PLC. OPC is a really important communication interface for integration between PLC and MATLAB. In this study, Simatic Net OPC was used as the OPC platform.

Since the output of PLC is 24V and the motors used in this study work with lower voltage, a motor driver circuit is needed. A4988 driver circuit was used as stepper motor driver. The resolution of the driver can be changed with MS1, MS2, and MS3 inputs. In the study, these inputs were operated in full step by making them 0 volts. After the driver was turned into operation by jumping to 0 volts with the EN input of the driver, it was moved by the direction and position pulses of the motor with the DIR and STEP inputs.

In this study, Siemens S7-1215C DC/DC/DC was used as the controller of the delta robot. In this PLC, the function blocks written for motion control were programmed to control stepper motors. After setting up all three stepper motors, PLC code was written in Ladder Logic Language. Ladder logic was chosen in this work since it's faster and easy to do debugging in this language [9-16].

2. Test Setup

Before we can move the robot to the desired coordinates provided by the image processing, we need to set it to the home position. This can be done using an inductive sensor. After it is set to its home position, we can continue to take the image and get the coordinates of objects. The coordinates that we get from image processing would be still in *x*, *y*, *z* dimensions. These need to be converted into the trajectory of each leg of the robot. Kinematic Analysis takes a very important place in this step. After we get the trajectory of each leg, we then calculate the velocity of each step. The velocity of each leg is saved in an array named *V1, V2, V3*. In this study, an electromagnet was used to hold the object. The working logic keeps the object when the control signal is applied to the electromagnet and leaves the object when the control signal is not applied. Object coordinate values are stored in

an array (*M*) and the electromagnet control signal is applied according to these coordinate data. The data that we get from image processing (*L1, L2, L3, V1, V2, V3, M*) is sent to PLC through OPC. Then the data is saved in the OPC_Data Block in the PLC. This data will be used to control the movement of each stepper motor. The test setup is shown in Figure 1. The flow diagram of the system is shown in Figure 2.
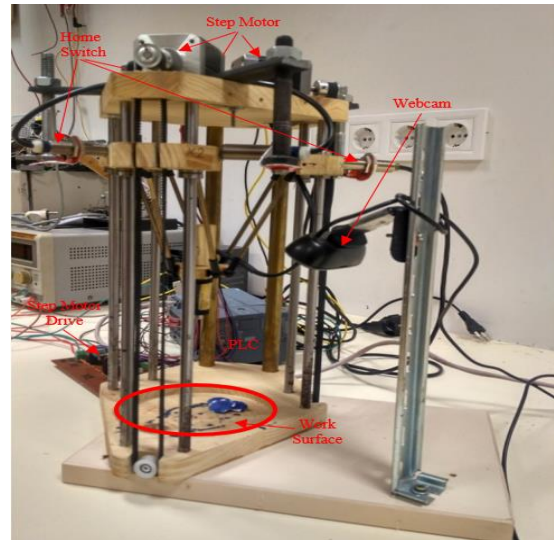
Figure 1. Test Setup of Delta Robot
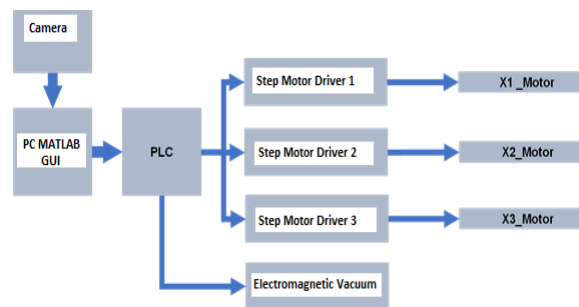
Figure 2. Flow diagram of the system

3. Image Processing Method

The camera was calibrated before starting the image processing to obtain the coordinates of the objects. Camera calibration was done to find the internal and external parameters of the camera. These parameters are then used to calculate real-world coordinates.

The algorithm for obtaining the coordinates of the location of objects is given in Figure 3. First, the photo is taken and converted to HSV. Then, the properties of the obtained two-dimensional image are extracted. By using these features, it is ensured that the desired objects and other objects around them are distinguished. This process is often called segmentation. In this study, the color thresholding method was used for segmentation. In color thresholding, the value of each layer of a given color space is used as a mask to separate objects of interest by color. In

the study, HSV color space was used to create segmentation masks. After segmentation, the HSV image was converted to a binary image. The conversion was done to start the BLOB analysis process. The purpose of the BLOB analysis is to construct pixels in close binary images as a group of pixels, which it identifies as objects. In this study, objects were found by grouping pixels with similar gray values or color values in squares as a result of the 8-pixel connection method. A filter was used to ensure that all residual noise from the segmentation process was removed. From the BLOB analysis process, the object's center of mass was obtained. These dots were still in pixel form. By following the calculations from the pinhole camera models, the coordinates of the objects in the real world were estimated.

Figure 3. Image processing algorithm

This work gives an approach to recognizing colors in a two-dimensional image using the color thresholding technique in MATLAB with the help of HSV color space to detect a selected color by a user in an image. Color detection is the fundamental step in many computer vision systems. In this work, Image Processing Toolbox in MATLAB is used for the detection of a particular color in a given image. The Image Processing toolbox provides a wide variety of referenced algorithms, methods, and applications for image processing, visualization, and segmentation. An image can be represented using many color models like Gray-scale, RGB, HSV, etc. Here, HSV color space is used to detect the colors in an image [14].

3.1. Feature Extraction of a Two-Dimensional Image

In this study, the color thresholding method was used to identify the object. The HSV color space is used to segment objects in stored images by applying the specific HSV value as a mask. The resulting mask was then converted to a binary image and enhanced by filtering. The feature extraction algorithm of the two-dimensional image is shown in Figure 4.
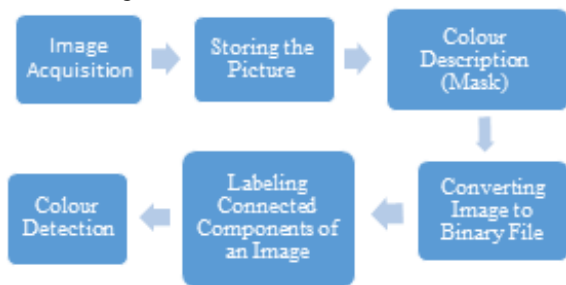
Figure 4. Feature extraction algorithm of two-dimensional image

3.2. HSV Color Space

The HSV color space shown in Figure 5 is separated by the luminance component and the chrominance component. While the brightness component was created from V (Intensity value - Value), the chrominance component was created from H (Hue - Hue) and S (Saturation - Saturation) values. In the HSV model, colors such as red, yellow, green, blue, or the combination between these colors are defined by hue. The tone value is between 0-360º. The degree of dilution of pure color with white light is given by saturation, and the intensity of the color between light and dark is shown by the intensity value [9].
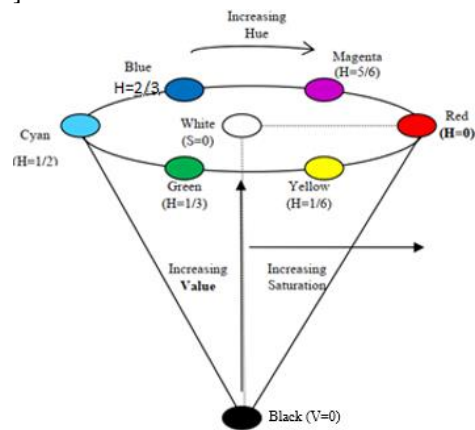
Figure 5. HSV Color Space

The HSV color space works very similarly to the color perception of the human eye and can be used as an ideal model in the image processing algorithm. In the study, more than one mask was applied to isolate the colors. Low threshold and high threshold masks are used for hue, saturation, and intensity value. Any pixels within these thresholds will be set to one and the remaining pixels will be set to zero. HSV color space masks used in the study are given in Table 1.

Table 1. HSV color space masks

Color	Hmin	Hmax	Smin	Smax	Vmin	Vmax
Yellow	0.1	0.18	0.4	1	0.4	1
Green	0.9	0.41	0.3	1	0.1	1
Red	0.97	0.047	0.4	1	0.35	1
Purple	0.7	0.96	0.1	1	0.1	1
Blue	0.58	0.68	0.25	1	0.25	1

3.3. Camera Calibration

Camera calibration is a method to see the camera parameters. These parameters can be used to make adjustments for lens distortion, scale the size of an object in world units, or determine the camera's location in the scene. These tasks are practiced in applications such as machine vision to identify and measure things. They are also applied in robotics, navigation systems, and 3-D scene reconstruction [12]. This calibration is used in applications such as machine vision to detect and measure objects. The algorithm of the camera calibration process performed in the study is given in Figure 6. In the study, the camera calibration process was started by taking a few sample checkerboard photographs with the camera. All sample photos were saved in a single folder. By detecting the corners of the checkerboard, image points and checkerboard size were obtained. The board size and the corner size of the checkerboard square in the previous step were used to obtain the world points of the checkerboard. With the two inputs (image points and world points) from the previous two steps, the camera calibration process was started. After this process, the internal parameters of the camera were obtained. To obtain the external parameters of the camera, three inputs are required, namely image points, world points, and camera parameters. The viewport used in this step was the viewport of the image found in the previous step. Also, the external parameters of the camera, namely rotation matrix and transformation matrix would be obtained. The camera calibration flowchart is shown in Figure 6. The camera calibrated image is shown in Figure 7.
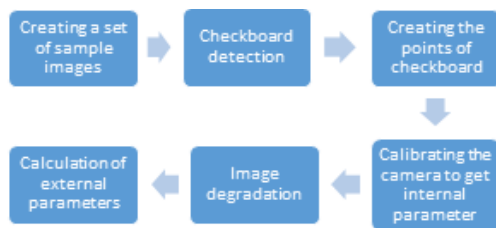
Figure 6. Camera Calibration Scheme

Figure 7. Camera calibration images

3.3.1. External and Internal Parameters

External Parameters: The external parameters consist of a rotation (R) and a transformation (t). The origin of the

camera's coordinate system is at its optical center, and the x and y-axis are defined as the image plane.

Internal Parameters: Internal parameters include focal length (fx, fy), optical center (also known as a principal point (cx, cy)) and skew coefficient (s). The camera's inner matrix K is shown in Equation (1) [12, 17].

$$K = \begin{bmatrix} f_x & 0 & 0 \\ s & f_y & 0 \\ c_x & c_y & 1 \end{bmatrix} \tag{1}$$

3.3.2. Calibration Process

The camera calibration process passes through 5 stages and then is saved to a file. These processes start with pattern selection. The selected pattern is mounted on a flat, stable surface. Then, pictures of the placed surface are taken from various angles and distances. The ones in focus from the captured images are selected and the rest are eliminated. Then, with the help of the remaining focused pictures, the process ends and the calibration process is concluded by saving them to the file.

The internal and external parameters obtained from the camera calibration will then be used to estimate the coordinates of the objects in the delta robot's workspace. In this study, the checkerboard was used as a sample pattern. The best calibration results have been achieved by placing the checkerboard unsymmetrically and between 45 and 90 degrees from the camera.

Logitech C310 HD Webcam is used in this project. As the more sample photos are used for camera calibration, the more accurate the camera parameters estimation results will be, so 25 photo samples were used for camera calibration, as shown in Figure 8.
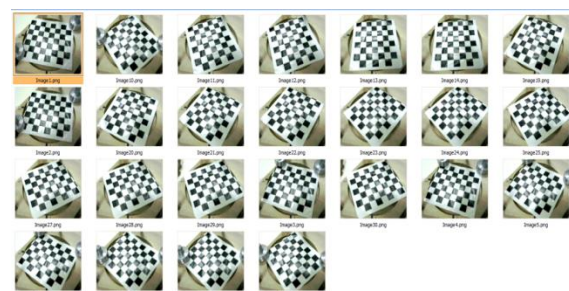
Figure 8. Sample images for camera calibration

Internal and external parameters K (Intrinsic Matrix), rotation matrix R (Rotational Matrix), and transformation matrix t (Translation Vectors) were obtained as a result of the calibration process are given in Figure 9.
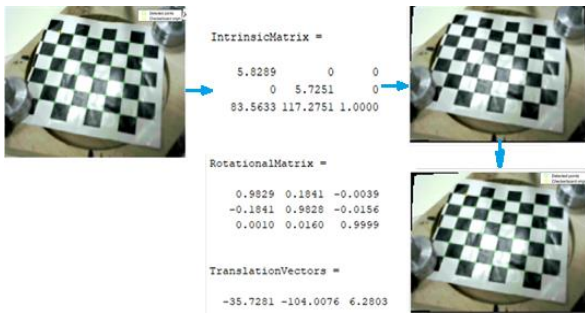
Figure 9. Internal and external parameters achieved from the checkerboard pattern

3.4. BLOB Analysis

BLOB stands for Binary Large Object and refers to the group of connected pixels in the binary image. It is indicated by the term "Large" that only objects of a certain size are processed and "small" binary objects are classified as noise.

3.4.1. BLOB extraction

The purpose of BLOB extraction is to isolate BLOBs (objects) in a binary image. The BLOB is composed of a group of connected pixels. Whether two pixels are connected or not is defined by the connection, that is, which pixels are neighbors and which are not. The two most common types of connections are given in Figure 10. The results of BLOB 4 and 8 connections applied to the same image were extracted as two and one object, respectively. 8 connections give a better result than 4 connections.
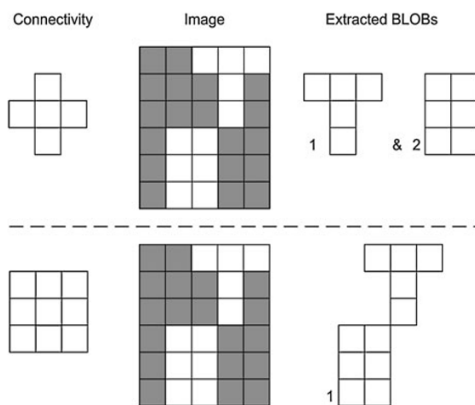
Figure 10. 4 and 8 connections. The effect of applying two different connection types

3.4.2. Obtaining a Coordinate using BLOB analysis

Several features can be extracted from the BLOB analysis. Only Bounding Box and Centroid (Center of mass) were used in this study.

Bounding Box: The minimum rectangle that contains the BLOB. It is defined for a BLOB by going through all pixels and finding four pixels with minimum x value, maximum x value, minimum y value, and maximum y value respectively. From these values, the width of the bounding box is given as x_{max} - x_{min} and the height as y_{max} - y_{min}.

Center of mass: The location on the object where we would place our finger to balance the thing. The focus of size for a binary image is similar. It is the standard x and y positions of the binary object. It is defined as a point whose x-value is calculated by summing the x coordinates of all pixels in the BLOB and dividing by the total number of pixels. A similar process is done for the y-value. In mathematical terms, the center of mass, (x_c, y_c) is measured as

$$x_c = \frac{1}{N}\sum_{i=1}^{N} x_i, \qquad y_c = \frac{1}{N}\sum_{i=1}^{N} y_i \qquad (2)$$

N is the number of pixels in the BLOB and x_i and y_i are the x and y coordinates of N pixels, respectively. In cases where the BLOB contains "additional pieces", the median can be changed. The collection box is shown in Figure 11.
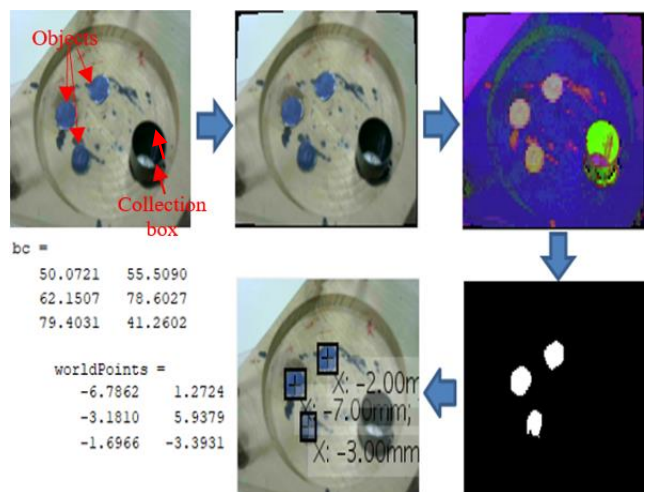
Figure 11. Coordinates of Real World Points

3.5. Real World Coordinate

In this study, the pixel position of the object obtained from the pinhole model and BLOB analysis feature is used to obtain the real-world coordinate. At this stage, rotational and translation of external parameters from the inner camera matrix, the resulting camera calibration, are important. The greater the accuracy of the results from the

calibration, the greater the accuracy of the real-world coordinates.

3.6. Pinhole Camera Model

The pinhole camera is a simple model without a lens and with a single small aperture, as shown in Figure 12 Light rays pass through the aperture and project an inverted image to the opposite side of the camera. The virtual image plane is in front of the camera and contains a vertical view of the scene.
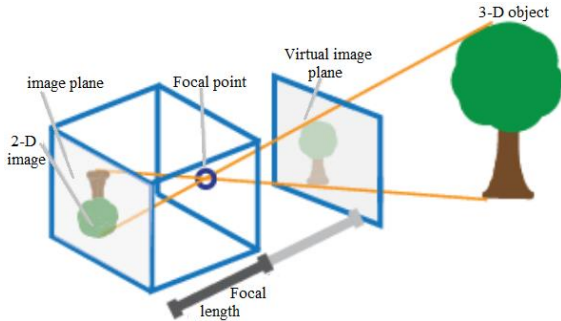
Figure 12. Pinhole Camera Model [17]

The pinhole camera parameters are represented in a 4x3 matrix called the camera matrix. This matrix maps the 3D world scene to the image plane. The camera matrix is calculated using the calibration algorithm, external and internal parameters. The external parameters are represented by the position of the camera in the 3D scene. The internal parameters represent the optical center and focal length of the camera. Using these three parameters, the real-world coordinates can be calculated in equations (3) and (4).

$$w \begin{bmatrix} x \\ y \\ 1 \end{bmatrix} = \begin{bmatrix} X \\ Y \\ Z \end{bmatrix} P \tag{3}$$

$$P = [R \quad t]\, K \tag{4}$$

w : scale factor
x, y : image points (pixels)
X, Y, Z : world points (mm)
P : camera matrix
R : rotational matrix
t : translation matrix
K : inner matrix

World points were mapped to camera coordinates using external parameters, and camera coordinates were mapped to the image plane using internal parameters [17].

4. Kinematic Analysis

One of the most essential tools in controlling a robot is the Inverse and Forward Kinematic solutions. The Inverse Kinematics is practiced to define the angle of each motor shaft for an end effector location in (x, y, z) coordinates [12]. The Inverse Kinematics is particularly significant in the control of the robot because they play a role in every move made by the robot [11]. The Inverse Pose Kinematics is required for the control of any robot. The Forward Kinematics is utilized to arrange the end effector location in (x, y, z) coordinates if the angle of each motor shaft is identified. The Coordinates of motion surface is shown in Figure 13. The L1, L2, L3 Orbit is shown in Figure 14. The Inverse and Forward Kinematics Result is shown in Figure 15.
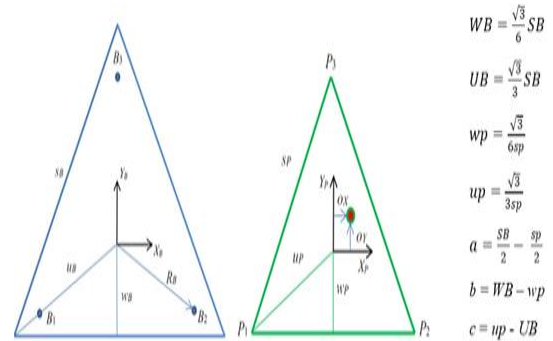
Figure 13. Coordinates of motion surface
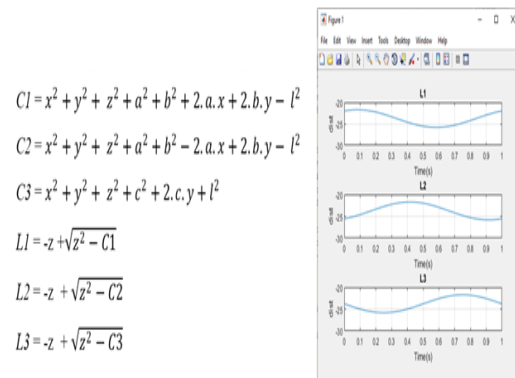
Figure 14. *L1, L2, L3* Orbit
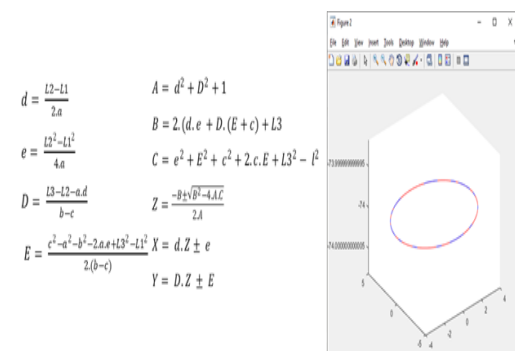
Figure 15. Inverse and Forward Kinematics Results

5. Visual Positioning Based on Proposed Techniques

In this work, before we can move the robot to the desired coordinate from image processing, we need to set it to the home position. This can be done using an inductive sensor. After it is set to its home position, we can continue to take the image and get the coordinates of objects.

The coordinates that we get from image processing are still in x, y, z. This has to convert into the trajectory of each robot leg. Kinematic Analysis plays a significant role in this step. [16].

After we get the trajectory of each leg, we then calculate the velocity of each step. The velocity of each leg is saved in an array named *V1, V2, V3*. In this study, an electromagnet is used. The electromagnet will turn on if we give logic "1" and will turn off if we give logic "0". The electromagnet will be ON during picking and lifting the object from the found coordinates and carrying it to the box and will be OFF during placing and lifting from the box to the next object. The required Logic Data for electromagnet is saved into an array named M. Then the data that we get from image processing (*L1, L2, L3, V1, V2, V3, M*) is sent to PLC through OPC.

The data is saved into OPC_Data Block in PLC. This data will be used to control the movement of each stepper motor [18]. The PLC Programming Map is shown in Figure 16. The Image taken from camera is shown in Figure 17. The Schematic drawing of the experimental air conditioning system is shown in Figure 18.
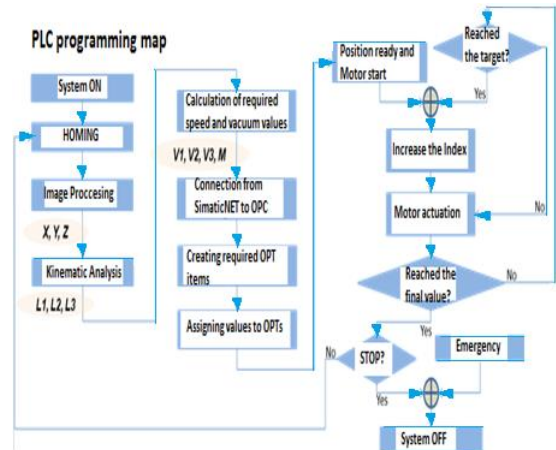
Figure 16. PLC Programming Map
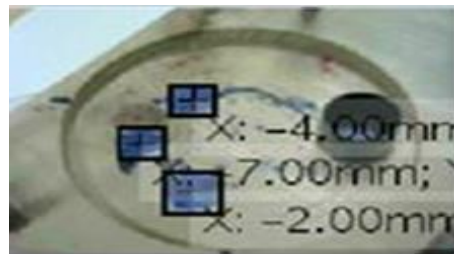
Figure 17. Image taken from camera

	X	Y	Z
0	0	0	0
1	-6.79	2.97	-90
2	-6.79	2.97	-76.80
3	-6.79	2.97	-90
4	8	0	-90
5	8	0	-76.80
6	8	0	-90
7	-2.12	7.21	-90
8	-2.12	7.21	-76.80
9	-2.12	7.21	-90
10	8	0	-90
11	8	0	-76.80
12	8	0	-90
13	-4.45	-2.54	-90
14	-4.45	-2.54	-76.80
15	-4.45	-2.54	-90
16	8	0	-90
17	8	0	-76.8
18	8	0	-90
19	0	0	0

Indeks	L1	L2	L3	V1	V2	V3	M
0	0	0	0	0	0	0	0
1	-9.8182	-3.717	-9.1024	0.8182	0.3097	0.7585	0
2	-23.018	-16.917	-22.302	3.3	3.3	3.3	0
3	-9.8182	-3.717	-9.1024	3.3	3.3	3.3	1
4	-3.9002	-11.041	-7.5395	1.4795	1.831	0.3907	1
5	-17.1	-24.241	-20.74	3.3	3.3	3.3	1
6	-3.9002	-11.041	-7.5395	3.3	3.3	3.3	0
7	-6.66	-4.732	-11.221	0.69	1.5772	0.9204	0
8	-19.86	-17.932	-24.421	3.3	3.3	3.3	0
9	-6.66	-4.732	-11.221	3.3	3.3	3.3	1
10	-3.9002	-11.041	-7.5395	0.69	1.5772	0.9204	1
11	-17.1	-24.241	-20.74	3.3	3.3	3.3	1
12	-3.9002	-11.041	-7.5395	3.3	3.3	3.3	0
13	-10.33	-6.3913	-6.416	1.6076	1.1624	0.2809	0
14	-23.53	-19.591	-19.616	3.3	3.3	3.3	0
15	-10.33	-6.3913	-6.416	3.3	3.3	3.3	1
16	-3.9002	-11.041	-7.5395	1.6076	1.1624	0.2809	1
17	-17.1	-24.241	-20.74	3.3	3.3	3.3	1
18	-3.9002	-11.041	-7.5395	3.3	3.3	3.3	0
19	0	0	0	0.325	0.9201	0.6283	0

Figure 18. Location data and values that written to OPC

6. Conclusions and Recommendations

Delta Robot takes a very important place in industry 4.0. Its ability to work fast and in precision is the reason why this robot is used worldwide in the industry.

Delta robots are mostly used for packaging, 3D printing, pick and place, etc. This robot can be controlled using programmable logic controller (PLC) devices. In recent years, image processing methods have been widely used in many robot applications. This study, it is aimed to ensure that the robot successfully moves to the determined points by using image processing methods. For the study, images were obtained by attaching a camera to the robot system. All objects on the workstation of the robot can be

detected according to their colors. HSV color space is preferred since its mask is more accurate than RGB. In this study, color thresholding was preferred because of its easy use and high success rate. The number of samples used in the calibration is one of the factors that increase the accuracy in determining the real-world coordinates.

In this study, the coordinates are determining methods are chosen according to the needs of the robot. Coordinates from outside the study area are not suitable. It needs such manipulation that it suits the need. The coordinates taken from image processing are 100% successful in being reconstructed by kinematic analysis and the data of each trajectory of the leg is successfully transferred to OPC Data in PLC Data Block through SimaticNet OPC Server.

Some mechanical errors are found in this work; some coordinates need a different z position   than the others. These errors are caused by the lack of ability of the robot design itself. The accuracy of movement is limited to a certain point. This is why for pick and place jobs; parallel delta robot is more preferred than linear delta robot.

Declaration of Ethical Standards

The author of this article declares that the materials and methods used in this study do not require ethical committee permission and/or legal-special permission.

Conflict of Interest

The author declares that she has no known competing financial interests or personal relationships that could have appeared to influence the work reported in this paper.

References

[1] Köse İ., Öztürk S., Kuncan M., 2019. Pantography application with real-time PLC based on image processing in gantry robot system. European Journal of Technique (EJT), **9**, pp. 219-229.

[2] Çubukçu A., Kuncan M., İmren M., Erol F., Ertunç HM., Öztürk S., & Kaplan K., 2015. Görüntü işleme ile 3 eksenli robot mekanizması üzerinde nesne ayırt edilmesi ve sıralanması. Otomatik Kontrol Ulusal Toplantısı, pp. 637-641.

[3] Bakır A., Güney ÖF., Kuncan M., Ertunç HM., 2012. 3 Eksenli Robot Mekanizmasına Monte Edilmiş Bir Kamera Vasıtasıyla Farklı Rotasyon ve Boyutlardaki Geometrik Cisimlerin Tanımlanarak Vakum Tutucu ile Ayrılması. Otomatik Kontrol Ulusal Toplantısı, Niğde, Turkey, pp. 606-609.

[4] Horoz E., Öten HF., Kuncan M., Ertunç HM., 2013. Kamera Yardımı ile Ayırt Edilen ve Tanımlanan Cisimlerin 3 Eksenli Robot Mekanizması ile Taşınması. Otomatik Kontrol Ulusal Toplantısı, Malatya, Turkey, pp. 1236-1240.

[5] Warin P., Kamol C., and Ratchatin C., 2013. VISUAL POSITIONING OF A DELTA ROBOT, Mechanical Engineering Department, Chulalongkorn University, Bangkok, 10330, Thailand, April 20.

[6] Vishesh G., Tarun J., Sahil S., Silica K., 2017. Specific Color Detection in Images using RGB Modelling in MATLAB, International Journal of Computer Applications, **161**, March 2017, pp. 0975 – 8887.

[7] Robert L., Williams II., 2015. Ph.D., The Delta Parallel Robot: Kinematics Solutions, Mechanical Engineering, Ohio University, April.

[8] Joseph Q., 2016. Oberhauser, Design, Construction, Control, and Analysis of Linear Delta Robot, the faculty of the Russ College of Engineering and Technology of Ohio University, April.

[9] Priyanto H., Miftahuddin Z., 2015. Color-Texture Based Object Tracking Using HSV Color Space and Local Binary Pattern, International Journal on Electrical Engineering and Informatics, 7, June.

[10] Senthilkumaran N., Vaithegi S., 2016. Image Segmentation by Using Thresholding Techniques for Medical Images, Computer Science & Engineering: An International Journal (CSEIJ), 6, February.

[11] Seth H., Gregory DH., Peter IC., 1996. A Tutorial on Visual Servo Control, IEEE Transanctions on Robotics and Automation, 12, October.

[12] Burger W., 2016. Zhang's camera calibration algorithm: in-depth tutorial and implementation. 16, pp. 1-6.

[13] Vocetka M., Huňady R., Hagara M., Bobovský Z., Kot T., & Krys V., 2020. Influence of the Approach Direction on the Repeatability of an Industrial Robot. Applied Sciences, 10, 8714.

[14] Bolton W., 2015. Programmable logic controllers. Newnes.

[15] Krawczyk M., 2022. Project and implementation of the control of the loading and unloading station of the technological line for surface treatment of metal bottles (Doctoral dissertation, Instytut Automatyki Robotyki).

[16] Guzmán HSG., 2017. OOP with S7-SCL, implemented to plastic welding machines.

[17] Fetić A., Jurić D., & Osmanković D., 2012. The procedure of a camera calibration using Camera Calibration Toolbox for MATLAB. In 2012 Proceedings of the 35th International Convention MIPRO, pp. 1752-1757.

[18] Tekinalp Z., Öztürk S., Kuncan M., 2013. OPC Kullanılarak gerçek zamanlı haberleşen Matlab ve PLC kontrollü sistem. Otomatik Kontrol Ulusal Toplantısı, TOK2013, pp. 26-28.

Kocaeli University

Kocaeli Journal of Science and Engineering

http://dergipark.org.tr/kojose

Mapping of Gradient Patterns Generated with Helmholtz Coils for Localized Magnetic Fluid Hyperthermia

Serhat KÜÇÜKDERMENCİ [1, *] (iD)

[1] Department of Electrical and Electronics Engineering, Balıkesir University, Balıkesir, 10463, Turkey, **ORCID:** 0000-0002-6421-7773

Abstract

Magnetic fluid hyperthermia (MFH) is a new generation cancer treatment method under development. One of the challenges that arise in the practical applications of MFH is the limited control of magnetic nanoparticles (MNP). In order to overcome this problem, new approaches are being investigated in MFH tests. Localization of MNP oscillations can be achieved through static magnetic field-free region (FFR) and static magnetic field (SMF) gradients generated by permanent magnets or electromagnets. In this study, Helmholtz coils were used as SMF source to generate gradient patterns (GPs). Finite element method simulation was used to predict GPs that would emerge in the study area. An experiment platform was produced in which the GP would be generated with parametric current changes. Measurements were taken when source currents were (1.1, 1.1), (2.2, 2.2), (4.4, 4.4) and (2.2, -2.2) A, respectively. It was observed that FFR form could be manipulated with coil current. The mapping of the GPs and determining FFRs for the use of localized MFH were discussed for the first time in this study. The findings provide insight into which GP is appropriate in which situations in localized MFH.

1. Introduction

Magnetic resonance imaging [1-2], targeted drug delivery technologies [3-4] and magnetic fluid hyperthermia (MFH) [5-6] can be counted as examples of magnetic nanoparticle (MNP) applications interacting with magnetic fields. MFH is a medical procedure in which cancerous cells are brought to a temperature between 42-46 °C with MNPs [7]. When MNPs are exposed to an alternating magnetic field (AMF), the magnetic energy is converted into heat energy with the oscillating movement. Cancerous cells lose their effectiveness with the high temperature in the environment. Inversely, healthy cells are more resistant to heat than cancer cells. The heat generating capacity of MNPs is defined as the specific absorption rate (SAR) and it is expressed by Eq. (1).

$$SAR = c \frac{V_s}{m_{MNP}} \times \frac{dT}{dt} \qquad (1)$$

In the formula above, c is the specific heat capacity of the medium, V_S is the volume of the sample, m_{MNP} is the mass of the MNPs, and dT/dt is the time derivative of the temperature difference.

The heat production of MNPs by the AMF effect is explained by the relaxation losses. The deflection motion of MNP moments is defined as Neel relaxation. In Brownian relaxation, MNPs interact with the medium fluid and make a mechanical motion. The Neel and Brownian characteristic relaxation times are expressed as τ_N and τ_B, respectively. The effective relaxation time (τ_{eff}) is given by Eq. (2).

$$\tau_{eff} = (\tau_B . \tau_N) / (\tau_B + \tau_N) \qquad (2)$$

One of the models describing the volumetric power density emitted by MNPs exposed to AMF is the Rosensweig model and it is expressed by Eq. (3).

$$P = \pi \mu_0 \chi_0 H_{ac}^2 f \frac{\omega\tau}{1+(\omega\tau)^2} [W/m^3] \qquad (3)$$

Here, χ_0 is magnetic susceptibility, H_{ac} and f are AMF amplitude and frequency, τ is effective relaxation time and ω is angular frequency, respectively.

---

* Corresponding Author: kucukdermenci@balikesir.edu.tr

The typical problem in MFH applications is the difficulty of localizing the heat to the tumor without damaging the healthy tissue, considering here is a tendency for MNPs to migrate from the tumor site to healthy tissue during the MFH tests. There are theoretical experimental studies [8-9] that show MNP behaviors under the influence of AMF can be changed by adding static magnetic field (SMF) patterns. If the SMF gradient pattern (GP) is added to the MFH test environment, MNPs may have different SAR values depending on their location. SMF sources are positioned such that the magnetic flux density vectors bend each other. A GP suitable for localized MFH is created. MNPs remaining in the field-free region (FFR) oscillate under the influence of AMF. The oscillations of MNPs under the influence of the SMF gradient are either restricted or completely blocked (see Figure 1).
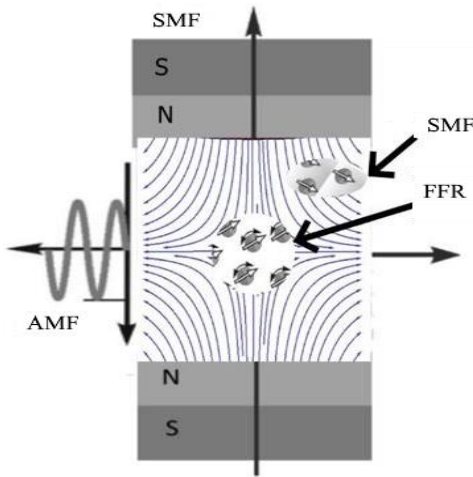
Figure 1. FFR pattern.

Among the studies on MFH, Tasci et al. [10] showed that the MNP temperature rise could be controlled in in vivo MFH experiments with their proposed method. The SMF source made with DC coils was positioned on both sides of the AMF generating coil in their study. SMF gradients surrounding the FFR in the study area were obtained by feeding the coils with equal and opposite DC currents. In another study, Hensley et al. established a system in which permanent magnets were used to focus the heat to the desired area with the help of FFR. The proposed system was capable of performing magnetic particle imaging and MFH operations [11]. In another study, Ma et al. [12] used neodymium iron boron (NdFeB) permanent magnets with dimensions of 40 mm × 40 mm × 20 mm as SMF source in their experiment setup. Magnets were located on both sides of the AMF generating coil. It was reported that MNP samples remaining within the FFR effectively generated heat and the SAR value of MNPs was limited in the static GP.

A brief literature comparison of MFH studies including SMF sources is presented in Table 1. According to the table, magnetic flux direction and intensities of SMF sources can take different values. These studies indicate that both DC current fed coils and permanent magnets can be used as SMF sources. In some experiments opposite SMF poles were placed facing the study area, resulting in magnetic flux vectors supporting each other and completely blocking the MNP oscillations. In other experiments the same SMF poles were placed facing the study area. Consequently, magnetic flux vectors generated FFR in some regions of the study area to allow MNPs to oscillate freely. Mapping of the GP has not been studied in detail in any of these studies.

Table 1. Comparison of MFH studies including SMF sources.

Ref.	SMF source /Intensity	SMF sources / Flux direction	Gradient pattern mapping	FFR measurements
[13]	Permanent magnet / 2,6 mT - 15,4 mT	Single magnet, magnet pair / same direction	-	-
[10]	DC fed coil	A pair / opposite direction	-	-
[12]	Permanent magnet / 5mT - 0.2 T	A pair / opposite and same direction	-	-
[14]	DC fed coil	A pair / same direction	-	-
[15]	DC fed coil	A pair / same direction	-	-
Proposed study	Helmholtz coil	A pair / same direction and opposite direction	Point probe measurements were taken in workspace	FFR major and minor axis measurements and area calculations were done.

Literature comparison of workspaces and target objects are shown in Table 2. Workspaces generally the inner volume of helical shaped work-coil. Ferrofluid containing test tubes and regional tumor masses of small animals can be considered as the target object. Small test tubes can be placed periodically with distance as shown in

Figure 2a. Focusing effect can be applied to test tubes separately or regionally. Another example can be a long test tube containing MNP. This tube may have a length of 47.5 mm and an outer diameter of 9.6 mm. The height and diameter is labelled with letters *A* and *B* in Figure 2b. When this type of tube is placed horizontally, the focusing of FFR

can be applied to some parts of the tube. When the target object is the tumor mass in the small experimental animal, targeting FFR is up to the experiment conditions. For instance tumor mass can be in the shape of line-like or surface-like geometries as shown with the letters *L* and *S* in Figure 2c.

Table 2. Specifications of the instrumentation from MNP tests.

Properties of the workspace	Properties of the target objects	Ref.
Radius of the coil ≈ 5 cm Cross-section area of workspace ≈ 78.5 cm²	One test-tube located in the center of the coil, the radius of the tube, r ≈ 0.5 cm, Target area ≈ 0.785 cm²	[13]
Radius ≈2 cm, height ≈ 6 cm Cross-section area of workspace ≈ 24 cm²	Spherical plastic cups, r ≈ 0.2 cm, target area ≈ 0.126 cm²	[10]
Coil diameter = 3 cm	Two phantoms stay close to the heating region of the coil (20mm).	[12]
Coil with a diameter = 3 cm	Tube diameter = 8 mm, target area ≈ 0.502 cm²	[14]
Solenoid coil diameter = 4 cm, length = 10 cm. Cross-section area of workspace ≈ 40 cm²	Spherical core with a radius of 4.9 mm	[15]
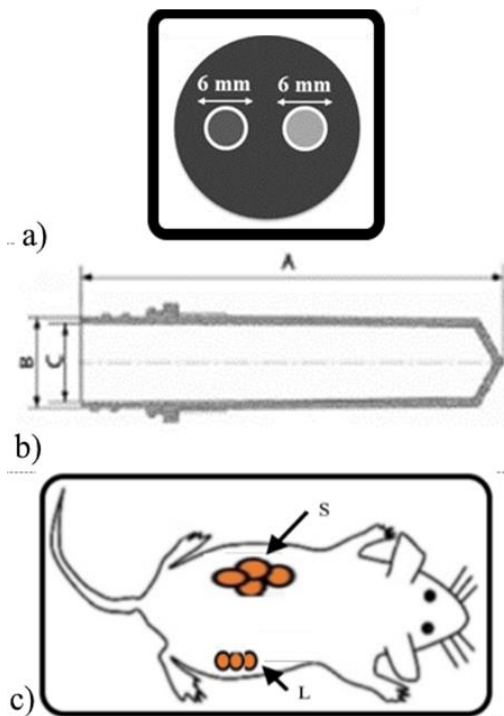
Figure 2. Schematic representation of target objects (a) periodically arranged test tubes, (b) horizontally located test tube, (c) small test animal.

In bioelectromagnetic applications, either current fed electromagnets [16] or permanent magnets [17] are preferred as SMF sources. NdFeB permanent magnets produce stronger magnetic flux density compared to conventional magnets [18]. However, the positions of the magnets must be changed in order to change the magnetic flux patterns in the workspace. Helmholtz coils are a pair of thin, parallel and identical coils separated by a distance. To change the magnetic flux density generated by Helmholtz

coils, it is sufficient to change source currents while the coil positions stay fixed. These coils are commonly used to generate highly uniform magnetic fields in the space between the coils. Furthermore, this concept can be reversed to use the coils as gradient source by changing the electric current directions, which allows Helmholtz coils to generate FFR instead of uniform magnetic field for specific purposes like localized MFH. In addition, flux densities can be changed with good resolution by fine-tuning source currents of the coils.

The shape and size of the FFR is very important in studies of localized hyperthermia. The compatibility of FFR with the target object in terms of form and size increases the success rate of protecting healthy tissue from unwanted heating. However, as seen in Table 1, this issue has not been discussed in detail. The aim of this study is to determine FFR properties using gradient pattern mapping and measurements. In various studies, coil or magnet configurations have been used as SMF sources. For the reasons mentioned above, Helmholtz coils were preferred as the SMF source in this study.

2. Materials and Methods

2.1. Simulation Medium

A multiphysics simulation software (COMSOL® Multiphysics, COMSOL AB, Stockholm, Sweden) was used for GP modeling. This software uses finite element analysis method to discretize the computational areas. Simulation medium consists of Helmholtz coils and a target object as shown in Figure 3a. Helmholtz coils used in this study had diameter of 205 mm and 250 turns. The distance between the center of the coils was 144 mm. The target

object was a cylinder with its center of gravity at (-50, 0, 0) mm. It had a radius of 10 mm and 100 mm height. Target object was a representative illustration of a sample tube or a small test animal for in vivo or in vitro tests. The distances of coil centers from the origin were kept fixed at (-72, 72) mm on the x-axis. First, the coils were fed by symmetrical currents to generate FFR. Coil currents (I_1, I_2) for left and right coils were (1.1, 1.1) , (2.2, 2.2) and (4.4, 4.4) A, respectively. Then one of the poles was reversed by changing current direction to generate MNP oscillation blocking effect in all workspaces when coil currents were (2.2, -2.2) A.

2.2. Experiment Setup

The experiment setup consisted of Helmholtz coils, power supplies, experiment platform and measuring area. Helmholtz coils with 182.5 mm average diameter and 30 mm thickness were used. The coils were made of copper wire with 1 mm diameter and 250 turns. The distance between the center of the coils was 144 mm. The power supplies for the coils were indicated by *A* in Fig 3b. The distance could be adjusted without disturbing the alignment by inserting the Helmholtz coil into the sliding parts indicated by *B*. The region indicated by *C* was the workspace where the FFR would be generated and measured. By placing the measurement paper as shown in Figure 3b, a total of 81 measurement points were determined on the x and y axes with 10 mm intervals from -40 mm to 40 mm. A transparent magnetic field indicator plate was placed in the workspace as shown in Figure 3c. This plate contained independent compass arrows arranged in matrix form. With the help of these compass arrows, the poles of the source magnets could be determined visually. The FFR in the middle and SMF gradient around the FFR could be easily detected.
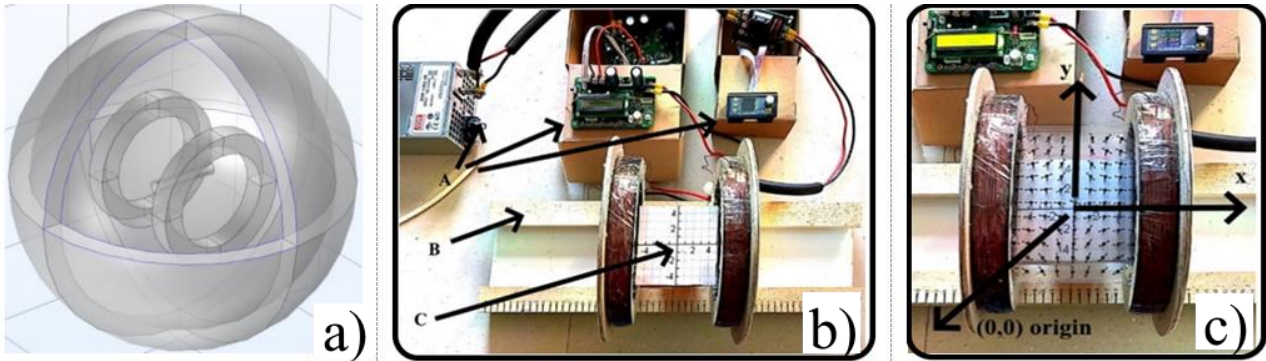
Figure 3. a) simulation medium, b) experiment setup, c) placement of the magnetic field indicator plate.

3. Results and Discussion

3.1. Simulation Results

Magnetic field color maps and arrow representation of flux lines for different current values are shown in Figure 4 a-d, respectively. The FFR form can be manipulated by current change. It was found that the more the current level rose the more the FFR shrunk. To determine the shrinking effect numerically, measurements were done on contour representations of GPs as shown in Figure 5. Conditions of MFH experiments in the literature vary widely. For example, AMF intensity can range from 0.8 to 115 kA/m [19]. Ideally the limit value of SMF can be selected as 10 G (≈0.8 kA/m).

Major axis (MA_1) and minor axis (MA_2) of FFRs were measured. MA_1 and MA_2 were (15.2, 6.7), (6.4, 3.3) and (3.1, 1.8) cm when (I_1, I_2) were (1.1, 1.1), (2.2, 2.2) and (4.4, 4.4) A, respectively. It was found that if current rose to high levels, FFR could transform to a so-called field free point. And FFR could be focused into a very small area. When current applied to coils were (2.2, -2.2) A, there was no FFR occurring in the workspace (see Figure 4d). This uniform field can be used to block MNP oscillations across the entire workspace.

Magnetic flux density measurements were taken at 81 locations spaced 10 mm between -40 mm and 40 mm in the x and y axes. Measurements were taken for four different current values. Point measurement tables in the simulation environment of GPs can be found as a file in the supplementary material.

It was found that FFR can be focused on the target object and its form can be manipulated by changing source current. Point-like or rod-like forms of FFR can be achieved if suitable experiment conditions are provided. Fine tuning of flux densities is also available with coil source currents. FFR (B ≤ 10 G) areas shown in Figure 5 can be considered as ellipses.

The area of an ellipse *A* can be calculated with semi major axis *a* and semi minor axis *b* by Eq. (4).

$$A = \pi ab \qquad (4)$$

When (I_1, I_2) are (1.1, 1.1), (2.2, 2.2) and (4.4, 4.4) A, the lengths *a* and *b* are (7.6, 3.35), (3.2, 1.65) and (1.55, 0.9) cm and surface areas are 79.98, 16.58 and 4.38 cm^2, respectively.
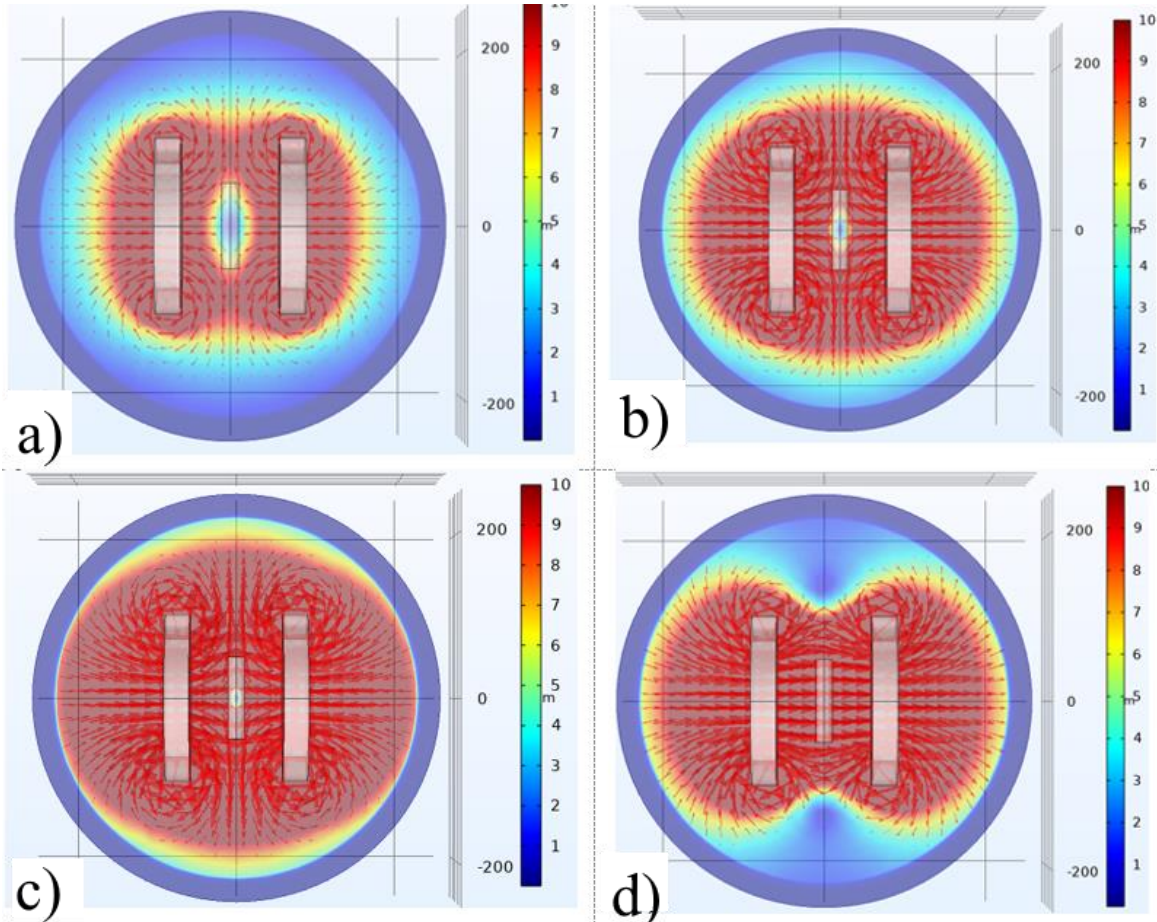
Figure 4. Magnetic field color maps and arrow representation of flux lines when (I_1, I_2) are a) (1.1, 1.1), b) (2.2, 2.2), c) (4.4, 4.4) and d) (2.2, -2.2) A.
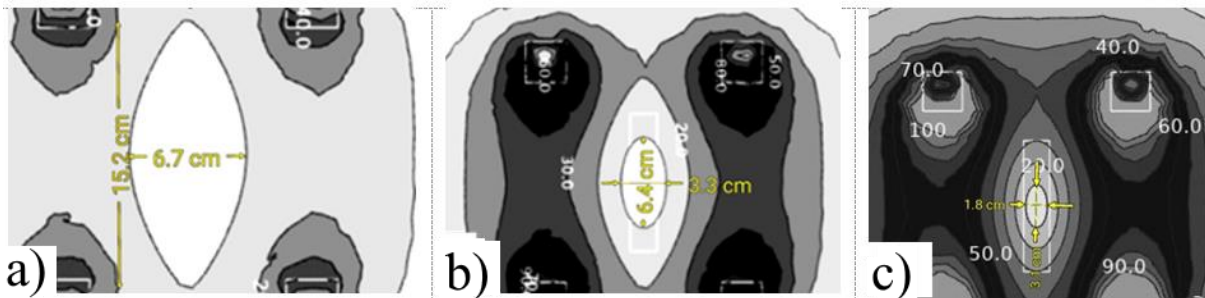
Figure 5. Major and minor axis measurements of FFR when (I_1, I_2) are a) (1.1, 1.1), b) (2.2, 2.2) and c) (4.4, 4.4) A.

3.2. Experiment Results

Measurements were taken at 81 probe locations (see Figure 3b) which are identical with the simulation. Magnetic flux density measurements in the x and y directions (B_x and B_y) were taken for all cases with WT10A magnetic flux meter. The magnitude of the resultant magnetic flux density vector for every point was calculated by Eq. (5),

$$B = \sqrt{B_x^{\,2} + B_y^{\,2}} \tag{5}$$

The magnitude of the vector measurements obtained when (I_1, I_2) were (1.1, 1.1), (2.2, 2.2), (4.4, 4.4) and (2.2, -2.2) A are listed in Table 3. The measurements were repeated 4 times in a row and the average values were transferred to the table. Differences between the simulation environment and experiment setup measurements may be due to ideal conditions in the simulation environment, probe positioning in the experiment setup, measuring device calibration.

Table 3. Magnetic flux density experiment setup measurements.

	(I_1, I_2) = (1.1, 1.1) A									(I_1, I_2) = (4.4, 4.4) A								
	x-axis probe position (mm)									x-axis probe position (mm)								
B (G)	-40	-30	-20	-10	0	10	20	30	40	-40	-30	-20	-10	0	10	20	30	40
40	16	13	10	10	6	8	12	11	17	58	45	37	30	24	29	38	47	59
30	13	11	9	7	7	9	10	13	16	53	43	32	25	20	22	32	42	53
20	15	13	8	7	6	7	7	13	14	49	41	27	18	13	20	27	40	52
10	13	12	6	4	2	5	9	11	12	50	36	27	17	6	14	27	37	50
0	12	12	8	4	3	5	9	12	13	50	37	25	12	2	12	25	39	49
-10	13	11	8	5	2	5	7	11	15	47	38	25	15	6	15	26	37	48
-20	13	12	8	4	6	4	10	11	15	50	40	27	18	14	18	30	39	50
-30	16	12	9	8	7	9	10	11	14	55	44	31	24	19	25	34	41	55
-40	15	11	10	8	8	10	10	11	17	58	46	38	30	25	29	38	46	57

(Left row labels: **y-axis probe position**)

	(I_1, I_2) = (2.2, 2.2) A									(I_1, I_2) = (2.2, -2.2) A								
	x-axis probe position (mm)									x-axis probe position (mm)								
B (G)	-40	-30	-20	-10	0	10	20	30	40	-40	-30	-20	-10	0	10	20	30	40
40	32	23	17	17	13	16	19	23	32	43	39	36	35	34	35	35	38	46
30	29	22	18	13	11	12	17	23	29	45	40	40	35	37	36	38	39	44
20	26	19	16	11	9	12	15	20	26	44	42	37	37	36	38	37	40	45
10	27	18	12	10	3	8	13	19	26	42	40	41	38	38	40	38	42	43
0	26	19	12	9	1	7	15	21	26	43	41	41	38	37	38	38	40	42
-10	25	20	15	10	3	7	14	20	26	44	42	38	39	37	37	39	40	43
-20	26	20	17	11	8	12	16	21	27	42	42	38	38	39	38	40	43	45
-30	29	24	16	13	11	12	18	23	28	45	39	40	35	36	36	38	42	42
-40	31	25	20	16	15	15	20	23	32	43	42	36	36	35	36	36	39	45

(Left row labels: **y-axis probe position**)

In agreement with simulation results, if source current gets high, the FFR shrinks in the center and its shape changes from the surface area to a linear form or a point-line form. When (I_1, I_2) are (1.1, 1.1), (2.2, 2.2), (4.4, 4.4), and (2.2, -2.2) A, the number of points creating FFR (red colored regions in Table 3 , B ≤ 10 G) are 44, 11, 3 and 0, respectively.

4. Conclusions

The shape and size compatibility of the FFR with the target object helps localize the heating effect. This highlights the importance of controlling the size and shape of the FFR in MFH applications. However, it appears that the issue of determining FFR characteristics in hyperthermia studies has not been investigated extensively.

In this study, properties of FFR were analyzed in detail with major and minor axis measurements, area calculations and gradient pattern mapping. The obtained results provide data for in vitro and in vivo MFH tests performed prior to clinical trials.

The ability to ablate a tumor of any possible geometry by moving the FFR over the tumor is critical for future studies. FFR and target tissue overlap can be achieved by appropriate placement of the SMF source and/or target object for localized MFH. In the future, designs can be considered to localize the FFR with highly sensitive robotic devices for each patient's unique individual conditions.

Supplementary Material

The point measurements of GPs in simulation medium are available online at https:// docs.google.com/do cument/d/1CytWgKJinuYSahHmord5I2qhti6WDVC1.

Declaration of Ethical Standards

The author of this article declares that the materials and methods used in this study do not require ethical committee permission and/or legal-special permission.

Conflict of Interest

The author declares that there are no known competing financial interests or personal relationships that could have appeared to influence the work reported in this paper.

References

[1] Huang J., Zhong X., Wang L., Yang L., Mao H., 2012. Improving the magnetic resonance imaging contrast and detection methods with engineered magnetic nanoparticles. Theranostics, **2**, pp. 86–102.

[2] Estelrich J., Sánchez-Martín M.J., Busquets M.A., 2015. Nanoparticles in magnetic resonance imaging: From simple to dual contrast agents. Int. J. Nanomedicine, **10**, pp. 1727–1741.

[3] Arruebo M., Fernández-Pacheco R., Ibarra M.R., Santamaría J., 2007. Magnetic nanoparticles for drug delivery. Nano Today, **2**, pp. 22–32.

[4] Mura S., Nicolas J., Couvreur, P., 2013. Stimuli-responsive nanocarriers for drug delivery. Nat. Mater., **12**, pp. 991–1003.

[5] Mahmoudi K., Bouras A., Bozec D., Ivkov R., Hadjipanayis C., 2018. Magnetic hyperthermia therapy for the treatment of glioblastoma: a review of the therapy's history, efficacy and application in humans. Int. J. Hyperth., **34**, pp. 1316–1328.

[6] Zhao L.-Y., Liu J.-Y., Ouyang W.-W., Li D.-Y., Li L., Li L.-Y., Tang J.-T., 2013. Magnetic-mediated hyperthermia for cancer treatment: Research progress and clinical trials. Chinese Phys. B, **22**, 108104.

[7] Deatsch A.E., Evans B.A., 2014. Heating efficiency in magnetic nanoparticle hyperthermia. J. Magn. Magn. Mater., **354**, pp. 163–172.

[8] Dhavalikar R., Rinaldi C., 2016. Theoretical predictions for spatially-focused heating of magnetic nanoparticles guided by magnetic particle imaging field gradients. J. Magn. Magn. Mater., **419**, pp. 267–273.

[9] Cantillon-Murphy P., Wald L.L., Zahn M., Adalsteinsson E., 2010. Proposing magnetic nanoparticle hyperthermia in low-field MRI. Concepts Magn. Reson. Part A Bridg. Educ. Res., **36**, pp. 36–47.

[10] Tasci T.O., Vargel I., Arat A., Guzel E., Korkusuz P., Atalar E., 2009. Focused RF hyperthermia using magnetic fluids. Med. Phys., **36**, pp. 1906–1912.

[11] Lu Y., Rivera-Rodriguez A., Tay Z.W., Hensley D., Fung K.L.B., Colson C., Saayujya C., Huynh, Q., Kabuli L., Fellows B., 2020. Combining magnetic particle imaging and magnetic fluid hyperthermia for localized and image-guided treatment. Int. J. Hyperth., **37**, pp. 141–154.

[12] Ma M., Zhang Y., Shen X., Xie J., Li Y., Gu N., 2015. Targeted inductive heating of nanomagnets by a combination of alternating current (AC) and static magnetic fields. Nano Res., **8**, pp. 600–610.

[13] Bauer L.M., Situ, S.F., Griswold M.A., Samia A.C.S., 2016. High-performance iron oxide nanoparticles for magnetic particle imaging-guided hyperthermia (hMPI). Nanoscale, **8**, pp. 12162–12169.

[14] Murase K., Takata H., Takeuchi Y., Saito S., 2013. Control of the temperature rise in magnetic hyperthermia with the use of an external static magnetic field. Phys. Medica, **29,** pp. 624–630.

[15] Zhao Q., Wang L., Cheng R., Mao L., Arnold R.D., Howerth E.W., Chen Z.G., Platt S., 2012. Magnetic nanoparticle-based hyperthermia for head & neck cancer in mouse models. Theranostics, **2**, pp. 113–121.

[16] Ristic-Djurovic J.L., Gajic S.S., Ilic A.Z., Romcevic N., Djordjevich D.M., De Luka S.R., Trbovich A.M., Jokic V.S., Cirkovic S., 2018. Design and Optimization of Electromagnets for Biomedical Experiments With Static Magnetic and ELF Electromagnetic Fields. IEEE Trans. Ind. Electron., **65**, pp. 4991–5000.

[17] Ren Z.H., Mu W.C., Huang S.Y., 2019. Design and Optimization of a Ring-Pair Permanent Magnet Array for Head Imaging in a Low-Field Portable MRI System. IEEE Trans. Magn., **55**, pp. 1–8.

[18] Mahadi W.N.L.W., Adi S.R., Nor K.M., 2003. Application of the rare earth permanent magnet in a linear generator driven by an internal combustion engine. In Proceedings of the National Power Engineering Conference, PECon 2003 – Proceedings, pp. 256–261.

[19] Vilas-Boas V., Carvalho F., Espiña B., 2020. Magnetic hyperthermia for cancer treatment: Main parameters affecting the outcome of in vitro and in vivo studies. Molecules, 25.

Consolidation of Time Series Models for the Prediction of XUTEK Index and Technology Stocks in Istanbul Stock Exchange during Pandemic Period

Zeynep Hilal KİLİMCİ [1, *] (iD)

[1] Department of Information Systems Engineering, Kocaeli University, Kocaeli, 41001, Turkey, **ORCID:** 0000-0003-1497-305X

Abstract

Due to the closure experienced during the pandemic, many investors divert their investments to different exchanges. In this sense, it has been observed that while sectors such as transportation, banking, and services have seriously lost value, especially the technology sector has come forward and gained value. In this research, we move the study one step forward by proposing a consolidated forecast system instead of employing a model to estimate the price of the Istanbul Stock Exchange Technology Index (XUTEK) which consists of 19 technology companies traded in BIST, and technology stocks. Stock movements during the pandemic period between 01.01.2020 and 01.09.2020, when technology stocks gained considerable value, are investigated to estimate the price of XUTEK. For each technology stock and XUTEK index, five different time series models are modeled namely, Holt's linear trend, simple exponential smoothing, Holt–Winter's additive, Holt–Winter's multiplicative, and ARIMA. After that, five different time series models are consolidated with six diverse consolidation methods, namely, SA, SATA, MB, VB, VBP2 and VBP3 in order to get a more robust stock price prediction model. Experiment results demonstrate that the utilization of the VBP2 consolidation technique presents remarkable results with 2.6903 of MAPE for estimating the price of the XUTEK index and 19 technology stocks.

1. Introduction

The Istanbul Stock Exchange defined as BIST 100 index, is a generally used abridgment of Turkey's stock exchange. ISE includes the index of national all stocks, the index of national 30 stocks, the index of national 50 stocks, the index of national 100 stocks, the indices of the sector and its sub-sectors, the index of the second national market, the index of the novel economy market and the index of investment trusts. The index of national 100 stocks covers both the index of national 50 stocks and the index of national 30 shares and is employed as a fundamental index of the national market of it. The technology index (XUTEK), which is covered by this study and contains 19 technology companies, is a sector index on the Istanbul Stock Exchange (BIST).

Stock price forecasting is an important and active research field for investors, researchers, and analysts. Stock prices are readily influenced by different external factors to contemplate, being complicated to acquire results with high accuracy due to their often complex and variable nature. Investors, analysts, and researchers assess their investments, analysis, and research with various parameters by conducting fundamental or technical analysis of them. The fundamental analysis investigates the value of an investment by exploring financial and economic elements while the movement direction of any investment is forecasted by employing various parameters such as volume, and price that is gathered from previous time periods of that investment. On the other hand, technical analysis is a method of predicting future prices based on information available in hand by employing past prices, volumes, and technical indicators to appraise the next movement in asset prices on historical data. In this work, we focus on technical indicators in order to forecast the price of the XUTEK index and technology stocks using time series models and a combination of them.

Time series forecasting is a statistical method of using a model to forecast future values based upon formerly observed time series values. It facilitates to analysis of patterns through time series are trend,

---

* Corresponding Author: zeynep.kilimci@kocaeli.edu.tr

seasonality, cyclicity, and irregularity. There are many application areas in time series analysis such as stock market analysis [1-2], economic forecasting [3-4], inventory studies [5-6], budgetary analysis [7-8], census analysis [9-10], yield projection [11-12], sales forecasting [13-14]. Utilizing time series analysis models such as simple exponential smoothing (SES), Holt–Winters (HW), Holt's linear trend (HLT), and autoregressive integrated moving average (ARIMA), it is proposed to comprehend the main elements giving a lead to the trend on the time series and perform a prudential stock price estimation.

In this work, we propose to predict the price of 19 technology stocks and the BIST Technology Index (XUTEK), which consists of 19 technology companies traded in BIST. Stock movements during the pandemic period between 01.01.2020 and 01.09.2020, when technology shares gained significant value, are investigated to estimate the price of the XUTEK. For 19 technology stocks and XUTEK index, five different time series models are modeled namely, simple exponential smoothing, Holt's linear trend, Holt–Winter's additive, Holt–Winter's multiplicative, and ARIMA. Finally, five different time series models are consolidated in order to get a more robust stock price prediction model. To our knowledge, this is the very first attempt in terms of consolidating time series models for the prediction of technology stocks and the XUTEK index in BIST during the pandemic period. Experiment results demonstrate that the combination of the time series model is an effective method to obtain robust results for forecasting the stock price of technology stocks and the XUTEK index instead of using individual forecasts.

The remaining article is designed followingly: Section 2 maintains an abstract of studies utilizing time series analysis. Section 3 includes time series analysis techniques presented under the proposed system. The proposed framework, the results of the experiments, discussion and conclusion sections are presented in Sections 4–6, respectively.

2. Related Work

A summary of the literature studies on time series analysis and different methods is presented to forecast the price or direction of different investment instruments. In financial markets, there are many studies that focus on making price forecasts of stocks, digital currencies, mineral commodities such as funds, gold, bonds, silver and such products.

In a study [15], authors propose to clarify the issue of macroeconomic prediction by defining whether generally well-accepted prediction methods that are commonly

utilized to discover forecasts for Western macro economies are also helpful for China. These forecasting models include 19 different techniques which vary from straightforward methods to more complicated models namely, ARMA, Bayesian VAR, and factor models in order to estimate two distinct measures of price inflation and real activity. Authors conclude the study that AR, ARMA, VAR, and Bayesian VAR techniques ensure superior 1-month-ahead estimates of the producer price index when compared to basic models. In another study [16], the author aims to estimate Egyptian Exchange Price Index (EGX30) using vector autoregressive models (VARS). For this purpose, different versions of ARIMA and VAR models are carried out in the experiments. The author reports that five estimated values of all stationary time series, employing VARS (1) models, are forecasted.

In another study [17], authors propose to estimate the direction of the US Dollar/Turkish Lira exchange rate thereby combining deep learning methods and time series analysis. The combination of proposed model is based on time series analysis (TSA) and financial sentiment analysis (FSA). To conduct the FSA model, word embedding methods Word2vec, GloVe, fastText, and deep learning models such as CNN, RNN, and LSTM are employed. In order to construct the TSA model, simple exponential smoothing, versions of Holt-Winters, ARIMA models, and Holt's linear are utilized. They suggest that any user who wants to make a US Dollar/Turkish Lira exchange rate estimate using the proposed model can make a more consistent and strong exchange rate estimate. In a study [18], authors present a mixed model based on ARIMA and eXtreme gradient boosting (XGBoost) techniques to forecast the stock market volatility. The consolidation of ARIMA and XGBoost is performed by employing the discrete wavelet transform (DWT) approach. Experiment results show that the proposed hybrid method remarkably enhances the predictive performance of an individual ARIMA technique or an individual XGBoost method in forecasting stock prices. Pandey and Bajpai investigate the predictive efficiency of artificial neural network (ANN) and ARIMA approaches by evaluating Nifty Fifty in Indian Stock Market as a case study [19]. For this aim, the authors employ only closing, open, maximum and minimum data of indices as independent variables between January 2007 to December 2016. The paper is concluded that ANN exhibits better predictive performance in case of long span of time and nonlinear volatile series as of the Indian Stock Market Index NSE.

In addition to the usage of time series models, different models are also evaluated for forecasting the price or direction of any investment instrument. In a study [20], authors utilize the closing values of one, two, and three days ago, as well as the US Dollar rate, overnight

interest rate and the Japanese Stock Exchange (NIKKEI), Brazilian Stock Exchange (Bovespa), UK Stock Exchange (FTSE), French Stock Exchange (CAC), German Stock Exchange (DAX) stock exchange index values between 2005 and 2012 to estimate the BIST100 index. Authors estimate the BIST index value using feed-forward artificial neural networks and support vector machine methods. As a result of the study, they note that stock market index forecasting with artificial neural networks and support vector machine methods yields significant results. In another similar study [21], it is indicated that the index value can be successfully modeled with feedforward neural networks using BIST data. In a study [22], it is proposed that a one-dimensional convolutional neural networks (CNNs) model predicts financial market movement, they evaluate the futures of six indices between 2010 and 2017. The results of the experiment demonstrate that the CNN model can effectively infer more generalized and informative features than traditional technical indicators and that more robust and profitable financial performance can be achieved from traditional machine learning approaches.

In another study [23], a new forecasting method using the temporal correlation between global stock markets and various financial products is presented to predict the next day's stock trend employing the support vector machine (SVM) method. The results are 74.4% of accuracy on the NASDAQ, 76% of accuracy on the S&P500 and 77.6% of accuracy on the DJIA. In a study [24], authors utilize the CNN-LSTM model to estimate the price of gold, which uses convoluted neural networks to extract useful information and learn the representation of time series data, as well as the effectiveness of long-short-term memory (LSTM) networks to identify short-and long-term dependencies. They report that the use of LSTM layers in conjunction with convolution layers can provide a significant increase in improving forecasting performance.

Moreover, there are many studies to analyze the BIST index during the pandemic period. In [25], the authors propose to investigate the effects of COVID-19 on the BIST-30 index in a short term. For this aim, daily prices between March 2020 and April 2020 are assessed. They report that Istanbul Stock Exchange demonstrates a negative reaction. In [26], Ilhan and Akdeniz focus on the importance of macroeconomic parameters on the stock market in Turkey during the pandemic period. The Flexible Least Squares technique is employed to observe the effect of the exchange rate, interest rate, CDS premium, oil and VIX prices on the BIST100 index between 2019 September and 2020 September. Authors conclude the study that all features investigated for impacts on the BIST100 have an importance during a pandemic period. In detail, it is also stated that CDS premium, and exchange rate exhibit a negative impact on BIST100. In [27], the reaction of the BIST 100 index against the Covid-19 pandemic is investigated. For this purpose, long and short-term estimations are performed employing robust and error correction models to analyze the impact of Covid-19 on BIST100 index. The rate of mortality, fair index, exchange rate, infectious diseases, volatility index, international equity index, and capital markets are evaluated as features of the proposed system. Experiment results indicate that features chosen for determining the effect of Covid-19 on the BIST 100 index are effective in both short and long term. In [28], Pakel and Ozen concentrate on daily volatility analysis of BIST 100 constituents between 2018 and 2020. To analyze the volatility of the daily revenues on stocks in BIST 100, the GARCH model is employed. The proposed model exposes that the volatility of the stock market has grown fairly during the periods in Turkey consolidated with two shocks, namely a currency and the Covid-19 pandemic. In [29], market risk premiums in BIST 100 in the COVID-19 pandemic period are studied. For this purpose, the dataset is gathered monthly through the Reuters database and the Central Bank of Turkey including BIST100 and 17 diverse sector indexes between 2019 and 2020. Authors conclude the study that the Covid-19 pandemic remarkably raises the volatilities and market risk premiums of the Turkish market.

3. Time Series Analysis

In this section, methods used in this work, including time series analysis models are briefly introduced. Time series analysis embraces the use of a number of statistical analysis methods in which the history is evaluated to make a significant deduction from the regular data coming through the time order, and to have an opinion of the future with predictive methods. Thus, the data acquired in time order are named time series. In other words, time series data implies that the data are gathered at a certain time period.

$$\{Y_t\} \ or \ \{Y_1, \ Y_2, \dots Y_t\} \tag{1}$$

In Eq. (1), the time series gathered by a continuous and discrete period is demonstrated. The fundamental objective of time series analysis is to comprehend whether time impacts the variety in the value of X, which comprises the variable Y.

$$Y_t = \beta_0 + \beta X_t + u_t \tag{2}$$

where Y denotes the unit of time t, and Y_t implies the value that Y has picked up at time t. In Eq. (2), a two-variable dependent regression model beggared for a time series is stated. Because most machine learning models are not appropriate for running with missing values, the time series

should be continual for these models to be employed efficaciously and favorably. To refrain from this issue, the incomplete values should be completed with the convenient data or the rows with the incomplete data should be removed. In this work, since technology stocks located in BIST100 at the weekends and holidays are not trading, the missing data is filled instead of deleting the lines that comprised the missing data, on condition that convenient data are available. For this reason, the missing values of weekends and holidays are filled in according to the closing values of the shares on the last trading day. In other words, the missing data for the weekend and holidays are filled in with the closing value of the last trading working day.

Simple exponential smoothing (SES) is a technique of exponential smoothing that gives exponentially downward weights based upon the recent and earliest samples from these data, utilized to forecast data that have no certain trend or seasonality [30]. Because simple exponential smoothing employs a weighted moving average with exponentially decrescent weights, it is convenient for short-term predictions although long-term estimates employing this method can be highly unfaithful.

$$S_t = \alpha y_t + (1-\alpha)S_{t-1} \tag{3}$$

where t implies to the time interval, y_t denotes current observation, S_t indicates the simple weighted average of y_t, and α demonstrates the smoothing constant, that is adjusted between 0 and 1 in Eq. (3).

Holt's linear trend method is a broadened model of the simple exponential smoothing technique. It is assumed that the trend is constant, continually enhancing or reducing in the future. This technique is carried out on data that are not seasonality but trend [31].

$$\hat{y}_{t+h|t} = \ell_t + hb_t \tag{4}$$

$$\ell_t = \alpha_{y_t} + (1-\alpha)(\ell_{t-1} + b_{t-1}) \tag{5}$$

$$b_t = \beta^*(\ell_t - \ell_{t-1}) + (1-\beta^*)b_{t-1} \tag{6}$$

where ℓ_t indicates to the level in Eq. (4), Eq. (5), and Eq. (6), b_t implies the trend and α, β^* specify smoothing parameters.

The Holt-Winters seasonal model, also known as the triple exponential smoothing technique, is acquired by performing exponential smoothing three times. Essentially, the Holt–Winters method is a broadened model of Holt's linear trend model since a seasonal component is evaluated as an extra [32]. Different versions of the seasonality of this method are carried out with two different techniques namely, multiplicative and additive. The multiplicative method is opted provided that the seasonal modifications are constant throughout the time series, and providing that

the seasonal modifications vary proportionally throughout the time series. The additive model is described in Eq. (7), Eq. (8), Eq. (9), and Eq. (10) as follows:

$$\hat{y}_{t+h|t} = \ell_t + hb_t + s_{t+h-m(k+1)} \tag{7}$$

$$\ell_t = \alpha(y_t - s_{t-m}) + (1-\alpha)(\ell_{t-1} + b_{t-1}) \tag{8}$$

$$b_t = \beta^*(\ell_t - \ell_{t-1}) + (1-\beta^*)b_{t-1} \tag{9}$$

$$s_t = \gamma(y_t - \ell_{t-1} - b_{t-1}) + (1-\gamma)s_{t-m} \tag{10}$$

The multiplicative model is denoted in Eq. (11), Eq. (12), Eq. (13), and Eq. (14) as below:

$$\hat{y}_{t+h|t} = (\ell_t + hb_t)s_{t+h-m(k+1)} \tag{11}$$

$$\ell_t = \alpha \frac{y_t}{s_{t-m}} + (1-\alpha)(\ell_{t-1} + b_{t-1}) \tag{12}$$

$$b_t = \beta^*(\ell_t - \ell_{t-1}) + (1-\beta^*)b_{t-1} \tag{13}$$

$$s_t = \gamma \frac{y_t}{(\ell_{t-1} - b_{t-1})} + (1-\gamma)s_{t-m} \tag{14}$$

where ℓ_t shows to the level, b_t demonstrates to the trend, α and β^* specify smoothing parameters, and m means the frequency of seasonality.

The most commonly utilized model in time series analysis and prediction is the autoregressive moving average (ARMA) method, along with the generalized autoregressive integrated moving average (ARIMA) model. Both methods are employed to better comprehend time series or to estimate the futurity values in time series. The ARIMA method consolidates the autoregressive (AR) and the moving average (MA) models to provide the time series stationary with a novel pre-processing stage named integration [33]. It is confessed that the future point of a variable is a linear function of previous samples and random errors in the autoregressive integrated moving average technique [34]. The ARIMA model comprises three several phases. The first stage is the value p (AR), the second phase is q (MA), and the last one is d(I), which is demonstrated as the weighted total amount of delayed forecasted errors of the time series. The ARIMA model is demonstrated in Eq. (15) as below:

$$ARIMA(p,d,q)$$

$$X_t = c + \sum_{i=1}^{p} \varphi_i X_{t-i} + \varepsilon_t \tag{15}$$

$$X_t = \mu + \varepsilon_t + \sum_{i=1}^{q} \theta_i \varepsilon_{t-i}$$

where c represents the parameter interrupt that is predicted by the method. Φ and θ display the coefficient of delayed

times forecasted by the method. μ is the expected point of X_t, X shows the delay value, and ε defines the randomly defined error variable.

4. Proposed Framework

In this section, data collection and proposed methodology are presented. In this work, stock movements during the pandemic period are proposed to analyze in order to forecast the price of the XUTEK index and 19 different technology stocks. For both 19 technology stocks and the XUTEK index, the values of the indicators that affect the direction of the technology index and stocks daily between 1 January 2020 and 1 September 2020, when technology shares gained significant value are collected. Indicators that are efficient in identifying the direction of the stocks and XUTEK index are collected via investing.com with the aid of Selenium library. The value of the "DayClass" parameter included in the features is obtained by subtracting the intraday opening value from the intraday closing value. If the resulting value is greater than 0, it is negative, if it is less than 0, the label value of that day is labeled positive. Some indicators of stocks are also added to the feature set to increase the feature diversity of the data set. These indicators consist of the 5, 10, 20, 50 and 100-day simple moving average (SMA), 14-day relative strength index (RSI) and the upper, middle and lower values of the Bollinger band. These indicators consist of the 5, 10, 20, 50,100 and 200-day simple moving average (SMA), relative strength index (RSI) and the upper, middle and lower values of the Bollinger band. Although there is no difficulty in gathering the opening and closing values of the technology stocks in the relevant date range via the Selenium crawler, the values of the technical indicators could not be obtained. For this reason, the technical analysis library named TA-lib [35] is used to obtain the historical indicator values and the values of the indicators mentioned above are calculated. The parameter details of the dataset to be used in the modeling are presented in Table 1.

Table 1. The parameter details of the 20 datasets.

Parameter	Explanation
Date	Date information
CloseP	Closing value of stock on that day
OpenP	Opening value of stock on that day
HighDay	The highest value of stock on that day
AvgDay	The average value of stock on that day
LowDay	The lowest value of stock on that day
DayClass	Value indicating whether the stock closed positive that day.
SMA_5	5-day simple moving average of the stock

Table 1. (Cont.) The parameter details of the 20 datasets.

Parameter	Explanation
SMA_10	10-day simple moving average of the stock
SMA_20	20-day simple moving average of the stock
SMA_50	50-day simple moving average of the stock
SMA_100	100-day simple moving average of the stock
SMA_200	200-day simple moving average of the stock
RSI	14-day Relative Strength Index of the stock
BollingerUpper	Top band value of daily Bollinger band for the stock
BollingerMiddle	Middle band value of daily Bollinger band for the stock
BollingerLower	Lower band value of daily Bollinger band for the stock

At the next step, 20 different datasets are ready to be modeled using simple exponential smoothing (SES), Holt's linear trend (HLT), Holt–Winter's additive (HWA), Holt–Winter's multiplicative (HWM), and ARIMA methods for 19 technology stocks and XUTEK index. Then, price forecasts for each technology stock and XUTEK index are acquired through the aforementioned models. Finally, five different time series methods are consolidated to acquire a final decision and a sturdier stock price prediction method. With this aim, 6 different combination techniques are assessed for linear forecasts. These are namely, simple average, simple average with trimming averages, median-based, variance-based, variance-based pooling with two clusters, and variance-based pooling with three clusters. All methods are appointed equal weights in the simple average approach (SA) [36-37] while individual estimates are consolidated simple arithmetic mean, excepting the worst n% of the methods in simple average with trimming averages (SATA) [36-37].

On the other hand, the consolidation function is the median of the individual estimates in the median-based (MB) consolidation method [38-39] while the ideal weights are assigned via the minimization of the total sum of squared error in the variance-based methodology (VB) [37, 40]. In variance-based pooling approach with clusters, previous performance is utilized group estimates into two (VBP2) or three clusters (VBP3) by a k-means technique as proposed in a study [41].

Finally, the best successful method is determined as a final decision among six different combination results in order to forecast the prediction of the XUTEK index and technology stocks in BIST during the pandemic period. To our knowledge, this is the very first work in terms of consolidating time series models for the prediction of the XUTEK index in BIST during the pandemic period. Experiment results demonstrate that the combination of the time series model is an effective method to obtain robust results for forecasting the stock price of technology stocks

and the XUTEK index. In Figure 1, the architecture of the proposed framework is presented.
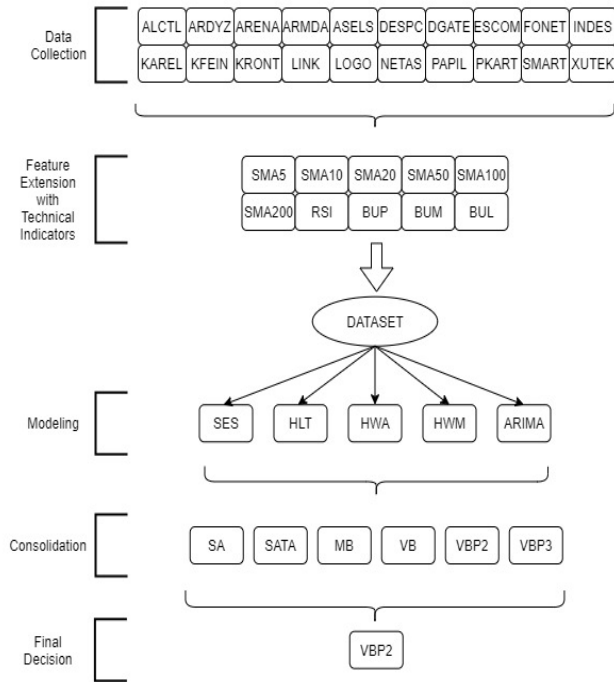
Figure 1. The architecture of proposed framework.

5. Experiment Results

In this study, comprehensive experiments are carried out to analyze the effectiveness of both combination of time series models and base time series methods for the estimation of XUTEK index and technology stocks in BIST during pandemic period. For empirical verification of forecasting performances of the proposed technique, twenty real world time series are employed as datasets that include XUTEK index and technology stocks in BIST100. Predicting success of all methods are evaluated with the well-known and widely-applied error statistics, viz the Mean Absolute Percentage Error (MAPE), mean absolute error (MAE), mean squared error (MSE), and R-squared (R^2) as defined below:

$$MAPE = \frac{1}{N}\sum_{i=1}^{N}\left|\frac{y_a - y_f}{y_a}\right| \times 100 \tag{18}$$

$$MAE = \frac{1}{N}\sum_{i=1}^{N}|y_a - y_f| \tag{19}$$

$$MSE = \frac{1}{N}\sum_{i=1}^{N}(y_a - y_f)^2 \tag{20}$$

$$R^2 = 1 - \frac{\sum(y_a - y_f)^2}{\sum(y_a - y_m)^2} \tag{21}$$

where N is the size of test set, y_a and y_f are the actual and forecasted observations, respectively. The following abbreviations are utilized for the time series and consolidation models: SES: Simple exponential smoothing, HLT: Holt's linear trend, HWM: Holt–Winter's multiplicative, HWA: Holt–Winter's additive, ARIMA: Autoregressive integrated moving average, SA: Simple average approach, SATA: Simple average with trimming averages, MB: Median-based consolidation, VB: Variance-based consolidation, VBP2: Variance-based pooling approach with two clusters, VBP3: Variance-based pooling approach with three clusters. All techniques are implemented on Google Colab provided free GPU usage by Google.

Table 2. Forecasting mean absolute percentage error results of individual time series models in 20 datasets.

Dataset	Models				
	SES	**HLT**	**HWM**	**HWA**	**ARIMA**
ALCTL	3.425	3.351	3.169	3.095	2.993
ARDYZ	3.583	3.598	3.464	3.382	3.231
ARENA	3.441	3.403	3.381	3.350	3.271
ARMDA	3.473	3.451	3.442	3.440	3.352
ASELS	3.423	3.402	3.331	3.302	3.210
DESPC	3.455	3.413	3.425	3.403	3.251
DGATE	3.401	3.352	3.341	3.345	3.239
ESCOM	3.351	3.320	3.341	3.340	3.125
FONET	3.724	3.694	3.671	3.650	3.423
INDES	3.563	3.500	3.472	3.445	3.157
KAREL	3.254	3.227	3.200	3.179	2.897
KFEIN	3.389	3.352	3.341	3.317	3.054
KRONT	3.360	3.334	3.292	3.260	2.980
LINK	3.124	3.095	3.051	3.065	2.835
LOGO	3.270	3.210	3.184	3.154	2.893
NETAS	3.320	3.308	3.279	3.260	2.900
PAPIL	3.428	3.391	3.381	3.332	2.995
PKART	3.312	3.284	3.257	3.264	2.982
SMART	3.291	3.230	3.224	3.203	2.894
XUTEK	3.179	3.147	3.140	3.107	2.882
Average	3.388	3.353	3.319	3.295	**3.078**

The best performing MAPE scores are represented in bold. In Table 2 and Table 3, forecasting results of individual time series and consolidation models are presented in 20 datasets, respectively. In Table 2, MAPE results of five different time series models are demonstrated. It is clearly observed that average result for

twenty datasets with 3.0786 of MAPE outperforms others. It is followed by HWA, HWM, HLT, SES, respectively. Moreover, ARIMA results of each dataset generally performs well for 20 datasets when the success of other techniques is considered. Among 20 datasets, XUTEK, SMART, NETAS, LINK, LOGO, and KAREL stocks exhibit more successful MAPE results in terms of ARIMA performance.

On the other hand, it is obviously seen that SES model presents the poorest success with 3.3886 of average MAPE. Thus, SES model is not convenient to estimate both the price of XUTEK index and technology stocks. When average MAPE scores are considered, HLT method maintains 0.03 improvement. On the other hand, HWM model provides 0.07 enhancement in difference between error statistic in comparison with the performance of SES. In addition, ARIMA shows 0.31 progress while HWA model presents 0.09 improvement compared to the SES. Enhancement in MAPE of ARIMA model is clearly observed with 0.31 difference. Hereby, ARIMA as an individual technique is convenient to estimate the price of XUTEK index and 19 technology stocks in BIST100.

Table 3. Forecasting mean absolute percentage error results of consolidation models in 20 datasets.

Dataset	Models					
	SA	SATA	MB	VB	VBP2	VBP3
ALCTL	2.840	2.834	2.795	2.881	2.653	2.692
ARDYZ	3.085	3.081	3.021	3.112	2.852	2.897
ARENA	3.114	3.101	2.782	3.143	2.641	2.684
ARMDA	3.203	3.193	3.157	3.247	2.995	3.057
ASELS	3.021	3.019	2.964	3.079	2.812	2.856
DESPC	3.062	3.058	3.001	3.135	2.854	2.890
DGATE	3.054	3.048	2.982	3.107	2.831	2.874
ESCOM	2.952	2.943	2.891	3.019	2.755	2.780
FONET	3.193	3.185	3.139	3.273	2.994	3.056
INDES	2.992	2.989	2.941	3.048	2.792	2.840
KAREL	2.684	2.680	2.635	2.771	2.501	2.546
KFEIN	2.900	2.889	2.854	2.940	2.703	2.754
KRONT	2.823	2.817	2.779	2.875	2.630	2.690
LINK	2.662	2.653	2.601	2.723	2.468	2.511
LOGO	2.683	2.680	2.645	2.774	2.492	2.537
NETAS	2.741	2.735	2.699	2.790	2.539	2.580
PAPIL	2.830	2.828	2.772	2.863	2.630	2.691
PKART	2.801	2.793	2.753	2.854	2.624	2.674
SMART	2.730	2.725	2.684	2.781	2.531	2.578
XUTEK	2.713	2.710	2.650	2.767	2.500	2.560
Average	2.904	2.898	2.837	2.959	**2.690**	2.737

In Table 3, forecasting results of consolidation models for XUTEK and 19 technology stocks are presented. It is obviously seen that all consolidation models remarkably excel all individual models in terms of forecasting the price of stocks and technology index when mean MAPE results are considered. Even the poorest consolidation model VB shows a 2.9595 MAPE value which means nearly 0.12 enhancement while the best individual models ARIMA exhibits a 3.0786 MAPE result. It is followed by 2.90 with SA, 2.89 with SATA, 2.83 with MB, 2.73 with VBP3, and 2.69 with VBP2.

The utilization of variance-based polling techniques remarkably provides enhancement compared to the other consolidation techniques. When the overall MAPE performance of VBP2 is observed, it demonstrates less MAPE compared to other models. The performance order between consolidation models can be summarized as VBP2> VBP3> MB> SATA> SA> VB. VBP2 technique ensures approximately 0.04, 0.14, 0.2, 0.21, 0.26 advancement in MAPE results compared to VBP3, MB, SATA, SA, VB, respectively. As a result of Table 2 and Table 3, VBP2 as a consolidation technique is more convenient with almost 2.69 MAPE value to forecast the price of the XUTEK index and 19 technology stocks in BIST100. Moreover, different evaluation metrics, namely MAE, MSE, and R^2 are presented in addition to MAPE values for the best prediction model VBP2 in Table 4.

In Figure 2, the actual price, the best predicted individual time series and consolidated models are compared for six datasets namely, XUTEK, SMART, NETAS, LOGO, LINK and KAREL. Black, red, and blue lines demonstrate the actual price, VBP2 prediction, and ARIMA estimation of the stocks, respectively. It is obviously observed that VBP2 exhibits remarkable experiment results during the pandemic period because it exhibits very close performance to the actual price of each dataset. On the other hand, ARIMA as an individual time series model is not capable to forecast the XUTEK index and technology stocks as much as VBP2 for each dataset although ARIMA outperforms other individual time series techniques.

Table 4. MAPE, MAE, MSE, and R2 results of VBP2 consolidation model in all datasets.

Dataset	Evaluation Metrics			
	MAPE	MAE	MSE	R^2
ALCTL	2.6530	0.0114	0.0032	0.9971
ARDYZ	2.8522	0.0145	0.0055	0.9929
ARENA	2.6415	0.0127	0.0028	0.9983
ARMDA	2.9952	0.0162	0.0076	0.9827
ASELS	2.8123	0.0140	0.0047	0.9975
DESPC	2.8540	0.0149	0.0058	0.9931

Table 4. (Cont.) MAPE, MAE, MSE, and R2 results of VBP2 consolidation model in all datasets.

Dataset	Evaluation Metrics			
	MAPE	MAE	MSE	R^2
DGATE	2.8315	0.0138	0.0031	0.9935
ESCOM	2.7550	0.0133	0.0044	0.9980
FONET	2.9948	0.0173	0.0073	0.9836
INDES	2.7925	0.0135	0.0052	0.9980
KAREL	2.5013	0.0079	0.0018	0.9989
KFEIN	2.7037	0.0129	0.0045	0.9984
KRONT	2.6309	0.0130	0.0025	0.9985
LINK	2.4688	0.0027	0.0012	0.9989
LOGO	2.4927	0.0045	0.0026	0.9989
NETAS	2.5394	0.0068	0.0034	0.9988
PAPIL	2.6302	0.0142	0.0020	0.9987
PKART	2.6240	0.0123	0.0014	0.9986
SMART	2.5319	0.0071	0.0025	0.9988
XUTEK	2.5006	0.0067	0.0015	0.9988
Average	**2.6903**	**0.0114**	**0.0036**	**0.9961**

As a result of this work, the consolidation of time series models performs well to estimate the price of the XUTEK index and 19 technology stocks in BIST100. It is clearly observed that usage of consolidation models performs better than traditional time series methods. Even the poorest performance of consolidation model VB excels the best individual time series model ARIMA. For this reason, the VBP2 consolidation model is convenient to estimate the price of the XUTEK index during the pandemic period. It is hard to compare the success of our results with other studies because of the lack of works with similar combinations of different methods, datasets, and consolidation approaches. Although a comparison of baseline time series models and consolidation techniques is given in this work, we also report the MAPE results of several works here.

In a study [16], it is proposed to forecast Egyptian Exchange Price Index (EGX30) using different versions of ARIMA. The author reports that the best MAPE result of the ARIMA model is obtained as 5.9954 while our ARIMA method exhibits a 3.0786 MAPE value. Moreover, the best consolidation method of this study (VBP2) presents 2.6903 of MAPE which demonstrates the success of our proposed system compared to the literature study [16]. In another work [17], the authors aim to forecast the direction of the US Dollar/Turkish Lira exchange rate by combining time series analysis and deep learning methods. Authors report MAPE results as 2.6432 for SES, 2.4576 for HLT, 2.6325 for HWM, 2.6273 for HWA, and 2.7144 for ARIMA while MAPE results in this study are 3.3886 for SES, 3.3535 for HLT, 3.3197 for HWM, 3.2951 for HWA, and 3.0786 for ARIMA model. This can arise in different experiment settings, datasets, number of features, and attributes. The same models exhibit a more successful performance in the study [17], while the proposed hybrid model in this work, namely VBP2 outperforms all models with 2.6903 of MAPE result. In a study [37], authors present a meta-learning approach for time series forecasting and consolidation of them employing SA, SATA, VB, VBP2, and VBP3 methods. Because they report experiment results using symmetric MAPE (sMAPE) results, we also calculate the sMAPE results of all consolidation methods used in this work in order to compare the success of models. Lemke and Gabrys report the sMAPE results for consolidation models as 17.5 for SA, 17.4 for SATA, 18.1 for VB, 16.4 for VBP2, 16.8 for VBP3 while sMAPE values in this work are 17.1 for SA, 16.9 for SATA, 16.4 for MB, 17.7 for VB, 15.6 for VBP2, and 15.9 for VBP3. This demonstrates that our proposed consolidation model, VBP2 exhibits similar performance to the study [37] by obtaining the best sMAPE result compared to the other models. As a result, it is obviously observed that the consolidation of time series models is an efficient way for the purpose of forecasting the XUTEK index and technology stocks in BIST during the pandemic period.
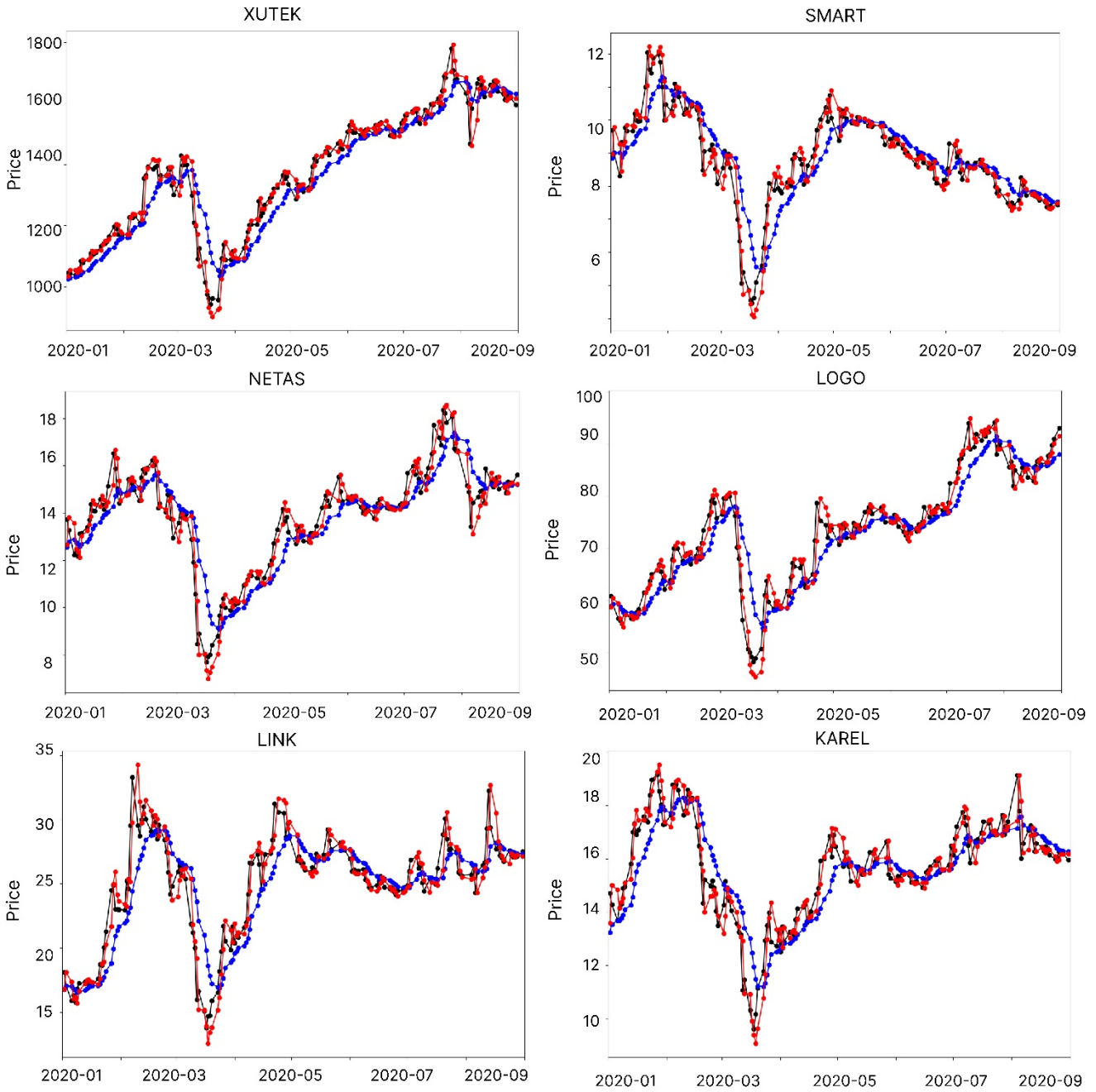
Figure 2. The comparison of actual price, forecasted prices of ARIMA (the best individual model), and VBP2 (the best consolidation model).

6. Discussion and Conclusion

Due to the closure experienced during the pandemic, many investors direct their investments to different exchanges. It is seen that while sectors such as transportation, banking, and services have seriously lost value, especially the technology sector has come forward and gained value. In this work, we propose a consolidated forecast system to forecast the price of the technology Index (XUTEK) which consists of 19 technology companies traded in BIST, and technology stocks in BIST.

Stock movements during the pandemic period between 01.01.2020 and 01.09.2020 are analyzed in order to estimate the price of XUTEK and stocks. For each technology stock, and XUTEK index, five different time series models are evaluated namely, SES, HLT, HWA, HWM, and ARIMA. Then, five different time series models are combined with six consolidation methods, namely, SA, SATA, MB, VB, VBP2, VBP3 in order to get a more robust stock price prediction model. Finally, the VBP2 technique outperforms both conventional time series models and consolidation methods. Comprehensive

experiment results demonstrate that the proposed consolidation model exhibits notable scores for estimating the price of the XUTEK index and 19 technology stocks. In the future, we plan to cover various fundamental and technical indicators to broaden the feature space for the purpose of boosting the performance of the system.

Declaration of Ethical Standards

The author of this article declares that the materials and methods used in this study do not require ethical committee permission and/or legal-special permission.

Conflict of Interest

The authors declare that they have no known competing financial interests or personal relationships that could have appeared to influence the work reported in this paper.

References

[1] Li F., Zhong J., He F., Wang H., Lin J., Yu M., 2022. Stock market fluctuation and stroke incidence: A time series study in Eastern China. Social Science and Medicine, **296**, pp. 1-6.

[2] Takyi P.O., Bentum-Ennin I., 2021. The impact of COVID-19 on stock market performance in Africa: A Bayesian structural time series approach. Journal of Economics and Business, **115**, pp. 1-10.

[3] Satrio C.B.A., Darmawan W., Nadia B.U., Hanafiah N., 2021. Time series analysis and forecasting of coronavirus disease in Indonesia using ARIMA model and PROPHET. Procedia Computer Science, **179**, pp. 524-532.

[4] Adebayo T.S., Akinsola G.D., Kirikkaleli D., Bekun F.V., Umarbeyli S., Osemeahon O.S., 2021. Economic performance of Indonesia amidst CO2 emissions and agriculture: a time series analysis. Environmental Science and Pollution Research, **28**(35), pp. 47942-47956.

[5] Reinosch, E., Gerke, M., Riedel, B., Schwalb, A., Ye, Q., & Buckel, J., 2021. Rock glacier inventory of the western Nyainqêntanglha Range, Tibetan Plateau, supported by InSAR time series and automated classification. Permafrost and Periglacial Processes, **32**(4), 657-672.

[6] Li, N., Arnold, D. M., Down, D. G., Barty, R., Blake, J., Chiang, F., ... & Heddle, N. M., 2022. From demand forecasting to inventory ordering decisions for red blood cells through integrating machine learning, statistical modeling, and inventory optimization. Transfusion, **62**(1), 87-99.

[7] Chen, T., Song, C., Ke, L., Wang, J., Liu, K., & Wu, Q., 2021. Estimating seasonal water budgets in global lakes by using multi-source remote sensing measurements. Journal of Hydrology, **593**, 125781.

[8] ElBerry N.A., Goeminne S., 2021. Fiscal transparency, fiscal forecasting and budget credibility in developing countries. Journal of Forecasting, **40**(1), pp. 144-161.

[9] Nguyen H.M., Turk P.J., McWilliams A.D., 2021. Forecasting covid-19 hospital census: A multivariate time-series model based on local infection incidence. JMIR Public Health and Surveillance, **7**(8), pp. 1-13.

[10] Fuladlu K., Riza M., Ilkan M., 2021. Monitoring urban Sprawl using time-series data: Famagusta region of Northern Cyprus. SAGE Open, **11**(2), pp. 1-13.

[11] Varela S., Pederson T., Bernacchi C.J., Leakey A.D., 2021. Understanding growth dynamics and yield prediction of sorghum using high temporal resolution Uav imagery time series and machine learning. Remote Sensing, **13**(9), pp. 1-17.

[12] Sun Z., Li Q., Jin S., Song Y., Xu S., Wang X., Jiang, D., 2022. Simultaneous Prediction of Wheat Yield and Grain Protein Content Using Multitask Deep Learning from Time-Series Proximal Sensing. Plant Phenomics, **2022**, pp. 1-13.

[13] Jha B.K., Pande S., 2021. Time series forecasting model for supermarket sales using FB-prophet. Paper presented at 5th International Conference on Computing Methodologies and Communication, Erode, India, 8-10 April.

[14] Özeroğlu A.İ., 2021. Personal loan sales forecasting through time series analysis. Prizren Social Science Journal, **5**(1), pp. 44-51.

[15] Heaton C., Ponomareva N., Zhang Q., 2020. Forecasting models for the Chinese macroeconomy: The simpler the better? Empirical Economics, **58**(1), pp. 139-167.

[16] Elsayed A.M.M., 2021. Forecasting EGX30 index time series using vector autoregressive models VARS. International Journal of Statistics and Applied Mathematics, **6**(2), pp. 6-20.

[17] Yasar H., Kilimci Z.H., 2020. US Dollar/Turkish Lira exchange rate forecasting model based on deep learning methodologies and time series analysis. Symmetry, **12**(9), pp. 1553-1571.

[18] Wang Y., Guo Y., 2020. Forecasting method of stock market volatility in time series data based on mixed model of ARIMA and XGBoost. Chin Commun, **17**(3), pp. 205-221.

[19] Pandey V.S., Bajpai A., 2019. Predictive efficiency of ARIMA and ANN models: A case analysis of nifty fifty in Indian stock market. Int J Appl Eng Res, **14**(2), pp. 232-244.

[20] Yakut E., Elmas B., Yavuz S., 2014. Yapay sinir ağları ve destek vektör makineleri yöntemleriyle borsa endeksi tahmini. Süleyman Demirel Üniversitesi İktisadi İdari Bilimler Fakültesi Dergisi, **19**(1), pp. 139-157.

[21] Kutlu B., Badur B., 2009. Yapay sinir ağları ile borsa endeksi tahmini. Yönetim Dergisi, **20**(63), pp. 25-40.

[22] Wang J., Sun T., Liu B., Cao Y., Wang D., 2018. Financial markets prediction with deep learning. Paper presented at 17th IEEE International Conference on Machine Learning and Applications, Orlando, Florida, USA, 17-20 December.

[23] Shen S., Jiang H., Zhang T., 2012. Stock market forecasting using machine learning algorithms. MSc, Stanford University, Department of Electrical Engineering, Stanford, CA, USA.

[24] Livieris I.E., Pintelas E., Pintelas P.A., 2020. CNN–LSTM model for gold price time-series forecasting. Neural Comput Appl, **32**(23), pp. 17351–17360.

[25] Keleş E., 2020. COVID-19 ve BİST-30 Endeksi Üzerine Kisa Dönemli Etkileri. Marmara Üniversitesi İktisadi ve İdari Bilimler Dergisi, **42**(1), pp. 91-105.

[26] İlhan A., Akdeniz C., 2020. The impact of macroeconomic variables on the stock market in the time of Covid-19: The case of Turkey. Ekonomi Politika ve Finans Araştırmaları Dergisi, **5**(3), pp. 893-912.

[27] Gülhan Ü., 2020. Covid-19 pandemisine BIST 100 reaksiyonu: Ekonometrik bir analiz. Electronic Turkish Studies, **15**(4), pp. 497-509.

[28] Pakel C., Özen K., 2020. Daily volatility analysis of BIST 100 constituents between 2018-2020. Marmara Üniversitesi İktisadi ve İdari Bilimler Dergisi, **42**(2), pp. 340-360.

[29] Teker S., Teker D., Demirel E., 2021. Market risk premiums in BIST 100 in the Covid era. Press Academia Procedia, **14**(1), pp. 110-112.

[30] Hyndman R.J., Athanasopoulos G., 2018. Simple Exponential Smoothing, Forecasting: Principles and Practice, 2nd ed. Otexts, Melbourne, Australia.

[31] Holt C., 2004. Forecasting seasonals and trends by exponential weighted moving averages. Int J Forecast, **20**, pp 5–10.

[32] Winters P.R., 1960. Forecasting sales by exponentially weighted moving averages. Manage Sci, **60**(6), pp. 324–342.

[33] Box G. E., Jenkins G.M., Reinsel G.C., Ljung G.M., 2016. Time Series Analysis: Forecasting and Control. 2nd ed. Wiley, Hoboken, NJ, USA.

[34] Zhang G.P., 2003. Time series forecasting using a hybrid ARIMA and neural network model. Neurocomp, **50**, pp. 159-175.

[35] https://github.com/mrjbq7/ta-lib Accessed on January 2022.

[36] Richmond V., Jose R., Winkler R.L., 2008. Simple robust averages of forecasts: Some empirical results. Int J Forecast, **24**, pp. 163–169.

[37] Lemke C., Gabrys B., 2010. Meta-learning for time series forecasting and forecast combination. Neurocomp, **73**, pp. 2006–2016.

[38] Agnew C., 1985. Bayesian consensus forecasts of macroeconomic variables. J Forecast, **4**, pp. 363–376.

[39] Stock J.H., Watson M.W., 1985. Combination forecasts of output growth in a seven-country data set. J Forecast, **23**, pp. 405–430.

[40] Aksu C., Gunter S., 1992. An empirical analysis of the accuracy of SA, OLS, ERLS and NRLS combination forecasts. Int J Forecast, **8**, pp. 27–43.

[41] Aiolfi M., Timmermann A., 2006. Persistence in forecasting performance and conditional combination strategies. J Econom, **127**(1–2), pp. 31–53.

Kocaeli University

Kocaeli Journal of Science and Engineering

http://dergipark.org.tr/kojose
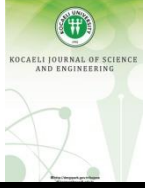
An Overview of Appetite Regulation Mechanisms

Kübra ŞENER [1, *] (iD) , Elif Naz ALVER [2] (iD) , Şule COŞKUN CEVHER [3] (iD)

[1] *Department of Biology, Faculty of Science, Gazi University, Ankara, 06500, Turkey,* **ORCID:** *0000-0002-8759-9444*
[2] *Department of Biology, Faculty of Science, Gazi University, Ankara, 06500, Turkey,* **ORCID:** *0000-0001-6204-2845*
[3] *Department of Biology, Faculty of Science, Gazi University, Ankara, 06500, Turkey,* **ORCID:** *0000-0003-4946-1185*

Abstract

Maintaining body weight is momentous in quality of life. Appetite takes an important role in establishing the balance of daily food absorption and spent energy and, accordingly, controlling body weight. There is a complex physiological control regulation in the maintenance of energy balance. The regulation of appetite is carried out by central and peripheral signals. The hypothalamus, brainstem, and reward centers, which are involved in central regulation, provide management of food absorption by integrating signals from the peripheral. Gastrointestinal hormones in the peripheral system regulate the digestion and absorption of nutrients. In the central nervous system, these hormones act as neurotransmitters. The ability to adjust food absorption in response to changes in energy status is an essential component of maintaining energy homeostasis. In cases where energy homeostasis cannot be balanced, it risks human life and causes a decrease in their quality of life. Diseases such as anorexia, which is characterized by low body weight, or obesity, which is characterized by increased body weight, may occur. A full understanding of the mechanism of appetite may offer new treatment opportunities in the elimination of diseases and complications that may develop due to these diseases. In this context, central and peripheral processes in the adjustment of food intake were reviewed in our study.

1. Introduction

Appetite, which is defined as the conscious desire for food, has a critical role in providing energy homeostasis and maintaining body weight [1]. There is a complicated physiological control mechanism in maintaining energy homeostasis. This system consists of afferent signals from the environment related to the energy requirement and efferent signals that affect the energy uptake and consumption [2]. This regulatory system maintains energy homeostasis through multiple interactions between signals from the gastrointestinal system and adipose tissue, and the central nervous system that responds to these signals [3]. In the disorder of this, basic energy homeostasis, body weight control cannot be realized and anorexia or obesity situations occur.

Anorexia nervosa is a disease that causes low body weight and is characterized by endocrine abnormalities, altered adipocyte function, and appetite-regulating hormone levels [4]. Obesity, which has become a global public health problem caused by the same systemic pathways and affects many people around the world, is characterized by increasing body weight. While obesity reduces the quality of life, it also paves the way for the formation of many diseases such as diabetes and hypertension [5].

Investigating the physiological mechanisms operating in the modulating of appetite and body weight aimed to shed light on the treatments of these emerging diseases. Recently, knowledge about energy homeostasis has increased. The discovery of peptides that take a role in the transmission of the body's energy needs to the brain, and the illumination of the brain areas involved in the processing of these signals have been noted as important advances [6]. Our aim in this review is to give information about the central and peripheral functioning of these mechanisms in appetite control.

---

* Corresponding Author: kuubratan@gmail.com

2. Central Regulation of Appetite Control

The hypothalamus, an important brain area in regulating homeostasis, plays an important role in appetite control [7]. In the hypothalamus, afferent signals from the intestine and brain stem are used, and efferent signals are generated to regulate nutrition. The arcuate nucleus (ARC), paraventricular nucleus (PVN), dorsomedial nucleus (DMN), ventromedial nucleus (VMN), and lateral hypothalamic area (LHA) located in the hypothalamus are responsible for these arrangements [8].

In the models of Hetherington&Ranson [9] and Anand&Brobeck [10], it is suggested that the lateral hypothalamic nucleus is the "feeding center" and the ventromedial nucleus is the "satiety center". In addition to this information, it has recently been thought that the control of energy hemostasis is regulated by neuronal mechanisms that generate signals using specific neuropeptides, rather than hypothalamic nuclei. In particular, the ARC takes a critical role in the integration of appetite regulatory signals [6].

2.1. The Arcuate Nucleus

The arcuate nucleus (ARC), which is an organ rich with capillaries and located above the median superiority, has an important role in appetite control with its location [11]. Perception of hormonal and food metabolic signals is facilitated through the median eminence in the ARC peripheral circulation [12]. Peptide YY (PYY) and glucagon-like peptide 1 (GLP-1) cross the BBB through unsaturated mechanisms while leptin and other signals are actively transported from the blood to the brain through unsaturated reactions [13, 14]. Due to fact that these transition differences, BBB has mediatory actions in the transmission of some peripheral signals.

The ARC consists of two main neurons that regulate nutritional signals and energy balance. These are anorexigenic neurons that regulate proopiomelanocortin (POMC) and cocaine and amphetamine-regulated transcript (CART) and appetite. The other neuron group is orexigenic neurons that stimulate food intake, expressing neuropeptide-Y (NPY) and agouti-related peptide (AgRP) [15, 16]. It is known that POMC and NPY/AgRP neurons in ARC have common features. Both groups of neurons generally have catabolic effects. In their activation, appetite decreases, energy expenditure increases, and accordingly, the amount of body fat gradually decreases. The NPY/AgRP-induced pathway is anabolic and causes more food intake and increased body fat with increased activity [17] (Figure 1).
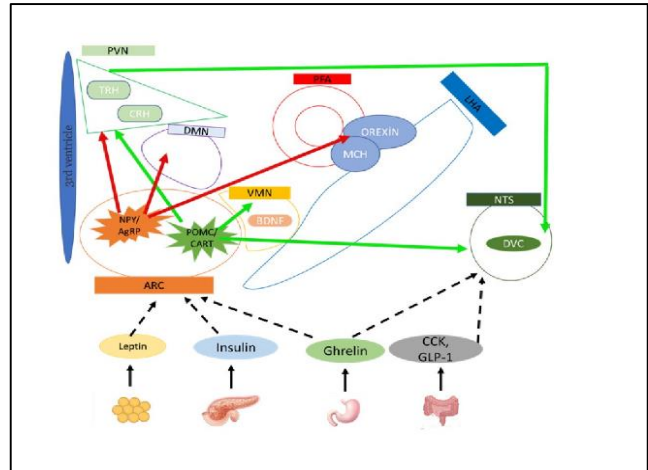
Figure 1. The ARC includes two main neurons, food intake-inhibiting anorexigenic neurons expressing POMC and CART.

2.1.1. Neuropeptide Y

Neuropeptide Y (NPY), the most numerous neurotransmitter in the brain, is part of the pancreatic polypeptide fold peptide family [18]. NPY binds to G-protein-coupled receptors named Y_1 and Y_6 [19]. It is assumed that the orexigenic effect of NPY on nutrition is mediated not by a single receptor, but by the combination of Y_1, Y_2, Y_4 and Y_5 receptors derived in the hypothalamus [8].

The NPY levels are associated with appetite in energy homeostasis. The major hypothalamic site of NPY release is the ARC [20]. While NPY release increases during fasting, it decreases after refeeding [21, 22]. NPY is more widely reflected in the central nervous system (CNS), in the hypothalamic nuclei such as the dorsomedial hypothalamus (DMH), LHA and perifornic area (PFA), and especially in the PVN [23, 24], NPY exerts its effect in appetite control by locally releasing GABA and increasing food intake by inhibiting the neighboring POMC neuron group [25]. Another effect of NPY increases the stimulation of hypothalamic Y1 and Y5, and AgRP exerts a selective antagonist effect on Melanocortin 3 (MC3R) and Melanocortin 4 (MC4R) in PVN [26]. Khrashes and coworkers (2013) found that after acute stimulation of AgRP neurons, NPY is required for rapid stimulation of feeding and, through action on MC4 receptors, the neuropeptide AgRP is sufficient to induce feeding over a delayed but prolonged period. [27].

Other studies on NPY have shown that the central application of NPY inhibits energy consumption, reduces brown fat thermogenesis [28], and suppresses sympathetic nerve activity [29]. It has also been shown to NPY is involved in the control of glucose homeostasis, and an increase in the basal plasma insulin level and especially in

the morning cortisol level, regardless of increased food intake [30].

2.1.2. Proopiomelanocortin

Proopiomelanocortin (POMC) molecule is one of the major molecules for appetite control. The amount of POMC regulation reflects the energy state of the organism [21]. Arcuate POMC neurons play a role in the regulation of energy and glucose homeostasis by sending signals to neurons located in the PVN, DMH, lateral hypothalamus (LH) and ventromedial hypothalamus (VMH) area. [31-33]. This arrangement in PVN transmits the received signal to the extrahypothalamic multiple neural networks. In this way, it creates a correlative route for energy intake and expenditure [34].

Melanocortin peptides for instance adrenocorticotropic hormone (ACTH) and α-melanocyte-stimulating hormone (α-MSH) are formed by cleavage of POMC and show their effects by binding to G-protein-coupled melanocortin receptors [35]. There are five melanocortin receptors (MC1R-MC5R), but exclusively MC3R and MC4R are transcribed in the brain [36]. MC3R and MC4R receptors are located in the hypothalamic nuclei involved in energy regulation [37].

POMC neurons are believed to suppress appetite by secreting α-MSH, an agonist of MC4Rs. In the study of Fan and coworkers (1997) with rodents, it was shown that MC4R deficiency takes a role in hyperphagia and obesity [38]. In a different study, polymorphism of this receptor was also associated with polygenic late-onset obesity in humans [39]. Most research is concerned with the regulation of α-MSH in the absence of β-MSH. However, it is supported that β-MSH acts in the regulation of energy homeostasis in humans by demonstrating those human mutations that diminish the ability of b-MSH to bind to and activate MC4R can lead to obesity [40, 41].

2.1.3. Cocaine and Amphetamine-Regulated Transcript

Cocaine and amphetamine-regulated transcript (CART) is one of the most known neuronal peptides in the hypothalamus. It is characterized in ARC, LHA and PVN [42, 43]. Many of the neurons that regulate POMC also co-regulate CART mRNA. In the fasting state, CART transcription is reduced.

In a study on starving animals, it decreases in CART mRNA was observed in the ARC while peripheral leptin administration to leptin-knock out *ob/ob* mice increased CART mRNA expression [44]. In other studies, it was observed that ICV application of CART caused a decrease

in food intake [45, 46] and this application increased the CART anti-serum [44]. In contrast to these studies, it was observed that streptozotocin-diabetic rats increased their appetite for feeding after CART injection into the hypothalamic nuclei [47]. As a result of this study, it was thought that CART might have an orexigenic or anorexigenic effect in relation to the triggered neural plexus. It is also hypothesized that there may be many CART-regulating neurons in the nutritional role of CART [48].

And orexigenic neurons expressing food intake-inducing NPY and AgRP. POMC and NPY/AgRP neurons in the ARC underlie pathways that project to other hypothalamic and brain areas. These two paths often occur in parallel. The POMC-derived pathway (indicated by the green arrow) has a general catabolic effect, when active food intake decreases, energy expenditure increases, and body fat is lost if prolonged. The NPY/AgRP-derived pathway (indicated by the red arrow) is anabolic, resulting in increased food intake and increased body fat with increased activity.

2.2. Paraventricular Nucleus

The Paraventricular nucleus (PVN) in the anterior hypothalamus is the main site where corticotropin-releasing hormone (CRH) and thyroid-releasing hormone (TRH) are synthesized. There are many neural pathways involved in energy stability in the PVN [49]. The PVN is responsible for integrating neuropeptide signals from multiple CNS areas, including the ARC and brainstem. PVN is sensible to many neuropeptides included in the diet, such as cholecystokinin (CCK) [50], NPY [51], ghrelin [52], orexin-A [53], leptin [54], and GLP-1 [54]. Potent inhibition of food intake can be achieved by direct administration of a melanocortin antagonist to the PVN [55], while inhibiting the orexigenic effect of NPY administration [56]. According to electrophysiological recordings obtained from PVN neurons, it was stated that neurons expressing NPY/AgRP decreased the inhibitory GABA-ergic signal and thus stimulated food intake while POMC neurons strengthened the GABAergic signal and reduced food intake [57].

Recent studies emphasize that neuropeptides involved in appetite control might signal through a general pathway in PVN containing AMP-activated protein kinase (AMPK). Studies have shown that 2-AMPK activity in ARC and PVN can be reduced by multiple anorectic signals (such as leptin, insulin and melanocortin agonist MT-II) while 2-AMPK activity can be increased by orexigenic signals such as AgRP and ghrelin [58]. In addition, Minokoshi and colleagues (2004) suggested that peripheral hunger mediators cannot modulate 2-AMPK activity in MC4R-deficient mice and that 2-AMPK activation might be

controlled by MC4R [59].

Co-regulation of signals in the PVN plays a role in initiating changes in other neuroendocrine systems. For instance, it also affects endocrine function, such as thyroid function and therefore energy expenditure. NPY/AgRP and melanocortin released from the ARC end in thyrotropin-releasing hormone (TRH) neurons in the PVN [60]. While pro-TRH gene expression is inhibited by NPY/AgRP [61], pro-TRH expression is stimulated by α-MSH [62]. PVN also contains neurons that express CRH. The regulation of CRH, which plays a role in energy balance, is controlled by NPY signals from the ARC [63].

2.3. Dorsomedial Nucleus

The dorsomedial nucleus (DMN) is involved in energy regulation. It is known that the DMN has strong connections with the hypothalamic nuclei, especially the ARC [25]. The DMN has NPY and α-MSH endpoints and cells expressing NPY [64]. α-MSH fibers from the DMN are projected to TRH-containing neurons in the PVN [65]. In studies examining the effects of orexigenic peptides on DMN, it has been observed that NPY, galanin and GABA increase food intake when injected into the DMN [66-68]. Loss of DMN results in hyperphagia and obesity [69].

2.4. Lateral Hypothalamic Area/Perifornical Area

The lateral hypothalamic area and the perifornical area (LHA/PFA) responsible for feeding control are involved in second-order signaling. This area is where melanin-concentrating hormone (MCH) is expressed [70]. MCH mRNA level increases in fasting state, it has been proven that repeated MCH administrations increase food intake, leading to obesity [71]. Conversely, when MCH-1 receptor antagonists are administered, nutrition is reduced, as a result of a reduction in body weight [72]. In studies on mice, it was shown that the defect in the MCH gene, despite POMC and circulating leptin, increased energy expenditure and decreased hypophagia and body weights in mice [70, 73]. It has also been revealed that the perifornical area is more sensitive to feeding stimuli by NPY than PVN [74].

2.4.1. Orexin

Orexin is produced by neurons in the LHA/PFA area and zona incerta. These synthesized products are prepro-orexin peptide products called orexin A and B or hypocretin 1-2 [75, 76]. Orexin neurons exert their effects in large areas, including the dorsal motor nuclei of the vagus and PVN, ARC, nucleus tractus solitarius (NTS) [77]. The affinity of orexin A and B varies according to different hypothalamic areas. For example, the orexin-1 receptor is regulated in VMN and has a higher connection for orexin-A than for orexin B [76].

Although prepro-orexin and mRNA levels were observed to increase in the fasting state, it was determined that prepro-orexin application acted centrally with both orexigenic and general stimulation [78]. In starvation states, orexin neuropeptides can regulate a stimulation response and a feeding response to begin foraging behavior simultaneously.

The effects of MCH and orexin on energy balance have not been fully elucidated. However, strong effects of central use of orexin-A on vagal gastric acid secretion and appetite have been identified [79]. Also, Orexin is thought to function like a peripheral hormone in energy balance. It has been described that orexin and leptin receptors activated during fasting are regulated by orexin [80]. Glucose-sensing neurons in the LHA allow peripheral signals to interact [81]. Supporting this idea, some studies have shown that orexin neurons take a part in sensing glucose levels and have shown increased orexin mRNA levels [82, 83]. Additionally, peripherally administered orexin has been observed to increase blood insulin levels [84].

2.4.2. Ventromedial Nucleus

It has been known for years that the ventromedial nucleus (VMH) takes an active role in energy homeostasis. In response to projections that VMN receives from immunoreactive neurons such as arcuate NPY, AgRP, and POMC, VMN neurons signals to other hypothalamic nuclei and brainstem areas such as NTS. Studies on the food intake control of VMN show that brain-derived neurotrophic factor (BDNF) is extremely expressed in VMH [85]. A decrease in the levels of BDNF in the brain generates uncontrolled appetite while the administration of BDNF to the CNS has been found to cause weight loss in animals. In addition, BDNF is involved in the regulation of appetite, along with the co-regulation of other factors such as leptin, insulin, cholecystokinin or corticotropin. In addition, BDNF is involved in the regulation of appetite, along with the co-regulation of other factors such as leptin, insulin, cholecystokinin or corticotropin [86]. However, BDNF also affects glucose metabolism [87].

Appetite Control of the Brainstem

The brain stem has a critical role in appetite control. It regulates energy homeostasis by establishing connections with the hypothalamus [88, 89]. The dorsal vagal complex (DVC), placed in the brainstem, is very important in the

transmission and interpretation of signals from the periphery to the hypothalamus. The DVC dwells in the dorsal motor nucleus of the vagus, the postrema area, and the NTS with POMC neurons [90].

NTS has an incomplete BBB, so it easily responds to signals from the peripheral circulation, such as ARC, and to vagal afferents from the gastrointestinal system [91]. NTS includes NPY, melanocortin and GLP-1 neuronal circuits. NTS has sites where NPY binds to it, rich in Y_1 and Y_5 receptors [92]. With feeding, changes occur in extracellular NPY concentrations in the NTS, and NPY neurons are transmitted from this area to the PVN [93]. In NTS, MSH is synthesized from POMC neurons as a result of feeding and peripheral CCK administration [38]. Also, MC4R is available on NTS [37]. Regulation of an MC3R/MC4R agonist reduces food absorption while MC3R/MC4R antagonists increase it [94]. GLP-1 forms the main brainstem circuitry that regulates energy balance. GLP-1 is regulated particularly in the NTS located in the CNS, and by the mechanism it is also responsible for the expression of leptin receptors in preproglucagon neurons. GLP-1 immunoreactive neurons are then broadly projected, but less specific to the PVN and DMN, the ARC (Table 1) [95].

Table 1. Central and peripheral appetite-related hormones and peptides

Hormone	Site of secretion	Major receptors
Leptin	Adipocyte	LEPR
Adiponectin	Adipocyte,	AdipoR1
	Skeletal muscle,	AdipoR2
	endothelial cells,	T-cadherin
	cardiomyocytes	
Resistin	Adipocyte	Unkown
Insulin	Pancreas beta cells	Insulin
Amylin	Pancreatic beta cells	AMY_{1-3}
Pancreatic polypeptit	Pancreatic PP cells	Y_4
Peptide YY (PYY)	Gastrointestinal L cells	Y_2
Ghrelin	Gastric fundal A cells	GSH-R
Glucagon-like peptide-1 (GLP-1)	Gastrointestinal L cells	GLP-1
Oxyntomodulin	Gastrointestinal L cells	GLP-1
Cholecystokinin	Intestinal cells	CCK-2

3. Peripheral Regulation of Appetite

Gut as known as the largest endocrine organ in the body is responsible for the secretion of over 30 different regulatory hormones. These hormones which interact with receptors are stimulated by gut nutrients at individual areas in the "gut-brain axis" which leads to affect hunger and appetite (Figure 2) [96].
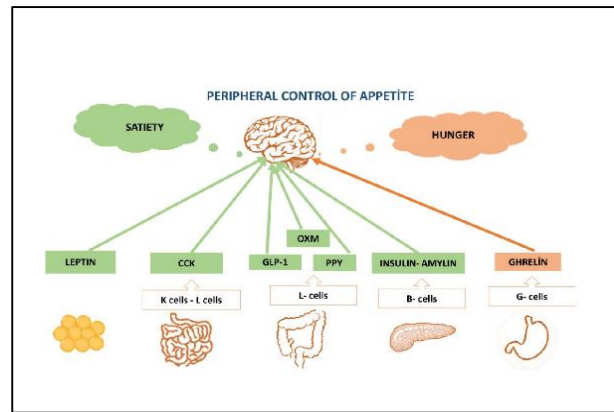
Figure 2. Demonstration of hormonal control of appetite

3.1. Leptin

Leptin is a peptide hormone and it- is originated from the *ob* gene. This hormone, which takes a part in energy balance, is specifically secreted from the adipose tissue [97]. The expression of leptin is greater in the subcutaneous than in body fat. Its concentration is parallel with the total body fat. The secretion of leptin is diminished all along with fasting and increased after feeding. The level of leptin is changed by several metabolic and hormonal factors [98].

Exogenous leptin restoration both centrally and peripherally decreases fast-induced hyperphagia [99]. Halaas and colleagues showed that with wild-type rodents, constant peripheral control of leptin diminished appetite, a deficit of body weight and fat mass [100].

Other studies, in rodents and humans, have shown that curative application of leptin can be used to correct starvation-induced changes in neuroendocrine axes [99, 101]. Hence, when the body's energy stores decrease, the response can be regulated by the leptin signal [8].

Leptin is known as a thruput of the *ob* gene that is transcribed in adipocytes [102]. However, it is expressed in the gastric epithelium [103] and placenta with low levels [104]. Leptin signals through the cytokine receptor family [105]. Through the Alternative mRNA splicing and post-translational operation, occurs multiple isoforms of the leptin receptor [106, 107]. These receptor variants could be grouped into three forms: long, short, and secreted forms [107, 108]. Long form is called Ob-Rb, and it is transcribed in the hypothalamus. However, it is located especially in the ARC, VMH and DMH, LHA and MPOA [109-111].

Pathways in the brain stem including appetite mechanisms are expressed Ob-Rb [112]. In this pathway, the domain of Ob-Rb binds to JAK-kinases [113] and to STAT. These interactions affect signal transmission and appetite mechanisms [107, 113, 114]. The expression of cytokine signalling-3 (SOCS-3)'s suppressor is induced by the JACK/STAT pathway. An *in vitro* study showed that

leptin activity blocks via reporter gene with overexpression of SOCS-3. It has been hypothesized that this re-moddelling experiment obesity-related leptin resistance and related be an outcome of boosted or enormous SOCS-3 expression. This theory lead Mori and colleagues (2004) conducted that neuronspecific depending on deletion of SOCS-3 in mice leads to in stand to diet-induced obesity. [115].This result shows, in deficiency circulating leptin is related to *ob* gene mutation [100, 116, 117].

Circulating leptin crosses the BBB [118]. It has been thought that the shorter forms take part in this leptin transportation [119]. The release of this form regulates the biological activity of circulating leptin [108].

3.2. Adiponectin and Resistin

Adiponectin, also known as adipocyte complement-related protein (Acrp30), apM1 or adipoQ, is a 244-amino acid protein released from adipose tissue [6]. Its plasma levels are higher than other circulating hormones [119].

The activity of adiponectin is essentially unexplained, but it is assumed to regulate energy balance [120]. Studies have suggested that adiponectin may contribute to insulin resistance and increase the sensitivity of peripheral tissues to insulin [121]. Additionally, Yang and colleagues (2001) conducted that adiponectin level is significantly increased after gastric partition surgery in corpulent humans [122]. The other study shows that plasma adiponectin levels in humans have been shown to be negatively correlated with body weight, body fat mass, and insulin resistance, and an increase in plasma adiponectin concentrations has been shown to occur with weight reduction in obese individuals [123]. It has also been proven by studies that the administration of recombinant adiponectin to rodents increases glucose uptake and fat oxidation in muscles and decreases hepatic glucose production [124, 125,126]. Nawrocki and colleagues (2006) in this study, it was shown that insulin resistance and glucose intolerance were observed in mice with adiponectin deficiency [127].

3.3. Amylin and Insulin

Insulin is known as a primary metabolic hormone. It is reproduced by the pancreas β-cells. This hormone is the primary adiposity signal to be defined [128]. Plasma insulin levels rest on peripheral insulin sensitivity [129]. Likewise leptin, plasma insulin level alters directly with changes in adiposity [130]. The changes in peripheral insulin levels can be interpreted by the brain as a reflection of the current level of adiposity [131].

Insulin acts as if anorectic signal in CNS. It varies the expression of some hypothalamic genes. This gene leads to

the regulation of food absorption [132]. By receptor-mediated process assistance, the insulin reach the blood-brain barrier (BBB) [133]. The latest findings showed that the brain itself also produces very small amounts of insulin [134, 135]. As soon as insulin arrives in the brain, it shows as an anorexigenic signal. This signal plays a role in reducing the amount of its uptake and body weight.

Insulin is the primary modulator of an important hypothalamic circuit extending from the ARC to the PVN and is involved in the regulation of food intake and satiety [136]. Insulin receptors are expressed in the paraventricular nucleus (PVN), dorsomedial hypothalamus (DMH), and ARC and inhibit food intake through intracerebral or hypothalamic insulin administration, suppression of NPY/AgRp neurons, and activation of POMC/CART neurons [137].

3.4. Pancreatic Polypeptide

Pancreatic polypeptide (PP) is a member of the PP-fold family of peptides. It originates from the pancreas. Its expression is usually regulated along with food intake [36].

In the islets of Langerhans cells is produced PP. But also it is produced in the exocrine pancreas and distal gastrointestinal tract. Pancreatic polypeptide increases the feeling of satiety, suppresses appetite, delays gastric emptying, inhibits gallbladder movement, and plays an important role in weight loss and energy expenditure [138]. PP release occurs at a low rate in the fasted state and increases markedly during all stages of digestion. However, some other regulatory hormones such as gastric bloat or ghrelin and secretin [139 –142] lower PP levels [143]. It is also known that circulating PP cannot cross the BBB [144]. Studies suggest that peripheral control of PP reduces food absorption and energy expenditure [140]. However, studies with rodents have shown that obese rodents have less susceptibility than normal-weight rodents [145].

3.5. Peptide Tyrosine Tyrosine

The peptide tyrosine tyrosine (PYY) is a member of the PP family [146]. PYY is released from the L cells of the GI [147, 148]. PYY mainly has a the role in calorie intake [147]. Besides, PYY levels in plasma are increased rapidly after food absorption before the supplements are coined the distal intestinal L cells. It is thought that this mechanism, this sudden contact between nutrients and cells, may be the result of a neural reflex of PYY release [149].

There are two known forms of PYY, which are released by the L cells of the distal intestine $PYY_{(1-36)}$ and $PYY_{(3-36)}$. It is known that among these forms, $PYY_{(1-36)}$ has a very high closeness to the Y_2 receptor, which is a

presynaptic auto-inhibitor. Therefore, it is known as a peripherally active and very strong anorectic signal. In addition to this information, there is not enough information about the plasma amounts of PYY$_{(1-36)}$ and PYY$_{(3-36)}$ after fasting and food absorption.

Studies have shown that some stomach functions (such as pancreatic and gastric secretions delay, and gastric emptying) are disrupted or delayed with PYY application. Dysfunctions in these mechanisms have led to increased intake of fluid and electrolytes from the ileum [147, 150-152]. Peripheral application of PYY$_{(3-36)}$ has been demonstrated to prevent appetite and reduce weight gain [153, 154], and studies with rodent models of diabetes prove that glycemic control is regulated and improved [155]. In addition, it is known that PYY, unlike PP, can cross the BBB by transmembrane diffusion [156]. Studies suggest that peripheral application of PYY$_{(3-36)}$ acts as an anorectic signal, and this signal is mediated by the presynaptic inhibitory Y2 receptor on arcuate NPY neurons [157]. In addition, PYY inhibits NPY neurons with negative feedback, [153] and this inhibition reduces NPY mRNA expression [153, 154].

3.6. Ghrelin

Ghrelin is an orexigenic factor and it is secreted mainly from the oxyntic cells of the stomach. Additionally, it is released from the duodenum, ileum, caecum and colon [158, 159]. Before food intake, ghrelin levels are increased and fall after meals. As a consequence that ghrelin is known as a 'hunger' hormone responsible for food intake. With this mechanism of ghrelin, which helps to reduce the use of fat and indirectly regulates food intake, it helps to regulate body weight in the long term [160].

Murakami and colleagues (2002) demonstrated that in rats, ghrelin has the highest level at the end of the light and dark periods [161]. Growth hormone secretagogue receptor 1a (GHS-R1a) helps regulate the effect of ghrelin on appetite. This receptor is highly expressed in cells where appetite and body homeostasis are regulated. The lack of orexigenic effects of ghrelin in GHS-R knockout mice confirms this theory [162].

Ghrelin acts orexigenically and helps regulate AgRP/NPY neurons in the ARC. Generally, ghrelin is synthesized peripherally, but it is known to be expressed centrally as well. Ghrelin neurons are located between DMN, VMH, PVN and ARC [163].

Further, it is known that hypothalamic ghrelin neurons end in the LHA on neurons expressing orexin [164]. Neurons are responsible for expressing orexin stimulated by central ghrelin administration [164]. However, the physiological roles of ghrelin are not fully understood.

3.7. Glucagon-like Peptides and Oxyntomodulin

Proglucagon is generally secreted in L cells of the intestine, pancreas and central nervous system. It is also known that the neuron group in NTS secretes pre-proglucagon [165].

Different products emerge with the tissue-specific degradation of proglucagon by prohormone convertase 1 and 2 enzymes [166]. For instance in the pancreas, the primary product of proglucagon is glucagon while in the brain and intestine, oxyntomodulin (OXM) and glucagon-like peptide (GLP) GLP-1 and GLP-2 are the primary products. The product released into the circulation after food intake is GLP-1. With the expression of GLP-1, the secretion of pancreatic insulin is positively regulated. This mechanism physically regulates glucose homeostasis by acting as incretin [167].

On the other hand, OXM is released by L cells with food intake [168, 169]. Studies in rodents show that OXM acutely inhibits food absorption, regardless of central or peripheral administration [170]. This mechanism is thought to play a role in reducing body weight and adiposity [171, 172].

3.8. Cholecystokinin

Cholecystokinin (CCK) is transmitted commonly in the gastrointestinal system [173]. However, it is also known to be found in the duodenum and jejunum. There are numerous known bioactive forms of cholecystokinin. These forms can be listed as CCK-58, CCK-33 and CCK-8 [174]. CCK is rapidly released locally and into the circulation in response to nutrients, the release of CCK into the bloodstream acts on CCK receptors, causing slowing gastric emptying and increasing the feeling of fullness [175]. In addition to hunger-satiety processes, CCK functions as a neurotransmitter in various mechanisms such as reward behavior, memory loss, and anxiety [176].

CCK takes a role with the G protein-coupled receptors CCKA and CCKB receptors [177]. These receptors are known to be found in every region of the brain. CCKA receptors are generally localized in pancreatic, vagal afferent and enteric neurons while CCKB receptors are afferent in the vagus nerve and stomach [177-179].

4. Conclusion

The appetite mechanisms are a complex process that occurs when central and peripheral controls work separately and/or together. Although the studies have not been able to fully elucidate all the mechanisms, it helps in determining

the effects of food intake on physiological and biochemical processes and for further studies.

Declaration of Ethical Standards

The author of this article declares that the materials and methods used in this study do not require ethical committee permission and/or legal-special permission.

Conflict of Interest

The authors declare that they have no known competing financial interests or personal relationships that could have appeared to influence the work reported in this paper.

References

[1] Fromentin G., Darcel N., Chaumontet C., Marsset-Baglieri A., Nadkarni N., Tomé D., 2012. Peripheral and central mechanisms involved in the control of food intake by dietary amino acids and proteins. Nutrition Research Reviews, **25**, pp. 29-39.

[2] Sandoval D., Cota D., Seeley R.J., 2008. The integrative role of CNS fuel-sensing mechanisms in energy balance and glucose regulation. Annu Rev Physiol, **70**, pp. 513-535.

[3] Boguszewski C.L., Paz-Filho G., Velloso L.A., 2010. Neuroendocrine body weight regulation: integration between fat tissue, gastrointestinal tract, and the brain. Endokrynologia Polska, **61**, pp. 194-206.

[4] Schorr M., Miller K.K., 2017. The endocrine manifestations of anorexia nervosa: mechanisms and management. Nature Reviews Endocrinology, **13**, pp. 174-186.

[5] Goodarzi M.O., 2018. Genetics of obesity: what genetic association studies have taught us about the biology of obesity and its complications. The Lancet Diabetes & Endocrinology, **6**, pp. 223-236.

[6] Stanley S., Wynne K., McGowan B., Bloom S., 2005. Hormonal regulation of food intake. Physiol Rev, **85**, pp. 1131-1158.

[7] Timper K., Brüning J.C., 2017. Hypothalamic circuits regulating appetite and energy homeostasis: pathways to obesity. Dis Model Mech, **10**, pp. 679-689.

[8] Wynne K., Stanley S., McGowan B., Bloom S., 2005. Appetite control. Journal of Endocrinology, **184**, pp. 291-318.

[9] Hetherington A., Ranson S., 1940. Hypothalamic lesions and adiposity in the rat. The Anatomical Record, **78**, pp. 149-172.

[10] Anand B.K., Brobeck J.R., 1951. Localization of a "feeding center" in the hypothalamus of the rat. Proceedings of the Society for Experimental Biology and Medicine, **77**, pp. 323-325.

[11] Rodríguez E.M., Blázquez J.L., Guerra M., 2010. The design of barriers in the hypothalamus allows the median eminence and the arcuate nucleus to enjoy private milieus: the former opens to the portal blood and the latter to the cerebrospinal fluid. Peptides, **31**, pp. 757-776.

[12] Myers M., Olson D., 2012. Central nervous system control of metabolism. Nature, **491**, pp. 357–363.

[13] Kastin A.J., Akerstrom V., Pan W., 2002. Interactions of glucagon-like peptide-1 (GLP-1) with the blood-brain barrier. Journal of Molecular Neuroscience, **18**, pp. 7-14.

[14] Nonaka N., Shioda S., Niehoff M. L., Banks W. A., 2003. Characterization of blood-brain barrier permeability to PYY3-36 in the mouse. Journal of Pharmacology and Experimental Therapeutics, **306(3)**, pp. 948-953.

[15] Gropp E., Shanabrough M., Borok E., Xu A.W., Janoschek R., Buch T., Plum L., Balthasar N., Hampel B., Waisman A., 2005. Agouti-related peptide–expressing neurons are mandatory for feeding. Nature neuroscience, **8**, pp. 1289-1291.

[16] Balthasar N., Dalgaard L.T., Lee C.E., Yu J., Funahashi H., Williams T., Ferreira M., Tang V., McGovern R.A., Kenny C.D., 2005. Divergence of melanocortin pathways in the control of food intake and energy expenditure. Cell, **123**, pp. 493-505.

[17] Woods S.C., Seeley R.J., Cota D., 2008. Regulation of food intake through hypothalamic signaling networks involving mTOR. Annu Rev Nutr, **28**, pp. 295-311.

[18] McConn B. R., Gilbert, E. R., Cline, M. A., 2018. Appetite-associated responses to central neuropeptide Y injection in quail. Neuropeptides, **69**, pp.9-18.

[19] Lindner D., Stichel, J., Beck-Sickinger A. G., 2008. Molecular recognition of the NPY hormone family by their receptors. Nutrition, **24**, pp. 907-917.

[20] Williams G., Bing C., Cai X. J., Harrold J. A., King P. J., Liu X. H., 2001. The hypothalamus and the control of energy homeostasis: different circuits, different purposes. Physiology & behavior, **74**, pp. 683-701.

[21] Sanacora G., Kershaw M., Finkelstein J.A., White J.D., 1990. Increased hypothalamic content of prepropneuropeptide Y messenger ribonucleic acid in genetically obese Zucker rats and its regulation by food deprivation. Endocrinology, **127**, pp. 730-737.

[22] Swart I., Jahng J., Overton J., Houpt T., 2002. Hypothalamic NPY, AGRP, and POMC mRNA responses to leptin and refeeding in mice. American Journal of Physiology-Regulatory, Integrative and Comparative Physiology, **283**, pp. R1020-R1026.

[23] Benarroch E. E., 2009. Neuropeptide Y: its multiple effects in the CNS and potential clinical significance. Neurology, **72**, pp. 1016-1020.

[24] Gonçalves J., Martins J., Baptista S., Ambrósio A. F., Silva A. P., 2016. Effects of drugs of abuse on the central neuropeptide Y system. Addiction Biology, **21**, pp.755-765.

[25] Kalra S. P., Kalra P. S., 2004. NPY—an endearing journey in search of a neurochemical on/off switch for appetite, sex and reproduction. Peptides, **25**, pp. 465-471.

[26] Suzuki K., Simpson K.A., Minnion J.S., Shillito J.C., Bloom S.R., 2010. The role of gut hormones and the hypothalamus in appetite regulation. Endocrine Journal, **57**, pp. 359-372.

[27] Krashes M. J., Shah B. P., Koda S., Lowell B. B., 2013. Rapid versus delayed stimulation of feeding by the endogenously released AgRP neuron mediators GABA, NPY, and AgRP. Cell metabolism, **18**, pp. 588-595.

[28] Billington C., Briggs J., Grace M., Levine A., 1991. Effects of intracerebroventricular injection of neuropeptide Y on energy metabolism. American Journal of Physiology-Regulatory, Integrative and Comparative Physiology, **260**, pp. R321-R327.

[29] Egawa M., Yoshimatsu H., Bray G., 1991. Neuropeptide Y suppresses sympathetic activity to interscapular brown adipose tissue in rats. American Journal of Physiology-Regulatory, Integrative and Comparative Physiology, **260**, pp. R328-R334.

[30] Qi Y., Lee N. J., Ip C. K., Enriquez R., Tasan R., Zhang L., Herzog H. 2022. NPY derived from AGRP neurons controls feeding via Y1 and energy expenditure and food foraging behaviour via Y2 signalling. Molecular Metabolism, **59**, pp. 101455.

[31] Mercer A.J., Hentges S.T., Meshul C.K., Low M.J., 2013. Unraveling the central proopiomelanocortin neural circuits. Frontiers in neuroscience, **7**, pp. 19.

[32] Kleinridders A., Könner A.C., Brüning J.C., 2009. CNS-targets in control of energy and glucose homeostasis. Current opinion in pharmacology, **9**, pp. 794-804.

[33] Waterson M.J., Horvath T.L., 2015. Neuronal regulation of energy homeostasis: beyond the hypothalamus and feeding. Cell metabolism, **22**, pp. 962-970.

[34] Roh E., Kim M.-S., 2016. Emerging role of the brain in the homeostatic regulation of energy and glucose metabolism. Experimental & molecular medicine, **48**, pp. e216-e216.

[35] Andermann M. L., Lowell B. B., 2017. Toward a wiring diagram understanding of appetite control. Neuron, **95**, pp.757-778.

[36] Abdalla M.M.I., 2017. Central and peripheral control of food intake. Endocrine Regulations, **51**, pp. 52-70.

[37] Garfield A. S., Li C., Madara J. C., Shah B. P., Webber E., Steger J. S., Lowell B. B. (2015). A neural basis for melanocortin-4 receptor–regulated appetite. Nature neuroscience, **18**, pp. 863-871.

[38] Fan W., Boston B.A., Kesterson R.A., Hruby V.J., Cone R.D., 1997. Role of melanocortinergic neurons in feeding and the agouti obesity syndrome. Nature, **385**, pp. 165-168.

[39] Argyropoulos G., Rankinen T., Neufeld D.R., Rice T., Province M.A., Leon A.S., Skinner J.S., Wilmore J.H., Rao D., Bouchard C., 2002. A polymorphism in the human agouti-related protein is associated with late-onset obesity. The Journal of Clinical Endocrinology & Metabolism, **87**, pp. 4198-4202.

[40] Lee Y.S., Challis B.G., Thompson D.A., Yeo G.S., Keogh J.M., Madonna M.E., Wraight V., Sims M., Vatin V., Meyre D., 2006. A POMC variant implicates β-melanocyte-stimulating hormone in the control of human energy balance. Cell metabolism, **3**, pp. 135-140.

[41] Biebermann H., Castañeda T.R., van Landeghem F., von Deimling A., Escher F., Brabant G., Hebebrand J., Hinney A., Tschöp M.H., Grüters A., 2006. A role for β-melanocyte-stimulating hormone in human body-weight regulation. Cell metabolism, **3**, pp. 141-146.

[42] Elias C.F., Lee C., Kelly J., Aschkenasi C., Ahima R.S., Couceyro P.R., Kuhar M.J., Saper C.B., Elmquist J.K., 1998. Leptin activates hypothalamic CART neurons projecting to the spinal cord. Neuron, **21**, pp. 1375-1385.

[43] Couceyro P.R., Koylu E.O., Kuhar M.J., 1997. Further studies on the anatomical distribution of CART by in situ hybridization. Journal of chemical neuroanatomy, **12**, pp. 229-241.

[44] Kristensen P., Judge M.E., Thim L., Ribel U., Christjansen K.N., Wulff B.S., Clausen J.T., Jensen P.B., Madsen O.D., Vrang N., 1998. Hypothalamic CART is a new anorectic peptide regulated by leptin. Nature, **393**, pp. 72-76.

[45] Aja S., Sahandy S., Ladenheim E.E., Schwartz G.J., Moran T.H., 2001. Intracerebroventricular CART peptide reduces food intake and alters motor behavior at a hindbrain site. American Journal of Physiology-Regulatory, Integrative and Comparative Physiology, **281**, pp. R1862-R1867.

[46] Rohner-Jeanrenaud F., Craft L., Bridwell J., Suter T., Tinsley F., Smiley D., Burkhart D., Statnick M., Heiman M., Ravussin E., 2002. Chronic central infusion of cocaine-and amphetamine-regulated transcript (CART 55-102): effects on body weight homeostasis in lean and high-fat-fed obese rats. International Journal of Obesity, **26**, pp. 143-149.

[47] Hou J., Zheng D.Z., Zhou J.Y., Zhou S.W., 2010. Orexigenic effect of cocaine-and amphetamine-regulated transcript (CART) after injection into hypothalamic nuclei in streptozotocin-diabetic rats. Clinical and Experimental Pharmacology and Physiology, **37**, pp. 989-995.

[48] Dhillo W., Small C., Stanley S., Jethwa P., Seal L., Murphy K., Ghatei M., Bloom S., 2002. Hypothalamic interactions between neuropeptide Y, agouti-related protein, cocaine-and amphetamine-regulated transcript and alpha-melanocyte-stimulating hormone in vitro in male rats. Journal of neuroendocrinology, **14**, pp. 725-730.

[49] Neary N.M., Goldstone A.P., Bloom S.R., 2004. Appetite regulation: from the gut to the hypothalamus. Clinical endocrinology, **60**, pp. 153-160.

[50] Hamamura M., Leng G., Emson P., Kiyama H., 1991. Electrical activation and c-fos mRNA expression in rat neurosecretory neurones after systemic administration of cholecystokinin. The Journal of physiology, **444**, pp. 51-63.

[51] Lambert P., Phillips P., Wilding J., Bloom S., Herbert J., 1995. c-fos expression in the paraventricular nucleus of the hypothalamus following intracerebroventricular infusions of neuropeptide Y. Brain research, **670**, pp. 59-65.

[52] Lawrence C.B., Snape A.C., Baudoin F.M.-H., Luckman S.M., 2002. Acute central ghrelin and GH secretagogues induce feeding and activate brain appetite centers. Endocrinology, **143**, pp. 155-162.

[53] Edwards C., Abusnana S., Sunter D., Murphy K., Ghatei M., Bloom S., 1999. The effect of the orexins on food intake: comparison with neuropeptide Y, melanin-concentrating hormone and galanin. Journal of Endocrinology, **160**, pp. R7.

[54] Van Dijk G., Thiele T.E., Donahey J., Campfield L.A., Smith F.J., Burn P., Bernstein I.L., Woods S.C., Seeley R.J., 1996. Central infusions of leptin and GLP-1-(7-36) amide differentially stimulate c-FLI in the rat brain. American Journal of Physiology-Regulatory, Integrative and Comparative Physiology, **271**, pp. R1096-R1100.

[55] Giraudo S.Q., Billington C.J., Levine A.S., 1998. Feeding effects of hypothalamic injection of melanocortin 4 receptor ligands. Brain research, **809**, pp. 302-306.

[56] Wirth M.M., Olszewski P.K., Yu C., Levine A.S., Giraudo S.Q., 2001. Paraventricular hypothalamic α-melanocyte-stimulating hormone and MTII reduce feeding without causing aversive effects. Peptides, **22**, pp. 129-134.

[57] Cowley M.A., Pronchuk N., Fan W., Dinulescu D.M., Colmers W.F., Cone R.D., 1999. Integration of NPY, AGRP, and melanocortin signals in the hypothalamic paraventricular nucleus: evidence of a cellular basis for the adipostat. Neuron, **24**, pp. 155-163.

[58] Andersson U., Filipsson K., Abbott C.R., Woods A., Smith K., Bloom S.R., Carling D., Small C.J., 2004. AMP-activated protein kinase plays a role in the control of food intake. Journal of Biological Chemistry, **279**, pp. 12005-12008.

[59] Minokoshi Y., Alquier T., Furukawa N., Kim Y.-B., Lee A., Xue B., Mu J., Foufelle F., Ferré P., Birnbaum M.J., 2004. AMP-kinase regulates food intake by responding to hormonal and nutrient signals in the hypothalamus. Nature, **428**, pp. 569-574.

[60] Legradi G., Lechan R.M., 1999. Agouti-related protein containing nerve terminals innervate thyrotropin-releasing hormone neurons in the hypothalamic paraventricular nucleus. Endocrinology, **140**, pp. 3643-3652.

[61] Fekete C., Sarkar S., Rand W.M., Harney J.W., Emerson C.H., Bianco A.C., Lechan R.M., 2002. Agouti-related protein (AGRP) has a central inhibitory action on the hypothalamic-pituitary-thyroid (HPT) axis; comparisons between the effect of AGRP and neuropeptide Y on energy homeostasis and the HPT axis. Endocrinology, **143**, pp. 3846-3853.

[62] Fekete C., Légrádi G., Mihály E., Huang Q.-H., Tatro J.B., Rand W.M., Emerson C.H., Lechan R.M., 2000. α-Melanocyte-stimulating hormone is contained in nerve terminals innervating thyrotropin-releasing hormone-synthesizing neurons in the hypothalamic paraventricular nucleus and prevents fasting-induced suppression of prothyrotropin-releasing hormone gene expression. Journal of Neuroscience, **20**, pp. 1550-1558.

[63] Sarkar S., Lechan R.M., 2003. Central administration of neuropeptide Y reduces α-melanocyte-stimulating hormone-induced cyclic adenosine 5′-monophosphate response element binding protein (CREB) phosphorylation in pro-thyrotropin-releasing hormone neurons and increases CREB phosphorylation in corticotropin-releasing hormone neurons in the hypothalamic paraventricular nucleus. Endocrinology, **144**, pp. 281-291.

[64] Chen P., Williams S.M., Grove K.L., Smith M.S., 2004. Melanocortin 4 receptor-mediated hyperphagia and activation of neuropeptide Y expression in the dorsomedial hypothalamus during lactation. Journal of Neuroscience, **24**, pp. 5091-5100.

[65] Mihály E., Fekete C., Légrádi G., Lechan R.M., 2001. Hypothalamic dorsomedial nucleus neurons innervate thyrotropin-releasing hormone-synthesizing neurons in the paraventricular nucleus. Brain research, **891**, pp. 20-31.

[66] Stanley B.G., Chin A., Leibowitz S.F., 1985. Feeding and drinking elicited by central injection of neuropeptide Y: evidence for a hypothalamic site (s) of action. Brain research bulletin, **14**, pp. 521-524.

[67] Kyrkouli S., Stanley B., Seirafi R., Leibowitz S., 1990. Stimulation of feeding by galanin: anatomical localization and behavioral specificity of this peptide's effects in the brain. Peptides, **11**, pp. 995-1001.

[68] Kelly J., Rothstein J., Grossman S.P., 1979. GABA and hypothalamic feeding systems. I. Topographic analysis of the effects of microinjections of muscimol. Physiology & behavior, **23**, pp. 1123-1134.

[69] Bernardis L.L., Bellinger L.L., 1987. The dorsomedial hypothalamic nucleus revisited: 1986 update. Brain Research Reviews, **12**, pp. 321-381.

[70] Marsh D.J., Weingarth D.T., Novi D.E., Chen H.Y., Trumbauer M.E., Chen A.S., Guan X.-M., Jiang M.M., Feng Y., Camacho R.E., 2002. Melanin-concentrating hormone 1 receptor-deficient mice are lean, hyperactive, and hyperphagic and have altered metabolism. Proceedings of the National Academy of Sciences, **99**, pp. 3240-3245.

[71] Qu D., Ludwig D.S., Gammeltoft S., Piper M., Pelleymounter M.A., Cullen M.J., Mathes W.F., Przypek J., Kanarek R., Maratos-Flier E., 1996. A role for melanin-concentrating hormone in the central regulation of feeding behaviour. Nature, **380**, pp. 243-247.

[72] Borowsky B., Durkin M.M., Ogozalek K., Marzabadi M.R., DeLeon J., Heurich R., Lichtblau H., Shaposhnik Z., Daniewska I., Blackburn T.P., 2002. Antidepressant, anxiolytic and anorectic effects of a melanin-concentrating hormone-1 receptor antagonist. Nature medicine, **8**, pp. 825-830.

[73] Shimada M., Tritos N.A., Lowell B.B., Flier J.S., Maratos-Flier E., 1998. Mice lacking melanin-concentrating hormone are hypophagic and lean. Nature, **396**, pp. 670-674.

[74] Stanley B.G., Magdalin W., Seirafi A., Thomas W.J., Leibowitz S.F., 1993. The perifornical area: the major focus of (a) patchily distributed hypothalamic neuropeptide Y-sensitive feeding system (s). Brain research, **604**, pp. 304-317.

[75] De Lecea L., Kilduff T., Peyron C., Gao X.-B., Foye P., Danielson P., Fukuhara C., Battenberg E., Gautvik V., Bartlett F.n., 1998. The hypocretins: hypothalamus-specific peptides with neuroexcitatory activity. Proceedings of the National Academy of Sciences, **95**, pp. 322-327.

[76] Sakurai T., Amemiya A., Ishii M., Matsuzaki I., Chemelli R.M., Tanaka H., Williams S.C., Richardson J.A., Kozlowski G.P., Wilson S., 1998. Orexins and orexin receptors: a family of hypothalamic neuropeptides and G protein-coupled receptors that regulate feeding behavior. Cell, **92**, pp. 573-585.

[77] Peyron C., Tighe D.K., Van Den Pol A.N., De Lecea L., Heller H.C., Sutcliffe J.G., Kilduff T.S., 1998. Neurons containing hypocretin (orexin) project to multiple neuronal systems. Journal of Neuroscience, **18**, pp. 9996-10015.

[78] Hagan M.M., Rushing P.A., Benoit S.C., Woods S.C., Seeley R.J., 2001. Opioid receptor involvement in the effect of AgRP-(83–132) on food intake and food selection. American Journal of Physiology-Regulatory, Integrative and Comparative Physiology, **280**, pp. R814-R821.

[79] Takahashi N., Okumura T., Yamada H., Kohgo Y., 1999. Stimulation of gastric acid secretion by centrally administered orexin-A in conscious rats. Biochemical and biophysical research communications, **254**, pp. 623-627.

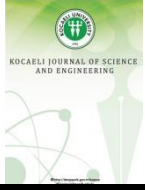[80] Kirchgessner A.L., Liu M.-t., 1999. Orexin synthesis and response in the gut. Neuron, **24**, pp. 941-951.

[81] Bernardis L.L., Bellinger L.L., 1996. The lateral hypothalamic area revisited: ingestive behavior. Neurosci Biobehav Rev, **20**, pp. 189-287.

[82] Moriguchi T., Sakurai T., Nambu T., Yanagisawa M., Goto K., 1999. Neurons containing orexin in the lateral hypothalamic area of the adult rat brain are activated by insulin-induced acute hypoglycemia. Neuroscience letters, **264**, pp. 101-104.

[83] Cai X.J., Widdowson P.S., Harrold J., Wilson S., Buckingham R.E., Arch J., Tadayyon M., Clapham J.C., Wilding J., Williams G., 1999. Hypothalamic orexin expression: modulation by blood glucose and feeding. Diabetes, **48**, pp. 2132-2137.

[84] Nowak K.W., Maćkowiak P., Świtońska M.M., Fabiś M., Malendowicz L.K., 1999. Acute orexin effects on insulin secretion in the rat: in vivo and in vitro studies. Life sciences, **66**, pp. 449-454.

[85] Xu B., Goulding E.H., Zang K., Cepoi D., Cone R.D., Jones K.R., Tecott L.H., Reichardt L.F., 2003. Brain-derived neurotrophic factor regulates energy balance downstream of melanocortin-4 receptor. Nature neuroscience, **6**, pp. 736-742.

[86] Dhillon H., Zigman J.M., Ye C., Lee C.E., McGovern R.A., Tang V., Kenny C.D., Christiansen L.M., White R.D., Edelstein E.A., 2006. Leptin directly activates SF1 neurons in the VMH, and this action by leptin is required for normal body-weight homeostasis. Neuron, **49**, pp. 191-203.

[87] Piotrowicz Z., Chalimoniuk M., Czuba M., Langfort J., 2020. Rola neurotroficznego czynnika pochodzenia mózgowego w kontroli łaknienia. Postępy Biochemii, **66**, pp. 205â 212-205â 212.

[88] Ricardo J.A., Koh E.T., 1978. Anatomical evidence of direct projections from the nucleus of the solitary tract to the hypothalamus, amygdala, and other forebrain structures in the rat. Brain research, **153**, pp. 1-26.

[89] Ter Horst G., De Boer P., Luiten P., Van Willigen J., 1989. Ascending projections from the solitary tract nucleus to the hypothalamus. A Phaseolus vulgaris lectin tracing study in the rat. Neuroscience, **31**, pp. 785-797.

[90] Schwartz G.J., 2010. Brainstem integrative function in the central nervous system control of food intake. Frontiers in Eating and Weight Regulation, **63**, pp. 141-151.

[91] Kalia M., Sullivan J.M., 1982. Brainstem projections of sensory and motor components of the vagus nerve in the rat. Journal of Comparative Neurology, **211**, pp. 248-264.

[92] Härfstrand A., Fuxe K., Agnati L., Benfenati F., Goldstein M., 1986. Receptor autoradiographical evidence for high densities of 125l-neuropeptide Y binding sites in the nucleus tractus solitarius of the normal male rat. Acta physiologica scandinavica, **128**, pp. 195-200.

[93] Sawchenko P., Swanson L., Grzanna R., Howe P., Bloom S., Polak J., 1985. Colocalization of neuropeptide Y immunoreactivity in brainstem catecholaminergic neurons that project to the paraventricular nucleus of the hypothalamus. Journal of Comparative Neurology, **241**, pp. 138-153.

[94] Williams D.L., Kaplan J.M., Grill H.J., 2000. The role of the dorsal vagal complex and the vagus nerve in feeding effects of melanocortin-3/4 receptor stimulation. Endocrinology, **141**, pp. 1332-1337.

[95] Turton M., O'shea D., Gunn I., Beak S., Edwards C., Meeran K., Choi S., Taylor G., Heath M., Lambert P., 1996. A role for glucagon-like peptide-1 in the central regulation of feeding. Nature, **379**, pp. 69-72.

[96] De Silva A., Bloom S.R., 2012. Gut hormones and appetite control: a focus on PYY and GLP-1 as therapeutic targets in obesity. Gut and liver, **6**, pp. 10.

[97] Klok M.D., Jakobsdottir S., Drent M., 2007. The role of leptin and ghrelin in the regulation of food intake and body weight in humans: a review. Obesity reviews, **8**, pp. 21-34.

[98] Friedman J.M., 2004. Modern science versus the stigma of obesity. Nature medicine, **10**, s. 563-569.

[99] Ahima R.S., Prabakaran D., Mantzoros C., Qu D., Lowell B., Maratos-Flier E., Flier J.S., 1996. Role of leptin in the neuroendocrine response to fasting. Nature, **382**, pp. 250-252.

[100] Halaas J.L., Gajiwala K.S., Maffei M., Cohen S.L., Chait B.T., Rabinowitz D., Lallone R.L., Burley S.K., Friedman J.M., 1995. Weight-reducing effects of the plasma protein encoded by the obese gene. Science, **269**, pp. 543-546.

[101] Chan J.L., Heist K., DePaoli A.M., Veldhuis J.D., Mantzoros C.S., 2003. The role of falling leptin levels in the neuroendocrine and metabolic adaptation to short-term starvation in healthy men. The Journal of clinical investigation, **111**, pp. 1409-1421.

[102] Zhang Y., Proenca R., Maffei M., Barone M., Leopold L., Friedman J.M., 1994. Positional cloning of the mouse obese gene and its human homologue. Nature, **372**, pp. 425-432.

[103] Bado A., Levasseur S., Attoub S., Kermorgant S., Laigneau J.-P., Bortoluzzi M.-N., Moizo L., Lehy T., Guerre-Millo M., Le Marchand-Brustel Y., 1998. The stomach is a source of leptin. Nature, **394**, pp. 790-793.

[104] Masuzaki H., Ogawa Y., Sagawa N., Hosoda K., Matsumoto T., Mise H., Nishimura H., Yoshimasa Y., Tanaka I., Mori T., 1997. Nonadipose tissue production of leptin: leptin as a novel placenta-derived hormone in humans. Nature medicine, **3**, pp. 1029-1033.

[105] Tartaglia L.A., Dembski M., Weng X., Deng N., Culpepper J., Devos R., Richards G.J., Campfield L.A., Clark F.T., Deeds J., 1995. Identification and expression cloning of a leptin receptor, OB-R. Cell, **83**, pp. 1263-1271.

[106] Chua Jr S.C., Koutras I.K., Han L., Liu S.-M., Kay J., Young S.J., Chung W.K., Leibel R.L., 1997. Fine structure of the murine leptin receptor gene: splice site suppression is required to form two alternatively spliced transcripts. Genomics, **45**, pp. 264-270.

[107] Tartaglia L.A., 1997. The leptin receptor. Journal of Biological Chemistry, **272**, pp. 6093-6096.

[108] Ge H., Huang L., Pourbahrami T., Li C., 2002. Generation of soluble leptin receptor by ectodomain shedding of membrane-spanning receptors in vitro and in vivo. Journal of Biological Chemistry, **277**, pp. 45898-45903.

[109] Elmquist J.K., Bjørbæk C., Ahima R.S., Flier J.S., Saper C.B., 1998. Distributions of leptin receptor mRNA isoforms in the rat brain. Journal of Comparative Neurology, **395**, pp. 535-547.

[110] Fei H., Okano H.J., Li C., Lee G.-H., Zhao C., Darnell R., Friedman J.M., 1997. Anatomic localization of alternatively spliced leptin receptors (Ob-R) in mouse brain and other tissues. Proceedings of the National Academy of Sciences, **94**, pp. 7001-7005.

[111] Håkansson M.-L., Brown H., Ghilardi N., Skoda R.C., Meister B., 1998. Leptin receptor immunoreactivity in chemically defined target neurons of the hypothalamus. Journal of Neuroscience, **18**, pp. 559-572.

[112] Mercer J.G., Moar K.M., Hoggard N., 1998. Localization of leptin receptor (Ob-R) messenger ribonucleic acid in the rodent hindbrain. Endocrinology, **139**, pp. 29-34.

[113] Lee G.-H., Proenca R., Montez J., Carroll K., Darvishzadeh J., Lee J., Friedman J., 1996. Abnormal splicing of the leptin receptor in diabetic mice. Nature, **379**, pp. 632-635.

[114] Vaisse C., Halaas J.L., Horvath C.M., Darnell J.E., Stoffel M., Friedman J.M., 1996. Leptin activation of Stat3 in the hypothalamus of wild–type and ob/ob mice but not db/db mice. Nature genetics, **14**, pp. 95-97.

[115] Mori H., Hanada R., Hanada T., Aki D., Mashima R., Nishinakamura H., Torisu T., Chien K.R., Yasukawa H., Yoshimura A., 2004. Socs3 deficiency in the brain elevates leptin sensitivity and confers resistance to diet-induced obesity. Nature medicine, **10**, pp. 739-743.

[116] Pelleymounter M.A., Cullen M.J., Baker M.B., Hecht R., Winters D., Boone T., Collins F., 1995. Effects of the obese gene product on body weight regulation in ob/ob mice. Science, **269**, pp. 540-543.

[117] Campfield L.A., Smith F.J., Guisez Y., Devos R., Burn P., 1995. Recombinant mouse OB protein: evidence for a peripheral signal linking adiposity and central neural networks. Science, **269**, pp. 546-549.

[118] Banks W.A., Kastin A.J., Huang W., Jaspan J.B., Maness L.M., 1996. Leptin enters the brain by a saturable system independent of insulin. Peptides, **17**, pp. 305-311.

[119] Tsao T.S., Lodish H.F., Fruebis J., 2002. ACRP30, a new hormone controlling fat and glucose metabolism. Eur J Pharmacol, **440**, pp. 213-221.

[120] Scherer P.E., Williams S., Fogliano M., Baldini G., Lodish H.F., 1995. A novel serum protein similar to C1q, produced exclusively in adipocytes. Journal of Biological Chemistry, **270**, pp. 26746-26749.

[121] Scherer P. E., 2006. Adipose tissue: from lipid storage compartment to endocrine organ. Diabetes, **55,** pp. 1537-1545.

[122] Yang W.-S., Lee W.-J., Funahashi T., Tanaka S., Matsuzawa Y., Chao C.-L., Chen C.-L., Tai T.-Y., Chuang L.-M., 2001. Weight reduction increases plasma levels of an adipose-derived anti-inflammatory protein, adiponectin. The Journal of Clinical Endocrinology & Metabolism, **86**, pp. 3815-3819.

[123] Kadowaki, T., Yamauchi, T., Kubota, N., Hara, K., Ueki, K., Tobe, K., 2006. Adiponectin and adiponectin receptors in insulin resistance, diabetes, and the metabolic syndrome. The Journal of clinical investigation, **116**, pp. 1784-1792.

[124] Berg A. H., Combs T. P., Du X., Brownlee M., Scherer P. E., 2001. The adipocyte-secreted protein Acrp30 enhances hepatic insulin action. Nature medicine, **7**, pp. 947-953.

[125] Yamauchi T., Kamon J., Waki H., Terauchi Y., Kubota N., Hara K., Kadowaki T., 2001. The fat-derived hormone adiponectin reverses insulin resistance associated with both lipoatrophy and obesity. Nature medicine, **7**, pp. 941-946.

[126] Fruebis J., Tsao T. S., Javorschi S., Ebbets-Reed D., Erickson M. R. S., Yen F. T., Lodish H. F., 2001. Proteolytic cleavage product of 30-kDa adipocyte complement-related protein increases fatty acid oxidation in muscle and causes weight loss in mice. Proceedings of the National Academy of Sciences, **98**, pp. 2005-2010.

[127] Nawrocki A. R., Rajala M. W., Tomas E., Pajvani U. B., Saha A. K., Trumbauer M. E., Scherer P. E., 2006. Mice lacking adiponectin show decreased hepatic insulin sensitivity and reduced responsiveness to peroxisome proliferator-activated receptor γ agonists. Journal of Biological Chemistry, **281**, pp. 2654-2660.

[128] Schwartz M.W., Figlewicz D.P., Baskin D.G., Woods S.C., Porte Jr D., 1992. Insulin in the brain: a hormonal regulator of energy balance. Endocrine reviews, **13**, pp. 387-414.

[129] Porte Jr D., Baskin D.G., Schwartz M.W., 2002. Leptin and insulin action in the central nervous system. Nutrition reviews, **60**, pp. S20-S29.

[130] Dimitriadis G., Mitrou P., Lambadiari V., Maratou E., Raptis S.A., 2011. Insulin effects in muscle and adipose tissue. Diabetes research and clinical practice, **93**, pp. 52-59.

[131] Begg, D. P., Woods, S. C., 2013. The endocrinology of food intake. Nature Reviews Endocrinology, **9**, pp. 584-597.

[132] Air E.L., Strowski M.Z., Benoit S.C., Conarello S.L., Salituro G.M., Guan X.-M., Liu K., Woods S.C., Zhang B.B., 2002. Small molecule insulin mimetics reduce food intake and body weight and prevent development of obesity, Nature medicine, **8**, pp. 179-183.

[133] Rhea E. M., Banks W.A., 2019. Role of the blood-brain barrier in central nervous system insulin resistance, Frontiers in neuroscience, **13**, pp. 521.

[134] Woods S.C., Seeley R.J., Baskin D.G., Schwartz M.W., 2003. Insulin and the blood-brain barrier, Current pharmaceutical design, **9**, pp. 795.

[135] Banks W.A., 2004. The source of cerebral insulin. European journal of pharmacology, **490**, pp. 5-12.

[136] Chen W., Cai, W., Hoover B., Kahn C. R., 2022. Insulin action in the brain: cell types, circuits, and diseases. Trends in Neurosciences, **45**, pp. 384-400

[137] Harada N., Inagaki N., 2022. Regulation of food intake by intestinal hormones in brain. Journal of diabetes,**13**, pp.17-18.

[138] Bewick G. A., 2012. Bowels control brain: gut hormones and obesity. Biochemia medica, **22**, pp. 283-297.

[139] Arosio M., Ronchi C.L., Gebbia C., Cappiello V., Beck-Peccoz P., Peracchi M., 2003. Stimulatory effects of ghrelin on circulating somatostatin and pancreatic polypeptide levels. The Journal of Clinical Endocrinology & Metabolism, **88**, pp. 701-704.

[140] Katsuura G., Asakawa A., Inui A., 2002. Roles of pancreatic polypeptide in regulation of food intake. Peptides, **23**, pp. 323-329.

[141] Peracchi M., Tagliabue R., Quatrini M., Reschini E., 1999. Plasma pancreatic polypeptide response to secretin. European journal of endocrinology, **141**, pp. 47-49.

[142] Christofides N., Sarson D., Albuquerque R., Adrian T., Ghatei M., Modlin I., Bloom S., 1979. Release of gastrointestinal hormones following an oral water load. Experientia, **35**, pp. 1521-1523.

[143] Parkinson C., Drake W.M., Roberts M.E., Meeran K., Besser G., Trainer P.J., 2002. A comparison of the effects of pegvisomant and octreotide on glucose, insulin, gastrin, cholecystokinin, and pancreatic polypeptide responses to oral glucose and a standard mixed meal. The Journal of Clinical Endocrinology & Metabolism, **87**, pp. 1797-1804.

[144] Whitcomb D., Taylor I., Vigna S., 1990. Characterization of saturable binding sites for circulating pancreatic polypeptide in rat brain. American Journal of Physiology-Gastrointestinal and Liver Physiology, **259**, pp. G687-G691.

[145] McLaughlin C.L., Baile C.A., Buonomo F.C., 1985. Effect of CCK antibodies on food intake and weight gain in Zucker rats. Physiology & behavior, **34**, pp. 277-282.

[146] Lin S., Boey D., Herzog H., 2004. NPY and Y receptors: lessons from transgenic and knockout models. Neuropeptides, **38**, pp. 189-200.

[147] Sam A. H., Gunner D. J., King A., Persaud S. J., Brooks L., Hostomska K., Bewick G.A., 2012. Selective ablation of peptide YY cells in adult mice reveals their role in beta cell survival. Gastroenterology, **143**, pp. 459-468.

[148] Ekblad E., Sundler F., 2002. Distribution of pancreatic polypeptide and peptide YY. Peptides, **23**, pp. 251-261.

[149] Fu-Cheng X., Anini Y., Chariot J., Castex N., Galmiche J.-P., Roze C., 1997. Mechanisms of peptide YY release induced by an intraduodenal meal in rats: neural regulation by proximal gut. Pflügers Archiv, **433**, pp. 571-579.

[150] Allen J., Fitzpatrick M., Yeats J., Darcy K., Adrian T., Bloom S., 1984. Effects of peptide YY and neuropeptide Y on gastric emptying in man. Digestion, **30**, pp. 255-262.

[151] Adrian T., Savage A., Sagor G., Allen J., Bacarese-Hamilton A., Tatemoto K., Polak J., Bloom S., 1985. Effect of peptide YY on gastric, pancreatic, and biliary function in humans. Gastroenterology, **89**, pp. 494-499.

[152] Hoentjen F., Hopman W., Jansen J., 2001. Effect of circulating peptide YY on gallbladder emptying in humans. Scandinavian journal of gastroenterology, **36**, pp. 1086-1091.

[153] Batterham R.L., Cowley M.A., Small C.J., Herzog H., Cohen M.A., Dakin C.L., Wren A.M., Brynes A.E., Low M.J., Ghatei M.A., 2002. Gut hormone PYY 3-36 physiologically inhibits food intake. Nature, **418**, pp. 650-654.

[154] Challis B., Pinnock S., Coll A., Carter R., Dickson S., O'rahilly S., 2003. Acute effects of PYY3–36 on food intake and hypothalamic neuropeptide expression in the mouse. Biochemical and biophysical research communications, **311**, pp. 915-919.

[155] Pittner R., Moore C., Bhavsar S., Gedulin B., Smith P., Jodka C., Parkes D., Paterniti J., Srivastava V., Young A., 2004. Effects of PYY [3–36] in rodent models of diabetes and obesity. International journal of obesity, **28**, pp. 963-971.

[156] Nonaka N., Shioda S., Niehoff M.L., Banks W.A., 2003. Characterization of blood-brain barrier permeability to PYY3-36 in the mouse. Journal of Pharmacology and Experimental Therapeutics, **306**, pp. 948-953.

[157] Broberger C., Landry M., Wong H., Walsh J.N., Hökfelt T., 1997. Subtypes Y1 and Y2 of the neuropeptide Y receptor are respectively expressed in pro-opiomelanocortin-and neuropeptide-Y-containing neurons of the rat hypothalamic arcuate nucleus. Neuroendocrinology, **66**, pp. 393-408.

[158] Date Y., Kojima M., Hosoda H., Sawaguchi A., Mondal M.S., Suganuma T., Matsukura S., Kangawa K., Nakazato M., 2000. Ghrelin, a novel growth hormone-releasing acylated peptide, is synthesized in a distinct endocrine cell type in the gastrointestinal tracts of rats and humans. Endocrinology, **141**, pp. 4255-4261.

[159] Sakata I., Nakamura K., Yamazaki M., Matsubara M., Hayashi Y., Kangawa K., Sakai T., 2002. Ghrelin-producing cells exist as two types of cells, closed-and opened-type cells, in the rat gastrointestinal tract. Peptides, **23**, pp. 531-536.

[160] Castaneda T., Tong J., Datta R., Culler M., Tschöp M., 2010. Ghrelin in the regulation of body weight and metabolism. Frontiers in neuroendocrinology, **31**, pp. 44-60.

[161] Murakami N., Hayashida T., Kuroiwa T., Nakahara K., Ida T., Mondal M., Nakazato M., Kojima M., Kangawa K., 2002. Role for central ghrelin in food intake and secretion profile of stomach ghrelin in rats. Journal of Endocrinology, **174**, pp. 283-288.

[162] Sun Y., Wang P., Zheng H., Smith R.G., 2004. Ghrelin stimulation of growth hormone release and appetite is mediated through the growth hormone secretagogue receptor. Proceedings of the National Academy of Sciences, **101**, pp. 4679-4684.

[163] Cowley M.A., Smith R.G., Diano S., Tschöp M., Pronchuk N., Grove K.L., Strasburger C.J., Bidlingmaier M., Esterman M., Heiman M.L., 2003. The distribution and mechanism of action of ghrelin in the CNS demonstrates a novel hypothalamic circuit regulating energy homeostasis. Neuron, **37**, pp. 649-661.

[164] Toshinai K., Date Y., Murakami N., Shimada M., Mondal M.S., Shimbara T., Guan J.-L., Wang Q.-P., Funahashi H., Sakurai T., 2003. Ghrelin-induced food intake is mediated via the orexin pathway. Endocrinology, **144**, pp. 1506-1512.

[165] Tang-Christensen M., Vrang N., Larsen P., 2001. Glucagon-like peptide containing pathways in the regulation of feeding behaviour. International journal of obesity, **25**, pp. S42-S47.

[166] Holst J.J., 2004. Treatment of type 2 diabetes mellitus with agonists of the GLP-1 receptor or DPP-IV inhibitors. Expert opinion on emerging drugs, **9**, pp. 155-166.

[167] Holst J., 2004. On the physiology of GIP and GLP-1. Hormone and Metabolic Research, **36**, pp. 747-754.

[168] Ghatei M., Uttenthal L., Christofides N., Bryant M., Bloom S., 1983. Molecular forms of human enteroglucagon in tissue and plasma: plasma responses to nutrient stimuli in health and in disorders of the

upper gastrointestinal tract. The Journal of Clinical Endocrinology & Metabolism, **57**, pp. 488-495.

[169] Le Quellec A., Kervran A., Blache P., Ciurana A., Bataille D., 1992. Oxyntomodulin-like immunoreactivity: diurnal profile of a new potential enterogastrone. The Journal of Clinical Endocrinology & Metabolism, **74**, pp. 1405-1409.

[170] Dakin C.L., Gunn I., Small C., Edwards C., Hay D., Smith D., Ghatei M., Bloom S., 2001. Oxyntomodulin inhibits food intake in the rat. Endocrinology, **142**, pp. 4244-4250.

[171] Dakin C.L., Small C.J., Park A.J., Seth A., Ghatei M.A., Bloom S.R., 2002. Repeated ICV administration of oxyntomodulin causes a greater reduction in body weight gain than in pair-fed rats. American Journal of Physiology-Endocrinology and Metabolism, **283**, pp. E1173-E1177.

[172] Dakin C.L., Small C.J., Batterham R.L., Neary N.M., Cohen M.A., Patterson M., Ghatei M.A., Bloom S.R., 2004. Peripheral oxyntomodulin reduces food intake and body weight gain in rats. Endocrinology, **145**, pp. 2687-2695.

[173] Larsson L., Rehfeld J., 1978. Distribution of gastrin and CCK cells in the rat gastrointestinal tract. Histochemistry, **58**, pp. 23-31.

[174] Reeve Jr J.R., Eysselein V.E., Ho F., Chew P., Vigna S.R., Liddle R.A., Evans C., 1994. Natural and synthetic CCK-58. Novel reagents for studying cholecystokinin physiology. Annals of the New York Academy of Sciences, **713**, pp. 11-21.

[175] Warrilow, A., Turner, M., Naumovski, N., & Somerset, S., 2022. Role of cholecystokinin in satiation: A systematic review and meta-analysis. Published online by **Cambridge University Press**: 14 February 2022, British Journal of Nutrition, pp. 1-25.

[176] Crawley J.N., Corwin R.L., 1994. Biological actions of cholecystokinin. Peptides, **15**, pp. 731-755.

[177] Wank S.A., Harkins R., Jensen R.T., Shapira H., De Weerth A., Slattery T., 1992. Purification, molecular cloning, and functional expression of the cholecystokinin receptor from rat pancreas. Proceedings of the National Academy of Sciences, **89**, pp. 3125-3129.

[178] Moran T.H., Robinson P.H., Goldrich M.S., McHUGH P.R., 1986. Two brain cholecystokinin receptors: implications for behavioral actions. Brain research, **362**, pp. 175-179.

[179] Wank S.A., Pisegna J.R., De Weerth A., 1992. Brain and gastrointestinal cholecystokinin receptor family: structure and functional expression. Proceedings of the National Academy of Sciences, **89**, pp. 8691-8695.

Kocaeli University

Kocaeli Journal of Science and Engineering

http://dergipark.org.tr/kojose

Trend Analysis of Meteorological Variables in the Lake Van Basin, Turkey

Nadire ÜÇLER [1, *] iD

[1] *Van Vocational School of Higher Education, Van Yuzuncu Yil University, Van, 65040, Turkey, **ORCID**: 0000-0001-6407-121X*

Abstract

Climate change is one of the most important issues of our century and its effects are manifested in different ways around the world. In this study, both the aligned and the intra-block methods were used to detect trends to see climate change's impact. 6 meteorological parameters were selected in the Lake Van basin, which contains Turkey's largest lake. The 47-year time series of mean monthly temperature (°C), total monthly rainfall (mm), mean monthly relative humidity (%), total monthly surface evaporation (mm), mean monthly snow depth (cm), and total monthly insolation intensity (cal/cm^2) parameters of 15 stations in the basin were evaluated for each month using non-parametric tests. In the series in which a statistically significant trend was detected, the beginning year and slope of the change were also determined. For the temperature parameter, the increasing trends were detected at all seasons. In the total monthly rainfall series, the upward trends were determined in March and September in the northeastern part of the basin. Upward trends were detected in the average monthly relative humidity series in winter. From the total monthly insolation intensity time series, autumn and spring were determined to have increasing trends. The trend analysis of mean monthly snow depth showed that there were downward trends in November and February. For the evaporation parameter, a decreasing trend was detected only in October.

1. Introduction

As a result of climate change, the increase in surface temperature, rise in sea level, deterioration in the water cycle, decrease in glaciers, changes in ecosystems, and excessive salinization in agricultural soils are becoming common problems in many countries. While factors such as the current growth rate and water consumption habits put significant pressure on water resources, climate change affects especially the hydrological cycle, spatial and temporal distribution of water. Additionally, with the impact of climate change on the hydrological cycle, there may be more variability in precipitation and water flows, and the intensity of extreme hydrological events may increase. In this case, significant changes are estimated to occur in the supply and quality of water resources. These changes will negatively affect energy, health, tourism, transportation, flood and drought events, and ecosystem integrity, including drinking use and agricultural production, where water is vital. Therefore, the assessment

of the climate change effect has recently received great concern.

Since changes in the seasonal distribution and amount of precipitation are among the main effects of climate change, numerous studies have been conducted to detect these changes throughout the world over the years. For instance, Serrano et al. [1] analyzed total monthly and annual precipitation data for the Iberian Peninsula using the Mann-Kendall test for trends. Duhan and Pandey [2] studied annual and seasonal records to detect the trend of precipitation in Madhya Pradesh, India. Monotonic trend direction was detected by the Mann–Kendall test and Sen's slope estimator test was applied to detect the magnitude of a trend over time. Limsakul and Singhruck [3] applied Kendall's slope estimator to detect trends in the precipitation records of Thailand during 1955–2014. The Mann–Kendall test and Modified Mann–Kendall test were applied to ascertain the trends in rainfall and temperature values in India [4]. The Mann-Kendall test and the Sen's T test were applied to the precipitation records of Turkey to detect variability [5]. In addition, temperature [6-9], humidity [10,11], snow depth [12,13], evaporation [14,15], and sunshine [16,17] are among the parameters that are

* Corresponding Author: nadireucler@yyu.edu.tr

worth examining.

Because of its geographical location, Turkey is among the countries that will be influenced significantly by climate change, and it has already experienced an increased rate of sudden rains, floods, and drought [18]. For example, as a result of heavy rains in the Western Black Sea region of Turkey on August 11, 2021, floods occurred in the cities of Bartın, Kastamonu, and Sinop and eleven people lost their lives [19]. Besides floods, Turkey is under the threat of desertification and drought due to its climatic characteristics and topographic structure. Considering the winter season and the annual precipitation changes in Turkey, the most severe and widespread drought events occurred in 1971-1974, 1983-1984, 1989-1990, 1996, 2001, and 2007-2008 [20]. Considering the 30 years, annual maximum rainfall data by 2010 in Turkey, Mann-Kendall and linear regression trend test results specified that about 90% of them are trend-free while the increasing and decreasing trends are around 10 % and 2%, respectively [21].

Due to the decreasing precipitation amounts and drought reasons, decreases are observed in the water levels of the lakes in Turkey [22]. For instance, the results of a study on Lakes Mogan and Eymir located in Central Anatolia indicated that precipitation and temperature have a significant effect on the lakes' levels, and an estimated rise in temperature and reduction in precipitation in the future may cause the drying of both lakes [23]. Additionally, in another study, besides temperature, and precipitation; wind speed, cloud cover, humidity, sunshine duration, and pan evaporation parameters were also examined to understand the mechanism of the variations of the levels of these lakes [24].

To see the climate change-induced changes in hydro-meteorological parameters in the Kizilirmak basin, the precipitation, temperature, streamflow, and groundwater data were analyzed using linear regression and Mann–Kendall, modified Mann–Kendall, and Spearman's Rho tests. According to the results, generally decreasing trends were observed in streamflow, and the majority of the stations had increasing trends in groundwater levels [25].

As there is a hydrologic relationship between water resources and meteorological parameters, learning more about the long-term trends of meteorological parameters is crucial for sustainable water resource management [26]. The Van Lake basin, chosen as the study area, is an important region in terms of hosting the largest lake in the country. For this reason, it is important to investigate the effects of climate change in this region, take the signals of possible extreme meteorological events in advance, and consider the necessary precautions. Therefore, almost all meteorological parameters with long-term data in the basin were used. Furthermore, both intrablock and aligned rank types have been applied and the results were compared by applying three different methods to determine the trend. The severity of climate change was investigated by determining the inclinations of trends. Trend starting years were determined to compare with previous and next studies.

2. Materials and Methods

2.1. Study Area

Lake Van is the largest soda lake in the world located in Eastern Anatolia, Turkey (Figure 1). High salinity prevents the usage of lake water for drinking and irrigation purposes. Rainfall, stream flows, and snowmelt feed the lake and there is no artificial or inartificial outlet except evaporation. The change in meteorological variables directly affects the lake level. The Lake Van basin is one of the most important basins of Turkey with a 1788007-hectare area.
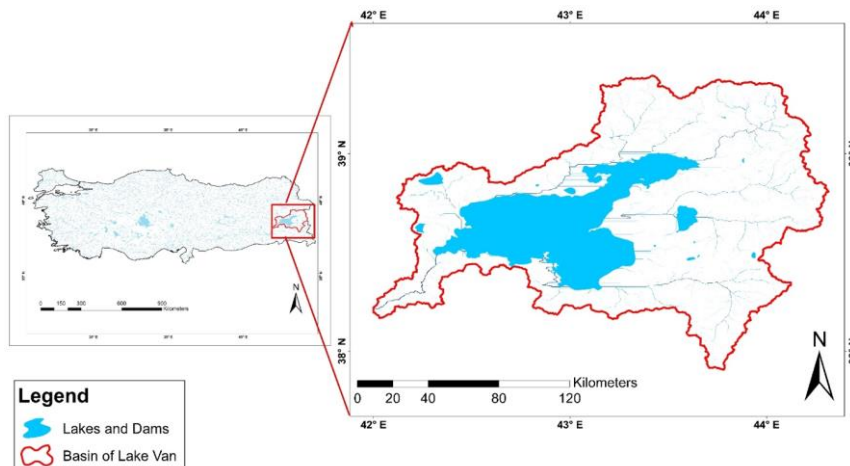
Figure 1. Map of Turkey and Lake Van basin.

2.2. Data

The methods were applied to the time series of meteorological variables obtained from the Turkish State Meteorological Service to reflect regional hydroclimatic conditions. The time series of five rainfall (mm) stations (Ercis, Baskale, Ozalp, Muradiye, Gevas), four temperature (°C) stations (Tatvan, Ahlat, Van, Muradiye), three relative humidity (%) stations (Tatvan, Ahlat, Van), one insolation intensity (cal/cm^2) station (Van), one snow depth (cm) station (Van) and one evaporation (mm) station (Van) were used to detect a trend. Locations of stations have been shown in Figure 2. All stations have continuous records for the period of 47 years (1970–2016) on a monthly basis except the Gevas-rainfall, Van-insolation intensity, and Van-snow depth station which have 37 years' worth of records from 1980 to 2016.
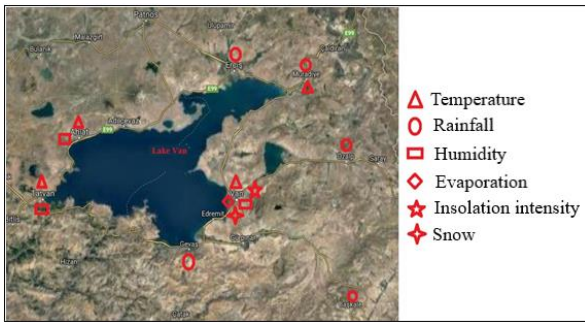

Figure 2. Location of stations used in the study.

Before the application of the tests, outliers were investigated for all meteorological variables at each station and month. Although outliers were found in almost every variable, especially in the rainfall variable, it was preferred to use raw data instead of extracting outliers, since these values were not so extreme as to be considered to cause incorrect measurements or incorrect recordings.

2.3. Methodology

Classical parametric methods have some assumptions such as normality, linearity, and independence while general meteorological data do not have these characteristics due to missing values or seasonality. Therefore, several more flexible nonparametric tests that can cope with these problems more easily in meteorological records have been used for trends. Van Belle and Hughes [27] defined two types of methods namely intrablock and aligned ranks. Intrablock methods calculate the statistics for each block and then sum up these to create the overall statistics. Aligned ranks at the beginning move away from the block impact of data and then sum the data over blocks, and finally use these sums

to generate statistics. In this study, the results are compared using intrablock and aligned rank methods respectively. The methodology is summarized in Figure 3. The first step is applying the Sen's T test, Seasonal Mann-Kendall test and Spearman's Rho test for specifying trends. The second step is estimating slopes of time series with Sen's estimator and the last one is using Mann-Kendall Rank Correlation test for estimating the starting year of possible climate changes.
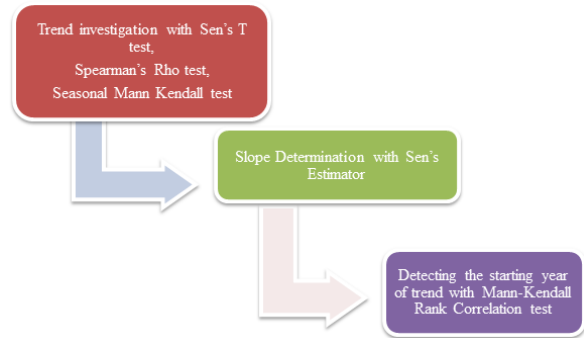
Figure 3. The methodology of study.

2.3.1. The Sen's T test

The Sen's T Test, an ordered rank test, was originally propounded by Sen in 1968 and was improved by Farrell in 1980 [28]. The test statistics, which are independent of the distribution and are not affected by seasonal events, can be calculated in the following order of operation.

X_{ij} is the variable value measured at the observation station.

here;
i: years (i = 1, 2, ..., n) and j: months (j = 1, 2, ..., 12).
The average for j (months) is calculated with equation 1.

$$X_{.j} = \frac{\sum_i X_{ij}}{n} \tag{1}$$

The average for each month is calculated and afterward removed from corresponding months in the n-year data. Therefore, the seasonal effects are eliminated.

The order of all differences from 1 to 12xn is calculated with the following equation 2.

If the results have the same value (bindings), the average of the rank values should be taken.

$$R_{ij} = Rank(X_{ij} - X_{.j}) \tag{2}$$

The average of the ranks is calculated by implementing equation (3) for each month.

$$R_{.j} = \frac{\sum R_{ij}}{n} \tag{3}$$

Finally, the Sen's T test statistics are calculated with (4). (Here m = 1)

$$T = \left[\frac{12m^2}{n(n+1)\sum_{i,j}(R_{ij}-R_{.j})^2}\right]^{\frac{1}{2}} \left[\sum_{i=1}^{n}\left(i-\frac{n+1}{2}\right)\left(R_{i.}-\frac{nm+1}{2}\right)\right] \tag{4}$$

If the value of the statistical test $|T|$ is larger than the normal distribution value z, which is determined at the significance level α, the zero (H_0) hypothesis is that there is no trend rejected and the alternative hypothesis (H_1) claims that there is a certain trend accepted.

2.3.2. The Spearman's rho test

This test is used to determine whether there is a correlation between two observation series. It is a quick and simple test to investigate the presence of linear trends and is a metric based on sequence statistics. The rank statistic R (x_i) is determined by the order of the data from small to large or the other way around.

The observation series is represented by the vector X = (x_1, x_2, ..., x_n). According to the H_0 hypothesis, x_i (i = 1, 2, 3, ..., n) are all equally probable distributions. According to the H_1 hypothesis, x_i (i = 1, 2, 3, ..., n) values increase or reduce with time. Spearman's Rho test statistic, r_s, is calculated using the following equation.

$$r_s = 1 - 6\frac{[\sum_{i=1}^{n}(R(x_i-i)^2)]}{(n^3-n)} \tag{5}$$

Here:

(x_i): i. the sequence number of the observation.

i: the observation sequence of the data.

n: total observation adjective [29].

Spearman has given a table of maximum r_s values that show no correlation between rank numbers at a given significance level. Since the r_s distribution for n> 30 approaches normal, normal distribution tables can be used for hypothesis testing [30]. Therefore, the test statistic for r_s is found.

$$z = r_s\sqrt{1/(n-1)} \tag{6}$$

If the value of z is bigger than the value of z defined from the standard normal distribution tables at the significance level α, the hypothesis that the xi values are homogeneous is rejected, and the hypothesis that there is a specific trend is accepted.

2.3.3. The seasonal Mann–Kendall test

Hirsch and Slack [31] analyzed nonparametric trend tests applied to serially dependent seasonal data and proposed the Seasonal Mann-Kendall test and the modified Mann-Kendall test for the trend. They proved the superiority of this test against the serially dependent Monte Carlo Experiment.

For X = (x_1, x_2, ..., x_{12}) and X_i = (x_{i1}, x_{i2}, ..., x_{in}) arrays; X represents the observed values for each month and X_i represents the annual values for the i-th month; according to the H_o hypothesis, X is an example of the independent random variable x_{ij} while X_i (i = 1, 2, 3, ..., 12) is a sub-sample of independent and coarse random variables. According to the alternative hypothesis, sub-examples do not have a uniform distribution. Before the Seasonal Mann-Kendall test statistics are calculated, the test statistics are calculated separately for each month with the following equations.

$$S_i = \sum_{k=1}^{n_i-1}\sum_{J=k+1}^{n_i} sgn(x_{ij}-x_{ik}) \tag{7}$$

$$sgn(x_j-x_k) = \{(x_j-x_k) > 0 \rightarrow +1\ (x_j-x_k) = 0 \rightarrow 0\ (x_j-x_k) < 0 \rightarrow -1 \tag{8}$$

The variance of the test statistic S_i which has an asymptotically normal distribution and with zero mean is calculated by the following equation.

$$Var(S_i) = \frac{n_i(n_i-1)(2n_i+5)}{18} \tag{9}$$

In the case of similar values (ties) in each month, the following equation is used instead of the variance (Var) calculation.

$$Var(S_i) = \frac{n_i(n_i-1)(2n_i+5)-\sum_{t_i} t_i(t_i-1)(2t_i+5)}{18} \tag{10}$$

After the individual test statistics and variance calculations are made for each month, the Seasonal Mann-Kendall test statistic S' is defined with the equation (11). The variance of the test is found by equation (12).

$$S' = \sum_{i=1}^{12} S_i \tag{11}$$

$$Var(S') = \sum_{i=1}^{12} Var(S_i) + \sum_{i=1}^{12}\sum_{j=1}^{12} cov(S_i,S_j) \tag{12}$$

S_i and S_j are functions of independent random variables such that S_i = f (X_i) and S_j = f (X_j). Since all X_i and X_j values are independent i and j monthly data, the covariance term in (12) is neglected. Hence, the variance is calculated by (13).

$$Var(S') = \sum_{i=1}^{12} Var(S_i) \tag{13}$$

Once the monthly variance values are calculated

using equations (9) or (10), the variance of the Seasonal Mann-Kendall test statistic is calculated by equation (13). Whether the Seasonal Mann-Kendall test is important is determined by comparing the standard normal variable z with the critical z value by calculating the following equation [26].

$$z = \{S' > 0 \rightarrow \frac{S'-1}{\sqrt{Var(S\prime)}} \; S' = 0 \rightarrow 0 \; S' < 0 \rightarrow \frac{S'+1}{\sqrt{Var(S\prime)}}$$

(14)

Accordingly, if the value of $|z|$ less than or equal to the value of $z_{\alpha/2}$ determined from the standard normal distribution tables at the α significance level, the H_o hypothesis is accepted, otherwise, it is rejected. If the calculated S' value of the Seasonal Mann-Kendall test is positive, it is an upward trend, while if negative it is a downward trend.

2.3.4. The Sen's estimator

Linear slopes of the trends (change in unit time) were calculated using a nonparametric method introduced by Sen [27]. This method is not affected by datum failures or deficient values. xj and xk, are the data at times j and k respectively; Q_i (i = 1, 2, ..., N) is a parameter and is calculated according to the equation (15). Then, the Q_i values are sorted from the smallest to the largest.

$$Q_i = \frac{x_j - x_k}{j - k}$$

(15)

After the determination and sequencing of the Qi values, the median is estimated by computing the following steps; if the number N is odd, the change in the unit of observation is determined by using the equation (16); if the number N is even, the equation (17) is used for determining the change in the unit of observation.

$$Q = \{Q_{(N+1)/2}\}$$

(16)

$$Q = \{\frac{1}{2}[Q_{(N)/2} + Q_{(N+2)/2}]\}$$

(17)

The statistical significance of the Q value at 100(1-alpha) % is performed by computing the two-sided test.

2.3.5. The Mann-Kendall rank correlation test

This non-parametric test is used to find whether the applied series has an upward or downward trend over time. The test, which graphically expresses the results, can also

detect the starting year of the trend. Since three different tests were used to determine whether there was a trend in this study, and the results were supported by the slope method, the Mann-Kendall Rank Correlation test was performed to detect the trend starting year.

In this test, the rank (y_i) in the series is used instead of the actual data. Each y_i is defined by an integer number such as n_i, counting the largest of the previous ranks. If the consecutive sums of these integers are denoted by t, it is defined as:

$$t = \sum_{i=1}^{n} n_i$$

(18)

The mean E(t) and the variance Var(t) of that, and the Mann-Kendall test statistic u(t) are calculated using the equations (19), (20), and (21) respectively [32].

$$E(t) = \frac{n(n-1)}{4}$$

(19)

$$t = \frac{n(n-1)(2n+5)}{72}$$

(20)

$$u(t) = [t - E(t)]/\sqrt{t}$$

(21)

u'(t) is calculated backward in the series similar to u(t). Graphically, u(t) and u'(t) converge at the spot where the change begins and then move away from each other and show where the trend begins. If there is no trend in the series, u(t) and u'(t) will approach each other several times and make close oscillations.

3. Results and Discussion

Trend-detected stations and months, test statistics, trend results, trend slope values, and trend-starting years are given separately for each parameter in tables. If the absolute value of the test statistic values is greater than the 5% significance level value (±1.96), it is concluded that there is a trend. The sign of the Seasonal Mann-Kendall test statistic gives information about the trend direction. If the test statistic value is negative, the trend is downward and if it is positive, it is upward. Likewise, if the slope value is negative, it means that the trend is downward, and if it is positive, it means that the trend is upward.

3.1. Results of Tests in Temperature Parameter

Table 1 shows stations, slope values, and trend-starting years of the temperature parameter. It is seen from the results that Sen's T and Spearman's Rho tests yield almost the same results. Although the Seasonal Kendall

test did not detect the trend at Tatvan station in January, as Sen's T test and Spearman's Rho test detected trends at this station, these two tests' results were considered. Trends were determined in a span of 10 months. A trend was not detected in September and November. Only in June and August, the trend was determined at Ahlat station. All trends were an increasing direction. The slope values ranged between 0.028 and 0.094. The highest slope was determined at the Van station in February. The trend beginning years varied between 1978 and 2012.

Table 1. Results of the trend tests for the parameter of temperature.

Months	Stations	Sen's T	Spearman's Rho	Seasonal Mann-Kendall	α= % 5	Trend	Slope Value	Slope Starting Year
January	Tatvan	-2.09	-2.12	1.54	±1.96	upward	0.034	1978
	Van	-3.29	-3.31	2.71	±1.96	upward	0.082	1984
	Muradiye	-2.93	-3.04	2.50	±1.96	upward	0.066	1993
February	Van	-3.27	-3.34	3.03	±1.96	upward	0.094	1998
	Muradiye	-3.39	-3.34	3.13	±1.96	upward	0.085	1998
March	Van	-2.61	-2.65	2.55	±1.96	upward	0.058	2006
	Muradiye	-2.34	-2.31	2.36	±1.96	upward	0.078	2003
April	Van	-2.46	-2.48	2.49	±1.96	upward	0.040	2012
May	Van	-2.65	-2.70	2.75	±1.96	upward	0.040	2008
June	Tatvan	-3.15	-3.19	3.07	±1.96	upward	0.040	1997
	Ahlat	-2.51	-2.46	2.22	±1.96	upward	0.033	1998
	Van	-3.96	-4.08	3.94	±1.96	upward	0.050	1996
	Muradiye	-2.87	-2.96	2.97	±1.96	upward	0.046	2003
July	Tatvan	-2.89	-2.97	2.74	±1.96	upward	0.028	2007
	Van	-3.40	-3.32	3.36	±1.96	upward	0.043	1997
August	Tatvan	-3.56	-3.78	3.87	±1.96	upward	0.037	2002
	Ahlat	-2.31	-2.31	2.46	±1.96	upward	0.030	2009
	Van	-4.65	-4.80	4.85	±1.96	upward	0.064	1996
	Muradiye	-3.45	-3.56	3.87	±1.96	upward	0.050	2011
October	Van	-3.28	-3.36	3.70	±1.96	upward	0.044	1992
	Muradiye	-2.46	-2.51	3.12	±1.96	upward	0.040	1995
December	Muradiye	-2.46	-2.43	2.49	±1.96	upward	0.064	1978

The direction of temperature trends was upward across the basin in all seasons, in contrast to the study of Turkes et al. [33] which deduced that there was a cooling tendency in the last twenty years across Turkey. This result discloses the warming over the Van Lake basin due to climate change.

3.2. Results of Tests in Relative Humidity Parameter

Table 2 shows stations, slope values and trend-starting years of humidity parameter. Trends were determined in 9 months. The trend was not detected in July, October, and December. The Seasonal Kendall test did not detect the trend at the Ahlat station in February. However, Sen's T test and Spearman's Rho test detected trends at this station, so these two tests' results were considered. The trend was determined at Van station only in August. While the trends at the Ahlat station were increasing in January and February, the other trends were decreasing. The negative slope values ranged between -0.128 and -0.393. The highest slope was determined at the Tatvan station in August. The trend starting year varied between 1986 and 2013 being more common after 2010.

Table 2. Results of trend tests for the parameter of humidity.

Months	Stations	Sen's T	Spearman's Rho	Seasonal Mann-Kendall	α= % 5	Trend	Slope Value	Slope Starting Year
January	Ahlat	-2.93	-2.88	2.75	±1.96	upward	0.113	1986
February	Ahlat	-2.25	-2.29	1.90	±1.96	upward	0.090	2008
March	Tatvan	3.15	3.16	-3.25	±1.96	downward	-0.190	1992
April	Tatvan	2.63	2.62	-2.75	±1.96	downward	-0.211	2013
	Ahlat	2.00	1.97	-1.99	±1.96	downward	-0.128	2012
May	Ahlat	2.54	2.53	-2.40	±1.96	downward	-0.153	2012
June	Tatvan	2.08	2.09	-2.35	±1.96	downward	-0.246	2010
	Ahlat	3.51	3.50	-3.36	±1.96	downward	-0.261	2004
August	Tatvan	2.84	2.83	-3.66	±1.96	downward	-0.393	2012
	Ahlat	2.49	2.51	-2.40	±1.96	downward	-0.235	2013
	Van	2.37	2.37	-2.29	±1.96	downward	-0.164	2012
September	Tatvan	2.37	2.37	-2.29	±1.96	downward	-0.289	2010
November	Tatvan	2.46	2.45	-2.47	±1.96	downward	-0.209	2013

Upward trends were found in the monthly mean relative humidity time series in winter, while downward trends were obtained for other seasons. Alobaidi [10] analyzed surface relative humidity for the period 1951-2010 in Iraq which is the southwest neighbor of Turkey. Results showed a downward tendency in winter, spring, and autumn which differs from our results due to the winter and summer upward trends.

3.3. Results of Tests in Evaporation Parameter

The evaporation time series were recorded only at the Van station and in May, June, July, August, September, and October. Therefore, the tests were applied to these months. The results are shown in Table 3. The trend was detected only in October, which was downward. The slope of the trend is -0.67 and the trend starts in 2007.

Table 3. Results of trend tests for the parameter of evaporation.

Months	Stations	Sen's T	Spearman's Rho	Seasonal Mann-Kendall	α= % 5	Trend	Slope Value	Slope Starting Year
October	Van	2.72	2.54	-2.57	±1.96	downward	-0.67	2007

3.4. Results of Tests in Rainfall Parameter

The time series of 5 rainfall stations (Ercis, Baskale, Ozalp, Muradiye, Gevas) were used to detect trends but the trends were determined only at the Muradiye station in March and September. The slope values and trend-starting years of March and September were determined as 0.566 in 1999 and 0.465 in 1991, respectively. Results are shown in Table 4.

Table 4. Results of trend tests for the parameter of rainfall.

Months	Stations	Sen's T	Spearman's Rho	Seasonal Mann-Kendall	α= % 5	Trend	Slope Value	Slope Starting Year
March	Muradiye	-2.10	-2.11	2.10	±1.96	upward	0.566	1999
September	Muradiye	-2.93	-2.91	3.06	±1.96	upward	0.465	1991

In the total monthly rainfall series, the trend was determined only in one station and in two months. Contrary to a study by Partal and Kahya [5] for January, February and September over the period 1929-1993, the trends for March and September were upward.

3.5. Results of Tests in Snow Depth Parameter

The snow depth parameter was measured only at the Van station, and data is available only in November, December, January, February, and March. Tests were carried out during these months. The results can be seen in Table 5. In snow depth parameters, the Sen's T test results differ from other tests. It is thought that this is due to a lot of zero value measurements in the snow series. The Seasonal Kendall test did not detect the trend in November. However, the Sen's T test and the Spearman's Rho test detected trends at this station, so these two tests' results were considered. Decreasing trends were observed only in November and February with slope of -0.058 and -0.218, and the starting year of 2003 and 2007, respectively.

Table 5. Results of tests trend tests for the parameter of snow depth.

Months	Stations	Sen's T	Spearman's Rho	Seasonal Mann-Kendall	α= % 5	Trend	Slope Value	Slope Starting Year
November	Van	7.25	2.69	-1.80	±1.96	downward	-0.058	2003
February	Van	9.61	2.46	-2.40	±1.96	downward	-0.218	2007

3.6. Results of Tests in Insolation Intensity Parameter

Table 6 shows slope values and trend-starting years of insolation intensity parameter at the stations. Increasing trends were detected in March, April, May, and November with slopes between 0.964 and 1.161. These slope values are higher than the other parameters' slope values.

Observations show that the trend began the late 1980s for March and May, whereas it was observed in early 2010 for April and November. In the insolation intensity parameter, Sen's T test results are higher than other tests. Although the Seasonal Kendall test did not detect the trend at Van station in March and November, the trend was still considered to exist since Sen's T test and Spearman's Rho test showed significant results.

Table 6. Results of tests in the insolation intensity parameter.

Months	Stations	Sen's T	Spearman's Rho	Seasonal Mann-Kendall	α= % 5	Trend	Slope Value	Slope Starting Year
March	Van	-7.48	-2.01	1.90	±1.96	upward	1.059	1986
April	Van	-9.11	-2.24	2.01	±1.96	upward	1.161	2010
May	Van	-8.44	-2.28	2.18	±1.96	upward	0.964	1988
November	Van	-7.63	-2.14	1.85	±1.96	upward	1.091	2012

The stations with a trend are shown on the map in Figure 4 for each month. The stations, where the upward trend was detected, are shown as solid and the others as empty. During October, trends were detected only in temperature and evaporation parameters in the middle and northeast part of the basin. This month showed both positive and negative trends. When November came, parameters turned to humidity and snow and trend changes were only downward. Stations at which trends were detected, were located in the West and middle part of the basin. While August was the month with the highest number of trends, December was the month with the least number of trends. In July, the trend was determined only in the temperature parameter. In the rainfall parameter, trends could not be detect at Ercis, Gevas, Baskale, and Ozalp stations, but only at Muradiye station.
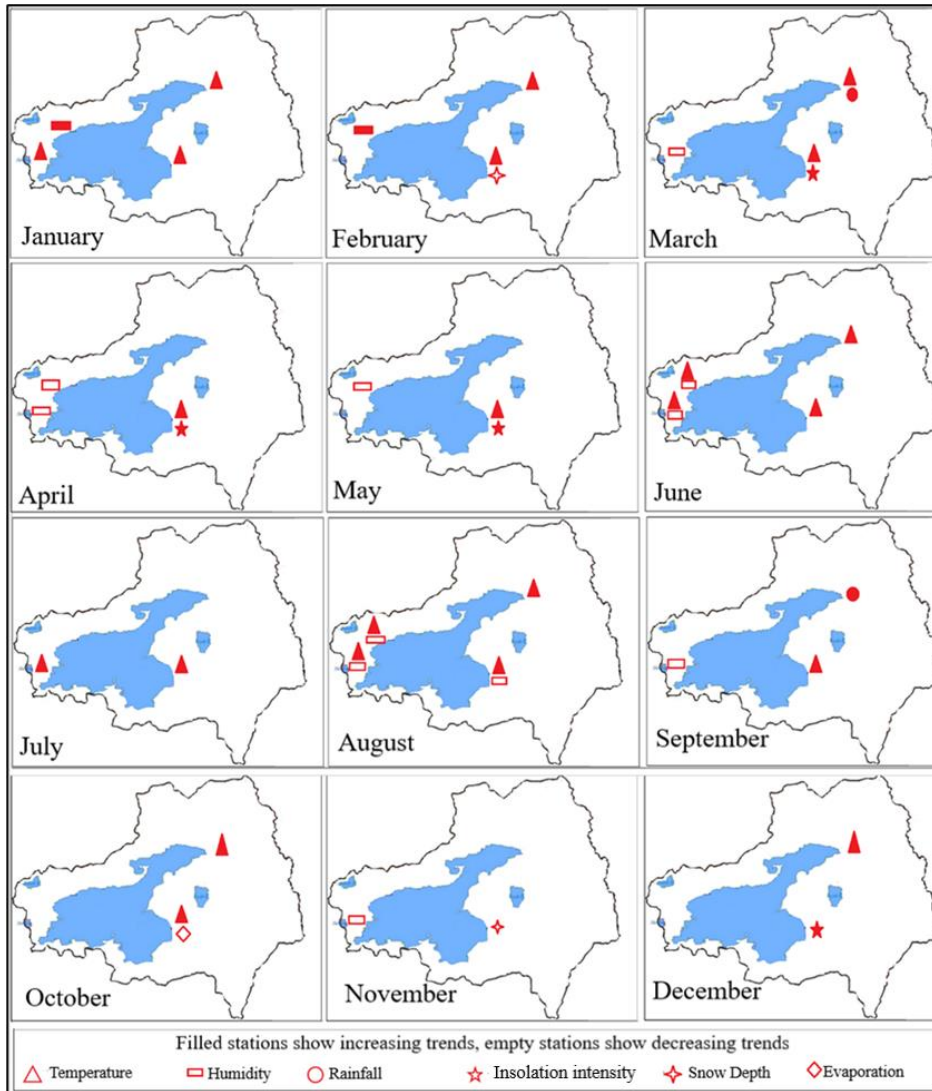
Figure 4. Distribution of significant monthly trends at the 5% significance level.

4. Conclusion

In this study, the trend analysis of the meteorological data of the stations in the Van Lake basin was made to identify the effects of climate change. It was found that the temperature had an increasing trend in all seasons, while rainfall and insolation intensity had an increasing trend in spring and autumn. Upward trends were detected in the average monthly relative humidity and the evaporation series in winter, and for the mean monthly snow depth parameter in autumn and winter. The reason for these detected trends may be climate change and significant inclinations in hydrological cycle parameters.

The highest slope was determined in the insolation intensity parameter as 1,161 in April and the lowest slope (0.028) was determined in the temperature parameter at the Tatvan station in July. Generally, significant trends start between 1990 and 2000 for temperature, while for other parameters the starting year is after 2000.

Declaration of Ethical Standards

The author of this article declares that the materials and methods used in this study do not require ethical committee permission and/or legal-special permission.

Conflict of Interest

The author declares that she has no known competing financial interests or personal relationships that could have appeared to influence the work reported in this paper.

References

[1] Serrano A., Mateos V.L., Garcia J.A., 1999. Trend analysis of monthly precipitation over the Iberian Peninsula for the period 1921–1995. Physics and Chemistry of the Earth, Part B: Hydrology, Oceans and Atmosphere, **24**(1-2), pp. 85-90. https://doi.org/10.1016/S1464-1909(98)00016-1

[2] Duhan D., Pandey A., 2013. Statistical analysis of long term spatial and temporal trends of precipitation during 1901–2002 at Madhya Pradesh, India. Atmospheric Research, **122**, pp. 136-149. https://doi.org/10.1016/j.atmosres.2012.10.010

[3] Limsakul A., Singhruck P., 2016. Long-term trends and variability of total and extreme precipitation in Thailand. Atmospheric Research, **169**, pp. 301-317. https://doi.org/10.1016/j.atmosres.2015.10.015

[4] Pingale S., Adamowski J., Jat M., Khare D., 2015. Implications of spatial scale on climate change assessments. Journal of Water and Land Development, **26**, pp. 37-55. https://doi.org 10.1515/jwld-2015-0015

[5] Partal T., Kahya E., 2006. Trend analysis in Turkish precipitation data. Hydrological Processes: An International Journal, **20**(9), pp. 2011-2026. https://doi.org/10.1002/hyp.5993

[6] Zhang X., Vincent L.A., Hogg W.D., Niitsoo A., 2000. Temperature and precipitation trends in Canada during the 20th century. Atmosphere-ocean, **38**(3), pp. 395-429. https://doi.org/10.1080/07055900.2000.9649654

[7] Liu X., Xu Z., Yu R., 2011. Trend of climate variability in China during the past decades. Climatic change, **109**(3), pp. 503-516. https://doi.org/10.1007/s10584-011-0097-6

[8] Karaca M., Anteplioĝlu Ü., Karsan, H., 1995. Detection of urban heat island in Istanbul, Turkey. Il Nuovo Cimento C, **18**(1), pp. 49-55. https://doi.org/10.1007/BF02561458

[9] Kadioĝlu M., 1997. Trends in surface air temperature data over Turkey. International Journal of Climatology: A Journal of the Royal Meteorological Society, **17**(5), pp. 511-520. https://doi.org/10.1002/(SICI)1097-0088(199704)17:5<511:: AID-JOC130>3.0.CO;2-0

[10] Alobaidi A.H., 2015. Analysis of Relative Humidity in Iraq for the Period. International Journal of Scientific and Research Publications, **5**(5), pp. 515-524.

[11] Van Wijngaarden W.A., Vincent L.A., 2004. Trends in relative humidity in Canada from 1953–2003. Bull. Am. Meteorol. Soc, pp. 4633-4636.

[12] Dyer J. L., Mote T. L., 2006. Spatial variability and trends in observed snow depth over North America. Geophysical Research Letters, **33**(16). https://doi.org/10.1029/2006GL027258

[13] Kunkel K.E., Robinson D.A., Champion S., Yin X., Estilow T., Frankson R.M., 2016. Trends and extremes in Northern Hemisphere snow characteristics. Current Climate Change Reports, **2**(2), pp. 65-73. https://doi.org/10.1007/s40641-016-0036-8

[14] Chattopadhyay N., Hulme M., 1997. Evaporation and potential evapotranspiration in India under conditions of recent and future climate change. Agricultural and Forest Meteorology, **87**(1), pp. 55-73. https://doi.org/10.1016/S0168-1923(97)00006-3

[15] Liu B., Xu M., Henderson M., Gong W., 2004. A spatial analysis of pan evaporation trends in China, 1955–2000. Journal of Geophysical Research: Atmospheres, **109**(D15). https://doi.org/10.1029/2004JD004511

[16] Aksoy B., 1999. Analysis of changes in sunshine duration data for Ankara, Turkey. Theoretical and Applied Climatology, **64**(3), pp. 229-237. https://doi.org/10.1007/s007040050125

[17] Rahimzadeh F., Pedram M., Kruk M.C., 2014. An examination of the trends in sunshine hours over Iran. Meteorological Applications, **21**(2), pp. 309-315. https://doi.org/10.1002/met.1334

[18] Presidency of Strategy and Budget, 2019. Eleven Development Plan 2019-2023. https://www.sbb.gov.tr/wp-content/uploads/2021/12/Eleventh_Development_Plan_2019-2023.pdf

[19] Ministry of Interior, 2021. Response to Floods Continues with 2,218 Personnel https://www.icisleri.gov.tr/yasanan-sel-ve-su-baskinlarina-mudahale-calismalari-2218-personel-ile-devam-ediyor

[20] Ministry of Agriculture and Forestry, 2018. Van Lake Basin Drought Management Plan, https://www.tarimorman.gov.tr/SYGM/Belgeler/Kura kl%C4%B1k%20Y%C3%B6netim%20Planlar%C4% B1/Van%20G%C3%B6l%C3%BC%20Havzas%C4% B1%20Kurakl%C4%B1k%20Y%C3%B6netim%20P lan%C4%B1%20Cilt%201.pdf

[21] Haktanir T., Citakoglu H. 2014. Trend, independence, stationarity, and homogeneity tests on maximum rainfall series of standard durations recorded in Turkey. Journal of Hydrologic Engineering, **19**(9), pp. 05014009.

[22] Dönmez S., 2018. Investigation of the recession of Akşehir Lake water level with meteorological and satellite data. Journal of the Faculty of Engineering and Architecture of Gazi University **33**(1), pp. 177-188.

[23] Yagbasan O., Yazicigil, H., Demir, V. 2017. Impacts of climatic variables on water-level variations in two shallow Eastern Mediterranean lakes. Environmental Earth Sciences, **76**(16), pp.1-11.

[24] Yagbasan O., Demir V., Yazicigil H. 2020. Trend analyses of meteorological variables and lake levels for two shallow lakes in central Turkey. Water, **12**(2), pp. 414.

[25] Citakoglu H., Minarecioglu N. 2021. Trend analysis and change point determination for hydro-meteorological and groundwater data of Kizilirmak basin. Theoretical and Applied Climatology, **145**(3), pp. 1275-1292.

[26] Hu M., Sayama T., Try S., Takara K., Tanaka K. 2019. Trend analysis of hydroclimatic variables in the Kamo River Basin, Japan. Water, **11**(9), pp. 1782.

[27] Van Belle G., Hughes J.P., 1984. Nonparametric tests for trend in water quality. Water resources research, **20**(1), pp. 127-136. https://doi.org/10.1029/WR020i001p00127

[28] Lettenmaier D.P., 1976. Detection of trends in water quality data from records with dependent observations. Water Resources Research, **12**(5), pp. 1037-1046. https://doi.org/10.1029/WR012i005p01037

[29] İçağa Y., 1994. Analysis of trends in water quality using nonparametric methods. Dokuz Eylul Üniversity, Institute of Sciences, (Dissertation), İzmir.

[30] Hirsch R.M., Slack J. R., 1984. A nonparametric trend test for seasonal data with serial dependence. Water Resources Research, **20**(6), pp. 727-732. https://doi.org/10.1029/WR020i006p00727

[31] Douglas E.M., Vogel R.M., Kroll, C.N., 2000. Trends in floods and low flows in the United States: impact of spatial correlation. Journal of hydrology, **240**(1-2), pp. 90-105. https://doi.org/10.1016/S0022-1694(00)00336-X

[32] Sen P.K., 1968. Estimates of the regression coefficient based on Kendall's tau. Journal of the American statistical association, **63**(324), pp. 1379-1389. https://doi.org 10.1080/01621459.1968.10480934

[33] Sneyers R., 1990. On the Statistical Analysis of Series of Observations. World Meteorol. Organ.

[34] Türkeş M., Süme, U M., Kiliç G., 1995. Variations and trends in annual mean air temperatures in Turkey with respect to climatic variability. International Journal of Climatology, **15**(5), pp. 557-569. https://doi.org/10.1002/joc.3370150507
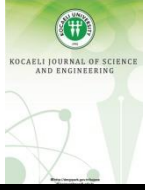
Investigation Of Separability Of DMC/Methanol Azeotropic Mixtures By Chitosan Hybrid Membrane

Nazlı YENIHAN YUZER [1] (iD) , Guler HASIRCI [2] (iD) , Nilufer HILMIOGLU [3, *] (iD)

[1] Department of Chemical Engineering, Kocaeli University, Kocaeli, 41001, Turkey, **ORCID:** 0000-0001-5112-5450
[2] Department of Chemical Engineering, Kocaeli University, Kocaeli, 41001, Turkey, **ORCID:** 0000-0001-7435-8118
[3] Department of Chemical Engineering, Kocaeli University, Kocaeli, 41001, Turkey, **ORCID:** 0000-0002-2627-8890

Abstract

Dimethyl carbonate (DMC) is a green solvent and an environmentally friendly fuel additive. It is produced by carbonylation of methanol The production cost of DMC is very high by conventional processes because DMC and methanol form azeotrope and cannot be separated by distillation. Its separation can be performed by pervaporation (PV) economically. Pervaporation (PV) is also an environmentally friendly membrane process in which liquid-liquid mixtures are separated under vacuum with high selectivity. Pervaporation selectivity is dependent on sorption selectivity and diffusion selectivity. Membrane used in the pervaporation process is a semi-permeable barrier and provides selective separation and transport. In PV development of an appropriate membrane material is important for obtaining pure substances. Hydrophilic membrane can separate methanol which is a polar component. Chitosan is a harmless, biodegradable, natural polymer and, despite having hydrophilic properties, cannot withstand aqueous conditions. Therefore, it should be modified by crosslinking. Tetraethoxysilan (TEOS) and tungstophosphoric acid (TPA) can be used as crosslinking agents and additive blending components in membrane production for increasing chemical and mechanical stability. In this study, sorption tests were carried out to determine the usability of chitosan-tetraethoxysilan (TEOS) and chitosan-Tungstophosphoric acid (TPA) hybrid membranes in separation of DMC-Methanol mixture with PV.

1. Introduction

Pervaporation (PV) draws attention as an effective process in separating azeotropic mixtures. It has been explained that PV provides up to 80% energy economy compared to distillation. Ethanol dehydration by PV using polymeric membranes is a commercial application. As a result of its strong interaction and affinity with water, hydrophilic membranes are used in the PV process is conducted in three stages: In the first stage, the components in the feed sorb on the upper surface of the membrane, in the second stage they diffuse through the membrane, in the third stage they are desorb into the lower surface of the membrane in vapor form. Since desorption is very fast, PV is controlled by the first two stages. The membrane; absorbs and passes the component of interest. PV performance depends on the surface properties of the membrane. Surface properties such as hydrophilicity and crystallinity can be

made with a correct crosslinking. The suitability of the PV process can be determined by examining the sorption of the mixtures to be separated on the membrane.

Dimethyl carbonate (DMC) is a versatile compound compatible with the environment. It can be used instead of harmful compounds in the chemical industry. The properties of DMC such as high oxygen content, low toxicity, rapid biodegradation and low impact on air quality; allows it to be used as a fuel additive instead of other additives. Excessive methanol is used in the production of environmentally friendly DMC by carbonylation of methanol, instead of the current production technique that causes environmental pollution. In this method, the formation of methanol azeotrope with DMC causes purification problems. Various separation processes such as extractive distillation, pressure swing distillation, liquid-liquid extraction, adsorption, low temperature crystallization have been tried. PV usage is rare in the literature [1]. In recent years, separation of organic-

---

organic mixtures by PV has gained importance in the chemical and petrochemical industries. Due to the similarity of the physical and chemical structures of organic components, it is difficult to separate them by a conventional separation method such as distillation or other membrane processes. Hydrophobic polymers are used as membrane material to separate organic components. However, these materials do not show high selectivity for organic components. For the separation of DMC-Methanol mixture, hydrophilic materials are preferred, as methanol is polar. Since the interaction of these materials with methanol is stronger than DMC, they have more affinity to methanol. Therefore, methanol selectivity increases with a hydrophilic membrane. In addition, molecular size and polarity difference give higher selectivity. Biocompatibility, biodegradability and non-toxic properties of Chitosan, which is widely used, make it the brightest material of the future. Reactive amine groups together with hydroxyl groups give chitosan hydrophilic properties. These groups in the Chitosan membrane preferentially allow polar components such as water to sorb to membrane and diffuse from the membrane. Since Chitosan has good film forming properties, chemical resistance and high water selectivity, it is also used in the dehydration of many industrial solvents. However, its weakening physical and mechanical properties limit its use in practice because it swells too much in aqueous systems. One way to overcome these limitations is chemical crosslinking [2]. Commonly used crosslinking agents are glutaraldehyde and sulfuric acid. Tetraethoxysilane (TEOS) and Tungsto phosphoric acid (TPA) can be the new effective agents for the modification of chitosan. In addition, with the synergy created by the combination of the properties of two different materials, organic-inorganic hybrid membranes have extraordinary properties and the potential to be the new generation membrane material. When the studies in the literature are examined, it is seen that the sorption selectivity in DMC-methanol separation by pervaporation using chitosan/silicotungstic acid (STA) hybrid membrane is much greater than diffusion selectivity. In other words; separation mechanism is determined by sorption. It has been stated that with the addition of STA to the polymer, the amorphous region is more intense and the preferential methanol sorption increases [3].In another study in which 3-aminopropyltriethoxysilane (APTEOS) was added to chitosan, it was noted that the amorphous region was denser with increasing additive content and the preferential water sorption increased when used for ethanol-water separation by PV [4].

Chitosan is commonly used as blend membrane component in membrane preparation applications due to high hydrophilicity, good film forming character, excellent chemical resistant [3]. Since hydrophilic membranes swell too much in aqueous systems, their weakening physical / mechanical properties limit their use in practice. Therefore, crosslinking agents are used in preparing membranes. Tetraethoxysilane (TEOS) contains four $SiOC_2H_5$ groups and can be a crosslinking agent in membrane production [5]. Tungstophosphoric acid (TPA) which is a heteropolyacid can be used as a modification agent and blending component in membrane production [6]. High hydrophilicity of chitosan causes high swelling in the high polar component content and reduces its stability. Crosslinking with suitable agents is the most appropriate method to increase selective permeability and stability by suppressing this swelling. The crosslinking between the crosslinking agent and chitosan makes the amorphous region in CHM denser and tighter. Thus, the diffusion path of the components is narrowed and the passage of large molecules is prevented. In this study, in order to increase flux and selectivity together, new chitosan hybrid membranes (CHM) were prepared by cross-linking chitosan with TEOS AND TPA. CHM's performances have been evaluated for its use in the separation of Dimethyl carbonate-methanol azeotropic mixture by PV. The effects of TEOS and TPA CONTENTS of CHM and methanol concentration in the feed mixture on sorption properties were investigated.

On the other hand, the importance of the subject can be explained as follows: Worldwide Fossil fuel consumption seriously and negatively our planet. Especially the air pollution caused by these fuels affects seriously and badly affects human health. Recently environmental issues have led countries to use energy sources that are alternative to fossil fuels. Biodiesel, which is an alternative to fossil fuels, is a renewable energy source and its production and consumption have increased in recent years. It is expected that worldwide biodiesel production will reach 23.57 billion liters by 2025 [7]. Biodiesel is obtained from renewable and sustainable sources by transesterification of vegetable oils or animal fats with methanol in the presence of acidic and basic catalysts. Glycerol is formed as a byproduct in a ratio of 1/10 (glycerol/biodiesel) by weight in biodiesel production [8]. In terms of sustainable and environmental economy, it is important to transform glycerol that is produced amounts as waste to other valuable chemicals. Glycerol is a versatile compound in the food, polymer and fuel industries [9]. It is an organic compound which is a low toxicity alcohol that consists of a three carbon chain with a hydroxyl group. Physically, it is a colorless, odorless, viscous, and sweet-tasting compound [10]. It can be transformed to other valuable chemicals by various reaction pathways. In addition, the conversion of glycerol into fuel additives has become an important research area. Glycerol carbonate production is one of these research areas. Glycerol carbonate (GC) (4-hydroxymethyl-1,3-dioxolan-2-one) is a five membered cyclic carbonate that synthesized

from glycerol [11]. It has low toxicity, low flammability, good biodegradability and high boiling point [7]. Additionally, it has potential to be used as a fuel additive that improves the property of fuel. Glycerol carbonate is used in chemical, pharmaceutical, cosmetic, polymer; industries as a surfactant, solvent and plasticizer, and in electrolytes in li-ion batteries [12]. It can be produced by transesterification reaction of glycerol with dimethyl carbonate (DMC) or diethyl carbonate (DEC) in the presence of basic catalysts [13]. This method prevents unfavorable thermodynamic equilibrium, low reaction rate, toxic materials, high reaction temperature and difficult reaction conditions [14]. Pervaporation is a membrane process in which liquid-liquid mixtures are separated under vacuum with high selectivity [15]. Due to low temperatures and pressures, it is considered as one of the clean technologies that can effectively replace traditional separation processes [16].

Additionally, pervaporation is effective process for separating azeotropic mixtures that cannot be separated by classical distillation [4]. For this study, DMC and methanol form an azeotrope mixture at specific concentrations [3]. Membrane used in the pervaporation process is a semi-permeable barrier where selective separation and transport occurs. Since hydrophilic membranes have an affinity for water molecules, they can hold or pass some compounds that dissolve in water [17, 18]. As methanol is a polar compound, hydrophilic membranes are preferred for the separation of the DMC-Methanol mixture. Therefore, methanol selectivity increases with the use of hydrophilic membrane in DMC-Methanol mixtures [3]. Dong et al. carried out pervaporation removal of methanol from methanol/DMC azeotrope using organosilica membranes. These membranes ensured preferential sorption of methanol [19]. Wang et al. prepared SAPO34 zeolite membranes and they used them for Vapor separation of methanol-dimethyl carbonate mixture [20]. Chitosan that is produced from the deacetylation of chitin is a harmless, bio-soluble, natural polymer. Due to its biodegradability, biocompatibility, and no toxicity, it is one of the most common substances used for the separation of mixtures in the present and future [21].

2. Materials and Methods

2.1. Pervaporation

Transportation in membrane is explained by the dissolution diffusion mechanism in pervaporation process. Dissolution diffusion model has three stages [15]:

1. Sorption stage: Transport of the component throughout the liquid boundary layer to the membrane surface.

2. Diffusion stage: Transport of the component throughout the membrane.

3. Desorption stage: Desorption of the component in vapor form from the other side of the membrane.

In the pervaporation process, the separation ability of the membrane is expressed by permeation flux and selectivity. Permeation flux and selectivity are inversely proportional to each other. [22]. Flux is mass flow per unit time, per unit area. Membrane permeability and thickness affects permeation flux [23]. It is calculated as:

$$J = \frac{m}{A.t} \tag{1}$$

J; The total mass flux (kg / m^2.h), m ; The weight of the permeate, A; Effective area in membrane A (m^2), t ; time
Pervaporation selectivity is the passing ratio of the components in the mixture in contact with the membrane [24]. It is calculated as in Eq. 2:

$$\alpha_{pv} = \frac{y_a/y_b}{x_a/x_b} \tag{2}$$

y_a and y_b are permeate concentrations of a and b, x_a and x_b are feed concentrations of a and b.
Sorption selectivity according to the dissolution-diffusion model defines the selectivity of the sorption process and is shown in Eq. 3:

$$\alpha_{sorp} = \frac{(z_a/z_b)}{(x_a/x_b)} \tag{3}$$

z_a and z_b are component concentrations in the membrane, respectively and x_α and x_b are concentrations in the feed.

$$\alpha_{pv} = \alpha_{sorp} \times \alpha_{dif} \tag{4}$$

Pervaporation selectivity is equal to multiplication of sorption and diffusion selectivities. The relationship between them is shown in Eq. 4 [25].

In general, pervaporation selectivity is related to sorption selectivity. PV operation proceeds through sorption. Therefore sorption tests provide information about the separability mixtures by PV.

2.2. Chemicals

Tungstophosphoric acid (TPA) (powder form) Tetraethoxysilane (TEOS) (99.0%), Chitosan (CS) from Sigma Aldrich; Methanol (99.0%) and Acetic Acid (99.0%), HCl (99.0%), methanol, dimethyl carbonate (DMC) were purchased from Merck.

2.3. Membrane Preparation Method

TPA/CS and TEOS/CS hybrid membranes were prepared from solution by pouring-evaporation method. The

powder chitosan, 1% by weight separately for both hybrid membranes, was dissolved in 1% acetic acid solution at 40 ° C for 24 hours until the solution became homogeneous. To the prepared homogeneous chitosan solutions, TPA was added in different proportions as 2, 4, 6, 8,10% and TEOS was added in different proportions as 1,3,5% to form a homogeneous mixture. They were mixed for a day. 0.5 M HCl was added to the TEOS loaded CS membrane for crosslinking. The homogeneous solutions obtained were poured into separate petri dishes and allowed to dry in a vacuum oven at 40 ± 1 ºC. TPA was used both as additive material and as crosslinking agent while TEOS was used only as additive material.

2.4. Sorption Test for Swelling Performance

The doped membrane films prepared as chitosan-teos and chitosan-tpa were weighed. The dry weights of the prepared doped membranes were weighed and prepared for use in sorption experiments (W_{dry}) and then immersed in solution in pure methanol and in different methanol concentration ranges for 24 hours at room temperature. At the end of 24 hours, the doped membrane pieces were removed from the solution mixtures and reweighed (W_{wet}). The formulation in Eq.5 is used to calculate the degree of swelling

$$Swelling\ Degree, (\%) = \frac{W_{wet} - W_{dry}}{W_{dry}} x100 \qquad (5)$$
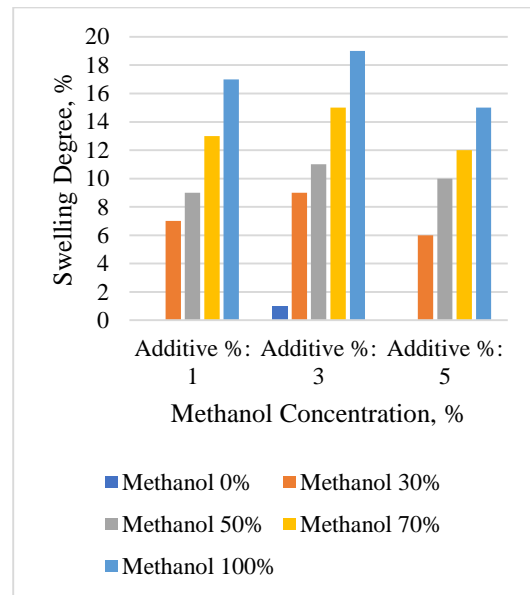
3. Results and Discussion

The swelling degree values for DMC / methanol mixture in TPA-added chitosan membrane were given in Figure 1.
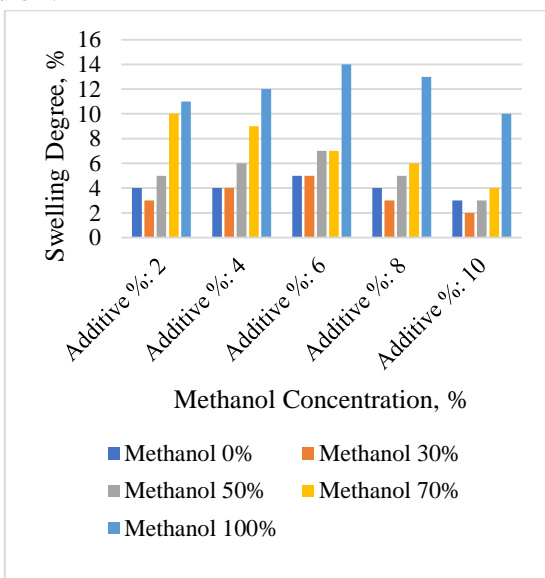
Figure 1. Swelling degree values for DMC/methanol mixture in TPA added chitosan membrane.

As shown in Figure 1 swelling increased by TPA addition until the TPA additive is 6%. After that value of swelling decreased with increased TPA addition. This may be because the additive material causes agglomeration in the polymer. All TPA doped membranes showed swelling in the pure DMC when the solution did not contain methanol. It indicates that these membranes will also pass DMC in the pervaporation application where DMC is sorbed.

The swelling degree values for DMC / methanol mixture in TEOS added chitosan membrane were given in Figure 2.

Figure 2. Swelling degree values for DMC/ methanol mixture in TEOS added chitosan membrane.

As seen in Figure 2, the swelling increased up to a TEOS of addition 3% and then decreased. Agglomeration may have caused the occurrence of this decrese. Only membranes with 3% TEOS added showed swelling in pure DMC. This indicates that the membrane will also pass DMC in the pervaporation application. The swelling degree value of the membrane with an added TEOS ratio of 1% is close to the one with the added TEOS ratio of 3%. The membrane with a TEOS ratio of 1% did not sorb. DMC. For this reason, it was understood in the study that the membrane loaded with TEOS at a ratio of 1% has optimum swelling degree and it can also be used in the pervaporation application. The relationship between methanol concentration and swelling degree for 6% TPA added membrane which shows the highest swelling degree among TPA doped membranes, was given in Figure 3.
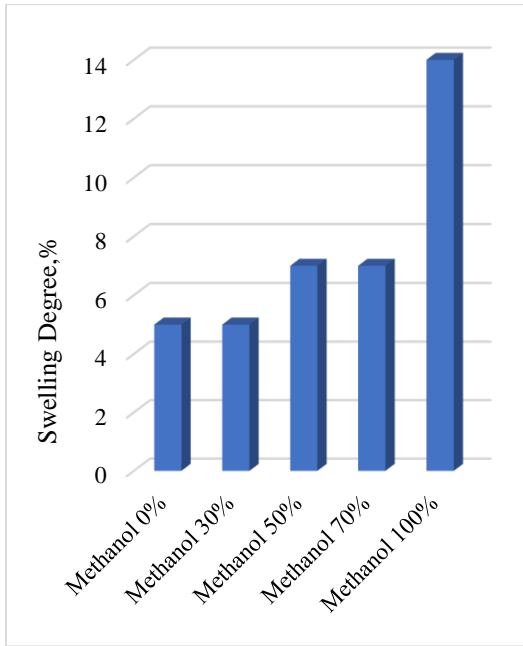
Figure 3. Methanol concentration and Swelling degree relationship for 6% TPA added membrane.

When looking at the relationship between the concentration of methanol and the degree of swelling in the 6% TPA added membrane, which has the highest sorption capacity for pure methanol, it was seen in Figure 3 that the swelling degree increased with the increase in methanol concentration and this membrane also retained DMC. The relationship between methanol concentration and the swelling degree in the chitosan membrane with a TEOS ratio of 1% was given in Figure 4.
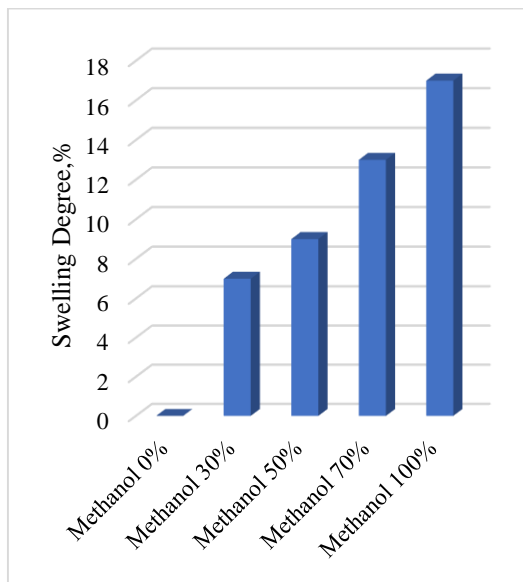
Figure 4. Methanol concentration and swelling degree relationship in chitosan membrane with 1% TEOS ratio.

As can be seen in Figure 4, it was observed that the degree of swelling of the chitosan membrane with 1% TEOS

ratio increased as the methanol concentration increased. It was observed that this membrane did not hold DMC. The results of swelling degree values obtained from sorption tests in pure methanol for Pristine chitosan membrane and doped chitosan membranes that had high swelling values were given in Figure 5.

Figure 5. The swelling degrees of pure methanol for pristine chitosan and membranes with high swelling values.
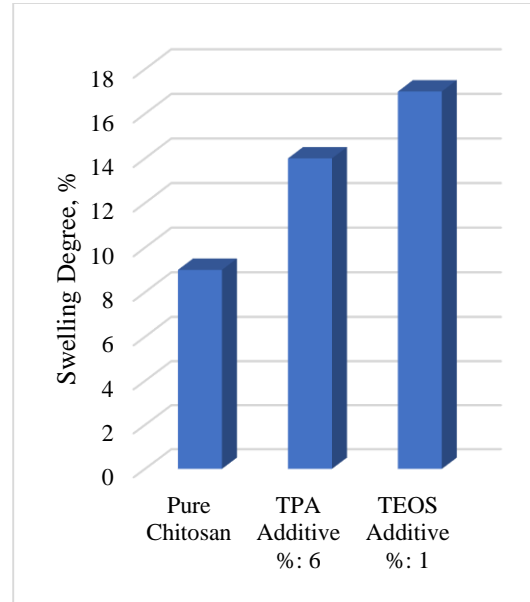
When the values of swelling degree that show sorption results for pristine chitosan membrane and added membrane in pure methanol were analyzed it was decided that chitosan membrane with 1% TEOS ratio was the most suitable membrane. This outcome was deduced from Figure 5.

4. Conclusions

In this study, sorption tests were conducted to examine the usability of chitosan-tetraethoxysilan (TEOS) and chitosan-Tungsto phosphoric acid (TPA) hybrid membranes in separation of DMC-Methanol mixture by PV. CHM was formed by crosslinking between chitosan and additive. The effects of additive content and methanol concentration in the feed on the degree of swelling, a measure of sorption, were studied. As the content of the additive increased, the amorphous region in CHM increased and the hydrophilicity increased. Sorption was affected by the content of additives in CHM and the concentration of methanol in the feed. It was observed that the degree of swelling increased with the concentration of methanol in the feed. It has been observed that the degree of swelling increases up to a certain amount of additive and decreases after that point. This is because excess crosslinking restricts the movement of polymer chains and prevents excessive swelling. The performance of

CHM has increased compared to the pristine Chitosan membrane. It has been understood that the prepared composite hybrid membrane can be used in the separation of DMC-Methanol azeotropic mixtures.

The sorption tests of chitosan membrane and TPA and TEOS loaded chitosan membranes for DMC/methanol mixtures were made. TPA loaded chitosan membranes have ability of sorption for both methanol and DMC while TEOS loaded chitosan membranes have ability of sorption for methanol only. 1% TEOS loaded chitosan membrane has a potential for separation of DMC/methanol mixtures by pervaporation.

Declaration of Ethical Standards

The author(s) of this article declare that the materials and methods used in this study do not require ethical committee permission and/or legal-special permission.

Conflict of Interest

The authors declare that they have no known competing financial interests or personal relationships that could have appeared to influence the work reported in this paper.

Acknowledgements

References

[1] Chen J., Liu Q., Fang J., Zhu A., Zhang Q., 2007b. Composite hybrid membrane of chitosan–silica in pervaporation separation of MeOH/DMC mixtures. Journal of Colloid and Interface Science, **316**, pp. 580-588.

[2] Won W., Feng X., Lawless D., 2003. Separation of dimethyl carbonate/methanol/water mixtures by pervaporation using crosslinked chitosan membranes. Separation and Purification Technology, **31**, pp.129-140.

[3] Chen J., Liu Q., Zhu A., Zhang Q., Fang J., 2008. Pervaporation separation of MeOH/DMC mixtures using STA/CS hybrid membranes. Journal of Membrane Science, **315**, pp. 74–81.

[4] Chen J., Liu Q., Zhang X., Zhang Q., 2007a. Pervaporation and characterization of chitosan membranes cross-linked by 3-aminopropyltriethoxysilane. Journal of Membrane Science, **292**, pp. 125–132.

[5] Tong B., Cheng C., Khan M., Wu Y., Xu T., 2017. Double cross-linking PVA-SiO2hybrid membranes for alkali recovery. Separation and Purification Technology, **174**, pp. 203-211.

[6] Ponce M. L., Prado L., Ruffmann B., Richau K., Mohr R., Nunes S. P., 2003. Reduction of methanol permeability inpolyetherketone–heteropolyacid membranes. Journal of Membrane Science, **217**, pp. 5-15.

[7] Chen W., Bhaskar T., Ong H., 2020. Biomass Processing for Biofuels, Bioenergy and Chemicals, Printed Edition of the Special Issue Published in Energies. MDPI, Basel, Switzerland.

[8] Trifoi A., Agachi Ş. P., Pap T., 2016. Glycerol acetals and ketals as possible diesel additives. A review of their synthesis protocols. Renewable and Sustainable Energy Reviews, **62**, pp. 804-814.

[9] Nanda M., Yuan Z., Qin W., Ghaziaskar H. S., Poirier M. A., Xu C.C., 2014. Thermodynamic and kinetic studies of a catalytic process to convert glycerol into solketal as an oxygenated fuel additive. Fuel, **117**, pp. 470-477.

[10] Talebian-Kiakalaieh A., Amin N. A. S., Najaafi N., Tarighi S., 2018. A Review on the Catalytic Acetalization of Bio-renewable Glycerol to Fuel Additives. Frontiers in Chemistry, **6**, pp. 573.

[11] Christy S., Noschese A., Lomelí-Rodriguez M., Greeves N., Lopez-Sanchez J. A., 2018. Recent progress in the synthesis and applications of glycerol carbonate. Current Opinion in Green and Sustainable Chemistry, **14**, pp. 99-107.

[12] Teng W. K, Ngoh G. C., Yusoff R., Aroua M. K., 2014. A review on the performance of glycerol carbonate production via catalytic transesterification: Effects of influencing parameters. Energy Conversion and Management, **88**, pp. 484-497.

[13] Kumar P., With P., Srivastava V. C., Gläser R., Mishra I. M., 2015. Glycerol Carbonate Synthesis by Hierarchically Structured Catalysts: Catalytic Activity and Characterization. Industrial and Engineering Chemistry Research, **54**, pp. 12543-12552.

[14] Wang S., Hao P., Li S., Zhang A., Guan Y., Zhang L., 2017. Synthesis of glycerol carbonate from glycerol and dimethyl carbonate catalyzed by calcined silicates. Applied Catalysis A, General, **542**, pp. 174-181.

[15] Jyoti G., Keshav A., Anandkumar J., 2015. Review on Pervaporation: Theory, Membrane Performance, and

Application to Intensification of Esterification Reaction. Journal of Engineering, **2015**, pp.1-24.

[16] Cannilla C., Bonura G., Costa F., Frusteri F., 2018. Biofuels production by esterification of oleic acid with ethanol using a membrane assisted reactor in vapour permeation configuration. Applied Catalysis A, General, **566**, pp. 121-129.

[17] Mulder M., 1996. Basic Principles of Membrane Technology, Second ed. Kluwer Academic Publishers, Dordrecht, Netherlands.

[18] Drioli E., Giorno L., 2016. Encyclopedia of Membranes, illustrated ed. Springer, Heidelberg. Berlin.

[19] Dong G., Nagasawa H., Yu L., Wang Q., Yamamoto K., Ohshita J., Kanezashi M., Tsuru T., 2020. Pervaporation removal of methanol from methanol/organic azeotropes using organosilica membranes: Experimental and modeling. Journal of Membrane Science, **610**, pp. 118284.

[20] Wang M., Li M., Chang N., Gao L., Wang M., Zhang Y., 2018. Vapor separation of methanol-dimethyl carbonate mixture on SAPO-34 zeolite membrane. Journal of Membrane Science, **565**, pp. 311-321.

[21] Ismail A. S., Darwish M. S. A., Ismail E. A., 2016. Synthesis and characterization of hydrophilic chitosan-polyvinyl acetate blends and their sorption performance in binary methanol–water mixture. Egyptian Journal of Petroleum, **26**, pp. 17-22.

[22] Huang R. Y. M., Yeom C. K., 1990. Pervaporation separation of Aqueous mixtures using crosslinked poly (vinyl alcohol) (PVA), II. Permeation of Ethanol-Water mixtures. Journal of membrane science, **51**, pp. 273-292.

[23] Feng X., and Huang R. Y. M., 2007. Liquid Separation By Membrane Pervaporation: A Review. Industrial & Engineering Chemistry Research, **36**, 1048-1066.

[24] Baker R. W., 2000. Membrane technology and application, second ed. John Wiley & Sons, West Sussex, England.

[25] Hilmioglu N., 1998. PhD Thesis, IPA/Su ve MTBE/Metanol Azeotropik Karışımlarının Pervaporasyon ile Ayrılması, İTU.

Kocaeli University

Kocaeli Journal of Science and Engineering
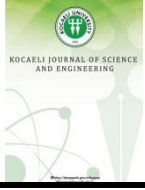
Towards a New Walking Evaluation Approach: Power of Surveys and Route-based Evaluations in GIS Environment

Hediye TUYDES-YAMAN [1] (iD) , Pınar KARATAS-SEVINEN [2, *] (iD) , Zeynep Pınar ONCU [3] (iD) , Gülcin DALKIC-MELEK [4] (iD)

[1] Department of Civil Engineering, Middle East Technical University, Ankara, 06800, Turkey, **ORCID:** *0000-0003-2053-992X*
[2] Department of Civil Engineering, Middle East Technical University, Ankara, 06800, Turkey, **ORCID:** *0000-0001-9998-2849*
[3] Garage Atlas Tasarim Teknoloji Anonim Şirketi, İstanbul, 34075, Turkey, **ORCID:** *0000-0002-1998-6944*
[4] Department of Civil Engineering, Middle East Technical University, Ankara, 06800, Turkey, **ORCID:** *0000-0001-9663-657X*

Abstract

Walking is a critical mode to be encouraged in sustainable urban mobility plans (SUMPs). However, the lack of analysis methodology is making it challenging to detect walkability aspects necessary to develop better policies. Middle East Technical University (METU) Campus was designed with a pedestrian-friendly layout which has been threatened recently by different factors (i.e. enlargement of the campus, changing traffic volumes, etc.). This necessitated further investigation of walking and walkability in the campus, which was the main scope of the most recent survey, designed to investigate a) pedestrian perspective and b) walking limits on campus. While the former was investigated via traditional questions, the latter was sought after via map-based 1844 routes from 623 participating students. Besides the descriptive statistics performed by the responses to the traditional evaluation questions, the route-based data resulted in enriched analyses, proving the power of the latter in evaluating walkability, which has a spatial variation by nature. Consideration of both traditional survey approaches accompanied by the route-based investigations enabled the development of a more comprehensive understanding of walkability of the study area, which should be used in the evaluation of pedestrian mobility in urban pedestrian analysis zones, i.e. city centers, metro station capture zones, campuses, etc.

1. Introduction

Walking is one of the main modes of transport which had an effect on many different areas such as health, sustainability, and planning. Two key concepts, "walking (activity)" and "walkability (quality of walking)", are required [1]to understand this transportation mode and support it as a part of our sustainable urban development plans. Walkability is identified as "walking- friendly" [2], which is supported by the good-quality walking environment (density, capacity, directness, etc.), identification and comparison of the conditions with different assessment techniques (reviewing, auditing, and rating). More recently, especially within the European Union (EU) region, local governments are encouraged to analyze and promote more sustainable modes (walking,

biking) and develop their sustainable urban mobility plans (SUMP), which are in process for Konya and Eskişehir, and being contracted out for other metropolitan cities such as İzmir, Ankara, etc. However, it is critical to developing an evaluation method to assess the current level of walkability as well as walking preferences of the pedestrians to develop policy tools encouraging it further, which requires consideration of both walking network infrastructure as well as pedestrian mobility data, analyzed in an engineering perspective. This paper focuses on assessment of both the traditional survey technique and GIS-based route evaluation option to support development of new pedestrian mobility evaluations in the future.

Within the scope of this study, both the conceptual and route-based walkability assessments were performed to compare the strength and weaknesses of both data collection methods. While the responses to the traditional survey questions enabled the statistical evaluation of sufficiency and the importance of selected walkway

---

* Corresponding Author: pkaratas@metu.edu.tr

features, the route-based data provided spatial distribution of the most used walkway segments. Gender differences in walking behavior are sought through both data types. Using the latter, it is possible to evaluate zone/building-based walkability [5]. Finally, a list of recommendations is provided to further improve walkability data collection and evaluation techniques, which may contribute to the further understanding and encouragement of walking not only on METU campus but other campuses and urban regions.

The case study is based on various walking and walkability evaluations performed for the Middle East Technical University (METU) Campus. The campus serves a population of approximately 30,000 people and was originally designed as a "walking-friendly" layout with a Central Pedestrian Alley (CPA) connecting all the academic buildings (old campus buildings) in the academic loop with no motorized traffic exposure (Figure 1). The continuation of the walkway among the recreational and dormitory regions made walking a major mode on the campus, but the expansion of the campus-built area (new campus buildings) over the years overturned this dominancy. Also, despite the existence of two metro stations at the northern border of the campus (at A1 and A2 entrances), the long walking distance (almost 2km to the nearest academic buildings) has been forcing campus users to use motorized modes more. Previous efforts on different pedestrian mobility data collection and estimation of Pedestrian Level of Service (PLOS) [3, 4] were further followed by a detailed survey conducted aiming to evaluate METU campus walking patterns among students, as well as in-campus transportation. In addition to traditional questions evaluating the key walkability factors discussed in the literature, a map-based inquiry regarding walking routes from departments to the most common destinations was included.
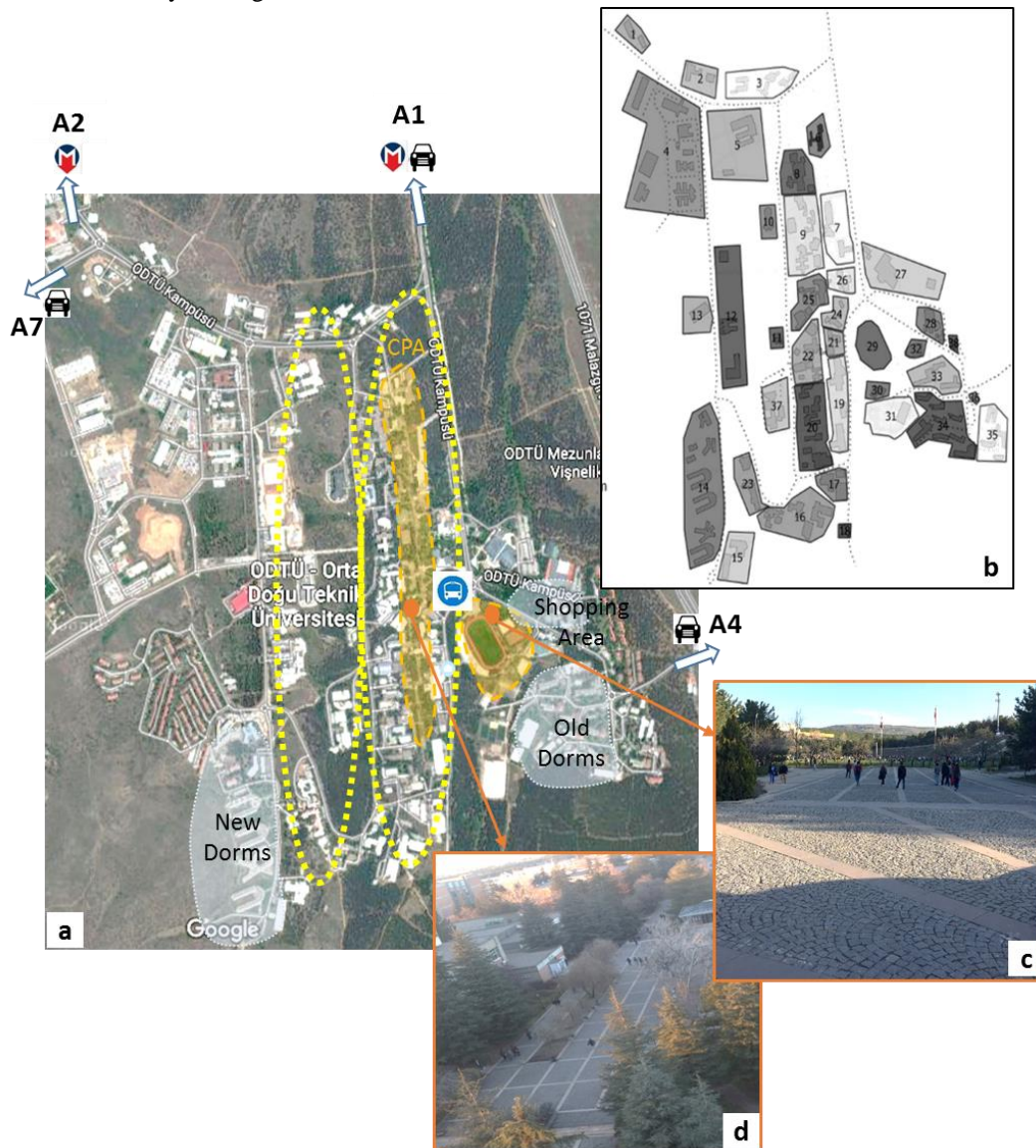
Figure 1. a) METU Campus layout b) Department-based walkability analysis zones c) Walkways around the stadium d) Central Pedestrian Alley serving the first academic loop.

2. Literature Review

The indicators of "pedestrian-friendly design" were investigated, for which three major aspects of walkability were defined as connectivity, quality of road network, proximity, etc [6]. In urban planning, the promotion of sustainable urban neighborhoods was discussed in association with walkability [7]. Results showed that wider walkway width, free barrier walkways, and more shaded walkways could encourage pedestrians to walk. With a planning focus, Blecic et. al. [8] presented the urban design support tool on pedestrian accessibility and walkability of places, which generates urban design, besides the evaluation process. As a recent perspective, Dovey and Pafka [9] focused on the concept of walkability as a combination of three key factors; density, functional mix, and access; but this concept should not be based on actual walking levels. In the study walkability is directly connected to the physical environment and facilities.

Shorter and simpler walkability evaluation tools have also been proposed by different researchers, such as a simple checklist by selecting some local destination points [10]. Scottish Walkability Assessment Tool which is an auditing-based tool, was designed to assess walkability according to functional elements (walking surface and permeability), safety (personal and traffic), aesthetic (streetscape, architecture, views), and destinations ("parking, land use mix, services, public transport, parks") [11]. Pedestrian Environment Index (PEI) was used to measure pedestrian friendliness in Chicago [12]. In the index available data for planners was used combining four components: i) land-use diversity, ii) population density, iii) commercial density, and iv) intersection density. The methodology investigated the areas for each sub-traffic analysis zone and component at a level and produced a comparative evaluation between zones. A comprehensive index for path walkability assessment (PWA) was developed based on pedestrian decision-tree-making (DTM) with 92 variables under 3 layers [13]. Model converts qualitative data to a walk score for shopping and retail walking in Taman University, but applicable to any region in the world. Synthetic Index of Walkability of public spaces (ISWAT) proposed a multi-criteria analysis and space syntax technique to determine walkability for different purposes [14]. The model determines scores for each indicator for 4 main categories (quality, movement potential, presence of anchor places, and distance from services and amenities) and summed up a value of ISWAT, which defines the walkability rating according to pre-defined intervals. A recent study combined street design measurement with thermal comfort under The Street Walkability and Thermal Comfort Index (SWTCI),

combining a questionnaire survey (measure 21 street design indicators), observations (evaluate pedestrian comfort indicators), and in situ measurements (include weather information) [15]. The method revealed the highest SWTCHI score when thermal perception is neutral, lowest when the thermal sensation is warm. An open-source website, "Walk Score®", had a patented system that analyzed hundreds of possible walking routes for the given addresses to nearby amenities and awarded points accordingly [16]. While amenities within a 5-minute walk were given maximum points, the point awarding decreases for the distances up to 30-minute walk. Any location that has 50 or fewer points was determined as "car-dependent". The neighborhood where METU Campus is located was rated as a score of 29 points (car-dependent), while METU campus (mostly the housing units with many catering options) were rated as 80 points (very walkable) and METU library was rated as 86 points (very walkable).

2.1. Walking Behavior Analysis via Surveys

A series of studies in Putrajaya, Malaysia, focused on different aspects of walking behavior and pedestrian perception [17, 18, 19]. Three walking behavior features (speed, direction, and experience) were studied in urban and rural regions, which revealed very small differences. In the follow-up survey, walking times (from home to the nearest community facilities) were asked to pedestrians to understand their perception and among the socio-demographic variables, household income and gender were found to have a small effect. In the evaluation of walking experience from "safety and security" and "convenience and attractiveness" perspectives, important aspects included the street lightenings, street crossing signals, safety during walking in the nighttime, volume of traffic and traffic speed along a nearby street, tree existence, and awning, environment attractiveness/ building articulation, cleanness, street furniture for resting, etc. In Wuhu, China, based on the street characteristics (length, location, and width) and pedestrian behavior characteristics (trip purpose, travel time information, trip frequency, etc.) Liu et. al. [20] suggested improving the quality and increasing the attraction of walking by a combined design (with business activity, landscape, circulation, transit services, and beyond). For a regional coastal Australian city, Humpel et al. [21] conducted a survey focusing on the relation between environmental attributes and different purposes of walking behavior (defined as "general neighborhood walking", "walking for exercise", "walking for pleasure" and "walking to get to and from places"). Weather, aesthetics, accessibility, and location were associated with neighborhood walking; safety and

accessibility were important in walking for pleasure, while weather and aesthetics were found to be associated with walking for exercise. In the San Francisco Bay Area, a "perception-based composite walkability index" was developed by three different surveys [22]. Among 42 "Path Walkability Indicators" defined (related with curb-to-curb roadways, pedestrian crossings, buffer zones, sidewalks and their facilities, street scale and enclosure, closer buildings, and their properties) 22 of them were used in the final formula. Investigated London Travel Demand Survey (LTDS) and Health Survey for England (HSfE) were applied to get predictors of walking variables with their direct effect on physical activity [23]. Small differences were highlighted in the results between the ethnic groups, age, and car ownership. Effect of street-level greenery investigated in Hong Kong, revealing high relation, and associated with total walking times [24]. In the study two-layer model was developed considering both associations of greenspaces and odds of walking and sensitivity analysis between greenspaces and total walking time. Li et.al. [25] focused on exploring the impact of perceptions and attitudes on walking in the historical neighborhood. Results reveal different perceptions and attitudes according to income, age, and employment status, and had a significant effect on walking frequency. Young, employed, and higher-income people walk less than the others. At Ohio State University a web-based survey was conducted to examine transportation choices of individuals conducted by getting information about mode choice and the factors affecting the choice [26]. In another study by Lee and Shepley [27], the aim was to examine how students evaluate the walking path and route characteristics when they are distracted by using the phone. The study used Analytical Hierarchy Process (AHP) method and results indicated that "Smartphone walkers" found the safety and quality of routes more important, while walkers without phones considered the shortest distance and positive walking experience to be important factors in their route choices.

When the studies investigated in Turkey are evaluated, it was seen that there are several walking behavior related researches conducted in İstanbul, Ankara, İzmir, Adana, Edirne [28 - 34]. In a study conducted in Istanbul [28], it was seen that utilitarian and recreational walking were influenced by perceived neighborhood safety and busy places were stated as a good place for both types of walking. A study conducted in Bursa [33] examined the principal factors affecting walkability by a survey conducted with 200 participants and the results showed that the most important factors were traffic safety, crime security, and connectivity.

A recent study by Rashidi [35] focused on walkability in the METU Campus and uses different methods such as direct observation, archival studies spatial analyses, and surveys with 240 users in different walking paths, etc. The study focused on the safety and security issues regarding the physical features, sense of safety, and traffic safety of the university campus. Among the walking routes, uncomfortable and comfortable ones were detected based on the results of the survey study and it was indicated that female participants feel significantly less safe than male users at night-time walks; they think lighting is not sufficient.

2.2. GIS-based Walking and Walkability Analysis

Starting in the early 1990s, walking access to the transit systems and development measures were investigated with Geographic Information System (GIS) to gain insights into the measurement of the pedestrian access, the effect of the street configuration on the pedestrian access, and whether the walking distance influenced the transit mode choice [36]. There are an increasing number of studies and applications suggesting the use of walkability, especially to develop a walkability index. Pedestrian-environment areas were evaluated in GIS by three visualization and quantification techniques: "street network classification (quality)", "pedestrian catchment areas (proximity)" and "intersection intensity (connectivity)" [37]. In the study, TIGER data was used in the GIS-based Pedestrian Assessment Tool. The relationship between pedestrian access and transit preferences was studied at the district levels based on environmental attributes such as dwelling density, street connectivity, land-use mix, and net retail area and sociodemographic characteristics of pedestrians [38]. Walkability was studied considering proximity and connectivity characteristics with a spatial data set to define a GIS-based "Walkability Index" in Australia [39]. Also, additional the street level audits and participant responses Hajna et al. [40] studied by GIS to derive land use mix, street connectivity, and residential density. As an alternative way, Cubukcu et al. [41] used the GIS method to measure the street level walkability "Walk Score®" for developing countries. Izmir, Turkey was evaluated by this method under 6500 street segments, and calculated the walkability score based on betweenness, centrality - and accessibility scores derived from the street network and land use. More recently, Ellis et al. [42] employed the six connectivity measures ("intersection density", "link-node ratio", "pedestrian route directness", "pedshed", "metric reach" and "directional reach") using the Belfast footpath network, North Ireland. Results reflected that metric reach and intersection density have seemed like the best

measures for connectivity.

GIS can also improve the analysis and the visualization of pedestrian activities. For the analysis of the change in walking behavior on a university campus due to the construction of additional 14 buildings, a "walking diary" included walk trip data (start and finish time, route, social content as in walk alone or with a group, and purpose) was conducted with users via a map-based survey [43]. When the data was mapped in the GIS environment and analyzed, results showed significant increases in walking distances. Sun et al. [44] studied the metro stations in Beijing, China to see the influence of the local environmental characteristics on walking behavior by the empirical data. In a survey about the walking trips beyond the metro station, the information on walking time from the station, destination, perceived environmental characteristics as well as objective built environmental measures, were coded in GIS with the walking routes to compare the perceived and measured built environment characteristics. Mean walking time from the stations was found as 8 minutes, and both perceived and measured travel times decreased with greater connectivity.

In a study conducted for Adana, Turkey [31], the level of serviceability of urban emergency shelters within maximum capacity, usability, sufficiency, and a certain walking time limit was evaluated by using spatial analysis techniques of GIS-Network Analyst and methodology was proposed. Another study [34] examined the walkability in

terms of urban design principles in 5 cities of Turkey using a hybrid method (fuzzy logic, space syntax analysis, and GIS). The study showed that the spatial design of the Turkish cities mostly provides the needs of motor vehicles rather than pedestrians and the success level of walkability was found as very low.

3. Methodology

METU Campus and Transportation Survey was designed to have information on i) perception of sustainability and sustainable transportation, ii) travel characteristics regarding access to METU and in-campus transportation, and iii) perspectives on traffic safety. The questionnaire had five main sections (see Table 1), starting with socio-demographic data collection (Section A). Walking and walkability were evaluated in Section D, which had both the traditional questions (Part 2) as well as the map-based walking route collection (Part 3). The survey was conducted face-to-face with METU students in two rounds in the Fall and Spring semesters. To estimate building/zone-based walkability on campus, sampling was planned proportional to the departmental student populations aiming 5%-10% rate. Based on the preliminary evaluation, revisions were made in the second round in some parts of the survey, which are discussed in detail below.

Table 1. 1Summary of the Survey Study

Survey Sections	Round 1	Round 2
A) Socio-demographic information	-Age, gender, income, on-/off-campus residence, registered department at METU, private car ownership, METU parking permit ownership	*-Remained as same-*
B) Perception of "sustainability/ sustainable transportation"	Technical definition, classes taken, related actions, METU Campus perception	---
C) Access to METU campus	*Not Included in this study*	*Not Included in this study*
D) In-campus transportation	**Part 1: Frequently used modes** (frequency and origin-destination)	**Part 1:** *Remained as same*
	Part 2: Assessment of walking conditions on: - sufficiency of walkway infrastructure and walking environment -the importance of proposed infrastructure improvements	**Part 2:** Assessment of walking conditions -sufficiency of walkway infrastructure and walking environment
	Part 3: Map-based walking routes from departments to stated destinations	**Part 3:** *Remained as same*
Survey Dates	November-December 2014	May 2015
Sample Size	307 participants	316 participants

3.1. Participant Profile and In-Campus Mode Choice

The survey study was conducted in two rounds,

which had almost equal sample sizes (see Table 2). Male and females were represented almost equally to be able to study the possible gender effects. Equal distribution among different classes was considered to catch academic

schedule differences. Note: Proportionality between the students residing in the city, and the dormitories was maintained according to the campus proportionality (about 1/3 of the total population lives on the campus).

Analysis of the responses to the Part 1 question in Section D, showed that 67.9% of the students preferred walking as their first choice in-campus trips, followed by in-campus shuttle services preferred by 11.3%. Among the second-best choice, students reported in-campus shuttles (29.6%) and hitchhiking (27.0%) while walking was preferred by 22.5% of the students.

Table 2. Participant Profile for METU Campus and Transportation Survey- Student Perspective

		Round 1 (N=307)			Round 2 (N=316)		
	N		F	(%)	N	F	(%)
Gender							
Male	(307)		153	49.8	(315)	149	47.3
Female			154	50.2		166	52.7
Housing Location							
On-campus	(306)		115	37.5	(315)	120	38.1
Off-campus			191	62.4		195	61.9
Class							
Prep School			18	5.9		20	6.3
1st year			45	14.7		39	12.3
2nd year	(307)		79	25.7	(316)	73	23.2
3rd year			70	22.8		107	33.9
4th year			73	23.8		64	20.3
Graduate			20	6.5		15	4.8

3.2. Student Perception on Sustainable Transportation

The participants were not technically familiar with the concept of sustainability in general and did not take any lessons on the subject. Yet, they commented that the concepts frequently found in the literature (alternative energy sources, transportation, global warming, energy saving, biodiversity, etc.) should be discussed under sustainability. The sustainable transportation was expected to have positive economic, environmental, and social contribution against major problems such as traffic, air pollution, noise, global warming, depletion of natural resources. Bicycle roads, environmentally friendly vehicles, high pedestrian access, ITS, high-quality public transportation were evaluated as very important sustainable transportation options. Evaluating METU Campus according to sustainable transportation vision, they concluded that campus was partially sufficient via in-campus ring services, personnel ring services, paratransit mode, walking areas, and vehicular roads, but, insufficient in terms of bicycle infrastructure and parking lots.

3.3. Traditional Survey Questions regarding Walkability

Part 1 (of Section D) focused on detection of major modes of in-campus transportation; a question was sought after the perspective of students on the sufficiency of walking environment/infrastructure based on selected 9 factors (i.e., quality of pavement, continuity, etc.). The following question required the rating of the importance of the proposed improvements on 20 factors regarding walkway infrastructure and walking environment (i.e., increasing the width of walkways, etc.) from "1 (not important)" to "4 (extremely important)".

Responses to the sufficiency question included trivial answers; furthermore, a simple choice of "sufficient/insufficient" did not reveal much about students' perception and some respondents wanted to rate the level of it. Stated levels of importance of certain features only validated the existing literature without contributing much. In the second round, these questions were replaced by a question seeking ratings of the sufficiency of 20 factors.

3.4. Walking Route Data Collection

The map-based route collection part had the exact question: "What are the destinations that you generally WALK from YOUR DEPARTMENT? Please indicate the route do you commonly take on the map and how much time it takes". The responses were drawn and noted on the METU map provided in the questionnaire by the pollster (see Figure 2a). While recording the route, the origin was selected as the department of the student, while the destination was selected as the building/zone (cafeteria, dormitory region, etc.) declared by the student on the map.

For each route, students' perceived time of walking was also recorded to be used for further studies.

The study area was divided into 38 zones by considering a major walking alley, the closeness of departments, and common behaviors of participants as seen in Figure 1b. While nearby buildings (i.e. Food Engineering and the Petroleum and Natural Gas Engineering buildings) are collected under the same zone (Zone 21), some buildings were shifted to another zone (Zone 10), if divided by vehicular roads or are not within walking perimeter of another one.

3.5. Digitization in GIS Environment

The stated walking routes were digitized in the GIS environment using a base map with all vehicular and pedestrian roads (sidewalks and pedestrian alleys) and buildings (see Figure 2b). Pedestrian roads were defined with links and nodes, where different entrances of large buildings were designated with different nodes to digitize routes more precisely. All routes were digitized individually by selecting every link one by one using the base map merged in a separate layer in Quantum GIS environment and saved as a shapefile (see Figure 2b). To validate the data, topological checks were performed; errors, such as unsnapped lines and nodes, were corrected automatically by the auto snapping tool of ESRI ArcGIS software. The manual overdrawn parts of the routes showing the destination zone roughly were not digitized, as they did not carry any specific information about the destination but were extended merely for taking notes (such as the name of the region). The digitalization process produced data for a total of 1844 routes from 623 participants.
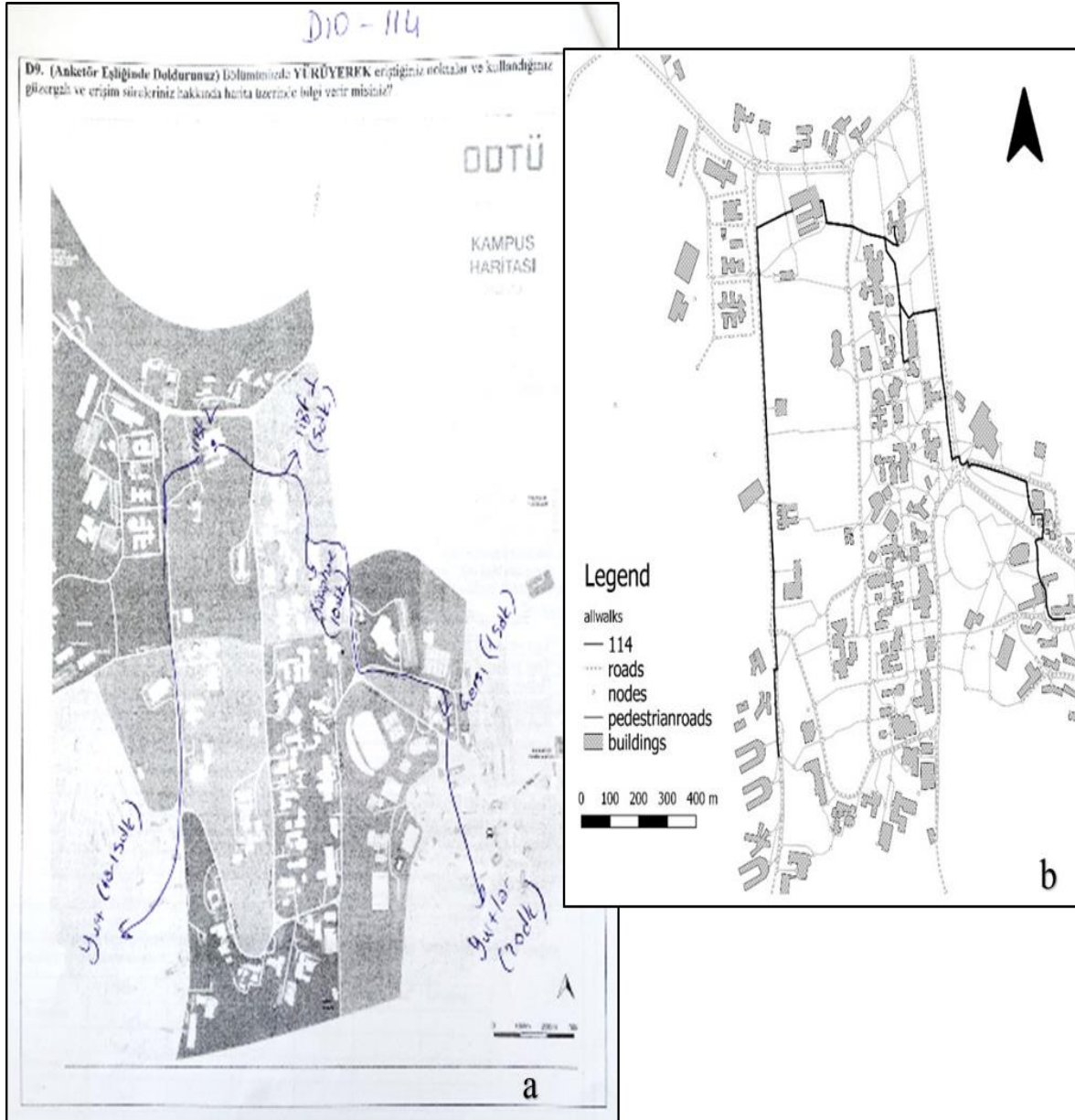

Figure 2. Walking route example of a respondent a) as coded in the survey b) digitized in GIS.

4. Evaluation of Perception of Walkability

4.1. Student Perception of Walkability Environment in METU Campus

Responses to traditional questions were analyzed in IBM SPSS Statistic V23 software. Descriptive statistics of Round 1 (see Table 3) revealed that more than half of the students found the walking infrastructure mostly enough, whereas almost 40% found it insufficient. A large majority had reported consensus on insufficiencies for lightning, safety precautions, and arrangements for disabled users. Rating of the importance of 20 selected factors revealed responses parallel to the findings in the literature: Walkway capacity, continuity, and width were identified as partially important features, while the improvements for sheltering against weather conditions, shortcuts, arrangement for disabled users, infrastructure, and lightning were found highly important. The existence of sidewalks on both sides of the road and the sidewalk widths were extremely important, as in the literature, as well as a decrease in man-made obstacles (i.e. signs, electric poles). However, any improvement to decrease in trees on sidewalks was not found necessary, most likely due to the long-lasting tradition of tree planting on the METU campus. 50% of the participants stated the importance of designing walkways for disabled persons as well as the avoidance of vehicle-pedestrian exposure with natural or man-made buffers.

Table 3. Sidewalk design evaluations and possible improvements for METU Campus walkways by students (Survey Questions–Round 1)

Q1) Sufficiency of walking areas	N	Insufficient (%)	Sufficient (%)	
a) Pavement Quality	(302)	40.4 %	**58.0 %**	
b) Continuity	(302)	32.2 %	**66.1 %**	
c) Width	(305)	40.7 %	**58.6 %**	
d) Shortcuts	(305)	32.2 %	**67.1 %**	
e) Shading	(300)	46.3 %	**51.5 %**	
f) Safe Lightning	(303)	**64.2 %**	34.5 %	
g) Planned according to the disabled person	(301)	**88.6 %**	9.4 %	
h) Other safety precautions (Stragglers, vehicle conflicts)	(302)	**79.8 %**	18.6 %	
i) Marked crosswalks	(295)	34.2 %	**61.9 %**	
Q2) Importance of proposed infrastructure improvements N	Not Important	Slightly Important	Moderately Important	Extremely Important
a) Walkways on Campus should be;				
a1) increased	(297)	14.7 %	**29.0 %**	**36.5 %**	16.6 %
a2) continuous	(302)	10.7 %	**24.4 %**	**44.6 %**	18.6 %
a3) widened	(304)	16.0 %	**27.0 %**	**36.5 %**	19.5 %
a4) sheltered against weather	(304)	7.2 %	12.1 %	**40.7 %**	**39.1 %**
a5) sheltered against the sun	(302)	10.7 %	22.8 %	**34.2 %**	**30.6 %**
a6) shortcuts	(305)	3.3 %	16.0 %	**38.1 %**	**42.0 %**
a7) designed for disabled	(300)	8.5 %	8.8 %	**32.6 %**	**47.9 %**
a8) improved in desing&material	(305)	7.5 %	20.5 %	**39.4 %**	**31.9 %**
a9) better lit	(297)	6.2 %	18.6 %	**36.2 %**	**35.8 %**
b) Sidewalks on Campus should be;				
b1) at both sides of the road	(304)	5.9 %	9.4 %	**42.7 %**	**41.0 %**
b2) widened	(305)	8.1 %	21.8 %	**37.1 %**	**32.2 %**
b3) cut by fewer obstacles	(304)	17.3 %	**32.2 %**	**30.0 %**	19.5 %
b4) obstructed less by trees	(305)	**52.1 %**	**20.2 %**	16.0 %	11.0 %
b5) designed for disabled user	(298)	7.5 %	6.5 %	**32.9 %**	**50.2 %**
b6) less exposed to vehicles	(303)	10.4 %	19.5 %	**32.9 %**	**35.8 %**
c) Marked Crosswalks on Campus should be;				
c1) increased	(305)	7.8 %	22.1 %	**42.3 %**	**27.0 %**
c2) designed with a refuge	(299)	12.7 %	**28.7 %**	**37.5 %**	18.6 %
c3) equipped with traffic lights	(300)	15.3 %	**29.0 %**	**36.5 %**	16.9 %
d) Speed limit decreased	(303)	13.7 %	22.8 %	**33.6 %**	**28.7 %**
e) Illegal parking e avoided	(302)	7.5 %	15.6 %	**32.6 %**	**42.7 %**

As for safety precautions, crosswalks, presence of a median, and traffic lights seemed important to students, who also found a decrease in the speed limit in the campus important. Descriptive statistics of Round 2 (see Table 4) were parallel to the sufficiency evaluations in Round 1, walking infrastructure seemed mostly enough, but lightning, safety precautions, and arrangement for disabled users seemed problematic. Also, sheltering of the walkways against weather conditions and sun effect seemed nearly insufficient. When the evaluation of the selected 20 factors was compared based on the responses between the first and second rounds, mainly focusing on their importance and sufficiency, it was observed that what students stated important in the first round were also those that were found insufficient in the second one. These features included the items such as sheltering against weather and sun effects, having shortcuts, lightning, etc. Because students were randomly selected at both rounds, this showed a consistency in the evaluation of factors affecting walkability in the perceptions among students.

Table 4. Sidewalk design evaluations for METU Campus walkways by students (Survey Questions – Round 2)

Sufficiency of the walking environment	N	Totally Insufficient	Insufficient	Moderately Sufficient	Sufficient
a) Walkways in terms of					
a1) existing capacity/network	(311)	4.5 %	14.8 %	**48.2 %**	**32.5 %**
a2) continuity	(316)	6.0 %	21.8 %	**45.3 %**	**26.9 %**
a3) width	(314)	6.1 %	28.3 %	**41.1 %**	**24.5 %**
a4) sheltering against weather	**(315)**	**30.8 %**	**44.4 %**	18.4 %	6.3 %
a5) sheltering against sun effects	(314)	24.8 %	33.4 %	28.3 %	13.4 %
a6) having shortcuts	(311)	8.4 %	25.4 %	**43.1 %**	23.2 %
a7) planning for disabled use	(314)	**54.1 %**	**34.4 %**	8.0 %	3.5 %
a8) pavement quality	(314)	25.2 %	**38.9 %**	**29.9 %**	6.1 %
a9) lightening	(316)	17.4 %	**36.4 %**	**37.3 %**	8.9 %
a10) safety against stragglers	**(313)**	**52.7 %**	**27.8 %**	14.1 %	5.4 %
b) Sidewalks in terms of,					
b1) existence at both sides	(315)	9.8 %	**36.2 %**	**39.4 %**	14.6 %
b2) width	(315)	12.4 %	**35.6 %**	**40.3 %**	11.7 %
b3) less disruption by obstacles	(316)	14.6 %	**32.9 %**	**40.2 %**	12.3 %
b4) less disturbance by trees	(313)	16.6 %	**28.4 %**	**33.9 %**	21.1 %
b5) avoiding vehicular conflicts	(312)	16.3 %	**37.2 %**	**35.6 %**	10.9 %
c) Crosswalks in terms of,					
c1) number	(311)	7.1 %	**37.6 %**	**45.7 %**	9.6 %
c2) having refuge	(312)	7.7 %	**31.4 %**	**46.2 %**	14.7 %
c3) having traffic lights	(314)	11.5 %	**39.2 %**	**35.4 %**	14.0 %
d) Speed limits on roads	(311)	8.7 %	**28.9 %**	**46.9 %**	15.4 %
e) Avoiding parking affectis the pedestrian flow	(314)	10.5 %	**34.4 %**	**43.3 %**	11.8 %

Traditional survey questions were investigated to capture the Gender perception difference, and significant results were shown in Table 5. According to the results of the chi-square test for the sufficiency of walking areas, there is a statistically significant difference between men and women for continuity, safe lightning, other safety precautions for stragglers/ vehicle conflicts (p<.05), and a highly significant difference for marked crosswalks (p<.01). When the evaluations were examined, while women put forward a much more negative point of view in negative situations, men evaluated positive situations at a higher level. Considering the importance of characteristics of campus walkways in terms of preferring walking, sheltered against the weather is evaluated statistically different (p<.05) according to gender, while sheltered against sun, designed for disabled, improved in design and material and better lighting are evaluated highly different (p<.01). When this difference is examined, it is seen that women consider all characteristics more important than men. Women evaluated the design of sidewalks suitable for the disabled as more important than men ($\chi^2(3, 300) = 14.49$, p<0.01). It is also seen that there is a significant difference between women and men in equipping the marked crosswalks with traffic lights ($\chi^2(3, 300) = 11.14$, p<0.05). In addition, a statistically high difference was observed in terms of reducing the speed limits on campus by gender ($\chi^2(3, 303) = 11.76$, p<0.01). Finally, the fact that walking paths have shortcuts was rated as more important by women.

Table 5. Chi-Square Analysis of the Survey Question by Gender Differences

ROUND 1						
Q1)	**N**	**Gender**	**Sufficient**		**Insufficient**	
b) Continuity*	(302)	Female	**61.8 %**		38.2 %	
		Male	**72.7 %**		27.3 %	
f) Safe Lightning *	(303)	Female	29.6 %		**70.4 %**	
		Male	40.4 %		**59.6 %**	
h) Other safety precautions (stragglers, vehicle conflicts)*	(302)	Female	14.4 %		**85.6 %**	
		Male	23.5 %		**76.5 %**	
i)Marked crosswalks **	(295)	Female	**55.7 %**		44.3 %	
		Male	**73.3 %**		26.7 %	
Q2)	**N**	**Gender**	**Not Important**	**Slightly Important**	**Moderately Important**	**Extremely Important**
Walkways on Campus should be,						
a4) sheltered against weather	(304)	Female	3.9 %	11.8 %	**37.9 %**	**46.4 %**
		Male	10.6 %	12.6 %	**44.4 %**	32.5 %
a5) sheltered against sun**	(302)	Female	6.0 %	19.9 %	**35.8 %**	**38.4 %**
		Male	15.9 %	**26.5 %**	33.8 %	23.8 %
a7) designed for disabled**	(300)	Female	2.7 %	9.4 %	32.9 %	**55.0 %**
		Male	14.6 %	8.6 %	33.8 %	**43.0 %**
a8) improved in design and material**	(305)	Female	3.9 %	16.3 %	**39.9 %**	**39.9 %**
		Male	11.2 %	**25.0 %**	**38.8 %**	24.3 %
a9) better lit**	(297)	Female	2.7 %	14.7 %	35.3 %	**47.3 %**
		Male	10.2 %	23.8 %	**39.5 %**	26.5 %
Sidewalks should be,						
b5) planned for disabled us**	(298)	Female	2.0 %	6.0 %	32.5 %	**59.6 %**
		Male	13.6 %	7.5 %	35.4 %	**43.5 %**
Marked Crosswalks should be						
c3) equipped with traffic lights*	(300)	Female	11.3 %	**24.7 %**	**44.7 %**	19.3 %
		Male	20.0 %	**34.7 %**	30.0 %	15.3 %
In campus speed limit should decrease	(303)	Female	7.9 %	21.1 %	**39.5 %**	**31.6 %**
		Male	19.9 %	25.2 %	28.5 %	26.5 %
ROUND 2						
	N	**Gender**	**Totally Insufficient**	**Insufficient**	**Moderately Sufficient**	**Sufficient**
Walkways in terms of						
a6) having shortcuts*	(310)	Female	9.7 %	18.8 %	**42.3 %**	**24.2 %**
		Male	6.9 %	**33.1 %**	**38.6 %**	21.4 %

Note:* p < .05, ** p < .01

4.2. GIS-Based Evaluation of Usage of Walkway Infrastructure

Using the digitized routes and calculating their frequencies at link levels, an intensity map showing the most preferred pedestrian road segments was created in the GIS environment as shown in Figure 3. Frequency seemed to be very high levels at the main alley and spread to the expected attractive points such as the shopping area, recreational area, and dormitories. Walkways at the outer parts of the first loop seemed to have very low demand, especially at the new dormitory region (Zone 14).

4.3. Walkability of Campus Zones

To compare the walking behaviors of participants

from different departments, 4 zones were selected which were located in different parts of the campus (see Figure 4).

• Zone 1 is located at the Northwest corner, far from central campus facilities and other departments (Figure 4a).

• Zone 6 is located at the northeast corner of the campus. It is in the alley and closer to the main attraction points such as the library, cafeteria, and shopping area (Figure 4b).

• Zone 21 is located on the southwest side of the campus. It is divided by a forest area through the campus center (Figure 4c).

• Zone 19 is located on the southeast side of the campus, which is also in the alley (Figure 4d).

The common destination points of all the paths

departing from these zones were found are library (Zone 26), cafeteria (Zone24), and shopping area (Zone 28). The students also preferred walking through the alley in their routes more than sidewalks along the roads as seen in Figure3. As a difference, walking to the campus entrances A1 and A2 (which also has metro stations) were preferred by the students from the northern zones, while students at the departments in the southern zones rarely walked to these destinations. It was also possible to display the route

differences between male and female students by simply dividing the routes and creating gender-based maps as shown in Figure 5. Even with this example, it was possible to point out the difference in the variety of destinations and lengths of pedestrian routes stemming from Zone 21. However, it is too soon to make any general comments on the matter without generating such maps for more buildings/zones.
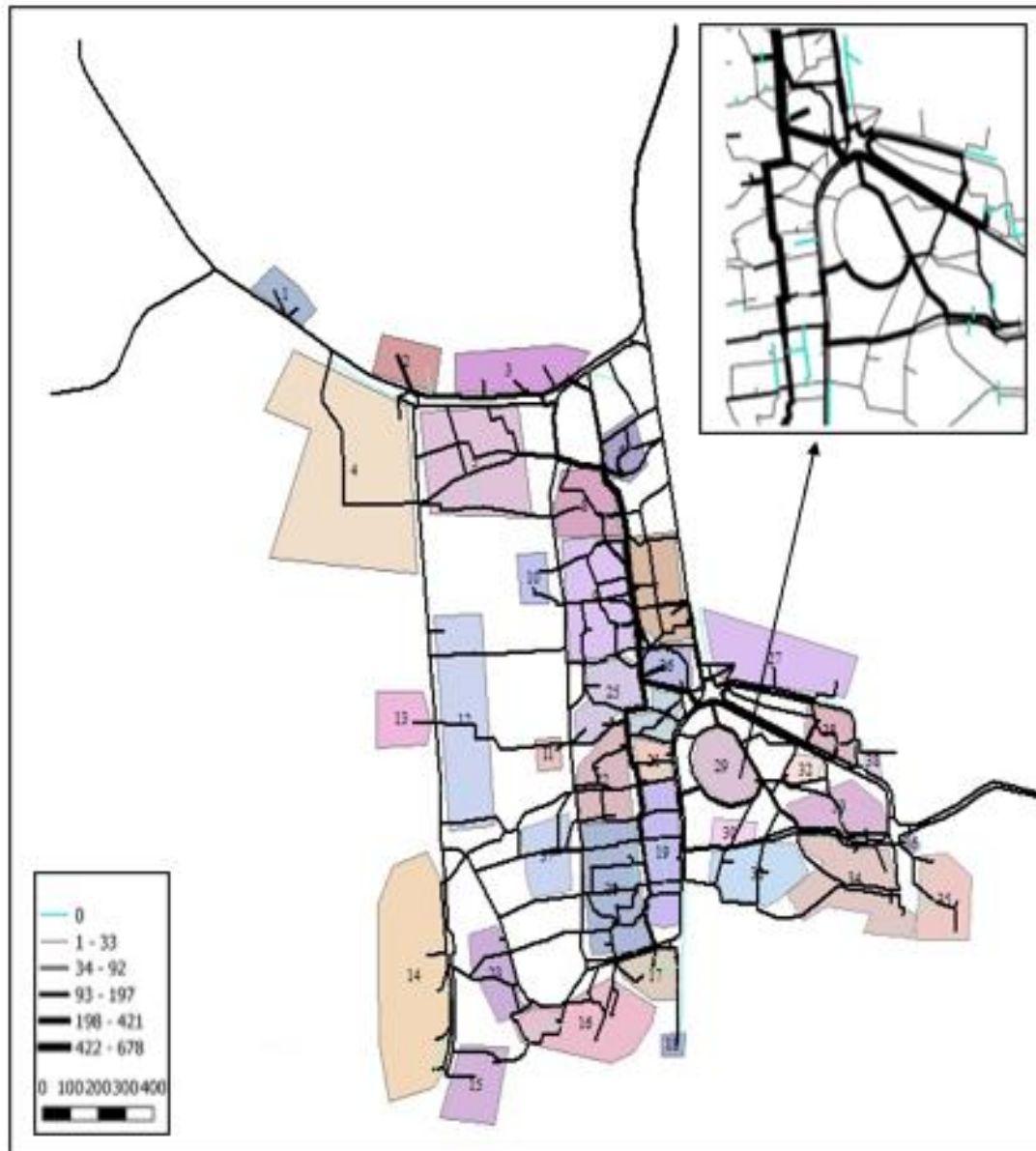

Figure 3. Usage of pedestrian roadway segments among stated routes.

## 5. Conclusions and Further Recommendation

This study showed the traditional questions assessing sufficiency or importance of various factors affecting walkability, were not capable of displaying the spatial distribution of their impact within a built environment. Also, unless asked specifically for a location, when asked to evaluate the campus as a whole, respondents were forced to state a more overall evaluation, whereas there were subregions with lower walkability levels. Also, when a question includes scales or choices (i.e. Sufficient/Insufficient or between 1 and 4) this does not produce insights per se. People do not differentiate the terms of sufficiency or importance and use them

interchangeably, which produced trivial responses (i.e. very important or very enough).

Route-based walking data is stronger in terms of network usage and infrastructure, revealing information about personal choices (i.e. preference of sidewalks versus pedestrian alleys, sheltered regions versus unsheltered ones, etc.). The data collection period does not present a serious deficiency in terms of reflecting the walkability of the campus in general due to the general built environment remaining similar. When digitized in a GIS environment and supported with land use and network data (i.e. traffic volumes, roadway type, pavement type, etc.), walking routes lead to better modeling of walking behavior in a region. Furthermore, analysis of building/zone-based walking behaviors gave information about willingness to walk for different attraction points. A major drawback of route-based data collection is the additional time consumption due to manual digitization of stated routes, which can be improved if real-time GIS-based data collection tool should be developed.
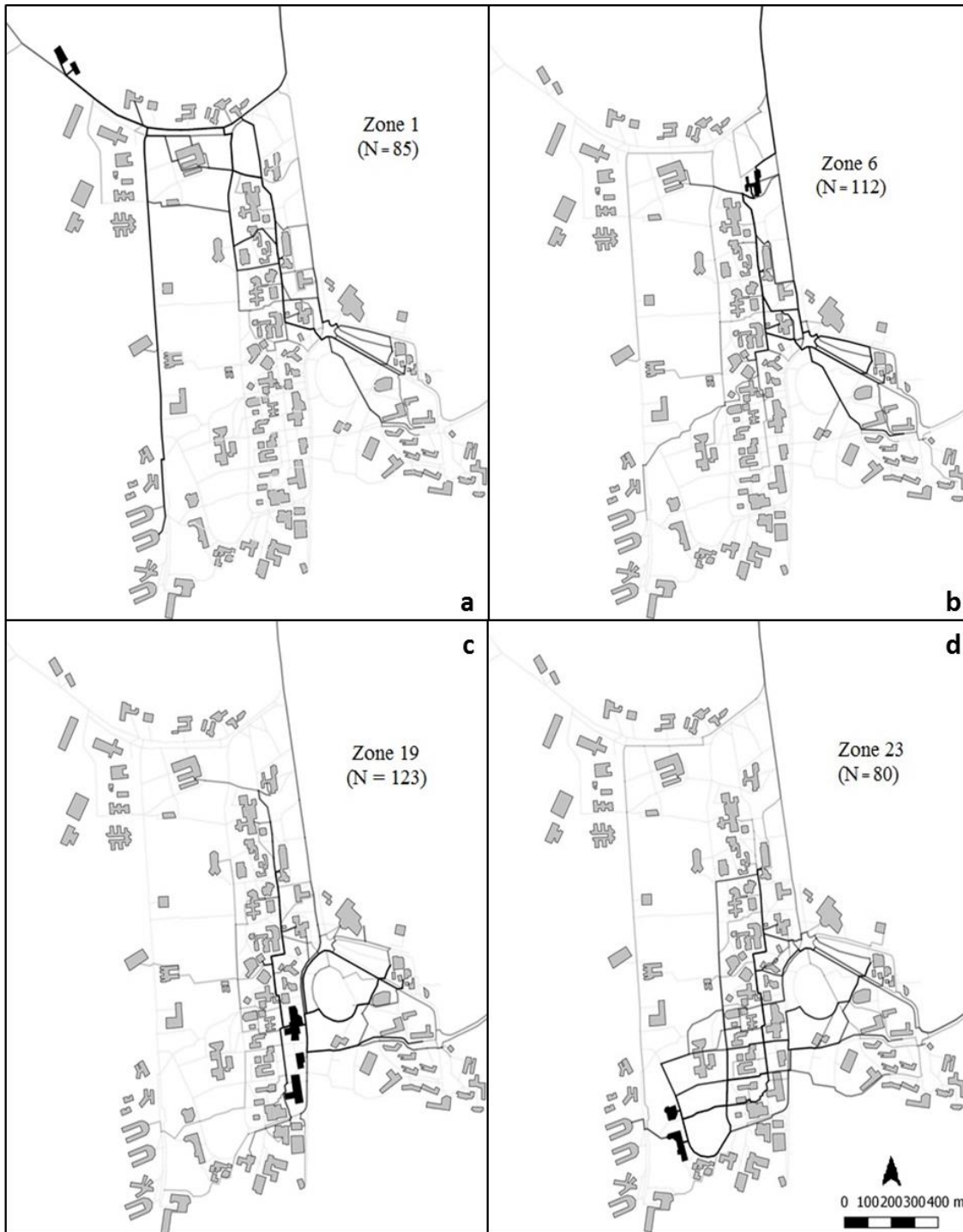
Figure 4. Zone-based stated walkway routes for a) Zone 1, b) Zone 6, c) Zone 19 and d) Zone 23
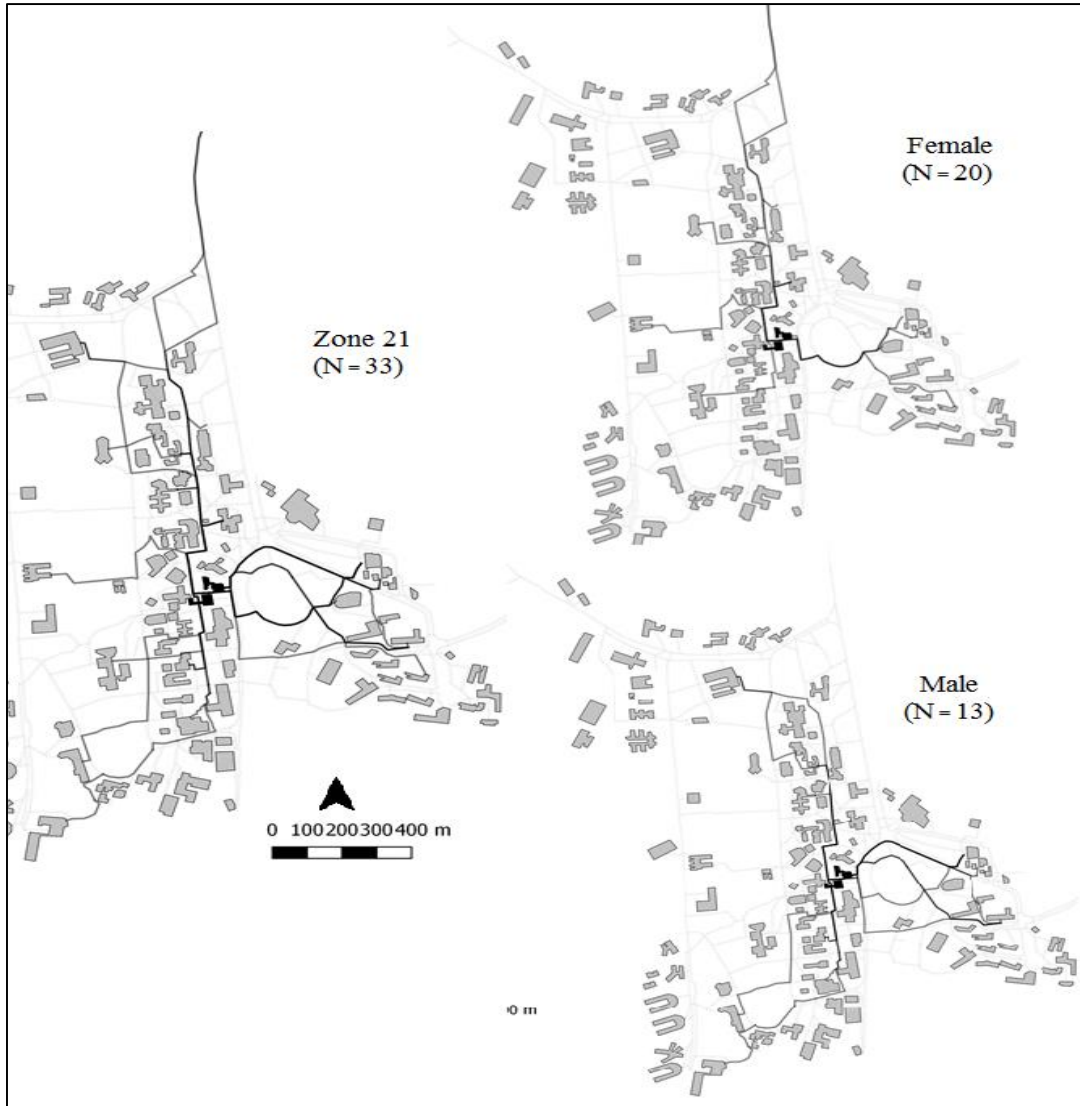
Figure 5. Zone-based stated walkway routes for a) Zone 1, b) Zone 6, c) Zone 19 and d) Zone 23

Acknowledgments

Declaration of Ethical Standards

The author of this article declares that the materials and methods used in this study do not require ethical committee permission and/or legal-special permission.

Conflict of Interest

The author declares that she has no known competing financial interests or personal relationships that could have appeared to influence the work reported in this paper.

References

[1] Litman, T., 2003. Economic Value of Walkability. Transportation Research Record, **1828** (1), pp. 3–11.

[2] Abley, S. 2005. Walkability Scoping Paper. Retrieved March, February 2.

[3] TuydesYaman, H., Karatas, P. and Altintasi, O. 2015. Lessons Learnt from METU Campus Walkability Evaluations. Transportation Research Board (TRB) 94th Annual Meeting, 11-15 January.

[4] Karatas, P. and TuydesYaman, H. 2016. A pairwise Comparison of Different Pedestrian LevelofService (PLOS) Ratings. Transportation Research Board (TRB) 95th Annual Meeting, 8-12 January.

[5] Manaugh, K., and El-Geneidy., A. 2011. Validating Walkability Indices: How Do Different Households Respond to the Walkability of Their Neighborhood. Transportation Research Part D: Transport and Environment, **16** (4). pp. 309–15.

[6] Gori, S., Nigro, M., &Petrelli, M. 2014. Walkability Indicators for Pedestrian Friendly Design. Transportation Research Board 93rd Annual Meeting, January 1–11.

[7] Azmi, D. I. and Hafazah, A. K. 2012. Implications of Walkability Towards Promoting Sustainable Urban Neighbourhood. Procedia - Social and Behavioral Sciences 50, July 04–13.

[8] Blecic, I., Cecchini, A., and Trunfio, G. A. 2015. Towards a Design Support System for Urban Walkability. Procedia Computer Science 51. Elsevier Masson SAS: 2157–67.

[9] Dovey, K. and Pafka, E. 2020. What is walkability? The Urban DMA. Urban Studies, **57** (1), pp. 93-108.

[10] Bias, T. K., Leyden, K. M., Abildso, C. G., Reger-Nash, B., & Bauman, A. 2010. The importance of being parsimonious: reliability of a brief community walkability assessment instrument. Health & Place, **16**(4), pp.755–758.

[11] Millington, C., Ward Thompson, C., Rowe, D., Aspinall, P., Fitzsimons, C., Nelson, N., &Mutrie, N. 2009. Development of the Scottish Walkability Assessment Tool (SWAT). Health & Place, **15**(2), pp.474–81.

[12] Peiravian, F., Derrible, S. and Ijaz, F. 2014. Development and Application of the Pedestrian Environment Index (PEI). Journal of Transport Geography 39. Elsevier Ltd: 73–84.

[13] Keyvanfar, A., Ferwati, M. S., Shafaghat, A., and Lamit, H. A. 2018. Path Walkability Assessment Index Model for Evaluating and Facilitating Retail Walking Using Decision-Tree-Making (DTM) Method. Sustainability10, 1035.

[14] Garau, C., Annunziata, A. and Yamu, C. A. 2020. Walkability Assessment Tool Coupling Multi-Criteria Analysis and Space Syntax: Case Study of Iglesias, Italy. European Planning Studies.

[15] Labdaoui, K., Mazouz, S., Moeinaddini, M., Cools, M., and Teller, J. 2021. The Street Walkability and Thermal Comfort Index (SWTCI): A new assessment tool combining street design measurements and thermal comfort. Science of Total Environment 795, 148663.

[16] Front Seat Management, LLC. Walk Score® Methodology. 2011. Retrieved from https://www.walkscore.com/methodology, at September 8,2021.

[17] Azmi, D. I., Hafazah, A. K., and Mohd Zamreen, M. A. 2012. Comparing the Walking Behaviour between Urban and Rural Residents. Procedia - Social and Behavioral Sciences 68. Elsevier B.V.: 406–16.

[18] Azmi, D. I., Hafazah A. K., and Puziah A. 2013. Comparative Study of Neighbourhood Walkability to Community Facilities between Two Precincts in Putrajaya. Procedia - Social and Behavioral Sciences 105. Elsevier B.V.: 513–24.

[19] Karim, H. A., and Diyanah I. A. 2013. Convenience and Safety of Walking Experience in Putrajaya Neighbourhood Area. Procedia - Social and Behavioral Sciences 101. Elsevier B.V.: 318–27.

[20] Liu, B., Zhi, W. W., and Yu B. Z. 2014. Investigating Pedestrian Behavior Differences of Walking Streets and Their Effect Factors with Three Wuhu Cases. Applied Mechanics and Materials 587-589: 1879–83.

[21] Humpel, N., Neville, O., Iverson, D., Leslie, E., and Bauman, A. 2004. Perceived Environment Attributes, Residential Location, and Walking for Particular Purposes. American Journal of Preventive Medicine **26** (2), pp.119–25.

[22] Park, S., Deakin, E., and Lee, J. S. 2014. Perception-Based Walkability Index to Test Impact of Microlevel Walkability on Sustainable Mode Choice Decisions. Transportation Research Record: Journal of the Transportation Research Board, **2464**, pp. 126–34.

[23] Fairnie, G A, Wilby, D. J. R. and Saunders, L. E. 2016. Active Travel in London: The Role of Travel Survey Data in Describing Population Physical Activity. Journal of Transport and Health, **3** (2). Elsevier: 161–72.

[24] Lu, Y., Sarkar, C., and Xiao, Y. 2018. The effect of street-level greenery on walking behavior: Evidence from Hong Kong. Social Science & Medicine 208, pp. 41-49.

[25] Li, S., Zhao, P., Zhang, H., and Quan, J. 2019. Walking behavior in the old downtown Beijing: The impact of perceptions and attitudes and social variations. Transport Policy, **73**, pp. 1-11.

[26] Akar, G., Flynn, C. and Namgung, M. 2012. Travel Choices and Links to Transportation Demand Management Case Study at Ohio State University. Transportation Research Record, no. 2319, pp. 77–85.

[27] Lee, J., Shepley, M.M. 2020. College Campuses and StudentWalkability Assessing the Impact of Smartphone Use on Student Perception and Evaluation of Urban Campus Routes. Sustainability 12, MPDI.

[28] Baran, P.K., Smith, W.R., Türkoğlu, H.D., Marans, R.W., Bölen, F. 2009. Walking Behavior in Istanbul: Individual Attributes, Neighborhood Context and Perceived Safety. A|Z ITU Journal of the Faculty of Architecture, **6**(1), pp. 21-40.

[29] Kirimtat, A., Paykoç Ozcelik, E. 2015. Walkability Assessment of Mavişehir-Alaybey Coast Region in İzmir, Turkey: Building, Green Area and Path Analyses. International Congress Energy and Environment Engineering and Management.

[30] Ozbil, A., Argin, G., Yesiltepe, D. 2016. Pedestrian route choice by elementary school students: the role of street network configuration and pedestrian quality attributes in walking to school. International Journal of Design Creativity and Innovation, **4**(2), pp. 67-84.

[31] Unal, M., Uslu, C. 2016. GIS-Based Accessibility Analysis of Urban Emergency Shelters: The Case of Adana City. The International Archives of the Photogrammetry. Remote Sensing and Spatial Information Sciences, Volume XLII-2/W1, 2016 3rd International GeoAdvances Workshop, 16–17 October 2016, Istanbul, Turkey

[32] Ceylan, R. 2018. A GIS-Based Walkable Service Area Analysis from a Smart Growth Perspective in the City of Edirne. Journal of Multidisciplinary Research in Sustainability, 2018.

[33] Vural-Arslan, T., Durak, S., Dizdar-Gebesce, F., Balcik, B. 2018. Assessment of Factors Influencing Walkability in Shopping Streets of Tourism Cities: Case of Bursa, Turkey. International Tourism Studies Association, **4**(3), pp. 330-341.

[34] Doğan, U. 2021. Examining Urban Design Characteristics of City Centers Using Walkability Criteria: Case of Turkey. ASCE Journal of Urban Planning and Development, **147**(2).

[35] Rashidi, S. 2019. Analyzing Safety Toward a Walkable Campus: A Case Study of Middle East Technical University. Master Dissertation, Middle East Technical University, City and Regional Planning Department, Ankara, Turkey.

[36] Hsiao, S., Lu, J, Sterling, J., and Weatherford, M. 1997. Use of Geographic Information System for Analysis of Transit Pedestrian Access. Transportation Research Record, **1604**(1), pp. 50–59.

[37] Schlossberg, M. 2006. From TIGER to Audit Instruments: Measuring Neighborhood Walkability with Street Data Based on Geographic Information Systems. Transportation Research Record, **1982**(1), pp. 48–56.

[38] Owen, N., Cerin, E., Leslie, E., duToit, L., Coffee, N., Frank, L.D., Bauman, A.E., Hugo, G., Saelens, B.E., and Sallis, J.F. 2007. Neighborhood Walkability and the Walking Behavior of Australian Adults American Journal of Preventive Medicine, **33** (5), pp. 387–95.

[39] Leslie, E., Coffee, N., Frank, L., Owen, N., Bauman, A., & Hugo, G. 2007. Walkability of local communities: using geographic information systems to objectively assess relevant environmental attributes. Health & Place, **13**(1), pp. 111–122.

[40] Hajna, S., Dasgupta, K., Halparin, M., & Ross, N. A. 2013. Neighborhood walkability: field validation of geographic information system measures. American Journal of Preventive Medicine, **44**(6), pp. 51–59.

[41] Cubukcu, E., Hepguzel, B., Onder, Z., and Tumer, B. 2015. Active Living for Sustainable Future: A Model to Measure 'Walk Scores' via Geographic Information Systems. Procedia, Social and Behavioral Sciences 168. Elsevier B.V.: pp. 229–37.

[42] Ellis, G., Hunter, R., Tully, M.A, Donnelly, M., Kelleher, L. and Kee, F. 2016. Connectivity and Physical Activity: Using Footpath Networks to Measure the Walkability of Built Environments. Environment and Planning B: Planning and Design **43** (1), pp. 130–51.

[43] Sun, G, Oreskovic, N M and Lin H. 2014. How Do Changes to the Built Environment Influence Walking Behaviors? A Longitudinal Study within a University Campus in Hong Kong. International Journal of Health Geographics [Electronic Resource] 13: 28.

[44] Sun, G., Zacharias, J., Ma, B., and Oreskovic, N. 2015. How Do Metro Stations Integrate with Walking Environments? Results from Walking Access within Three Types of Built Environment in Beijing. Cities 56. Elsevier B.V.: Forthcoming.